New approaches to treating cancer using immune-checkpoint blockade



Martin Fellermeyer

Somerville College

University of Oxford

A thesis submitted for the degree of

Doctor of Philosophy

Hilary 2023

Acknowledgements

First, I would like to thank my supervisors Simon Davis, Vincenzo Cerundolo and Uzi Gileadi for providing me with the opportunity to work in their labs. It was a pleasure to work on the exciting aspects of immune-checkpoint inhibitors and I am particularly grateful to have had the opportunity to test, sometimes far-fetched, ideas on how to modify antibodies. Thanks you Simon for giving me the freedom to try (and fail with some of) these ideas as well as for improving my writing skills, especially for compound-adjective-related hyphens. I would like to thank Uzi for sharing his animal expertise with me. Finally, while I only met Enzo briefly before he passed away in January 2020, I am grateful for the support and encouragement he provided.

While searching for interesting DPhil projects and groups, I paid a particular focus on how sociable the working environment is, and I am very grateful that the rumours in Oxford about the Davis lab were true. Thanks to all past and present members of the group for rigorously adhering to coffee and lunch breaks! Thank you Mai for your assistance throughout the past four years; despite your immense workload, you always found the time to explain, demonstrate or help with things. Thank you Mafalda for sharing your objective, careful assessment on lab- and life-related topics. Thank you Oliver for always being ready to help and sometimes even drop of pastéis de nata at my house at 11 pm. Rob, thanks for being the other 'antibody boy' in the lab (sorry João) and for sharing your practical and theoretical experience. It was great not to be the only one working on antibodies in the lab and I am very grateful for your calm, reassuring support during some 'breakdowns' in the Biacore room. Thanks Caitlin for being a great colleague & friend and for making this world a more social place; I am truly impressed by your tireless effort to organise things. Thank you João for all the engaging discussions, whether scientific or not, and for being one of the strongest supporters of coffee breaks. Thank you Ed for (pretending to?) care about extended antibodies, for being (the best?) DJ at WGSA parties and, more importantly, for founding the 'Documentary club'. Thank you Nicole for sharing my passion for bouldering and introducing me to my first (and last?) bubble tea. Thank you Sumana for sharing your great approach to science with me and for your patience teaching me statistics. Thanks Toby for your effort in keeping our lab tidy and organised

(a potentially impossible task?), as well as for organising the 'Science Discussion Group' meetings. Finally, thank you Janina for being a great honourable member of our lab, for joining the bouldering sessions and for all the great chat.

I would also like to thank the facilities within the University of Oxford for providing me with the technical assistance during my project. A special thanks goes to the WIMM Flow Cytometry facility, the BMS JR facility, the HIU lab management team as well as the WIMM canteen staff.

A big thank you goes out to all my close friends in Oxford. Thank you John, Rassin and Andrea for the countless memories we had together. Whether short walks in Oxford, longer walks around Oxford, formal dinners, pub nights, weekend trips or skiing holidays, we had an amazing time together and I'm looking forward to our future get-togethers. Thank you Mati, for being a great, intelligent, well-read friend and colleague, and for sharing my passion for Negronis.

Thanks to my housemates, Fabi, John, Antony, Laura and Katie for making this house such a wonderful, social place to live in. I could not have asked for a better 'home'. From chilled BBQ/movie/board game nights and intense political discussions to strobe-light techno parties, this was the perfect mix and I wouldn't want to miss any of those memories. Thanks for holding out the various COVID-19 lockdowns together and for providing an exceptional dinner plan throughout the time. It is a shame that the Michelin Guide-inspectors were not allowed in due to social distancing measures. Thank you Fabi for joining me here in Oxford, it is a great privilege to have a close friend from Germany not only in the same city, but also in the same house. Thank you for inspiring me, whether this is in the kitchen trying new recipes, sharing old-but-gold Scooter songs or taking me for cycle rides around Oxford.

Thank you Pawala, Olga, Jesús and Johannes for immediately accepting me as a friend when Lilli introduced us. I'm very happy to be able to call you my friends.

Another huge thanks goes to all my friends in Germany, that accompanied me on my way. Especially to the Lateinecke, Jannik and Thomas, as well as David and Max, my closest high school friends. Thank you Sina, Maxi and Steffen during my time in Munich and Bene, Carsten and Miki in Bonn.

Lilli, thank you for being there literally from day 1 (26^{th} of September 2017) of my time in Oxford. It was during the bus ride with the infamous # 10 line that I realised what an amazing person you are. Thank you for always supporting me, listening to me and believing in me. But also for challenging me, and for helping me to improve myself. Your never-ending energy, excitement to organise social events and ambition to make this world a better place is truly impressive and it's a great gift to have you in my life.

To my family. Ohne euch wäre ich nicht hier. Die Gewissheit zu haben, dass es immer drei Menschen gibt, die zu mir halten und mich ohne zu hinterfragen unterstützen, ist ein unglaublich wertvolles Privileg. Danke Mama für all deine Empathie und ernstgemeintes Interesse an meiner Arbeit. Danke Papa für deine ruhige, rationale Art mit Problemen umzugehen. Danke Simon für deine unermüdliche Unterstützung auf meinem Weg, ob persönlich oder akademisch. Danke für deinen Ehrgeiz, mit dem du mich angesteckt hast. Auch wenn es am Anfang nicht immer geklappt hat; du hast spannende Lösungsansätze gefunden wie einen 'kostenlosen, nicht-nichteinlösbaren Gutschein' zur Unterstützung bei Bewerbungen zu meinem Geburtstag.

Finally, I would like to comment on the invaluable contributions of the mice used in the course of my DPhil research. Animal experiments are crucial in advancing our understanding and scientific knowledge. It is essential to acknowledge the ethical responsibility that comes with such endeavours, and I wish to emphasise that the decision to include these animals in our studies was made with utmost consideration and respect for their well-being. Their sacrifice and the insights gained from their participation underscore the significance of ethical research practices and the pursuit of responsible scientific exploration.

Funding and Authorship Declaration

This work received support from multiple funding sources, which are shown here in alphabetical order:

- Oxford-Thatcher Graduate Scholarship
- Radcliffe Department of Medicine Scholarship

I declare that this thesis has never been submitted, either in the same or a different form, to this or another University for a degree or qualification. In some instances, the work of others is presented in this thesis. In particular, I wish to acknowledge that:

- The code for data analysis in R was provided by Sumana Sharma
- Imaging experiments and image analysis were carried out by Edward Jenkins and Daniel Heraghty (University of Cambridge)
- hCD200R-mFc-His protein was produced by Heather Brouwer
- mFcγRIIb-His protein was produced by Nicole Ashman
- AT128, an anti-mFcγRIIb blocking antibody, was provided by Mark Cragg (University of Southampton)
- Cloning of antibodies in Chapter 5 was supported by Mai Vuong
- Cloning of antibodies in Chapter 6 was carried out by Mai Vuong
- Experiments in Sections 6.2.4 and 6.2.5 were performed by Deborah Greis (University of Tübingen, Germany) under the supervision of the author

The work in this thesis was carried out during my time as a DPhil student at the Weatherall Institute of Molecular Medicine, under the supervision of Simon Davis, Vincenzo Cerundolo and Uzi Gileadi. Data in Chapters 3 and 4 have been published[1], which is indicated in the respective figures.

Approximate word count: 49,000

Martin Fellermeyer (21/04/2023)

Abstract

While immune-checkpoint blockade has truly revolutionised cancer treatment in many aspects, the benefits remain limited to certain tumour types. Furthermore, within those tumours that are likely to improve upon treatment, only a fraction of patients actually respond, which highlights the need for novel approaches to enhance this therapy. The work outlined in this thesis aimed to address this issue by employing two distinct strategies to improve on PD-1 blockade using the clinically-approved antibody nivolumab. As anti-PD-1 antibodies mostly act on T cells, the first approach trialled a new combination therapy comprising nivolumab mIgG1 and OX108, a CD200R blocking antibody. CD200R is an inhibitory immune receptor preferentially expressed on myeloid cells and, therefore, blocking PD-1 and CD200R should reactivate T cells and myeloid cells simultaneously. While the PD-1 blockade-resistant model LLC1 did not exhibit any improvements upon combination therapy, the sensitive model MC38 produced a trend towards more complete responses, which might be linked to the expression of CD200 on these cells. The second strategy focused on improving the design of monoclonal antibodies used for immune-checkpoint blockade in order to enhance their efficacy. Based on the kinetic-segregation model for receptor triggering, a potential agonistic effect of nivolumab mIgG1 on PD-1 was investigated, a phenomenon that should be reduced upon increasing the size of the receptor/antibody/FcγR complex. While nivolumab mIgG1 indeed exhibited FcγR-dependent agonistic activity *in vitro*, this could be diminished by (i) employing two different approaches to extend nivolumab mIgG1 or (ii) mutation of the FcγR-binding domain (nivolumab mIgG1 D265A). Intriguingly, whereas the extended antibodies produced a significantly decreased enrichment of PD-1 in 'close contacts' compared to nivolumab mIgG1 D265A, this did not translate into an increased T-cell activation. Finally, nivolumab mIgG1 D265A exhibited increased efficacy in the MC38 colorectal cancer model compared to nivolumab mIgG1, in accordance with previous studies investigating the confounding effects of FcγR binding on anti-PD-1 antibodies.

Contents

List of Figures xii

List of Tables xv

List of Abbreviations xvi

1 Introduction 1

1.1 Cancer immunology . . . 2
1.1.1 The hallmarks of cancer . . . 2
1.1.2 The cancer-immunity cycle and immunoediting . . . 3
1.1.3 The tumour microenvironment . . . 5
1.1.3.1 Macrophages . . . 5
1.1.3.2 Dendritic cells . . . 6
1.1.3.3 Myeloid-derived suppressor cells . . . 7
1.1.3.4 T cells . . . 7
1.1.3.5 NK cells . . . 8
1.1.3.6 B cells . . . 9
1.2 Non-catalytic tyrosine-phosphorylated receptors . . . 10
1.2.1 NTR triggering . . . 11
1.2.1.1 Aggregation models . . . 12
1.2.1.2 Conformational change models . . . 12
1.2.1.3 Segregation models . . . 13
1.2.2 KS-based triggering of NTRs by antibodies . . . 14
1.2.2.1 Other mechanisms for antibody agonism . . . 17
1.2.3 Immune checkpoints . . . 20
1.2.4 Inhibitory immune checkpoints in cancer . . . 21
1.2.4.1 CTLA-4 inhibitory functions . . . 21
1.2.4.2 PD-1 inhibitory functions . . . 24
1.2.4.3 CD200R inhibitory functions . . . 27
1.3 Monoclonal antibody therapy . . . 32
1.3.1 Antibody structure . . . 33
1.3.2 Fcγ receptors . . . 34

1.3.3 Monoclonal antibodies for cancer therapy . . . 36
1.3.3.1 Cytotoxic tumour-targeting antibodies . . . 37
1.3.3.2 Antibodies modulating tumour cell activation and growth . . . 38
1.3.3.3 Antibodies targeting immune checkpoints . . . 38
1.4 Anti-PD-1 antibodies for cancer therapy . . . 42
1.4.1 Cells targeted by anti-PD-1 therapy . . . 42
1.4.2 Biomarkers predicting PD-1 blockade efficacy . . . 45
1.4.3 Myeloid cell interaction with PD-1 blockade . . . 46
1.4.4 Rationale for combining PD-1 and CD200R blockade . . . 49
1.5 Work preceding this thesis . . . 51
1.6 Hypothesis and objectives of this thesis . . . 54

2 Materials and Methods **56**
2.1 List of materials . . . 57
2.1.1 List of general and molecular biology reagents . . . 57
2.1.2 List of plasmids . . . 58
2.1.3 List of enzymes . . . 59
2.1.4 List of solutions and buffers . . . 59
2.1.5 List of commercial assays . . . 60
2.1.6 List of cell lines . . . 60
2.1.7 List of cell culture reagents . . . 60
2.1.8 List of primers . . . 61
2.1.9 List of commercial antibodies . . . 62
2.2 Methods . . . 63
2.2.1 Cell culture . . . 63
2.2.1.1 Maintenance of cell lines . . . 63
2.2.1.2 Cryopreservation . . . 64
2.2.1.3 Lentivirus production and transduction . . . 65
2.2.1.4 Protein production . . . 65
2.2.1.5 *In vitro* IFN-γ stimulation . . . 66
2.2.1.6 *In vitro* T-cell activation assay . . . 67
2.2.2 Molecular cloning . . . 67
2.2.2.1 Overview . . . 67
2.2.2.2 Polymerase chain reaction . . . 68
2.2.2.3 Agarose gel electrophoresis . . . 68
2.2.2.4 Restriction enzyme digest . . . 69
2.2.2.5 Ligation . . . 69
2.2.2.6 Transformation . . . 69

2.2.2.7 Small-scale preparation of plasmid DNA 70
2.2.3 Protein purification 70
2.2.3.1 Protein A purification 70
2.2.3.2 His purification 71
2.2.3.3 Size-exclusion chromatography 71
2.2.3.4 Polyacrylamide gel electrophoresis 72
2.2.3.5 Endotoxin testing and removal 73
2.2.3.6 Final sample processing 73
2.2.3.7 Surface plasmon resonance 74
2.2.4 Flow cytometry 75
2.2.4.1 General 75
2.2.4.2 Antibody blocking assay 78
2.2.4.3 Quantibrite 79
2.2.4.4 *In vitro* T-cell activation assay 79
2.2.4.5 Fluorescence-activated cell sorting 79
2.2.5 RNA sequencing 80
2.2.5.1 RNA isolation 80
2.2.5.2 Data processing and differential gene expression analysis 80
2.2.5.3 STRING network analysis 81
2.2.6 Animal work 81
2.2.6.1 General 81
2.2.6.2 Subcutaneous tumour model 82
2.2.6.3 Spleen isolation 83
2.2.6.4 Tumour isolation 83
2.2.6.5 Lymph node isolation 84
2.2.7 Statistical analysis 84

3 Antibody production and cancer models 85
3.1 Rationale 85
3.2 Results 86
3.2.1 Design of mIgG1 antibodies 86
3.2.2 Purification of mIgG1 antibodies using Protein A and SEC 87
3.2.3 Endotoxin testing and optimisation 88
3.2.4 SPR validation of antibodies 89
3.2.5 *Ex vivo* validation of antibodies 89
3.2.6 *In vitro* characterisation of MC38 and LLC1 cells 91
3.2.7 *In vivo* profiling of MC38 and LLC1 tumours 93
3.2.8 Response to mNivo monotherapy 95

3.2.9 *In vivo* comparison of different MC38 cell lines 97
3.2.10 Differential gene expression analysis of MC38 cell lines . . 99
3.2.11 Identification of common pathways in resistant MC38 cells 102
3.3 Discussion 105

4 Combination therapy of nivolumab mIgG1 and OX108 108
4.1 Rationale 108
4.2 Results 109
4.2.1 *In vitro* validation of mNivo and OX108 109
4.2.2 Combination therapy in LLC1 tumours 113
4.2.3 Immune cell infiltration in LLC1 upon treatment 115
4.2.4 Combination therapy in PD-1 blockade-sensitive MC38 tumours 115
4.2.5 Immune cell infiltration in MC38-sensitive tumours upon treatment 117
4.3 Discussion 123

5 Extending nivolumab mIgG1 to increase efficacy 129
5.1 Rationale 129
5.2 Results 131
5.2.1 Design of extended antibodies 131
5.2.2 Purification of extended antibodies using Protein A and SEC 134
5.2.3 Comparison of size using SEC 135
5.2.4 SPR validation of extended antibodies 135
5.2.5 *In vitro* T-cell activation assay 143
5.2.6 *In vivo* tumour challenges with MC38 models 145
5.2.7 *In vivo* challenge with MC38-sensitive mFcγRIIb expressing tumours 149
5.2.8 Combination of PD-1 and mFcγRIIb blockade 152
5.2.9 Comparison of mNivo and mNivo D265A across experiments 152
5.3 Discussion 155

6 Rigid, extended forms of nivolumab mIgG1 to increase efficacy 162
6.1 Rationale 162
6.2 Results 164
6.2.1 Design of hinge-deleted antibodies and Fc-linker optimisation 164
6.2.2 Validation of hinge-deleted antibodies and Fc-linker optimisation 167
6.2.3 Design of rigid, extended antibodies 169

6.2.4 Purification of rigid, extended antibodies using Protein A and SEC . . . 171
6.2.5 Comparison of size using SEC . . . 173
6.2.6 SPR validation of rigid, extended antibodies . . . 173
6.2.7 *In vitro* T-cell activation assay . . . 176
6.2.8 Supported lipid-bilayers for studying nivolumab mIgG1-driven PD-1 contact enrichment . . . 177
6.3 Discussion . . . 181

7 Concluding remarks and future perspectives **185**
7.1 Summary and general discussion . . . 185
7.1.1 Antibody production and cancer models . . . 186
7.1.2 Combination therapy of mNivo and OX108 . . . 191
7.1.3 (Rigid) extended forms of nivolumab mIgG1 to increase efficacy . . . 193
7.2 Concluding remarks . . . 202

References **203**

Appendices

A Appendix **227**
A.1 Protein sequences . . . 227
A.1.1 hCD200R-hPD-1 . . . 227
A.1.2 hCD200 . . . 228
A.1.3 Truncated mFcγRIIb . . . 228
A.1.4 hPD-1-2xHis . . . 228
A.1.5 Mouse κ light chain . . . 229
A.1.6 Nivolumab light chain . . . 229
A.1.7 OX108 light chain . . . 229
A.1.8 MOPC21 light chain . . . 229
A.1.9 Mouse IgG1 heavy chain . . . 230
A.1.10 Nivolumab heavy chain . . . 230
A.1.11 OX108 heavy chain . . . 230
A.1.12 MOPC21 heavy chain . . . 230
A.1.13 Mouse CD43 sequences . . . 231
A.1.14 GCN4 sequences . . . 231
A.2 Fitting of SPR data . . . 232

List of Figures

1.1 The cancer-immunity cycle 4
1.2 Receptor triggering by ligands and antibodies based on the KS model 16
1.3 Distinct requirements for optimal antibody agonism 19
1.4 Overview of immune-checkpoint receptors and ligands 22
1.5 Overview of PD-1 signalling effects on TCR and CD28 pathways . 25
1.6 Overview of the CD200/CD200R axis 29
1.7 Structure of mouse IgG1 33
1.8 Combination of anti-PD-1 and anti-CD200R in the MC38 model . 52
1.9 Reduction of agonism through antibody extension 53

2.1 Gating strategy for lymphoid immune cells 76
2.2 Gating strategy for myeloid immune cells 77
2.3 Gating strategy for T-cell subsets 78

3.1 Size exclusion chromatography of mIgG1 antibodies 88
3.2 Binding validation of mNivo and OX108 through SPR 90
3.3 *Ex vivo* binding validation to hPD-1/hCD200R splenocytes 91
3.4 *In vitro* analysis of MHC-I, PD-L1 and CD200 92
3.5 *In vivo* tumour and immune cell analysis 94
3.6 *In vivo* response to mNivo in MC38 and LLC1 tumours 96
3.7 *In vivo* growth of MC38-sensitive and -resistant tumours 97
3.8 Rechallenge of MC38-sensitive survivors with tumour models . . . 98
3.9 *In vitro* RNA sequencing of MC38-sensitive and -resistant cells . . 100
3.10 Comparison of deregulated genes and pathways in different datasets 101
3.11 Identification of commonly enriched pathways in PD-1 blockade-resistant MC38 cells 103

4.1 *In vitro* T-cell activation assay 110
4.2 Expression levels of respective proteins on Jurkat and TCS cells . 111
4.3 *In vitro* blockade validation of mNivo and OX108 112
4.4 Combination therapy of mNivo and OX108 in LLC1 tumours . . . 114
4.5 Immune cell infiltration in treated LLC1 tumours 116

4.6 Combination therapy of mNivo and OX108 in MC38-sensitive tumours . . . 118
4.7 Immune cell infiltration in treated MC38-sensitive tumours 119
4.8 Immune cell infiltration in treated MC38-sensitive tumours 121
4.9 T cell and lymph node analysis of the MC38-sensitive tumour model 122

5.1 Design of extended antibodies . . . 132
5.2 SEC curves of extended antibodies . . . 136
5.3 Non-reducing SDS-PAGE analysis of extended antibodies 137
5.4 Size comparison of extended antibodies using SEC . . . 138
5.5 Comparison of the monovalent kinetics of extended antibodies using SPR . . . 139
5.6 Assessment of bivalent binding using SPR . . . 140
5.7 Comparison of binding affinity to mFcγRIIb-His . . . 141
5.8 *In vitro* T-cell activation assay to assess antibody agonism 143
5.9 *In vitro* T-cell activation assay comparing agonistic activity 144
5.10 Comparison of mNivo variants in the MC38-resistant model . . . 146
5.11 Comparison of mNivo variants in the MC38-sensitive model . . . 148
5.12 Validation of MC38-sensitive cells expressing mFcγRIIb 150
5.13 Comparison of mNivo and mNivo D265A in MC38-sensitive and MC38-sensitive-mFcγRIIb tumours . . . 151
5.14 Combination of mNivo or mNivo D265A with the anti-mFcγRIIb blocker AT128 . . . 153
5.15 Pooled data from experiments comparing MOPC21, mNivo and mNivo D265A . . . 154

6.1 Design of hinge-deleted antibodies and Fc-linker optimisation . . . 165
6.2 Validation of hinge-deleted antibodies and Fc-linker optimisation . 168
6.3 Design of hinge-deleted, extended antibodies . . . 170
6.4 Evaluation of purified antibodies using SEC and SDS-PAGE gels . 172
6.5 Analytical SEC to compare antibody sizes and assess purity . . . 174
6.6 SPR comparison of rigid, extended antibodies . . . 175
6.7 *In vitro* T-cell activation assay comparing stimulatory capacity . . 177
6.8 SLB2s presenting mFcγRIIb to study antibody-driven PD-1 contact enrichment . . . 179
6.9 Contact-enrichment analysis of SLB2s presenting mFcγRIIb . . . 180

A.1 SPR fitting for Figure 3.2 . . . 232
A.2 SPR fitting for Figure 5.5 . . . 232
A.3 SPR fitting for Figure 5.6 . . . 233

A.4 SPR fitting for Figure 5.6 233
A.5 SPR fitting for Figure 5.7 233
A.6 SPR fitting for Figure 6.2 234
A.7 SPR fitting for Figure 6.6 234

List of Tables

2.1 List of general and molecular biology reagents 57
2.2 List of plasmids 58
2.3 List of enzymes 59
2.4 List of solutions and buffers 59
2.5 List of commercial kits 60
2.6 List of cell lines 60
2.7 List of cell culture reagents 60
2.8 List of primers 61
2.9 List of commercial antibodies 62

3.1 Contribution of the Oxford and Sanofi dataset to identified clusters 104

5.1 Overview of different mNivo antibody constructs 134

6.1 Overview of different mNivo antibody constructs 171

List of Abbreviations

A/I . . . . . Activating-to-inhibitory ratio

aa . . . . . amino acids

ADC . . . . . Antibody-drug conjugate

ADCC . . . . . Antibody-dependent cellular cytotoxicity

ADCP . . . . . Antibody-dependent cellular phagocytosis

AML . . . . . Acute myeloid leukaemia

ANOVA . . . . . Analysis of Variance

AP-1 . . . . . Activator protein 1

BCR . . . . . B-cell receptor

BiTE . . . . . Bi-specific T-cell engager

BLI . . . . . Bio-layer interferometry

B_{reg} cell . . . . . Regulatory B cell

C1q . . . . . Complement component 1q

CAR . . . . . Chimeric antigen receptor

CCL . . . . . Chemokine (C-C motif) ligand

CCR . . . . . CC chemokine receptor

CD . . . . . Cluster of differentiation

CD200R . . . . . CD200 receptor

CD200RL . . . . . CD200 receptor-like

CDC . . . . . Complement-dependent cytotoxicity

CH . . . . . Constant heavy

CL . . . . . Constant light

CLL . . . . . Chronic lymphocytic leukaemia

cpm . . . . . counts per million

CR . . . . . Complete response

CSF . . . . . Colony-stimulating factor

CTL . . . . . Cytotoxic T lymphocyte

CTLA-4 . . . . . Cytotoxic T-lymphocyte-associated protein 4

CV . . . . . Column volumes

CXCL . . . . . Chemokine (C-X-C motif) ligand

CXCR . . . . . CXC chemokine receptor

Da . . . . . Dalton

DC . . . . . Dendritic cell

DD . . . . . Death domain

dLN . . . . . Draining lymph node

DMEM . . . . . Dulbecco's Modified Eagle Medium

DMSO . . . . . Dimethyl sulfoxide

DNA . . . . . Deoxyribonucleic acid

ECM . . . . . Extracellular matrix

EDTA . . . . . Ethylenediaminetetraacetic acid

ERK . . . . . Extracellular signal-regulated kinase

EU . . . . . Endotoxin Units

Fab . . . . . Fragment antigen binding

FACS . . . . . Fluorescence-activated cell sorting

FADD . . . . . FAS-associated death domain protein

FAE . . . . . Fab-arm exchange

FBS . . . . . Fetal Bovine Serum

Fc . . . . . Fragment crystallisable

FcγR . . . . . Fc gamma receptor

FcRn . . . . . Neonatal Fc receptor

FDA . . . . . Food and Drug Administration

FDR . . . . . False discovery rate

FMO . . . . . Fluorescence minus one

G-MDSC . . . . . Granulocytic myeloid-derived suppressor cell

GFP . . . . . Green fluorescent protein

GM-CSF . . . . . Granulocyte-macrophage colony-stimulating factor

HAMA . . . . . Human anti-mouse antibody

HBS . . . . . HEPES-buffered saline

HC . . . . . Heavy chain

hCD200R-mFc-His Human CD200R Fc-fusion protein with a His-tag

HEPES . . . . . 4-(2-hydroxyethyl)-1-piperazineethanesulphonic acid

hIgG4 . . . . . human IgG4

HMW . . . . . High-molecular weight

HPD . . . . . Hyperprogressive disease

hPD-1-2xHis . . . Human PD-1 protein with a double His-tag

HRP . . . . . Horseradish peroxidase

ICB . . . . . Immune-checkpoint blockade

IDO . . . . . Indoleamine 2,3-dioxygenase

IFN-γ . . . . . Interferon gamma

Ig . . . . . Immunoglobulin

IgG . . . . . Immunoglobulin G

IgSF . . . . . Immunoglobulin superfamily

IL . . . . . Interleukin

iNOS . . . . . Inducible nitric oxide synthase

irAE . . . . . Immune-related adverse events

IRES . . . . . Internal ribosome entry site

ITAM . . . . . Immunoreceptor tyrosine-based activation motif

ITIM . . . . . Immunoreceptor tyrosine-based inhibitory motif

ITSM . . . . . Immunoreceptor tyrosine-based switch motif

k_a . . . . . Association rate constant

kb . . . . . Kilobase

k_d . . . . . Dissociation rate constant

K_D . . . . . Equilibrium dissociation constant

kDa . . . . . Kilodalton

KEGG . . . . . Kyoto Encyclopedia of Genes and Genomes

KS . . . . . Kinetic-segregation

LAG-3 . . . . . Lymphocyte-activation gene 3

LB . . . . . Lysogeny broth

LC . . . . . Light chain

Lck . . . . . Lymphocyte-specific protein tyrosine kinase

LFC . . . . . Log-fold change

LMW . . . . . Low-molecular weight

M-CSF . . . . . Macrophage colony-stimulating factor

M-MDSC . . . . . Monocytic myeloid-derived suppressor cell

mAb . . . . . Monoclonal antibody

MAPK . . . . . Mitogen-activated protein kinase

mAU . . . . . Milli absorbance units

mCD43 . . . . . Mouse CD43

MCL . . . . . Markov Cluster

mFcγRIIb-His . . Mouse FcγRIIb protein with a His-tag

MFI . . . . . Median fluorescence intensity

MHC . . . . . Major histocompatibility complex

mIgG1 . . . . . mouse IgG1

min . . . . . Minutes

MM . . . . . Multiple myeloma

mNivo . . . . . Nivolumab mIgG1

mRNA . . . . . Messenger RNA

NEAA . . . . . Non-essential amino acids

NF-κB . . . . . Nuclear factor kappa-light-chain-enhancer of activated B cells

NFAT . . . . . Nuclear factor of activated T cells

NK cell . . . . . Natural killer cell

NOD/SCID . . . . Nonobese diabetic/severe combined immunodeficiency

NTA . . . . . Nitrilotriacetic acid

NTR . . . . . Non-catalytic tyrosine-phosphorylated receptor

OVA . . . . . Ovalbumin

PAGE . . . . . Polyacrylamide gel electrophoresis

PBMC . . . . . Peripheral blood mononuclear cell

PBS . . . . . Phosphate-buffered saline

PCR . . . . . Polymerase chain reaction

PD-1 . . . . . Programmed cell death protein 1

PD-L1 . . . . . Programmed cell death ligand 1

PD-L2 . . . . . Programmed cell death ligand 2

PDB . . . . . Protein data bank

PES . . . . . Polyethersulfone

PI3K . . . . . Phosphoinositide 3-kinase

PLC-γ . . . . . Phospholipase C gamma

PMA . . . . . Phorbol 12-myristate 13-acetate

pMHC . . . . . Peptide MHC

PTB . . . . . Phosphotyrosine-binding

pY . . . . . Phosphotyrosine

RBC . . . . . Red blood cell

RIPR . . . . . Receptor inhibition by phosphatase recruitment

RNA . . . . . Ribonucleic acid

RNA-seq . . . . . RNA sequencing

ROS . . . . . Reactive oxygen species

RPMI . . . . . Roswell Park Memorial Institute

RPTP . . . . . Receptor-type protein tyrosine phosphatase

RT . . . . . Room temperature

RTK . . . . . Receptor tyrosine kinase

RU . . . . . Response Units

scFv . . . . . Single-chain variable fragment

scRNA-seq . . . . Single-cell RNA sequencing

SDS . . . . . Sodium dodecyl sulfate

sec . . . . . Seconds

SEC . . . . . Size-exclusion chromatography

SFK . . . . . SRC-family kinase

SH2 . . . . . Src Homology 2

SHIP1 . . . . . SH2 domain-containing inositol polyphosphate-5-phosphatase 1

SHP-1 . . . . . SH2 domain-containing phosphatase 1

SHP-2 . . . . . SH2 domain-containing phosphatase 2

SLB . . . . . Supported lipid-bilayer

SLB2 . . . . . Second generation supported lipid-bilayer

SPR . . . . . Surface plasmon resonance

STR . . . . . Short tandem repeat

TAM . . . . . Tumour-associated macrophage

TAMC . . . . . Tumour-associated myeloid cell

TBE . . . . . Tris-Borate-EDTA

TCF1 . . . . . T-cell factor 1

TCR . . . . . T-cell receptor

TCS . . . . . T-cell stimulator

TE . . . . . Tris EDTA

TF . . . . . Transcription factor

TGF-β . . . . . Transforming growth factor beta

Th cell . . . . . T helper cell

TIL-B . . . . . Tumour-infiltrating B lymphocyte

TIRF . . . . . Total internal reflection fluorescence

TLR . . . . . Toll-like receptor

TLS . . . . . Tertiary lymphoid structure

TME . . . . . Tumour microenvironment

TNF . . . . . Tumour necrosis factor

TNFR . . . . . TNF receptor

T_{reg} cell . . . . . Regulatory T cell

VEGF . . . . . Vascular endothelial growth factor

VH . . . . . Variable heavy

VL . . . . . Variable light

WT . . . . . Wild type

ZAP70 . . . . . Zeta-chain-associated protein kinase 70

Don't let anyone rob you of your imagination, your creativity, or your curiosity. It's your place in the world; it's your life. Go on and do all you can with it, and make it the life you want to live.

— Mae Jemison

1 Introduction

Contents

1.1 Cancer immunology 2
1.1.1 The hallmarks of cancer 2
1.1.2 The cancer-immunity cycle and immunoediting 3
1.1.3 The tumour microenvironment 5
1.2 Non-catalytic tyrosine-phosphorylated receptors . . . 10
1.2.1 NTR triggering 11
1.2.2 KS-based triggering of NTRs by antibodies 14
1.2.3 Immune checkpoints 20
1.2.4 Inhibitory immune checkpoints in cancer 21
1.3 Monoclonal antibody therapy 32
1.3.1 Antibody structure 33
1.3.2 Fcγ receptors 34
1.3.3 Monoclonal antibodies for cancer therapy 36
1.4 Anti-PD-1 antibodies for cancer therapy 42
1.4.1 Cells targeted by anti-PD-1 therapy 42
1.4.2 Biomarkers predicting PD-1 blockade efficacy 45
1.4.3 Myeloid cell interaction with PD-1 blockade 46
1.4.4 Rationale for combining PD-1 and CD200R blockade . 49
1.5 Work preceding this thesis 51
1.6 Hypothesis and objectives of this thesis 54

1.1 Cancer immunology

1.1.1 The hallmarks of cancer

CANCER is a growing global burden on societies and healthcare systems. For 2020, the International Agency for Research on Cancer estimated that almost 10 million cancer deaths occurred and nearly 20 million new cancers were diagnosed[2]. Unlike external health threats like bacteria and viruses, cancer is a disease arising from our own cells. The understanding of this complex process has changed dramatically in recent decades, and still continues to evolve. While cancer with all its different types and subtypes is a very heterogeneous disease, there are some common capabilities that a tumour needs to acquire in order to survive. In 2000, Douglas Hanahan and Robert Weinberg first defined the 'hallmarks of cancer', attempting to summarise the current understanding of tumour development[3]. Back then, there was a tumour cell-centred view, mostly focusing on molecular processes that lead to cancerous cells, including i) evading apoptosis, ii) self-sufficiency in growth signals and iii) evasion of anti-growth signals as well as iv) replicative immortality. Only two traits focused on the tumour as a part of an organism, namely i) induction of angiogenesis and ii) activation of invasion and metastasis. The authors noted that the research so far was guided by 'a reductionist focus' of a tumour comprising of cancer cells only[3]; acknowledging the importance of further investigating the interactions between malignant cancer cells and host cells. However, the concept of cancer immunosurveillance was neglected. This hypothesis was proposed by Sir Macfarlane Burnet[4] and Lewis Thomas[5] in an attempt to explain the low frequency of cancer in long-lived mammals. They argued, due to the amount of potential genetic changes which can result in malignancy, there must be a mechanism for eliminating potentially dangerous cells, probably by immunological means[6]. A decade after their first description of the hallmarks of cancer, Hanahan and Weinberg published a new review acknowledging the importance of the immune system in the development and elimination of tumours[7]. Besides the existing hallmarks, they added four

new emerging hallmarks and enabling characteristics, namely i) evading immune recognition, ii) tumour-promoting inflammation as well as iii) reprogrammed metabolism and iv) genome instability[7]. In 2022, Hanahan proposed four additional features, including i) presence of senescent cells, ii) phenotypic plasticity, iii) polymorphic microbiomes and iv) epigenetic reprogramming[8].

1.1.2 The cancer-immunity cycle and immunoediting

The importance of the immune system during the development of a tumour is now well established and accepted in the scientific community. When malignant cancer cells first arise, they are recognised by immune cells and eliminated quickly. The cancer-immunity cycle describes this process in a simplified way (Figure 1.1)[9]. First, cancer cell antigens (neoantigens) are released and taken up by antigen-presenting cells (APCs), which subsequently travel to the draining lymph node (dLN). Here, APCs interact with T cells in order to prime and activate them. Upon activation, T cells exit the lymph node and migrate into the tumour, where they recognise their neoantigen-related peptide presented on MHC molecules and kill the corresponding cancer cell.

While this process should, in theory, effectively eliminate tumour cells from our body, a tumour can undergo a process termed immunoediting in order to evade immune-cell recognition[10]. Initially, most cancer cells are being killed (termed elimination, similar to cancer immunosurveillance), however some cells remain and continue to proliferate. Those cells have acquired certain mechanisms that prevent their recognition by immune cells. While the immune system is still active in the tumour, there is now an equilibrium of some cancer cells being killed, and others that continue to proliferate. Lastly, once a sufficient number of tumour cells acquire features that inhibit immune cells, the cancer escapes our immune system and immunoediting was 'successful'.

There are several cancer cell-intrinsic mechanisms to reduce anti-tumour immune activity, such as upregulation of ligands that can bind to inhibitory receptors on immune cells (Section 1.2.4) or downregulation of MHC-I to hinder

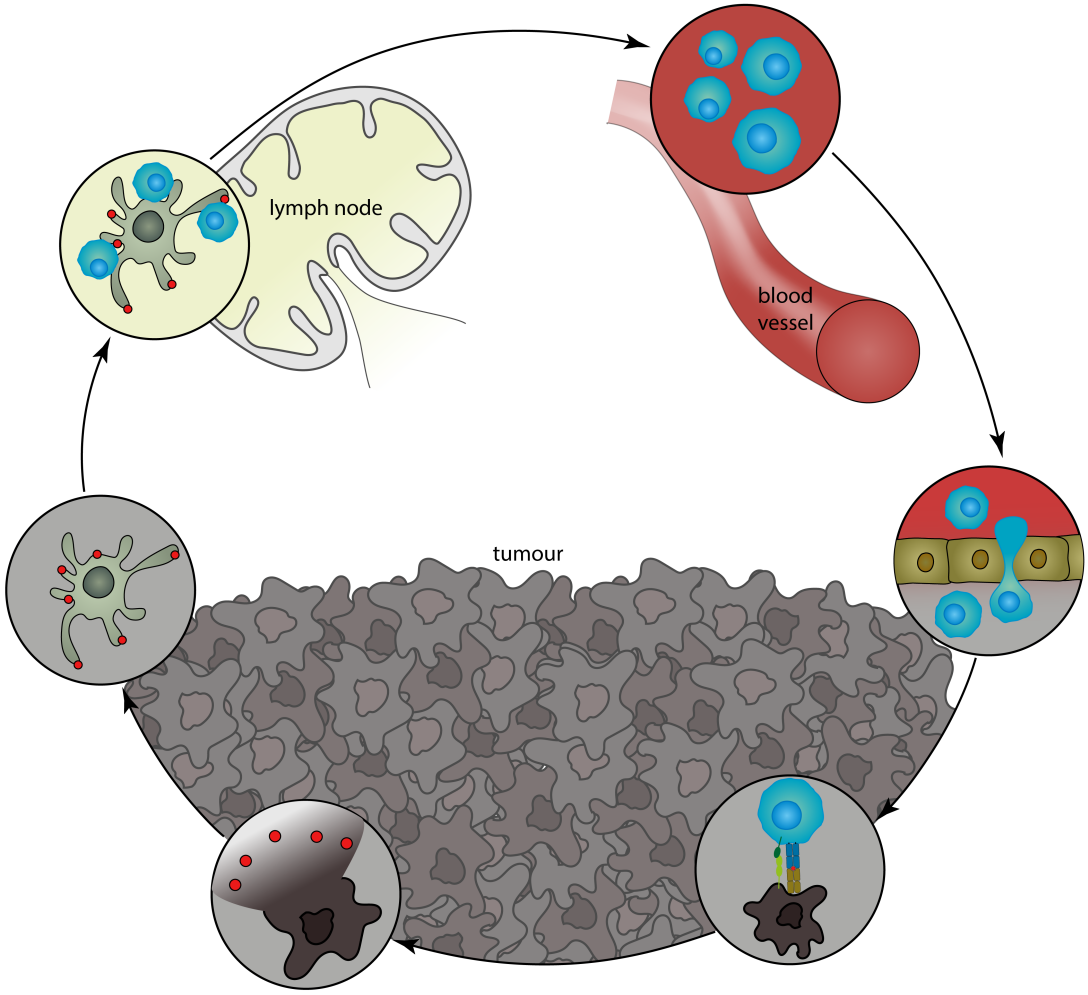


Figure 1.1: The cancer-immunity cycle
The cancer-immunity cycle starts with the release of antigen upon cell death (bottom left). The antigen is taken up by APCs, which migrate to the dLN for antigen presentation to T cells. Upon priming and activation in the dLN (top left), T cells migrate to the tumour (top right) and recognise the cancer antigen through the specific interaction of peptide MHC (pMHC)/T-cell receptor (TCR) (bottom left). Successful engagement of an antigen-specific TCR leads to immune cell-mediating killing of cancer cells and subsequent further release of antigens.
Adapted from Chen *et al.*[9]

recognition by antigen-specific T cells[11]. Additionally, tumours are infiltrated by host cells, which can be tumouricidal or tumour-promoting, and together make up the tumour microenvironment (TME). Following, an overview of the different immune cell subsets in the TME is given.

1.1.3 The tumour microenvironment

The TME is crucial for establishing a tumour, facilitating its growth and metastasis as well as immune evasion[12]. Besides immune cells, cancer-associated fibroblasts and endothelial cells are important components of the TME. In what follows, the characterised immune cell populations in this thesis will be introduced and their functions discussed. Of note, this is not a comprehensive review of all cell types within the TME. Furthermore, only certain main functions that are relevant to cancer will be described.

1.1.3.1 Macrophages

While macrophages are one of the most abundant immune cells in tumours[13], their origin, especially in pathological conditions, remains poorly understood[14]. In physiological, steady-state conditions, most tissue-resident macrophages are believed to originate from embryonic macrophages in the yolk sac, which are maintained by local proliferation. In contrast, while in murine breast cancer models tumour-associated macrophages (TAMs) were predominantly derived through differentiation of infiltrating monocytes from the bone marrow[14,15], a significant proportion of tissue-resident macrophages was found to be expanded in pancreatic adenocarcinoma[16]. Of note, monocyte-derived macrophages still accounted for a significant proportion of all TAMs, and they were distinct in regards to their function. There are various chemotaxis pathways involved in the recruitment of monocytes into the TME (reviewed by Hourani *et al.*[17]), such as the CCL2-CCR2 axis, as CCL2 blockade[18] or $CCR2^{-/-}$ monocytes[15] exhibited a reduced migration.

Macrophages are a highly diverse immune cell population, that get skewed by the local environment into different functions. When entering the tumour, several immunosuppressive cytokines (M-CSF, IL-10, IL-4, IL-13) polarise them towards an immunoregulatory phenotype, often referred to as M2 macrophages. This is in contrast to proinflammatory, tumouricidal M1 macrophages, which are induced by cytokines like GM-CSF, IFN-γ and TLR agonists[19]. Once polarised, TAMs produce additional immunosuppressive factors (TGF-β, IL-10) and can recruit other immunoregulatory cell types including regulatory T cells (T_{reg})[20].

Several correlation studies demonstrated that macrophage infiltration is associated with poor clinical outcome, supporting the idea that, overall, macrophages are immune inhibiting and tumour promoting[21]. Due to their abundance and important role, macrophages also became a target for immunotherapy. Different approaches try to modify the TAM population by i) depletion, ii) inhibition of recruitment or iii) reprogramming (described in more detail in Section 1.4.3)[22].

1.1.3.2 Dendritic cells

Dendritic cells (DCs) are professional APCs that are responsible for the uptake, processing and presentation of tumour antigens. As discussed in Section 1.1.2, they travel to the dLN to prime and activate T cells. Thus, DCs are generally considered a crucial immune-cell population for mounting an anti-tumour response.

However, there are also tumour-residing DCs with differing functions. Depending on the available stimuli within the TME, DCs might remain immature and therefore do not have the capacity to stimulate T cells sufficiently. Tolerogenic DCs have low levels of co-stimulatory molecules like CD80 and CD86, combined with a high expression of inhibitory molecules like PD-L1 and CTLA-4 as well as immunoregulatory enzymes (IDO, iNOS)[12].

Besides tolerogenic DCs, there are also plasmacytoid DCs and conventional DCs, with the latter being considered crucial for presentation of exogenous and endogenous antigens to T cells. Conventional DCs can be further subdivided into DC1s and DC2s. In cancer, many reports focused on DC1s, due to their

importance in cross-presentation of antigens to infiltrating $CD8^+$ T cells within the tumour[23–25]. In contrast, DC2s are believed to predominantly migrate to the dLN to present antigens to $CD4^+$ T cells, however, they are not as well studied[26]. The role of DC1s during anti-PD-1 therapy is introduced in Section 1.4.3.

1.1.3.3 Myeloid-derived suppressor cells

Myeloid-derived suppressor cells (MDSCs) originate from immature myeloid cells in the bone marrow. While they are a poorly defined, heterogeneous cell population, they have common biological functions such as their strong immunosuppressive activity towards T cells[27].

The maturation of MDSCs can be divided into expansion and activation. First, soluble factors secreted by tumour cells (e.g. VEGF, M-CSF, GM-CSF, prostaglandins) lead to the expansion of MDSCs through activation of STAT3[27]. This drives increased myelopoiesis in combination with a blockade of differentiation of these newly produced myeloid cells. Next, MDSCs get activated in the TME by factors secreted mainly by T cells, stromal cells or apoptotic cancer cells (e.g. IFN-γ, TLR ligands, IL-4, IL-13 and TGF-β)[27,28]. MDSC-activation potentiates their functions, including an increase in expression of iNOS and arginase 1, production of reactive oxygen species (ROS) and induction of T_{reg} cells.

MDSCs can be subdivided into granulocytic (G-MDSC) and monocytic (M-MDSC) MDSCs, classified by their respective cell of origin. Besides distinct surface markers used for identification of those two subsets (Ly-6G and Ly-6C in mice, respectively), there are also functional differences, as G-MDSCs produce more ROS and less NO compared to M-MDSCs[29].

1.1.3.4 T cells

T cells are essential in mounting an effective immune response against tumours[30]. Naïve T cells can be divided into two major subsets, $CD4^+$ and $CD8^+$ T cells, depending on their respective co-receptor expression as well as MHC restriction. Both subsets recognise processed antigens presented on MHC molecules through their T-cell receptor (TCR), with $CD4^+$ T cells binding to MHC-II on APCs and

$CD8^+$ T cells binding to MHC-I, which is present on all nucleated cells. Upon activation by a specific peptide MHC (pMHC), $CD8^+$ T cells differentiate into cytotoxic T lymphocytes (CTLs), which are crucial for tumour-cell killing, while $CD4^+$ T cells differentiate into different T helper (Th) cell subsets. Those subsets are polarised by the local microenvironment, resulting in distinct functions. Upon activation, CTLs can kill their target cells via induction of apoptosis, either through death receptor ligation (FasL, TRAIL) or by secretion of perforin and granzyme B. The significance of their functions is emphasised by the fact that increased infiltration of $CD8^+$ T cells is associated with a favourable prognosis in many solid tumours[31].

In contrast, T_{reg} cells, a subset of $CD4^+$ Th cells, are known to suppress immune responses and create an anti-inflammatory milieu. They can be further subdivided into natural T_{reg} cells which arise in the thymus, or inducible T_{reg} cells that are generated in the periphery in response to immunosuppressive stimuli like TGF-β and IL-10. The suppressive mechanisms of T_{reg} cells include i) expression of inhibitory cytokines, ii) cytolysis of effector cells, iii) metabolic disruption of other immune cells and iv) inhibition of DC maturation and function[32]. Therefore, infiltration of this subset is associated with poor prognosis and the ratio of $CD8^+/T_{reg}$ cells is often used to reflect both parameters[31].

Of note, there are different subsets of unconventional T cells that also have implications for cancer immunotherapy (reviewed by Godfrey *et al.*[33]). These subsets are in addition to the conventional T cells that have been described above.

1.1.3.5 NK cells

Natural killer (NK) cells are cytotoxic innate lymphoid cells. Unlike CTLs, NK cells are not MHC-restricted, but rather have a mix of activating and inhibiting NK-cell receptors that regulate their activity. Activating receptors trigger the release of perforin and granzymes, while inhibiting receptors counteract this[12]. In steady-state conditions, presence of MHC-I on healthy cells triggers several inhibiting NK-cell receptors, including NKG2A and inhibitory killer Ig-like

receptors, therefore suppressing NK-cell activation. In contrast, cancer cells can downregulate MHC-I to evade $CD8^+$ T-cell recognition, however, this also leads to reduced inhibitory activity on NK cells resulting in a potential subsequent activation. Similarly, MHC class I chain-related antigens A and B as well as ULBP1-6 get upregulated on infected and transformed cells and are ligands for the activating receptor NKG2D[34]. Another pathway that triggers the killing of target cells by NK cells is antibody-dependent cellular cytotoxicity (ADCC). Antibody-opsonised targets can be recognised by the activating Fc gamma receptor III (FcγRIII), which is expressed at high levels on NK cells[34].

The importance of natural anti-cancer activity of NK cells is emphasised by an 11-year follow-up study of 3625 individuals in Japan. Strikingly, medium and high natural cytotoxic baseline activity of NK cells correlated with a reduced risk of developing cancer, whereas the opposite was true for NK cells with low activity[35]. It should be noted that once a primary tumour is established, it can also polarise and inhibit NK-cell activity, for example through inducing the downregulation of activating NK-cell receptors, reducing degranulation and inhibition of IFN-γ production by NK cells[36].

1.1.3.6 B cells

B cells have been long overlooked in the field of cancer immunology, but there is increasing evidence for an important role of tumour-infiltrating B lymphocytes (TIL-Bs)[37]. TIL-Bs are generally correlated with a positive prognostic outcome, especially when they are forming tertiary lymphoid structures (TLS) with T cells in tumours[38]. TIL-Bs have different effector functions, supporting adaptive and innate immune responses: Besides the production of immunostimulatory cytokines such as IL-6, IFN-γ and TNF, they can also act as APCs to $CD4^+$ T cells[39]. This can not only lead to initiation and differentiation of tumour-specific T helper cells, but it can also promote the anti-tumour activity of $CD8^+$ T cells through production of IL-21 by $CD4^+$ T cells[40]. Furthermore, TIL-Bs can produce anti-tumour antibodies, which could trigger antibody-dependent

mechanisms such as antibody-dependent cellular phagocytosis (ADCP)[41], ADCC and complement-dependent cytotoxicity (CDC)[42]. Interestingly, while there are reports describing antibodies against neoantigens[43], most anti-tumour antibodies are directed against non-mutated self-proteins[44]. For example, the majority of antibodies against p53 were found to be directed against the N- or C-terminus instead of the highly mutated central region of the protein, suggesting that accumulation of p53 is the major driver for the humoral response[45]. It should be noted that most studies analysed serum antibodies instead of TIL-B-derived antibodies and there are reports suggesting that anti-tumour antibodies in the serum and TIL-B presence in the TME are uncoupled[46,47]. Importantly, there is also growing evidence of anti-tumour antibodies produced by TIL-Bs[37].

Similar to T cells, regulatory B cells (B_{reg} cells) have also been described, and there is a positive correlation between T_{reg} and B_{reg} cells in tumours[48]. B_{reg} cells can be activated by semi-mature DCs[49] and their main suppressive mechanisms are the production of IL-10 and IL-35[48].

1.2 Non-catalytic tyrosine-phosphorylated receptors

Immune cells express a wide range of surface molecules, including a class that is referred to as non-catalytic tyrosine-phosphorylated receptors (NTRs)[50], which modulate their cellular activity by integrating signals from their surrounding. The most prominent members include the TCR and B-cell receptor (BCR), the key receptors driving T- and B-cell activation. However, this one signal is typically not enough and immune cells integrate a diverse mix of activating and inhibiting stimuli, which determines their final response in the respective situation. This process is crucial to maintain tolerance and prevent responses to self-antigens.

NTRs share certain characteristics, such as i) they lack intrinsic kinase activity and therefore rely on external phosphorylation ii) their extracellular domains are rather small (< 20 nm) and iii) their ligands are anchored and not soluble[50]. An overview of certain NTR-ligand pairs is given in the top half of Figure 1.4.

Typically, NTRs are activated by SRC-family kinases (SFKs) kinases, such as Lck and Fyn, and dephosphorylated by receptor-type protein tyrosine phosphatases (RPTPs), including CD45 and CD148. NTRs have different phosphorylation motifs, the most common ones being immunoreceptor tyrosine-based activation, inhibitory and switch motifs (ITAMs, ITIMs and ITSMs, respectively). The phosphorylated tyrosines serve as a docking site for different downstream signalling molecules containing Src Homology 2 (SH2) domains[50].

ITAMs primarily lead to cell activation through recruitment of Syk-family kinases[51], while ITIMs counteract this by binding phosphatases such as SH2 domain-containing phosphatase 1 (SHP-1) and SHP-2, which dephosphorylate ITAMs and other downstream molecules[52]. Besides protein phosphatases, ITIMs can also recruit lipid phosphatases such as SH2 domain-containing inositol polyphosphate-5-phosphatase 1 (SHIP1) and SHIP2, which inhibit phosphoinositide 3-kinase (PI3K) by hydrolysing phosphatidylinositol (3,4,5)-triphosphate. Finally, ITSMs can fulfill inhibiting and activating roles, depending on the specific context. Similar to ITIMs, they can recruit the aforementioned phosphatases, thereby reducing cell activation. However, SLAM-associated protein can also bind to ITSMs, which can further interact with the SFK Fyn or protein kinase C θ[53].

1.2.1 NTR triggering

NTRs are typically activated upon ligand binding, leading to phosphorylation. While the downstream signalling is well described, the precise mechanism of how the receptor-ligand interaction triggers this signalling is poorly understood. Intriguingly, it was already demonstrated in 1993 that upon treatment with a phosphatase inhibitor (pervanadate), TCRs get phosphorylated and triggered, similarly to crosslinking via anti-TCR antibodies[54]. Due to these analogies, it was initially suggested that TCR triggering might also lead to a modulation of RPTP activity, and it was only later that a local balance between SFKs/RPTPs was considered[55]. Overall, while phosphatases manage to outcompete kinases

at resting conditions, this balance is perturbed upon ligand binding, however, the precise mechanism of this remains controversial.

Hereafter, different models of NTR triggering are discussed. Of note, most of the mentioned reports and models were explored using the TCR, but there is increasing evidence that other NTRs are triggered the same way[50].

1.2.1.1 Aggregation models

Similar to receptor tyrosine kinases (RTKs) and cytokine receptors[56], one model proposes that ligand-receptor interactions result in dimerisation or oligomerisation of receptors, leading to a local aggregation. Further, it was suggested that as the receptors lack intrinsic kinase activity, they are non-covalently associated with SFKs. Therefore, aggregation of receptors ultimately leads to a local enrichment of SFKs, driving phosphorylation and triggering[57].

This idea is supported by the observation that artificially induced crosslinking (aggregation) of NTRs leads to triggering. However, while this model can explain the triggering of RTKs and cytokine receptor as well as crosslinked NTRs, it fails to elucidate how dimerisation/aggregation is induced as some ligands are monovalent (Section 1.2.3).

1.2.1.2 Conformational change models

Conformational change models predict that ligand engagement results in a structural change that triggers initial phosphorylation. This can either be achieved through changes in the extracellular domains, leading to clustering and aggregation[58], or via an increased accessibility of the cytoplasmic domains to kinases[59]. Mechanical forces have been proposed to drive such a conformational change[60,61]. However, this mechanism fails to explain the observed ligand-independent TCR activation in 'close contacts'[62]. Finally, while conformational changes were initially observed in the TCRα constant domain upon ligand binding[63], this was not reproduced in other studies[64]. Recently, the structure of a fully assembled TCR complex ligated to pMHC was solved[65]. While this study did not observe any structural rearrangements within the extracellular

domains, it does not exclude the possibility of changes within the cytoplasmic domain. Furthermore, this study could not address the impact of mechanic forces applied onto the TCR.

1.2.1.3 Segregation models

Segregation models propose that ligand binding leads to the local separation of phosphatases and kinases, leaving the respective NTR in a kinase-rich and phosphatase-depleted microenvironment. Two different models try to explain the mechanism of segregation.

The lipid raft model suggests that ligand engagement results in the association of NTRs with lipid rafts that are enriched in SFKs and depleted of RPTPs[66]. However, it is not clear how ligand binding leads to the transition into lipid rafts. Furthermore, imaging studies showed that raft probes accumulated after the formation of TCR microclusters[67]. Similarly, partitioning of signalling proteins into membrane clusters that exclude CD45 through electrostatic repulsion was dependent on initial TCR signalling, indicating that TCR signalling precedes this event[68].

In contrast, the kinetic-segregation (KS) model proposes that the segregation is driven by size differences between SFKs and RPTPs, leading to the physical exclusion of the phosphatases[55]. The TCR/pMHC interaction spans a size of approximately 14 nm, which means that complexes can form in close contacts created by 'adhesive' proteins of similar size, whereas phosphatases such as CD45 (smallest isoform spans $\sim$ 21 nm) are sterically excluded[62]. Importantly, although unbound TCRs can also enter these phosphatase-depleted zones, their residence time is too short for functional TCR activation[69]. However, slowing the diffusion of TCRs at close contacts by attaching anti-CD3ϵ Fabs or pMHCs initiated signalling, as the residence time of the TCR in close contacts was increased, offering strong support for the theory[70]. Finally, the observed NTR triggering upon crosslinking can be readily explained by the KS model. Instead of size-dependent segregation through vertical limits, artificial aggregation can push out

large phosphatases due to crowding in the plane of the membrane. In contrast, as SFKs lack ectodomains they can still access the phosphorylation sites[50].

While the KS model was originally proposed to explain TCR triggering[55], there is also data supporting a size-dependent activation of chimeric antigen receptor (CAR) T cells[71] as well as bi-specific T-cell engagers (BiTEs)[72]. Furthermore, there is a growing body of evidence that this model can be generally applied to small NTRs. CD28, CTLA-4 as well as PD-1 are known to be co-engaged alongside the TCR/pMHC complex, suggesting they might be triggered in the same way through segregation of RPTPs[73–75]. Interestingly, elongation of the ligands of NK-cell receptors NKG2D and KIR2DL1 resulted in reduced receptor triggering without affecting the ligand/receptor binding interaction[76]. Furthermore, for the C-type lectin family receptor Dectin-1 it was shown that RPTP exclusion is required for receptor activation, ultimately driving phagocytosis[77].

1.2.2 KS-based triggering of NTRs by antibodies

In addition to pattern-recognition receptors like Dectin-1, phagocytosis can also be triggered by Fc gamma receptors (FcγRs) and it was shown that the uptake of antibody-opsonised targets also requires CD45 exclusion from close-contact zones, leading to ITAM phosphorylation on FcγRs[78]. Furthermore, it was demonstrated that this process is size-dependent as stepwise elongation of the target antigen resulted in reduced phagocytic capacity of macrophages. Therefore, antibodies that target short antigens will ultimately promote more efficient phagocytosis, driven by a better exclusion of phosphatases. While the study focused on the signal integration in macrophages[78], the same principle should hold true for the reverse setting, where small NTRs of the Immunoglobulin superfamily (IgSF) are bound by antibodies, which are held in close-contact zones by FcγRs. As FcγRs are also NTRs (defined in Section 1.2) and have similar structural features, i.e. they belong to the IgSF[50], a similar triggering mechanism is possible.

Predating the work on FcγR signalling, a lot of effort was put into understanding the different triggering capabilities of anti-CD28 antibodies. Most antibodies

binding CD28 induce co-stimulatory signalling, meaning the antibody alone does not trigger T-cell activation, but requires additional stimulation via an antibody targeting CD3. These antibodies are referred to as 'co-mitogenic' or 'conventional' agonists[55]. In contrast, a smaller proportion of anti-CD28 antibodies are mitogenic without an additional stimulus, so-called 'superagonists'[79]. Strikingly, the two groups could be distinguished not only by their stimulatory capacity, but also by their respective epitope location[80]. Superagonists bind to the 'side' of CD28, whereas the epitopes of conventional agonists are located near the ligand-binding site at the 'top' of the receptor[81]. When immobilised, this results in a $\sim$ 10 nm more compact close contact created by superagonists, which can explain the higher stimulatory capacity in accordance with the KS model[55].

The work on anti-CD28 antibodies resulted in the development of TGN1412, a superagonist targeting CD28 with the aim to specifically activate T_{reg} cells[82]. However, upon administration of TGN1412 to healthy volunteers in a phase I clinical trial, all six participants developed a severe cytokine release syndrome due to overactivation of T cells[82]. Follow-up studies revealed that while low-density cultured peripheral blood mononuclear cells (PBMCs) did not respond to treatment with soluble TGN1412, high-density cultured PBMCs did[83]. This effect was dependent on FcγRIIb, which was present on B cells but was highly upregulated on monocytes upon high-density culture[84]. Interestingly, while FcγRI had the highest affinity for TGN1412, it exhibited the lowest CD28 triggering capacity as measured by T-cell proliferation[85]. While this observation was not further investigated, it is important to note that FcγRI has three immunoglobulin (Ig) domains, compared to only two for the remaining FcγRs[86]. An additional Ig domain will likely increase the overall size of the CD28/antibody/FcγR complex, thereby, according to the KS model, reducing the efficiency of CD45 exclusion and CD28 triggering.

Recently, a study investigating agonistic PD-1 antibodies found that antibodies binding to membrane-proximal epitopes were agonistic, whereas ligand-blocking antibodies that bound more distal had no triggering activity[87]. Further, they

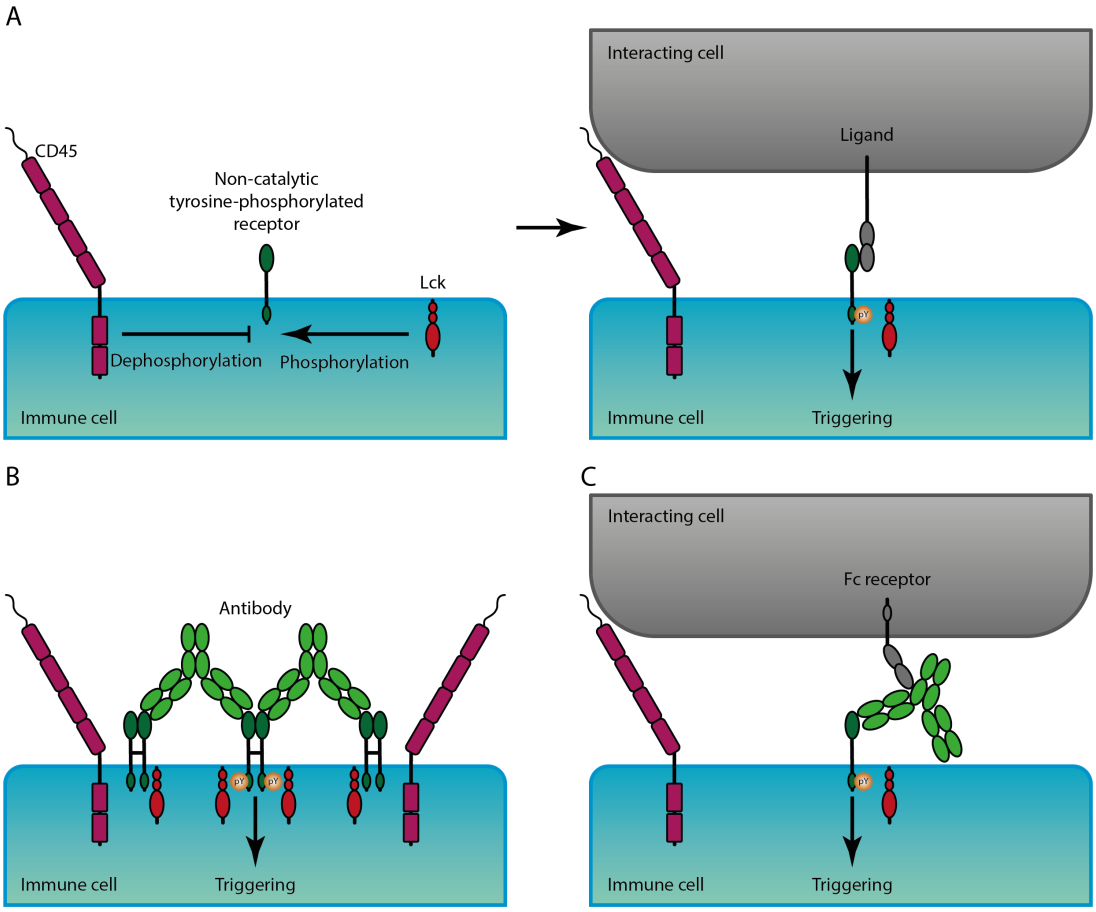


Figure 1.2: Receptor triggering by ligands and antibodies based on the KS model
(A) The KS model for ligand-induced signalling. Upon ligand binding, phosphatases like CD45 are sterically excluded, while kinases like Lck can remain within the close-contact zone formed between two cells. Overall, this results in an increased kinase activity within this zone, leading to phosphorylation and receptor triggering.
(B) Antibody-induced receptor triggering through aggregation. An antibody can crosslink receptors, leading to crowding in the horizontal space, and therefore exclusion of bulky phosphatases.
(C) Antibody-induced receptor triggering through FcγR binding. Antibodies that are bound by FcγRs and engage small NTRs can remain within the close-contact zone formed by two cells, resulting in receptor triggering.
Adapted from Paluch *et al.*[88]

demonstrated that this was FcγR-dependent, and increasing the affinity to FcγRIIb enhanced agonistic activity. While the authors argued that this agonism was dependent on crosslinking, they failed to explain why crosslinking with ligand-blocking antibodies did not lead to activation[87].

Taken together, the KS model can be used to explain not only ligand-induced

triggering of NTRs (Figure 1.2 A), but also antibody agonism (Figures 1.2 B and C)[55]. When an antibody that binds to a small NTR is bound by FcγRs, the NTR/antibody/FcγR complex can be held in this close-contact zone, resulting in triggering through exclusion of RPTPs (Figure 1.2 C). Importantly, when the epitope of an antibody is located closer to the cell membrane, the gap between the two interacting cells becomes smaller[80,87]. Of note, crosslinking of the NTR can also lead to phosphorylation through 'crowding out' of bulky phosphatases (Figure 1.2 B).

1.2.2.1 Other mechanisms for antibody agonism

It is crucial to note, that the aforementioned model for agonistic antibodies applies to NTRs, which were defined in Section 1.2. Other receptor families can have different triggering mechanisms, which will be discussed below.

RTKs, cytokine receptors as well as receptors of the TNF receptor (TNFR) and Toll-like receptor (TLR)/IL-1R superfamilies are triggered through oligomerisation. For RTKs, oligomerisation brings intrinsic kinases in close proximity, resulting in trans-phosphorylation, thereby triggering the receptors[56]. In contrast, TNFR and TLR/IL-1R families do not have intrinsic kinases, but instead rely on adapter proteins forming complexes with the receptors for initial enzymatic activity. For example, Fas receptor (TNFR family) and the adaptor protein FADD form a Fas-FADD death domain (DD) complex comprising 5-7 Fas DDs and 5 FADD DDs, allowing clustering and activation of caspase-8[89]. Similarly, the MyD88-IRAK4-IRAK2 DD complex, important for the TLR/IL-1R family, is composed of 6 MyD88, 4 IRAK4 and 4 IRAK2 DDs, and induces close proximity of the IRAK kinase domains, resulting in phosphorylation and receptor triggering[90].

Different receptor triggering mechanisms ultimately require agonistic antibodies with different properties. It was demonstrated for OX40[91], CD40[92] as well as 4-1BB[93] that membrane-proximal epitopes did not necessarily result in increased agonistic activity of the antibody. While FcγR-engagement was still beneficial, this was not strictly necessary, as long as the antibodies themselves allowed for

sufficient multimerisation of the receptors. In accordance with this, multimeric forms of an anti-CD40 antibody, which was FcγR-dependent as a monomer, allowed for agonistic activity independent of FcγRs[94]. Similarly, mutations that facilitate multimerisation of anti-OX40 antibodies on the cell surface also resulted in FcγR-independent agonism[95].

Furthermore, FcγR-independent agonism was described for antibodies of the human IgG2 isotype[92,96]. hIgG2 antibodies exist in different isoforms, hIgG2-A, hIgG2-B as well as the intermediate hIgG2-A/B, which differ in their disulfide bonds. A disulfide crossover in IgG2-B restricts the conformation and flexibility of this isoform[97]. It is believed that these rigid hIgG-2B antibodies allow for more efficient receptor clustering, and therefore agonism[98].

Finally, while blocking antibodies generally follow a sigmoidal dose-response curve, meaning that blocking efficacy increases dose-dependently until saturation is reached, there is evidence suggesting that this might not be the case for stimulating antibodies[99]. Bell-shaped dose-response curves have been observed for TNFR family agonists against GITR, OX40, 4-1BB[100] as well as the anti-CD28 superagonist TGN1412[101]. At low levels of receptor occupancy not all receptors are bound, leading to isolated complexes, sub-optimal multimerisation and reduced agonism. Increasing the antibody concentration to equimolar amounts compared to the receptor levels, results in optimal receptor clustering and triggering (Figure 1.3 A). Further increasing antibody levels leads to monovalent binding of antibodies, and therefore reduced receptor bridging and activation[99]. It should be noted that this has only been described for members of the TNFR superfamily and CD28; it remains to be determined whether this also applies to monomeric NTRs.

Again in contrast to the preferred properties for blocking antibodies, there were reports suggesting an inverse correlation between affinity, especially off-rate, and agonism[99,102]. However, this was only shown for a Fas receptor agonist[102], and it remained to be determined whether this is a general concept that could be applied to other receptors and antibodies. Recently, Cragg and colleagues used a structure-guided mutational approach to create low-affinity variants of antibodies against

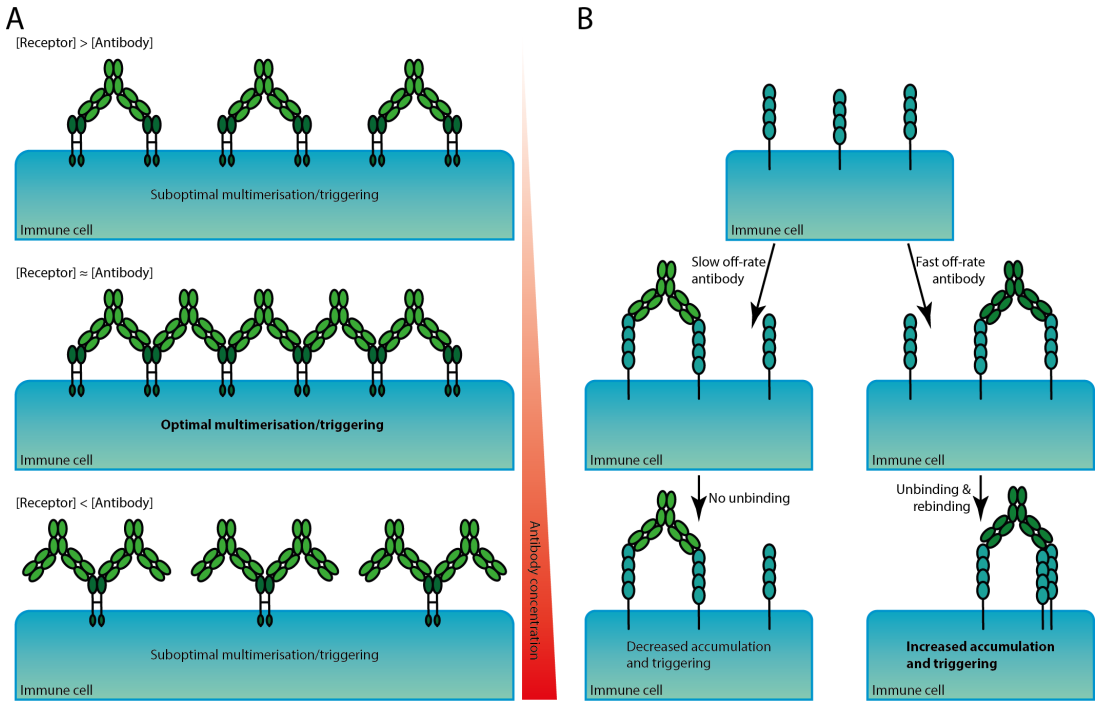


Figure 1.3: Distinct requirements for optimal antibody agonism
(A) Receptor occupancy influences triggering capacity. At low (top panel) and high (bottom panel) antibody concentrations, multimerisation of the receptor is not optimal. Low antibody concentrations lead to receptors only being bound by one antibody. In contrast, when the antibody concentrations are too high, the antibodies bind monovalently. At equimolar amounts (middle panel), every antibody arm as well as receptor epitope is occupied, resulting in the most efficient multimerisation.
(B) Antibodies with a fast off-rate have a greater agonistic potential. When a high affinity antibody with a low dissociation rate binds to its target, the antibody is unlikely to dissociate with one arm and recruit another molecule (left panel). In contrast, a fast off-rate antibody allows for un- and rebinding, thus leading to increased accumulation and triggering (right panel).
Adapted from Mayes *et al.*[99]

CD40, 4-1BB and PD-1[103]. Strikingly, they demonstrated that a fast off-rate indeed correlated with increased clustering ability and agonism for all investigated receptors. Importantly, the mutated PD-1 antibody was nivolumab, a blocking antibody currently used in the clinic[104]. The 'fast dissociation' model proposes that high-affinity antibodies with a slow off-rate only bind to two receptors, leading to suboptimal accumulation. In contrast, antibodies with a fast dissociation rate are more likely to un- and rebind another molecule, bridging more receptor monomers and ultimately resulting in greater accumulation (Figure 1.3 B)[99,102,103].

1.2.3 Immune checkpoints

Immune checkpoints are receptors expressed on immune cells, which regulate their cellular function and activation. During homeostasis they are crucial for maintaining self-tolerance, thereby preventing autoimmune responses. Immune tolerance is a two-step process. First, central tolerance aims to eliminate any self-reactive T and B cells during their development in the thymus and bone marrow, respectively. If central tolerance fails, autoreactive B and T cells can emigrate from their central lymphoid organs into the periphery. Here, peripheral tolerance describes the suppression of autoreactivity in tissues. Antigen recognition alone does not lead to immune cell activation, as more signals are needed for proper stimulation[105]. Those signals include pathways activated by immune checkpoints, which can be subdivided into signalling with a positive, immune-stimulating effect and immunosuppressive pathways, which dampen the immune response. If sufficient pro-inflammatory signals are present, immune cells get activated, resulting in proliferation and enhanced effector functions. In contrast, when there are insufficient stimulatory signals, or increased anti-inflammatory mediators, the cells enter apoptosis, become anergic or differentiate into regulatory cells[106].

Tumours take advantage of immune checkpoints by controlling infiltrating immune cells through the activation of immune-dampening pathways. The most prominent examples of inhibitory co-receptors are cytotoxic T-lymphocyte-associated protein 4 (CTLA-4) and programmed cell death protein 1 (PD-1). Their crucial immunoregulatory role is exemplified by the phenotypes displayed by the respective knockout-mice. CTLA-4$^{-/-}$ mice exhibited severe lymphoproliferative disease, with mice succumbing early due to lymphocyte infiltration into organs and tissue destruction[107,108], indicating a crucial role in central tolerance and during the early stages of T-cell activation. In contrast to this, PD-1$^{-/-}$ mice grew up normally and looked healthy[109], but aged mice were more susceptible to certain autoimmune diseases, including lupus-like diseases and glomerulonephritis[110]. This suggests that while central tolerance was still intact, peripheral tolerance

was impeded. An overview of immune-checkpoint receptor and ligand pairs is provided in Figure 1.4.

1.2.4 Inhibitory immune checkpoints in cancer

As discussed in Section 1.1.2, the immune system is crucial for eradicating potentially cancerous cells in our body. Following the immunostimulatory effects observed in CTLA-4$^{-/-}$[107,108] and PD-1$^{-/-}$[110] mice, blocking antibodies against these receptors were trialled in murine cancer models for anti-tumour effects. CTLA-4 blockade resulted in a significant increase of tumour rejections. Importantly, survivors of the primary challenge also exhibited immune memory responses, as they were protected against a secondary challenge with the same cells[111]. Similarly, PD-1 blockade resulted in increased infiltration of effector T cells and reduced metastasis burden in the B16 melanoma model and the CT26 colorectal cancer model[112]. In what follows, the distinct mechanisms of immune-cell inhibition through inhibitory immune checkpoints will be discussed using the most prominent examples, CTLA-4 and PD-1. Subsequently, another less-studied inhibitory immune checkpoint, CD200R, will be introduced and the reasons for investigating this receptor will be explored.

1.2.4.1 CTLA-4 inhibitory functions

The co-inhibitory receptor CTLA-4 is expressed on T cells and competes for its ligands, CD80 and CD86 (B7-1 and B7-2, respectively), with the co-stimulatory receptor CD28. CTLA-4 as well as CD28 are both members of the CD28 receptor family, contain a single extracellular Ig domain and form disulfide-based covalent homodimers. Their cytoplasmic domains contain a YxxM consensus motif which is phosphorylated upon receptor triggering[50]. CTLA-4 recruits phosphatases to dampen T-cell activation[113], but it also utilises 'signalling-independent' mechanisms. Because CTLA-4 has a higher affinity for both ligands (CD80 and CD86, $K_D = 2.0 \times 10^{-7}$ and 2.6×10^{-6} M, respectively[114]), it can outcompete CD28 for binding ($K_D = 4.0 \times 10^{-6}$ and 2.0×10^{-5} M, respectively[114]),

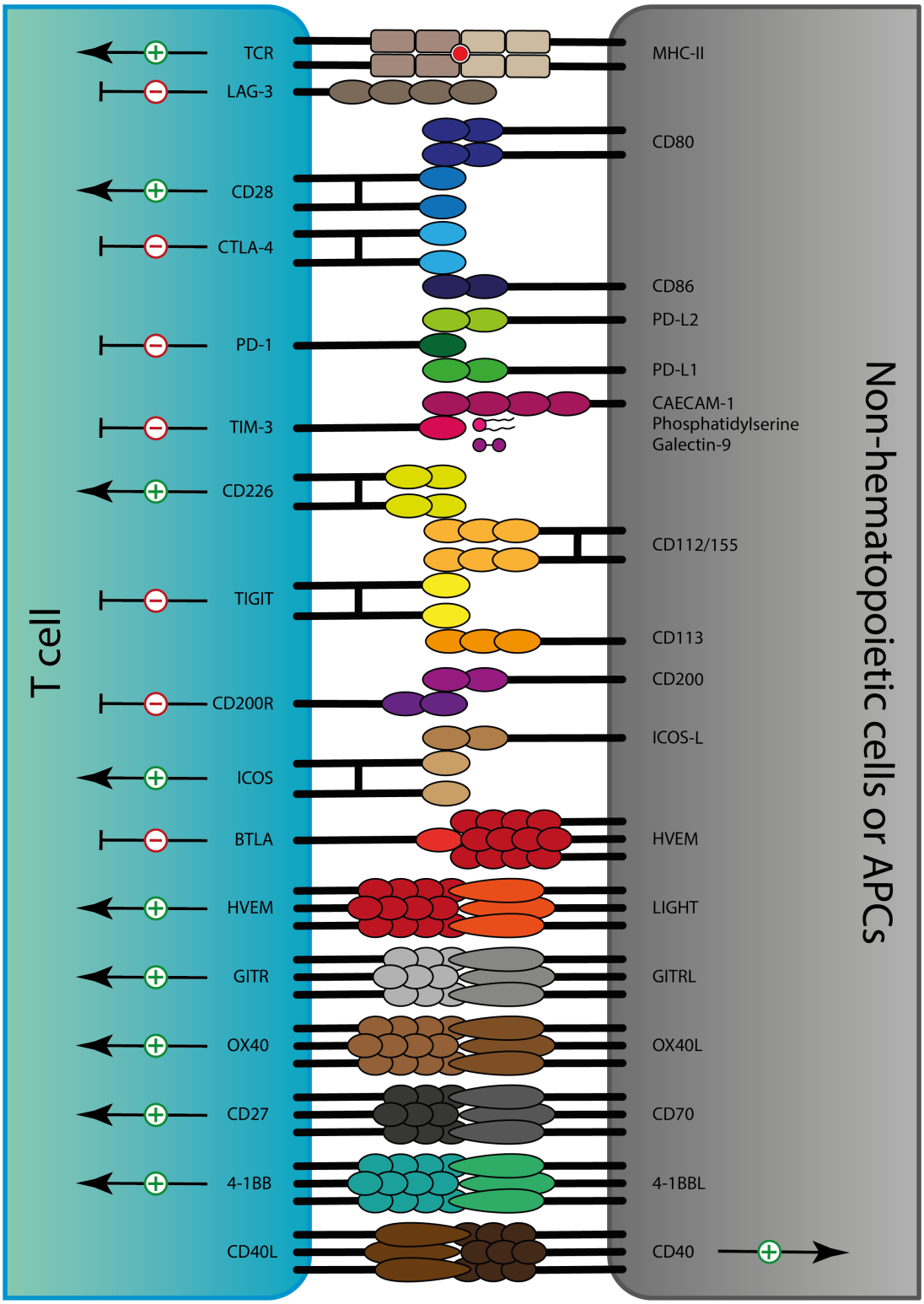


Figure 1.4: Overview of immune-checkpoint receptors and ligands
Schematic overview of different immune-checkpoint receptor/ligand pairs. The arrow indicates whether receptor activation results in pro- or anti-inflammatory signals. Some receptors and ligands share their binding partner with other molecules. Only ectodomains are depicted.

therefore reducing co-stimulatory signalling. Furthermore, CTLA-4 is constantly being endocytosed, which can result in trans-endocytosis of CD80 and CD86 whenever CTLA-4 is bound to its ligands[115]. This leads to additional cell-extrinsic suppressive functions by not only competing with CD28 for CD80/CD86 binding, but through complete removal of those ligands from the cell surface of APCs. Recently, it has been shown that while CD80 trans-endocytosis leads to degradation of both proteins, receptor and ligand, CTLA-4 is recycled back to the membrane after endocytosis with CD86[116]. This is regulated through a pH-dependent unbinding in the endosome of CTLA-4 and CD86, which allows further CTLA-4-mediated trans-endocytosis[116].

In contrast to being upregulated on activated T cells, CTLA-4 is constitutively expressed on T_{reg} cells at a high level. While CTLA-4-deficient T_{reg} cells develop normally, their function is defective as a conditional knockout caused fatal autoimmune disease in mice, albeit later than the full knockout[117]. While splenocytes from WT mice did not stop tumour progression, splenocytes from T_{reg}-conditional knockout mice reduced tumour growth, with 60 % complete regressions[117]. This dominant effect of CTLA-4 on T_{reg} cells was also confirmed by a study utilising CTLA-4-humanised mice and conditional knockout mice. Blockade of CTLA-4 function on T_{reg} cells, either through specific blocking using an anti-mouse-CTLA-4 antibody or conditional knockout, was more effective compared to targeting CTLA-4 on effector cells[118]. Interestingly, there was a synergistic effect when CTLA-4 was blocked on both populations, resulting in the most effective anti-tumour immune response[118]. Importantly, it was further demonstrated that anti-CTLA-4 blocking antibodies partly work through selective depletion of T_{reg} cells in an Fc-dependent manner[119,120], strengthening the idea of a crucial role for T_{reg} cells in CTLA-4-mediated immunosuppression. This is discussed in more detail in Section 1.3.3.3.

Ipilimumab was the first blocking antibody against an inhibitory immune checkpoint to be approved by the U.S. Food and Drug Administration (FDA)[121]. It is a recombinant human IgG1 antibody blocking the interaction of CTLA-4

with CD80/CD86. However, in line with the breakdown of central tolerance observed in CTLA-4$^{-/-}$ mice, treatment with ipilimumab led to a broad range of immune-related adverse events (irAEs) in 60-65 % of patients[122]. This could be explained by the activation of self-reactive T cells, as an enhanced diversity in the TCR repertoire was reported upon treatment with ipilimumab. This clonal expansion was associated with irAE frequency, and even preceded them, serving as a potential biomarker[123].

1.2.4.2 PD-1 inhibitory functions

PD-1 is also part of the CD28 receptor family and harbours a single Ig domain, but in contrast to CTLA-4 and CD28 it exists as a monomer. The cytoplasmic tail contains an ITIM and ITSM[50], and the latter was shown to be the crucial mediator for downstream signalling and T-cell inhibition[124]. PD-1 is upregulated on activated T and B cells and is only expressed at very low levels in naïve lymphocytes[125]. While most attention has been paid to the effects of PD-1 on T cells, the receptor is also found on activated NK cells, innate lymphoid cells as well as several myeloid cell populations[126].

PD-L1 (B7-H1) and and PD-L2 (B7-DC), the two ligands of PD-1, demonstrate a distinct expression pattern. While PD-L1 is found on heterogeneous cell populations, including different immune cells, stromal cells and cancer cells, PD-L2 is believed to be restricted to activated macrophages and DCs[126]. The expression levels of the two ligands also vary significantly, with mature DCs expressing 15-fold more PD-L1[127]. In contrast, PD-L2 has a 3-fold higher affinity for PD-1 compared to PD-L1 (3.7×10^{-8} M compared to 1.1×10^{-7} M)[128]. Overall, most reports have focused on the PD-1/PD-L1 axis as PD-L1 demonstrates a broader expression pattern, is expressed at higher levels and frequently upregulated in tumours[129]. Pro-inflammatory cytokines such as IFN-γ were shown to drive PD-L1 expression, acting as a natural negative feedback loop to dampen an ongoing immune response[130] and this immunoprotective mechanism is likely selected for during the immunoediting process of a tumour (Section 1.1.2).

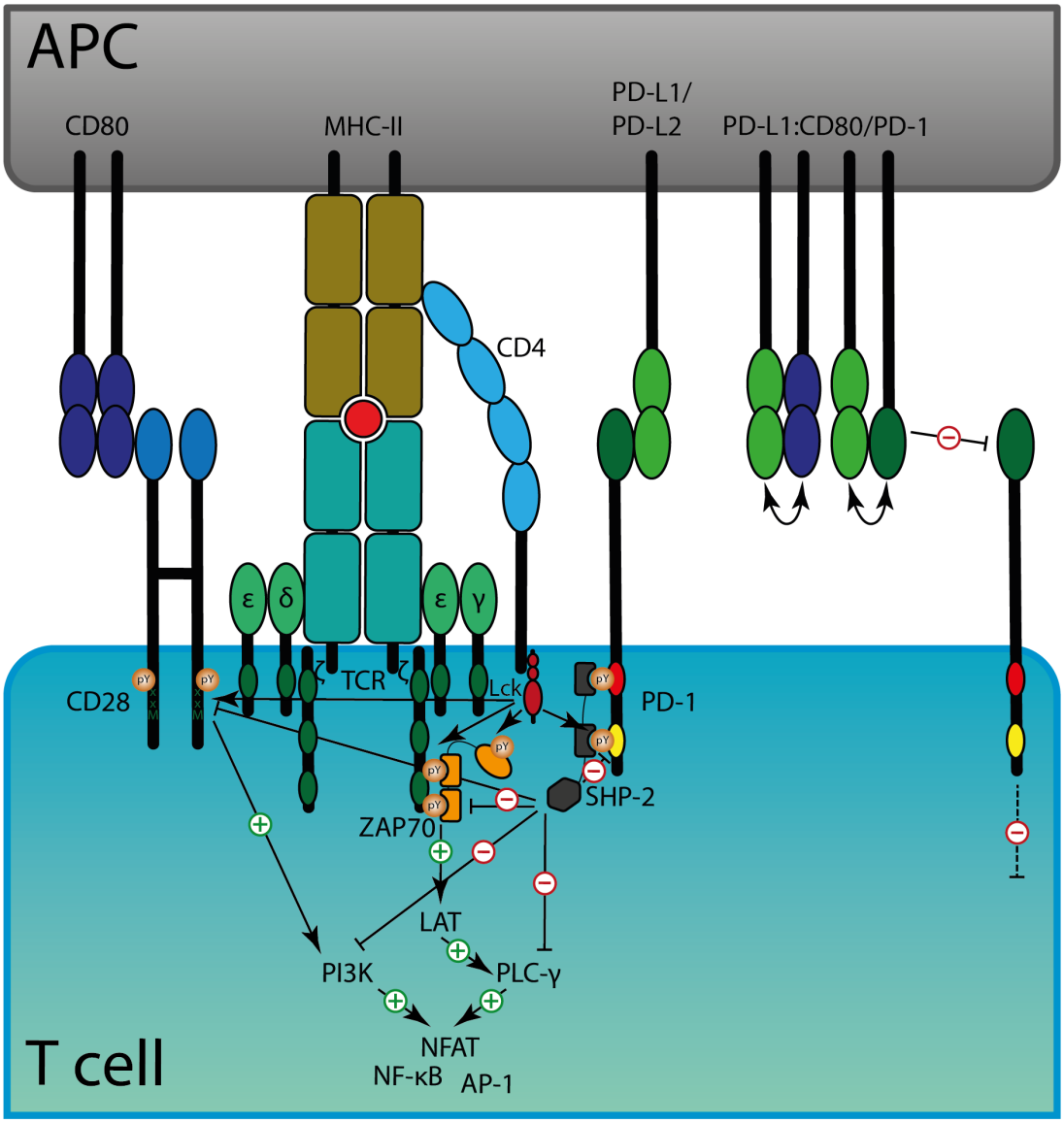


Figure 1.5: Overview of PD-1 signalling effects on TCR and CD28 pathways Upon TCR ligation to pMHC, Lck phosphorylates ITAMs (small green ellipses) on the TCR complex. Phosphotyrosines (pY) are only shown for one ITAM on CD3ζ. Phosphorylation of ITAMs leads to the recruitment of ZAP70 which binds with its SH2 domains to phosphorylated ITAMs. Next, ZAP70 gets phosphorylated by Lck and triggers subsequent phosphorylation of LAT, which activates different downstream pathways, including PLC-γ. Lck also phosphorylates CD28 (YxxM motif) and PD-1 (ITIM and ITSM; small red and yellow ellipses, respectively). Phosphorylation of CD28 leads to recruitment of PI3K, activating the PI3K/Akt pathway. Activation of TCR and CD28 pathways culminates in the nuclear translocation of transcription factors driving T-cell activation, including NFAT, NF-κB and AP-1. Counteracting this, phosphorylated PD-1 recruits SHP-2, which dephosphorylates multiple targets of the TCR/CD28 pathway, including CD28, PI3K, CD3ζ, ZAP70 and PLC-γ. Importantly, SHP-2 also dephosphorylates PD-1 in a negative feedback loop. Finally, CD80 and PD-1 can bind PD-L1 in *cis* to prevent PD-1 engagement in *trans*.

Figure 1.5 summarises the inhibitory effects of PD-1 on T-cell activation. Upon phosphorylation of the tyrosines within the ITIM (Y223) and ITSM (Y248), SHP-1 and SHP-2 can bind to those motifs. While SHP-2 is the dominant interaction partner in physiological settings *in vitro*[131,132] and *in vivo*[133], it is dispensable as PD-1 can exert its inhibitory functions also in absence of SHP-2. Whether SHP-1 can compensate for the loss of SHP-2, or potential other factors might facilitate PD-1 signalling, is still debated[131,134]. Interestingly, upon ligand binding, PD-1 co-localised with TCR/CD28 microclusters[75,135] and this was shown to be crucial for PD-1-mediated inhibition. This mechanism was size-dependent, as elongation of PD-1 via insertion of Ig domains resulted in exclusion of PD-1 from TCR microclusters as well as diminished inhibitory capacity[75].

While it is widely accepted that SHP-2 is the dominant phosphatase in physiological settings, the precise downstream signalling pathway remains controversial. Although one study suggested CD28 is the main target of PD-1 inhibition[135], others identified the TCR[75,136] or both TCR and CD28[131]. Importantly, SHP-2 can also dephosphorylate its binding target, PD-1, creating a negative feedback loop[75,135]. This has important consequences, as sustained PD-1 signalling is required for an exhausted T-cell phenotype (described in more detail in Section 1.4.1)[137]. Therefore, chronic antigen stimulation leading to TCR triggering, linked to phosphorylation of TCR and PD-1 through Lck, is required for constant PD-1 activity and the development of exhausted T cells.

CD80, a ligand for CD28 and CTLA-4, can also interact in *cis* with PD-L1. This interaction takes place on APCs, and inhibits the engagement of PD-L1 with PD-1, thus limiting PD-1-immunosuppressive functions (Figure 1.5)[138]. Furthermore, it was shown that *cis*-interaction of PD-L1 and CD80 disrupts binding of CD80 to CTLA-4, but not to CD28[139]. While CD80 binds CD28 monovalently, it bivalently interacts with CTLA-4[114]. As CD80 dimer formation is inhibited by PD-L1 *cis*-binding, this reduces overall avidity of CD80 to CTLA-4, but not CD28[139]. Therefore, the PD-L1/CD80 heterodimer can interfere with both inhibitory pathways, PD-1 and CTLA-4. However, this is in contrast to

another report which described reduced interaction of CD28/CD80 upon heterodimerisation of PD-L1/CD80[140]. Finally, PD-L1 was also reported to interact in *cis* with PD-1, preventing the ability of PD-L1 to engage PD-1 in *trans*[141].

Overall, the interaction network comprising CD28, CTLA-4 and PD-1, together with its ligands, CD80, CD86, PD-L1 and PD-L2, is highly complex and interconnected. Therefore, tissue-specific levels of expression are likely to play an important role in shaping overall signalling outcomes.

1.2.4.3 CD200R inhibitory functions

Due to the remarkable success of anti-PD-1 and anti-CTLA-4 antibodies in the clinic (Section 1.3.3.3), a lot of therapeutic development focused on these two targets. However, all these approaches focus on the reactivation of T cells in order to eradicate the tumour. As illustrated in Figure 1.1, although T cells play a crucial role by killing cancer cells, they require the support of other immune cell populations during key stages of the anti-tumour immune response. Therefore, there has been a growing interest in co-targeting T cells with other cells of the TME, including myeloid cells[142].

An important receptor controlling the activation of myeloid cells is CD200R. In mice, knocking out its ligand, CD200, resulted in a doubling of the $CD11b^+$ myeloid cell population in the spleen[143]. While, initially, it was believed that CD200R is restricted to the myeloid lineage, it was subsequently found to be expressed on T cells and B cells[144,145]. CD200R comprises two extracellular Ig domains, a transmembrane domain and a 67 amino acid long cytoplasmic tail with three conserved tyrosines[146]. The ligand, CD200 ($K_D = 5.0 \times 10^{-7}$ M[144]), has a similar structure[147], but only a short cytoplasmic domain (19 aa) with no apparent signalling capacity[146]. Instead of harbouring an ITIM or ITSM motif, the last tyrosine of CD200R is part of a NPXY motif, which gets bound by phosphotyrosine-binding (PTB) domain proteins with a distinct signalling pathway.

Phosphorylation of the first and last tyrosine, which is part of the NPXY motif, leads to optimal binding of the adaptor Dok2. Subsequently, Dok2 gets

phosphorylated and recruits RasGAP, leading to inactivation of Ras, which inhibits ERK as well as PI3K/Akt pathways (Figure 1.6)[148–150]. Recent studies suggested that the signalling events can be further divided into an inhibition of PI3K/Akt through Dok2 and Ras/ERK via RasGAP[151]. Overall, triggering of the CD200R pathway leads to immunosuppression, supported by the observation that loss of CD200 is associated with a more severe phenotype and accelerated disease onset in various autoimmune models[143,152]. On a cellular level, in mixed leukocyte cultures it was demonstrated that CD200R activation reduced type-1 cytokine production (IL-2, IFN-γ), while it induced type-2 cytokine release (IL-4, IL-10)[153].

CD200 is broadly expressed and was found on a variety of haematological and non-haematological cells (e.g. neurons and trophoblasts; Figure 1.6)[154–156]. Upon initiation of apoptosis in murine DCs, p53 induced the expression of CD200, reducing the inflammatory response to released self-antigens[157]. In an attempt to screen for other regulators of human CD200, C/EBPβ was identified as another transcription factor (TF) binding and inducing CD200 expression[158]. Overall, the broad tissue distribution of CD200 together with the restriction of CD200R to immune cells led to the suggestion that this axis is important to protect these tissues, such as placenta and brain, from the (myeloid) immune system[159].

Following the discovery of CD200R, CD200 receptor-like (CD200RL) proteins were identified. While one CD200RL protein was found in humans (CD200RLa), four were reported in mice (CD200RLa-d)[144]. Similar to CD200, they contain a short cytoplasmic domain which lacks signalling motifs. In contrast, they all include a conserved, positively charged amino acid (lysine) in the transmembrane region, which was shown to interact with the adaptor protein DAP12 (Figure 1.6)[144]. This protein harbours an ITAM, thereby creating the potential for activatory signal transduction. Thus, CD200R and CD200RL proteins are 'paired receptors', which are characterised by similar extracellular domains but contrasting signalling activity, i.e. inhibitory or activatory, respectively[160,161]. However, the natural CD200R ligand, CD200, does not bind CD200RL proteins and a host ligand of CD200RL proteins still remains to be identified[144,162]. It was

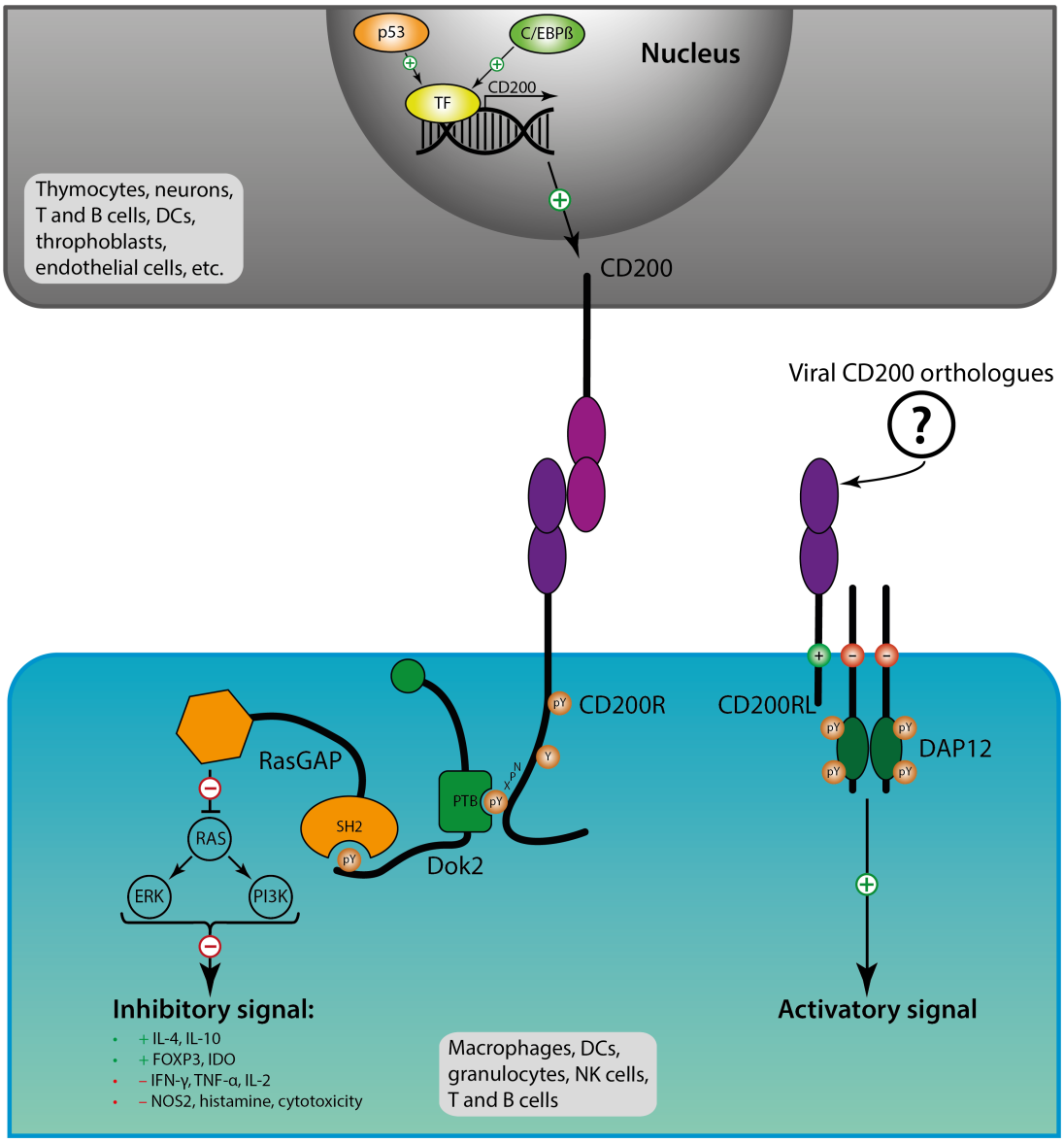


Figure 1.6: Overview of the CD200/CD200R axis
CD200 is broadly expressed and found on a variety of cells. The TFs p53 and C/EBPβ can bind to the CD200 promoter and induce gene expression. In contrast, CD200R expression is restricted to immune cells, with a preference for the myeloid lineage. Upon ligation of CD200/CD200R, phosphorylation of the tyrosine within the NPXY motif is crucial for the recruitment of Dok2. Dok2 in turn gets phosphorylated and recruits RasGAP, which inhibits the Ras/ERK and PI3K/Akt pathways. CD200RL proteins have a short cytoplasmic tail, but can bind to the adaptor protein DAP12, which harbours ITAMs, delivering an immune-stimulating signal. However, so far no ligands have been described for CD200RL proteins.

hypothesised that CD200R, just like other paired receptor families, was used by pathogens to suppress an immune response through viral orthologues that can bind host-inhibitory receptors. As a consequence, the human immune system evolved receptors with similar binding characteristics but opposite signalling functions to counterbalance the inhibitory effect of CD200R engagement by viral CD200 orthologues[163]. Indeed, human herpesvirus 8 and myxoma virus were found to express a CD200R ligand that reduced macrophage and basophil functions through engagement of CD200R[164–166]. However, the herpesvirus orthologues did not bind to the activating CD200RL proteins, suggesting that the virus further adapted to evade binding to immune-activating receptors[167]. Importantly, while murine CD200RL proteins were identified in various mouse strains[161], human CD200RLa was initially not found to be expressed on PBMCs, and it was suggested that this gene might be non-functional in humans[144]. In contrast, a recent study found CD200RLa on neutrophils and demonstrated that crosslinking of the receptor increased ROS and IL-8 production[168]. However, more research is needed to fully uncover the role and importance of CD200RLa in humans.

While all murine tumour studies demonstrated that CD200 inhibits CD200R$^+$ immune cells (reviewed by Choe *et al.*[169]), the overall effect on the anti-tumour immune response is still unclear. On the one hand, several studies claim that CD200R engagement dampens a tumouricidal immune response, characterised by reduced numbers of T cells producing IFN-γ and TNF-α, as well as an expansion of MDSCs[170–172]. On the other hand, there is also evidence for a tumour-suppressive role of CD200[173–177]. Instead of inhibiting effector cells, CD200 was shown to reduce the activity of immunosuppressive tumour-associated myeloid cells (TAMCs), by reducing IL-10 and stimulating TNF-α and IFN-γ expression[173,177]. Based on these reports, a study tested agonistic anti-CD200R antibodies in three syngeneic cancer models (B16-F10, EMT6 and LLC1) in order to inhibit TAMCs and MDSCs. However, no treatment benefit was observed in any of the models tested, and the authors recommended testing blocking antibodies

instead[178]. Ultimately, the specific composition and the baseline inflammation within the TME are likely driving the overall effect of CD200R engagement[175].

In contrast, most human studies support a pro-tumourigenic role of the CD200/CD200R axis as several cancers upregulate CD200, most prominently haematological malignancies[179–181], but also a variety of solid tumours[182–184]. Interestingly, on acute myeloid leukaemia (AML) patient blasts, CD200 expression correlated with PD-L1 levels and co-culture of $CD8^+$ T cells with CD200-expressing leukemic cancer cells led to the upregulation of PD-1 on T cells[185]. This was driven by CD200R engagement, as treatment with anti-CD200 antibodies reduced PD-1 levels, thereby creating the first link between CD200R and PD-1[185].

Overall, the human studies underpin the important role of CD200 in promoting tumour growth[169], which led to the development of blocking antibodies. Alexion Pharmaceuticals conducted a phase I clinical trial for a first-in-class anti-CD200 antibody (samalizumab, ALXN6000) for treatment of chronic lymphocytic leukaemia (CLL) and multiple myeloma (MM)[186]. While all MM patients (n = 3) exhibited disease progression, around 60 % of CLL patients (14/23) experienced a decreased tumour burden, but only one patient achieved a durable response[186]. Importantly, samalizumab had a good safety profile and the maximum tolerated dose was not reached. During pre-clinical development, it was demonstrated that NOD/SCID mice injected with human PBMCs and lymphoma cells expressing CD200, matched to levels observed in human CLL, were able to escape immune recognition[187]. Importantly, this effect was blocked upon treatment with anti-CD200 antibodies. In a follow-up study, it was shown that using an antibody with no effector functions (hIgG2/G4) was favourable compared to an Fc-engaging antibody (hIgG1)[156]. This was explained by ADCC of $CD200^+$ immune cells, including B cells, T cells, NK cells and $CD11c^+$ myeloid cells[156]. While the phase I clinical trial was terminated by the sponsor before completion due to administrative reasons[186], samalizumab will be further tested as part of the Beat AML phase Ib/II clinical trial investigating up to twelve novel therapeutic combinations for AML[188]. Similarly, Trillium Therapeutics Inc. developed a fully

human anti-CD200 hIgG4 antibody for treatment of AML[189], however, no reports of a phase I clinical trials have been announced and Trillium Therapeutics Inc. was recently acquired by Pfizer Inc.[190]. Finally, using their genetic and health survey data, the consumer genetics and research company 23andMe identified CD200R as a target for solid cancers[191]. They have developed a first-in-class CD200R-blocking antibody (23ME-00610)[192] and started a phase I clinical trial in 2022[193]. Recently, due to a good safety profile, this progressed into a phase II clinical trial[194].

Taken together, CD200R is an inhibitory immune checkpoint predominantly expressed on myeloid cells, which regulates their function by suppressing effector activity and inducing a regulatory phenotype. This has been linked to a tumour-promoting role and CD200 levels correlate with poor overall prognosis in a variety of tumours. Therefore, CD200R is an attractive target to reactivate myeloid cells using blocking antibodies. In combination with antibodies that predominantly stimulate T cells, this should result in a synergistic effect and promote tumour eradication.

1.3 Monoclonal antibody therapy

The first monoclonal antibody (mAb) approved by the FDA was the anti-CD3 mAb Orthoclone OKT3 (muromonab-CD3) in 1986 for the treatment of acute transplant rejection. Since then, monoclonal antibodies have revolutionised pharmaceutical drug development, becoming the predominant class of new drugs as well as the best-selling drugs[195].

The development of tools to create humanised or human antibodies led to a great acceleration in the development of mAbs, as it reduced potential side effects such as the induction of a human anti-mouse antibody (HAMA) response. HAMAs are the result of an immune response against the drug, which can lead to allergic side effects, but they also shorten the half-life of the antibodies. Furthermore, non-human antibodies have reduced capabilities to induce effector functions such as ADCC, ADCP or CDC[195], thus potentially diminishing the overall efficacy depending on the mode of activity of the drug.

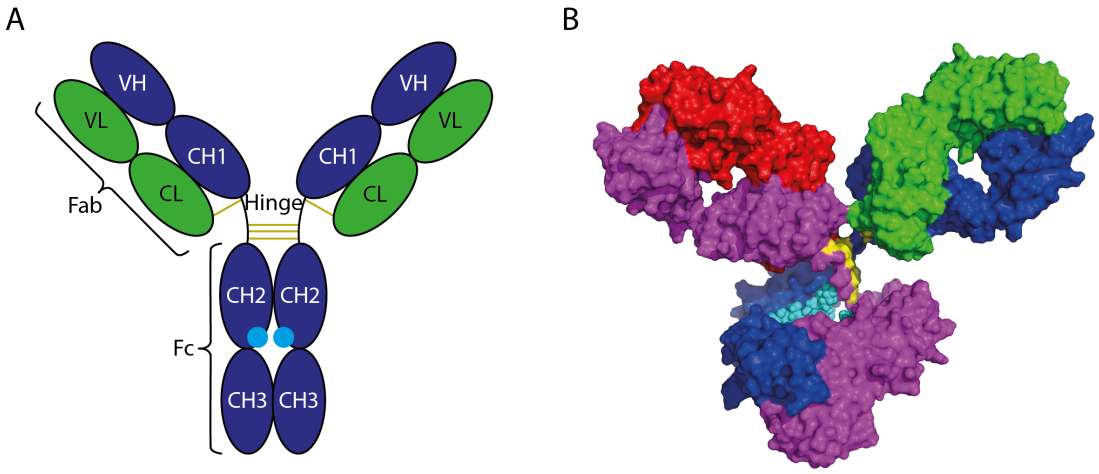


Figure 1.7: Structure of mouse IgG1
(A) A schematic overview of the structure of mIgG1. Heavy chains are coloured in blue, light chains in green. Glycans are depicted as cyan dots at CH2 and hinge disulfide bonds are shown in yellow.
(B) A cartoon representation of mIgG1, Protein Data Bank (PDB) ID: 1IGY[196]. Heavy chains are labelled in blue and purple and light chains in green and red. Glycans are shown in cyan and disulfide bonds in yellow.

In what follows, mAbs will be introduced in greater detail, with a focus on properties that can be modulated and engineered to enhance the efficacy of anti-cancer drugs.

1.3.1 Antibody structure

Antibodies are Y-shaped, globular proteins that are produced by B cells and have the capability to specifically target antigens. Antibodies are composed of two identical light and heavy chains (LCs and HCs, respectively). Also known as immunoglobulins, antibodies can be divided into five different classes based on their HC: IgA, IgD, IgE, IgG and IgM. Humans have two IgA and four IgG subclasses, whereas mice lack IgA subclasses. There are two classes of LCs, κ and λ. Because IgG is currently the most important antibody class for therapeutic development, the following discussion will solely focus on this class. Furthermore, as the worked described in this thesis only involved the mouse IgG1 isotype (mIgG1), this will be used as a representative example to discuss the structure.

As shown in Figure 1.7, each HC consists of four Ig domains, named variable heavy (VH) and constant heavy (CH1, CH2 and CH3), whereas the LC comprises

two domains, variable light (VL) and constant light (CL). This classification of variable and constant domains allows division of the antibody into the variable and constant region, respectively. The constant region is determined by the isotype and influences the effector functions[197], whereas the variable region contains the complementarity-determining regions, which are crucial for binding specificity.

The asparagine at residue 297 is the major glycosylation site of antibodies (Figure 1.7, cyan colouring), and this glycosylation facilitates biophysical stability[198] as well as effector functions[199]. The exact glycosylation pattern can vary and contributes to the specific properties of the antibody.

The four polypeptide chains are connected through disulfide bonds between the HC-LC and HC-HC (Figure 1.7, yellow colouring). These disulfide bonds also determine the fragments created by cleavage with different enzymes. The protease papain cleaves after the first disulfide bond connecting HC-LC. This creates two identical fragments that can bind antigens monovalently (fragment antigen binding, Fab) as well as the remaining constant domains (CH2-CH3) connected via disulfide bonds (fragment crystallisable, Fc). In contrast, pepsin digests most of the Fc region, but leaves all disulfide bonds intact, thereby creating a bivalent $F(ab')_2$, which lacks effector functions[200].

While antibodies are usually depicted as Y-shaped, ordered proteins (Figure 1.7 A), it is important to note that most isotypes are very flexible, which is better illustrated in the cartoon representation of a structure of mIgG1 (Figure 1.7 B). The inherently disordered and flexible hinge region allows antibodies to bind epitopes at various distances and arrangements[201].

1.3.2 Fcγ receptors

The choice of isotype and subclass is of great importance when developing a therapeutic mAb, as this heavily influences the affinity to different FcγRs as well as complement binding, which is responsible for ADCP, ADCC and CDC[197]. FcγRs are NTRs (Section 1.2) and, along with antibodies, belong to the Ig superfamily (IgSF). They are expressed on innate immune cells as well as B cells

and regulate their cellular activity upon binding to an antibody. In humans, there are five activating (FcγRI, FcγRIIa, FcγRIIc, FcγRIIIa, FcγRIIIb) and one inhibitory FcγR (FcγRIIb). Mice also have one inhibitory (FcγRIIb), but only three activating receptors (FcγRI, FcγRIII, FcγRIV)[86]. Only FcγRI and mFcγRIV are considered high-affinity receptors, with K_D values of around 1×10^{-8} – 10^{-9} M, in contrast to the affinities of the other FcγRs of around 1×10^{-6} – 10^{-7} M[202,203]. FcγRs have a distinct expression pattern that can change upon differentiation or activation[86], thereby allowing the immune system to fine-tune the response depending on the context.

Choosing the correct isotype of a therapeutic antibody is crucial for optimal efficacy, and there is a lot of effort to improve on this through antibody engineering to increase, decrease or completely abrogate certain interactions, thereby influencing effector functions. The cumulative binding properties of an isotype to either activating or inhibiting FcγRs is described as the activating-to-inhibitory (A/I) ratio[204]. A higher ratio means these isotypes bind preferentially to activating FcγRs, triggering ADCP and ADCC. In contrast, low ratios indicate a dominant binding of FcγRIIb, leading to an inhibition of effector functions. For mouse isotypes, IgG2a and IgG2b demonstrated the highest A/I ratios (70 and 7, respectively), whereas IgG1 had a low ratio (0.1)[204]. IgG3 does not bind FcγRs and therefore this ratio is not relevant[203,205]. It is important to note that the A/I ratios depend on the expression levels of FcγRs in the respective microenvironment. For example, immune cells from mice lacking the inhibitory FcγRIIb produced strong effector functions upon treatment with antibodies of the mIgG1 isotype, which was not the case for cells from WT mice[204]. Finally, interaction with the complement component 1q (C1q) can lead to the activation of the complement cascade, resulting in CDC. While for some antibodies, CDC does not play an important role in mediating cytotoxicity[204,206], pre-clinical studies using the anti-CD20 antibody rituximab demonstrated the opposite[207]. Similar to FcγRs, the overall level of CDC depends on the specific microenvironment, isotype as well as affinity of the antibody[208].

While there is a lot of effort in identifying novel mutations that change FcγR and complement engagement[209,210], this topic is beyond the scope of this thesis, and only two commonly used substitutions will be described in the following. As mentioned above, glycosylation is important for effector functions; thus, replacement of the asparagine at residue 297 with an alanine (N297A mutation) is a common method to remove *N*-linked glycans and diminish FcγR binding[211]. Furthermore, the aspartic acid at position 265 was found to be crucial for mediating Fc-associated effector functions. Therefore, substitution of the aspartic acid with an alanine (D265A mutation) is also commonly used for reducing effector functions[212]. It is important to note that while these mutations strongly reduced monomeric binding as measured by surface plasmon resonance (SPR) or flow cytometry[211,212], immune complexes of these antibodies could still be bound by cells expressing FcγRs, indicating that Fc-engagement was not completely abolished[213].

For human antibodies, the A/I ratios have not been determined, but, generally, IgG1 and IgG3 bind more strongly to activating receptors, leading to increased effector functions, compared to IgG2 and IgG4[202]. While IgG4 was initially considered to harbour very little effector function[214], it was subsequently demonstrated that the high-affinity FcγRI can bind to IgG4, though at reduced affinity[202]. This has important implications for anti-PD-1 therapeutic mAbs, which were designed as IgG4 isotype for reduced Fc-engagement (discussed in Section 1.3.3.3). While human IgGs can bind mouse FcγRs[203], there are nevertheless some discrepancies, making pre-clinical development of human mAbs in mouse models challenging. Alternative options include i) choosing a mouse isotype that resembles the behaviour of the corresponding human isotype closely or ii) using mice that are humanised for FcγRs[215,216].

1.3.3 Monoclonal antibodies for cancer therapy

As described in Section 1.1.2, the immune system plays a crucial role in preventing the development of cancerous cells. However, this system can fail leading to the

accumulation of mutated cells, which can ultimately progress to the formation of a tumour. In an effort to prevent this, the immune system can be manipulated with mAbs to facilitate the recognition and eradication of cancer cells. As of late 2019, the FDA approved 79 therapeutic mAbs, with 30 mAbs designated for cancer therapy[195]. These mAbs can be classified by their mode of action, such as (i) direct binding of tumour cells to induce ADCC, ADCP or CDC, (ii) modulating tumour cell activation and proliferation or (iii) targeting immune checkpoints to either trigger or block them. This is by no means a strict classification, and antibodies may inadvertently, or by design, function through several mechanisms. In what follows, the different mode of actions will be introduced, with a focus on targeting inhibitory immune checkpoints and the involvement of FcγRs (Section 1.3.3.3).

1.3.3.1 Cytotoxic tumour-targeting antibodies

Rituximab (IgG1) was the first mAb approved for cancer therapy in 1997[195]. It targets the antigen CD20, which is present on all B cells, except pro-B cells and plasma cells[217]. It is used to treat B cell-driven haematological diseases such as non-Hodgkin lymphomas and CLL. Rituximab binds to all $CD20^+$ cells, leading to rapid target cell depletion via ADCC and CDC[218]. Generally, antibodies inducing effector functions are most effective in treating haematological malignancies, as there is no issue with tumour penetration. Besides multiple CD20-targeting mAbs, other FDA-approved drugs include alemtuzumab, targeting CD52 on B-CLL cells, and daratumumab and isatuximab, both targeting CD38 on MM cells. Antibody-drug conjugates (ADCs) are mAbs that are coupled with a payload, often a cytotoxic drug, enabling a more specific drug release. Approved ADCs include gemtuzumab ozogamicin, targeting CD33 on AML cells, brentuximab vedotin, targeting CD30 on Hodgkin lymphoma cells, and inotuzumab ozogamicin, targeting CD22 on acute lymphoblastic leukaemia cells[121].

For cytotoxic tumour-targeting antibodies, a higher A/I ratio is usually associated with an increased efficacy[204] and mutating the Fc region to increase affinity to activating FcγRs results in more potent target-cell depletion[219]. It

is important to note that while antibody-effector functions lead to a rapid, innate immune response, they generally do not produce any immune memory-associated effects. However, there is accumulating evidence demonstrating a vaccinal or immunising effect of tumour-targeting mAbs[220]. It has been shown that macrophages were crucial for the initial antibody-mediated killing through hFcγRIIIa. Subsequently, DCs took up immune-complexes via hFcγRIIa and induced an anti-tumour T-cell response, which resulted in immune memory[221].

1.3.3.2 Antibodies modulating tumour cell activation and growth

Antibodies targeting EGFR (cetuximab, panitumumab, necitumumab)[222] and HER2 (trastuzumab, pertuzumab, trastuzumab emtansine)[223] exhibit two distinct mechanisms of action. First, they block the corresponding receptors, EGFR or HER2, preventing their activation and proliferative signalling. Additionally, as both proteins are also upregulated on tumour cells, mAb binding can trigger antibody effector functions, leading to cytotoxicity. Thus, they not only block important signalling pathways in tumour cells, but also recruit cytotoxic immune cells.

Lastly, bevacizumab and ramucirumab bind to VEGF-A and VEGFR2, respectively. The vascular endothelial growth factor (VEGF) axis is important for promotion of angiogenesis, a crucial process during carcinogenesis to allow for the increased demands for nutrients in tumours, which is one of the hallmarks of cancer[3] (Section 1.1). Therefore, neutralising the growth factor itself (bevacizumab) or blocking the binding to the receptor (ramucirumab) limits the blood supply into the tumour and the potential for proliferation[195].

1.3.3.3 Antibodies targeting immune checkpoints

Immune checkpoints (introduced in Section 1.2.3) are membrane proteins that regulate immune cells, either through delivery of a co-stimulatory signal or by inhibiting immune-cell activation. There are numerous antibodies targeting co-stimulatory receptors currently in pre-clinical and clinical development, for example against ICOS[224] or TNFR superfamily members such as CD27, CD40,

GITR, OX40 and 4-1BB[225]. mAbs directed against co-stimulatory proteins aim to agonise and activate. As discussed in Section 1.2.2.1, TNFR members require multimerisation for successful triggering. This is either facilitated through their trimeric ligands (Figure 1.4), or via antibodies that crosslink receptors, a process enhanced by FcγR binding[94,226]. However, so far, none of the tested antibodies has been approved by the FDA.

In contrast, antibodies blocking inhibitory immune receptors have revolutionised cancer treatment. In 2011, the FDA approved the first immune-checkpoint inhibitor, ipilimumab, which targets CTLA-4 and is used for the treatment of metastatic melanoma. This was followed by the approval of multiple mAbs blocking the PD-1/PD-L1 axis, such as nivolumab, pembrolizumab, cemiplimab, dostarlimab and retifanlimab binding to PD-1, as well as atezolizumab, avelumab and durvalumab directed against PD-L1[121,227]. In 2022, the first antibody targeting lymphocyte-activation gene 3 (LAG-3), relatlimab, was approved for the treatment of advanced melanoma, demonstrating superior survival in combination with nivolumab compared to nivolumab monotherapy[228]. LAG-3 in an inhibitory co-receptor that binds to MHC-II and reduces T-cell activation. For metastatic melanoma, the overall survival using the chemotherapy-based standard of care treatment (dacarbazine) was below 10 %[229], but ipilimumab as well as the combination with nivolumab increased the 3-year survival to 34 % and 58 %, respectively[230]. Although the indications that can be treated with immune-checkpoint blockade (ICB) is increasing, most patients still do not respond. Primary resistance relates to patients that do not respond during their first cycle. In contrast, acquired resistance is characterised by an initial treatment response, but the tumour subsequently develops new mechanisms and relapses[231]. It is crucial to understand the different modes of actions in greater detail, in order to overcome hurdles or develop promising biomarkers to better predict responses. While the involvement of FcγRs in cytotoxic tumour-targeting as well as agonistic antibodies was long known[232], there is now more and more appreciation of the importance of FcγRs for immune-checkpoint inhibitors[209,233].

CTLA-4 blocking antibodies were primarily designed to inhibit the interaction of CTLA-4 with CD80/CD86, and the effects of the Fc-region were discovered later. As discussed in Section 1.2.4.1, T_{reg} cells have the highest expression of CTLA-4 and it was subsequently demonstrated in several pre-clinical models that anti-CTLA-4 treatment depletes them, explaining how anti-tumour responses might be enhanced[119,120]. However, in a recent study, histologic examination of tumour biopsies from patients treated with ipilimumab and another anti-CTLA-4 blocking antibody, tremelimumab, did not demonstrate reduced infiltration of T_{reg} cells[234]. The authors suggested that anti-CTLA-4 antibodies do not elicit strong effector functions in humans and should therefore be engineered to better deplete T_{reg} cells[234].

A study by Ravetch and colleagues suggested that anti-PD-1 and anti-PD-L1 antibodies demonstrate opposing FcγR requirements for optimal efficacy[235]. As PD-L1 is often expressed on tumour cells, anti-PD-L1 antibodies can also function as cytotoxic tumour-targeting antibodies. Furthermore, PD-L1 is also expressed on myeloid cells and TAMs were reduced in an FcγR-dependent fashion upon treatment with anti-PD-L1 mAbs in the MC38 colorectal cancer model[235]. Additional studies are necessary as immunostimulatory APCs and T cells also express PD-L1, therefore becoming a potential target for antibody-dependent cytotoxicity. The currently approved PD-L1 blockers are all of the hIgG1 isotype, however, while atezolizumab and durvalumab have mutations to reduce FcγR binding (Fc-null antibodies), avelumab still retains Fc-engagement. Interestingly, Saban *et al.* demonstrated that avelumab and atezolizumab exhibit the same efficacy in the MC38 tumour model using FcγR-humanised mice[236]. Furthermore, the authors showed that the combination of an FcγRIIb-specific blocking antibody with avelumab led to a reduction in volume of MC38 tumours. Using an afucosylated form of avelumab, which increases binding to the activating FcγRIIIa and FcγRIIIb, resulted in greater efficacy, which was driven by increased infiltration and activation of neutrophils[236]. While this pre-clinical study suggests that the currently approved anti-PD-L1 are not designed optimally, more research

is needed to fully understand the consequence of FcγR engagement of anti-PD-L1 mAbs in humans.

In contrast to anti-PD-L1 antibodies, Dahan *et al.* demonstrated that the anti-tumour activity of Fc-null PD-1 blockers was increased compared to FcγR-engaging mAbs in the MC38 colorectal cancer model[235]. Furthermore, in Fcgr2b$^{-/-}$ mice, lacking the inhibitory FcγRIIb, proliferation of CD8^{+} T cells was augmented upon treatment with anti-PD-1 mAbs compared to WT animals, indicating suboptimal T-cell activation in WT mice[235]. A study by Pittet and colleagues demonstrated increased efficacy of a PD-1 blocking antibody upon combination with an FcγR blocker (clone 2.4G2) in MC38 tumours[237]. They showed that while PD-1 antibodies first bound to T cells (PD-1^{+}), they were subsequently captured by macrophages (PD-1^{-}) via FcγRs. Therefore, the authors argued, FcγR-antibody interactions limit the therapeutic response due to insufficient blockade[237]. Finally, Moreno-Vicente *et al.* showed that in a vaccination setting using OVA antigen, a mIgG1-N297A (Fc-null) PD-1 blocking antibody led to increased proliferation of antigen-specific T cells compared to the mIgG1 anti-PD-1 mAb[238]. Importantly, the authors demonstrated the same effect in FcγR-humanised mice using hIgG4 and hIgG4-FALA (Fc-null) PD-1 blockers. While they did not find a significant improvement in survival using two different tumour models (MC38 and 9464D), they showed increased levels of PD-1 on CD8^{+} T cells when using Fc-null blockers as well as more activated myeloid cells, underpinning a greater activation potential of the Fc-null antibodies[238].

The current anti-PD-1 mAbs approved by the FDA (nivolumab, cemiplimab, pembrolizumab, dostarlimab and retifanlimab) are all hIgG4 antibodies, a subclass which is considered to have relatively low, but some, FcγR binding potential. In contrast, BeiGene developed a high-affinity hIgG4 PD-1 blocker (BGB-A317, tislelizumab) with no FcγR binding. They demonstrated superior efficacy of the Fc-null blocker in a tumour xenograft model compared to the Fc-engaging antibody[239]. As a potential mode of action, they showed that hIgG4 has a

high affinity to FcγRI, which can lead to phagocytosis of $CD8^+$ T cells *in vitro*. Tislelizumab is currently in phase III clinical trials[240].

Of note, the human IgG4 isotype can undergo a process called fab-arm exchange (FAE), where the full antibody dissociates into two HC-LC pairs, which can create bispecific antibodies through association with a HC-LC molecule from a different antibody. FAE can be abrogated through the S228P mutation[241], which is incorporated in all FDA-approved PD-1 blockers, as well as antibodies undergoing clinical evaluation, including tislelizumab[209,240].

1.4 Anti-PD-1 antibodies for cancer therapy

As this thesis focused on the improvement of anti-PD-1 antibodies for cancer immunotherapy, the current research landscape on this topic will be discussed in greater detail, with a focus on the cells targeted by PD-1 blockers as well as predictive biomarkers. The involvement of FcγRs was discussed in the previous Section (1.3.3.3) and will not be explored again. Finally, combination approaches targeting myeloid cells will be considered and the rationale for combining anti-PD-1 antibodies with CD200R blockers will be discussed.

1.4.1 Cells targeted by anti-PD-1 therapy

As described in Section 1.2.4.2, PD-1 is expressed by a variety of immune cells, but most attention has been paid to the effects on T cells[126]. On T cells, PD-1 is mostly absent on naïve cells, but is transiently upregulated after activation[125]. Upon antigen stimulation, for example a viral infection, naïve T cells start proliferating and shift their phenotype on a transcriptional, epigenetic and metabolic level towards the delivery of effector functions. The duration and strength of TCR signalling is important for the degree of PD-1 upregulation, which is controlled via promoter demethylation[242]. Following clearance of the stimulus/virus, most effector T cells are short-lived and undergo apoptosis, with only around 10 % differentiating into memory T cells, which were found to remethylate their *Pdcd1* (the gene encoding mouse PD-1) locus

to downregulate PD-1[242]. In contrast, constant antigen exposure, i.e. during chronic viral infection or cancer, led to exhausted T cells rather than memory T cells. Due to the chronic TCR stimulation, PD-1 was constitutively upregulated, and even upon clearance of the antigen, the promoter remained demethylated[242]. Exhausted T cells are characterised by reduced effector functions, upregulation of several inhibitory receptors as well as an altered transcriptional, epigenetic and metabolic phenotype[243]. Importantly, exhausted T cells are not inert, as they still retain certain effector function, for example controlling a chronic viral infection[243]. One potential evolutionary advantage of exhausted T cells is the reduced immunopathology during chronic viral infections, as a constant T-cell response could result in severe tissue damage[244]. Generally, there are two different states of T-cell exhaustion. Progenitor-exhausted T cells are characterised by high expression of the TF Tcf-1, the chemokine receptor CXCR5 as well as intermediate levels of PD-1[245]. At this stage, T cells retain their proliferative capacity and can still be 'rescued', for example by blockade of the PD-1 axis. However, once T cells are terminally exhausted, they downregulate Tcf-1, upregulate Eomes and further increase PD-1 levels[245]. Treatment with PD-1/PD-L1 blockers fails to induce proliferation or reprogramming of these cells[246–248]. Of note, progenitor-exhausted T cells can not only self-sustain their population through proliferation, but they can also differentiate into the second type of exhausted cells, the terminally-exhausted T cells[248]. Although exhausted T cells were initially found in chronic viral infections[249], a very similar pattern has been described for tumour-infiltrating T cells[250,251]. Interestingly, while progenitor-exhausted T cells retain their proliferative capacity and are more polyfunctional as well as polyclonal, terminally-exhausted cells have a stronger cytotoxic capacity, but are short-lived. It has been shown that anti-PD-1 therapy targets progenitor-exhausted T cells, thereby stimulating their proliferation and differentiation into terminally-exhausted T cells, which can mediate tumour control through their cytotoxicity[250,251].

One topic of debate is the origin of these T cells. Administration of the sphingosine-1-phosphate receptor-1 agonist FTY720 inhibits egress of lymphoid cells from lymphoid organs, ultimately depleting them from blood[252]. Surprisingly, treatment of established tumours with FTY720 had no impact on tumour growth, indicating that the tumour-resident T cells are crucial for a successful anti-tumour immune response. More importantly, the combination of anti-PD-1 and anti-CTLA-4 antibodies was still efficacious, as FTY720 treatment did not stop the tumour control[250]. This data seems to contradict the proposed cancer-immunity cycle (Section 1.1.2), as T-cell migration from the dLN to the site of the tumour was inhibited with no effect on tumour control. However, it should be noted that this study was carried out using antigen-specific P14 T cells, which recognise a LCMV peptide from gp33, that was transduced into B16 melanoma cells[250]. Upon intravenous injection of P14 cells, B16-gp33 cells were subcutaneously inoculated one day later. The tumour-specific T cells are likely to have been primed by DCs and migrated into the tumour by day 16, when FTY720 treatment was initiated[250]. In contrast to this mouse study, single-cell RNA sequencing (scRNA-seq) of treatment-naïve human tumours and paired blood samples demonstrated a clear expansion of T cells in tumours, normal adjacent tissue and peripheral blood[253]. Importantly, expansion of T-cell clones in blood correlated with increased infiltration of these clones into the tumour. Interestingly, while a cluster of cells likely resembling exhausted $CD8^+$ T cells as well as effector T cells was expanded in all analysed locations, only exhausted T cells were expanded in a blood-independent fashion in tumours and adjacent tissues[253].

Overall, the mouse datasets suggest that progenitor-exhausted T cells are the key targets of anti-PD-1 blockade[250,251]. Furthermore, insights from human scRNA-seq underpin the importance of a constant replenishment of T cells from peripheral blood, rather than intratumoural T-cell proliferation[253]. It is important to note that while most studies only differentiate between two exhausted T-cell subsets, this is not a binary but rather a gradual state, with distinct functionality associated with each phenotype[254].

Lastly, while most attention has focused on $CD8^+$ T cells, $CD4^+$ T cells also express PD-1 and can be suppressed through its inhibitory functions[255]. Importantly, T_{reg} cells are also controlled through PD-1, and Nishikawa and colleagues demonstrated that intratumoural T_{reg} cells have very high levels of PD-1 and start proliferating upon PD-1 blockade[256]. Additionally, anti-PD-1 treatment led to increased suppressive activity in a model where PD-1 is only present on T_{reg} cells and a link to hyperprogressive disease (HPD) was established. HPD describes the phenomenon of a rapidly progressing cancer immediately after treatment initiation. In a follow-up paper, the authors propose the ratio of PD-1 levels between $CD8^+$ and T_{reg} cells as a new biomarker[257]. Interestingly, another report found increased M2 macrophage infiltration in patients with HPD and hypothesised that this is dependent on Fc/FcγR interactions. They demonstrated that while nivolumab hIgG4 accelerated tumour progression in a patient-derived xenograft, nivolumab $F(ab')_2$ treatment reduced tumour growth, indicating an Fc-dependent effect[258].

1.4.2 Biomarkers predicting PD-1 blockade efficacy

As only a subset of patients responds to PD-1 blockade, there has been a lot of effort trying to find biomarkers to stratify the patient populations to achieve greater efficacy, but also understand the mechanisms of resistance.

One indicator predicting response to immune-checkpoint inhibitors is a dysregulation of the respective immune axis within the TME. IFN-γ, secreted by infiltrating $CD8^+$ T cells, can lead to the upregulation of PD-L1 on tumour cells, ultimately reducing the killing capacity of T cells[259]. Indeed, response towards atezolizumab (anti-PD-L1) correlated with expression of PD-L1 in the TME, especially when PD-L1 was found on tumour-infiltrating leukocytes[260,261]. Similarly, a phase III clinical trial demonstrated greater efficacy of pembrolizumab (anti-PD-1) compared to chemotherapy in PD-L1-positive non-small-cell lung cancer, which led to a subsequent FDA approval[262]. PD-L1 expression was also a predictor for response in metastatic melanoma, however the presence of

$CD8^+$ T cells within the cancer or at the tumour margin correlated more strongly, indicating the importance of immune cell infiltration in the TME[263]. As mentioned in Section 1.4.1, the ratio of PD-1 levels on $CD8^+$ and T_{reg} cells can further strengthen the predictive value of the state of the immune microenvironment[257].

Besides the TME, there are also genetic determinants influencing the therapy response. The overall mutational load was shown to be a positive correlate for the efficacy of anti-CTLA-4 therapy using ipilimumab[264,265]. Subsequently, a positive association was also demonstrated for mutational load and number of neoepitopes for anti-PD-1 therapy with pembrolizumab[266]. Finally, a meta-study of 27 tumour types and subtypes compared the objective response rate with the median tumour mutational burden and identified a striking positive correlation between the two parameters[267]. A high degree of somatic mutations can be caused by a deficiency in the mismatch-repair machinery, which is a system preventing DNA mutations during DNA replication[268]. A faulty DNA repair machinery leads to an increased tumour mutational burden, which can be easily detected as mutations in microsatellite regions, also referred to as microsatellite instability. In fact, high microsatellite instability or deficient mismatch-repair were the first genetic biomarkers that led to a FDA approval, instead of the location of the primary tumour[268–270].

Novel predictive biomarkers include certain commensal microbiota[271,272] as well as maximal heterozygosity for human leukocyte antigen class I loci[273], which are discussed in greater detail in a review by Li *et al.*[274].

1.4.3 Myeloid cell interaction with PD-1 blockade

As described in the cancer-immunity cycle (Section 1.1.2), there are several steps where an immune response against a tumour can be inhibited. While anti-PD-1 therapy aims to reactivate the tumour-infiltrating T cells, that alone might not be sufficient in some cases, as demonstrated by the fact that the majority of patients cannot benefit from this therapy.

In order to elicit a fully functional immune response, there is a constant cross-talk between the innate and the adaptive immune system. Translating this into the tumour setting, APCs are required to take up antigens from the tumour and present it to T cells in lymphoid organs. Subsequently, T cells need to migrate to the tumour in order to kill the cancerous cells[9]. Importantly, at this final step, T cells are not only controlled by tumour-intrinsic factors like PD-L1 expression, but also by inhibitory TAMCs, namely MDSCs and TAMs. The lack of cross-presenting APCs, or the presence of inhibitory myeloid cells might be one of the reasons why some patients do not respond to PD-1 blockade. Thus, targeting those cells provides a novel therapeutic option for enhancing anti-PD-1 immunotherapy[22].

Indeed, multiple studies have already investigated the influence of the myeloid cell compartment on the anti-tumour immune response. While there are different APCs present in the TME, several reports have demonstrated that most subtypes are rather immunosuppressive and inhibit a productive T-cell response[23,275,276]. TAMs as well as CD11b$^+$ DCs were found to interact with CTLs, but not stimulate their cytotoxic functions by cross-presentation of tumour antigens[275,276]. Only a very small population of CD103$^+$ DCs (DC1s) exhibited those features, however the numbers within the TME are often too low to induce an adequate response[23,25]. In what follows, an overview of the current understanding of DC1s during anti-PD-1 therapy is given.

A DC-specific knockout of *Sec22b*, a trafficking protein involved in antigen cross-presentation, resulted in resistance to anti-PD-1 therapy[277]. In contrast, expansion of DC1s through treatment with FLT3L, followed by maturation via poly I:C, synergised with anti-PD-L1 treatment, demonstrating the importance of T cell/DC cross-talk for ICB[25]. Subsequent studies have further revealed the distinct mechanisms of this interaction. For example, PD-1 blockade stimulated the release of IFN-γ by CD8$^+$ T cells, activating DC1s to secrete IL-12, which in turn 'licensed' T cells, resulting in tumour regression[278]. Blockade of IFN-γ, IL-12 or IFN-γRs on DCs abrogated tumour clearance. More importantly,

IL-12 secretion could be enhanced via treatment with an anti-CD40 agonist and combination of an anti-PD-1 blocking antibody and an anti-CD40 agonist enhanced efficacy in PD-1 blockade-sensitive as well as resistant mouse models, once again emphasising the importance of the cross-talk between innate and adaptive immune cells[278]. Another study investigated the role of the CXCR3-CXCL9 chemokine axis for mounting an appropriate T-cell response[279]. $CD103^+$ DCs increased production of CXCL9 upon PD-1 blockade, which was crucial for the efficacy of anti-PD-1 therapy. Binding of CXCL9 to CXCR3 on T cells resulted in enhanced $CD8^+$ T-cell effector functions, proliferation and anti-tumour activity. Interestingly, migration of $CD8^+$ T cells into the tumour was not important, as treatment with FTY720 had no impact on T-cell abundance as well as tumour growth[279], supporting the idea that intratumoural T-cell proliferation is sufficient[250]. The authors hypothesised that increased CXCL9 secretion by $CD103^+$ DCs upon PD-1 blockade allowed DCs to interact with $CXCR3^+CD8^+$ T cells. However, they did not demonstrate the mechanism of CXCL9-induction in DCs upon PD-1 blockade.

Although DC1s displayed a diverse phenotype across the different studies, the following key features were commonly observed: (i) dependency on the TFs BATF3 and IRF8[23,25,278], (ii) expression of CD103[23,25,279], (iii) expansion upon treatment with FLT3L[23,25], (iv) production of IL-12[23,278] and, most importantly, (v) indispensability for anti-PD-1/anti-PD-L1 therapy[25,278,279].

In contrast to DC1s, TAMs and MDSCs have been associated with pro-tumourigenic functions[22,280] and infiltration of TAMs correlates with worse prognosis[281]. In accordance with this, macrophages were found to support several hallmarks of cancer, such as tumour-promoting inflammation, angiogenesis and metastasis[282]. Thus, there has been a lot of effort in targeting these immunosuppressive myeloid cells to create a more inflammatory, tumouricidal immune microenvironment[142]. Several tumours recruit macrophages through secretion of CCL2 and CSF1, therefore, blocking these pathways is a promising approach. In addition to recruitment, CSF1 is also crucial for the survival of

macrophages and depletion of CSF1 or inhibition of CSF1R forces macrophages into apoptosis[283]. While several pre-clinical studies showed promising results in targeting the CSF1/CSF1R axis, there are concerns regarding toxicity, as this therapy depletes most macrophages in the body[22]. Thus, instead of depleting, an alternative approach is to reprogram TAMs towards a more pro-inflammatory, tumouricidal phenotype[284]. In this respect, two important signalling axes are CD47-SIRPα as well as CD40-CD40L. CD47 is upregulated on tumour cells as a 'don't eat me' signal, binding to SIRPα on macrophages and inhibiting phagocytosis[285]. Blocking this pathway with antibodies triggered macrophage-mediated phagocytosis of cancer cells and also led to increased priming of $CD8^+$ T cells[285]. On the other hand, agonistic anti-CD40 antibodies stimulated macrophages to upregulate MHC molecules and pro-inflammatory mediators, leading to a tumouricidal reprogramming of macrophages within the TME[286,287]. Importantly, antibodies targeting both pathways, blocking anti-CD47[288] or activating anti-CD40[289] antibodies, were shown to enhance PD-1 blockade in mouse tumour models.

1.4.4 Rationale for combining PD-1 and CD200R blockade

The previous section illustrated the synergistic potential of cancer immunotherapy when both arms of the immune system, innate and adaptive immune cells, are targeted. The various approaches used to manipulate different subsets are reviewed in greater detail elsewhere (DCs[26], MDSCs[142] and TAMs[22]). One objective of this thesis was to investigate the combination blockade of PD-1 and CD200R. An introduction to the PD-1 and CD200R pathways was given in Sections 1.2.4.2 and 1.2.4.3, respectively. In what follows, the rationale for choosing this combination immunotherapy will be elucidated.

Importantly, while PD-1 is believed to mostly act on T cells, more specifically on activated and exhausted T cells (Section 1.4.1), CD200R is primarily expressed on myeloid cells, including DCs, macrophages and granulocytes[144]. Thus, blocking both receptors should target a separate set of immune cells, leading to

the restoration of different, non-redundant immune phenotypes. Furthermore, although PD-1 is also found on myeloid cells[126] and CD200R is upregulated on activated T cells[145], potentially suggesting some overlapping functions, both receptors have a distinct signalling cascade, resulting in different pathways of inhibition. While PD-1 recruits phosphatases such as SHP-1 and SHP-2[131], CD200R primarily acts through the inhibition of Ras, leading to the inactivation of MAPK/ERK and PI3K/Akt pathways[150]. Overall, the distinct expression patterns as well as separate signalling cascades holds promise that the co-blockade of CD200R and PD-1 results in a synergistic, non-redundant reactivation of the anti-tumour immune response.

As discussed in Section 1.2.4.3, multiple human tumours upregulate CD200, which is correlated with poor prognosis[180,182]. As CD200R was reported to be associated with a M2-macrophage phenotype[290], ligation of tumour-intrinsic CD200 to CD200R could potentially trigger the differentiation of TAMs into M2 macrophages in the TME. Therefore, one potential mechanism of action of CD200R blocking antibodies could be the reduction of M2 macrophages, either through the blockade of M2 differentiation or via reprogramming of existing M2 macrophages into more pro-inflammatory M1 macrophages. With the potential upregulation of MHC molecules and stimulatory molecules such as CD80 and CD86, this can further influence other immune cells within the TME.

So far, most studies investigating a manipulation of the CD200R pathway in cancer relied on monotherapies or single gene deletions. There are a few exceptions, such as the combination of TLR7/TLR8 stimulation (resiquimod, R848) with an anti-CD200R agonistic antibody (OX110)[291]. While anti-CD200R agonist monotherapy did not influence tumour growth of the CT26 colorectal cancer model, it was able to boost the anti-tumourigenic effect of R848. Similarly, in a follow-up study, Rygiel and colleagues found no effect of OX110 monotherapy in LLC1, B16-F10 and EMT6 tumour models[178]. Interestingly, they demonstrated reduced tumour growth of the B16-F10 model in mice lacking CD200, and this effect was diminished upon transduction of CD200 into B16-F10 cells. Thus, due

to the tumour-promoting role of CD200, they concluded that CD200R blocking antibodies should be explored. Finally, it is important to note that, in both studies, the authors did not observe a change in tumour growth upon anti-CD200R agonist monotherapy[178,291], suggesting that a combination approach is advisable.

Thus, with the growing efforts of trying to identify novel combination strategies for anti-PD-1 antibodies[292], it is worth exploring the co-blockade of PD-1 and CD200R. The fact that already two anti-CD200/CD200R blockers are tested in clinical trials[186,194] underscores the therapeutic potential of targeting this inhibitory immune axis. To our knowledge, a combination CD200R/PD-1 blockade approach has not been investigated in mouse models before, but, on theoretical grounds, this approach seems to hold promise.

1.5 Work preceding this thesis

Work in the Davis laboratory established the transgenic mouse used in this study. First, a humanised PD-1 (hPD-1) knock-in mice was generated by replacing the extracellular region of mouse PD-1 with the human counterpart. The production of this mouse was outsourced to Taconic Biosciences, and the characterisation was performed by Billur Akkaya[293]. Similarly, a humanised CD200R (hCD200R) knock-in mouse was generated by Ingenious Targeting Laboratory and validated by Christopher Paluch[294]. Both mouse strains were bred to homozygosity and subsequently crossbred to create a humanised PD-1 and CD200R (hPD-1/hCD200R) mouse. Importantly, the murine ligand bound the mouse/human CD200R receptor with a similar affinity[294], and the same was reported for mouse/human PD-L1 interacting with human PD-1 (Paluch *et al.*, unpublished data)[295].

An initial survival study combining anti-PD-1 and anti-CD200R antibodies was carried out by the contract research organisation Crown Bioscience. Using the colorectal cancer model MC38, it was demonstrated that complete responses increased upon combining both antibodies, compared to PD-1 blockade monotherapy (Figure 1.8).

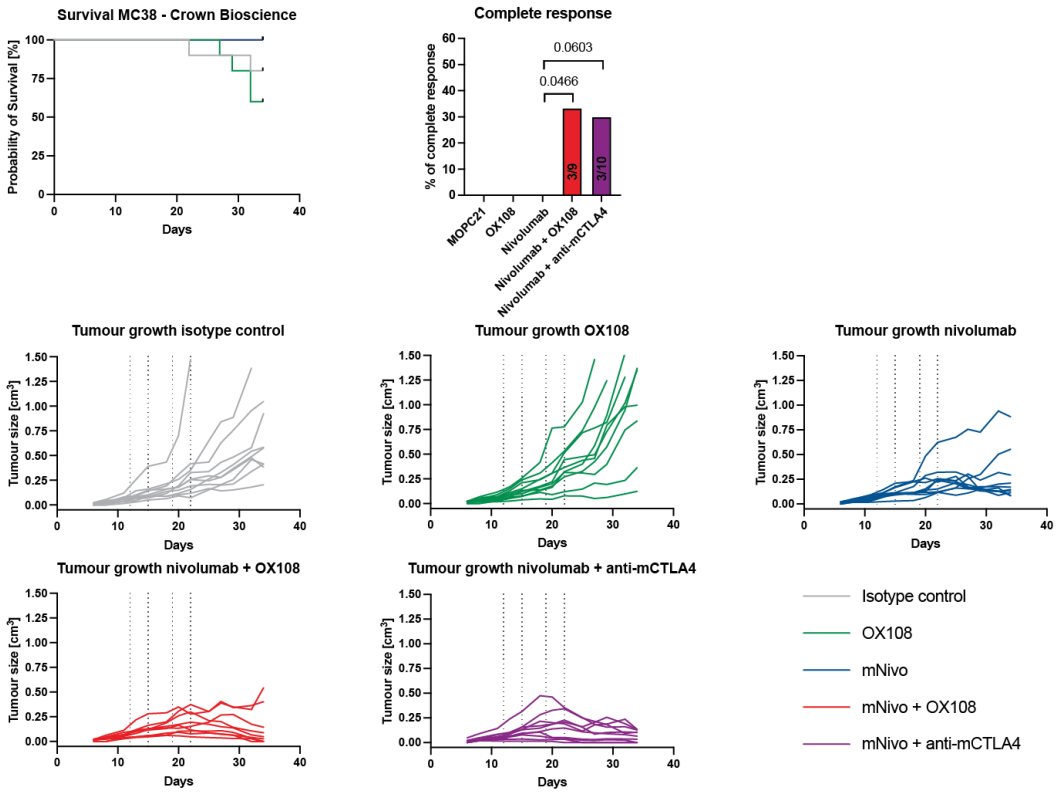


Figure 1.8: Combination of anti-PD-1 and anti-CD200R in the MC38 model
1×10^6 MC38 cells were subcutaneously injected into mice and tumour volume was measured three times a week. On day 11 (average tumour volume 58 mm^3), mice were randomised into groups and treatment was started the next day. Mice were treated with 10 mg/kg per antibody, receiving four treatments over two weeks. Treatment groups included isotype control (MOPC21), OX108 (anti-CD200R blocking antibody), nivolumab (anti-PD-1 blocking antibody) as well as the combination of the latter two and a combination of anti-PD-1 with anti-CTLA4 antibodies. n = 10/group; one mouse in the nivolumab + OX108 group was excluded from the study at day 12 due to convulsions.
This experiment was carried out by the contract research organisation Crown Bioscience. The data shown here were published by Fellermeyer *et al.*[1].

As discussed in Section 1.2.2 and illustrated in Figure 1.2, antibodies can trigger NTRs. According to the KS model, this requires segregation of the receptor/antibody/FcγR complex from large phosphatases such as CD45, and this may apply to all antibodies binding to small receptors. These effects should be tuneable by enlarging the complex by extending either the receptor, the ligand or the antibody. Indeed, using the anti-rat CD28 superagonist antibody JJ316, Meike Aßmann demonstrated that extension of the superagonist removed its stimulatory

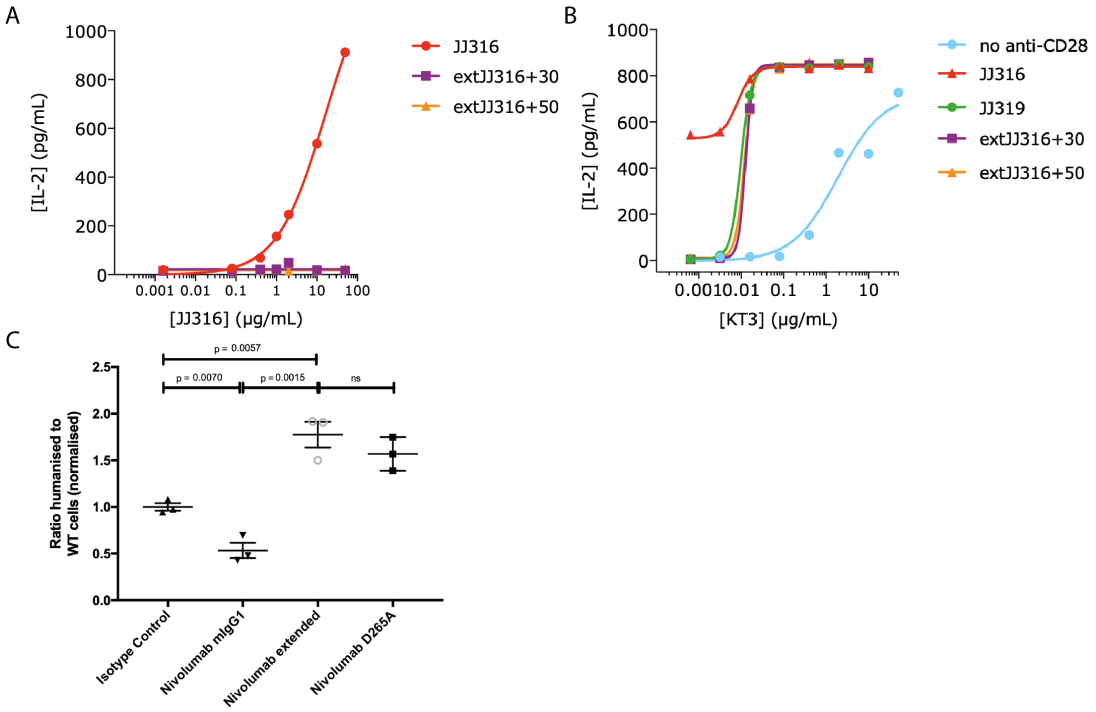


Figure 1.9: Reduction of agonism through antibody extension
(A) BW5147 T cells expressing a rat-mouse CD28 chimeric protein were stimulated with varying amounts of JJ316 and JJ316 with a 30 or 50 aa extension of mCD43. Antibodies were immobilised on a glass surface. IL-2 secretion was measured after 24 hours. Data were taken from the DPhil thesis of Meike Aßmann[296].
(B) BW5147 T cells expressing a rat-mouse CD28 chimeric protein were stimulated with varying amounts of KT3 (anti-CD3). Additionally, cells were incubated with 10 µg/mL of JJ319, JJ316 and JJ316 with a 30 or 50 aa extension of mCD43. Antibodies were immobilised on a glass surface. IL-2 secretion was measured after 24 hours. Data were taken from the DPhil thesis of Meike Aßmann[296].
(C) Identical amounts of ovalbumin-specific hPD-1 and WT $CD4^+$ T cells were injected into recipient mice on day 0. On day 1 mice were immunised with ovalbumin, followed by antibody treatment (200 µg) on day 2. Spleens were harvested on day 8 and the ratio of hPD-1 to WT cells was measured by flow cytometry. Data were normalised to the average ratio of the isotype control. Data were taken from the DPhil thesis of Christopher Paluch[294].

effect on BW5147 T cells, which expressed a chimeric protein comprising the rat CD28 extracellular domain followed by the mouse transmembrane and cytoplasmic domains (Figure 1.9 A)[296]. The antibody-extension was achieved by inserting a heavily glycosylated mucin-like sequence from mouse CD43 (mCD43) into the hinge region. The insertion was made between the cysteines forming disulfide bonds across HC-LC and HC-HC. In a different assay, anti-CD3 antibodies (KT3) were titrated with a constant amount of anti-rCD28 antibodies (JJ319 (a co-

mitogenic antibody), JJ316 and extended versions of JJ316). Again, insertion of 30 or 50 amino acids (aa) of mCD43 into the hinge region resulted in a loss of the superagonistic activity, however, the antibodies were still costimulatory, indicating that some agonistic potential remained (Figure 1.9 B).

A similar observation was made for the anti-PD-1 antibody nivolumab, which retained FcγR-dependent agonistic activity despite ligand-blocking capacity[294]. In this experiment, identical numbers of WT and hPD-1 antigen-specific $CD4^+$ T cells (OT-II cells, CD45.2) were injected into CD45.1 recipient mice. Twenty-four hours after cell injection, the mice were injected with ovalbumin, followed by antibody treatment on day two (isotype control, nivolumab mIgG1, nivolumab mIgG1 extended or nivolumab mIgG1 D265A). On day eight, the ratio of hPD-1 to mPD-1 (WT) cells was assessed. As shown in Figure 1.9 C, nivolumab mIgG1 harboured agonistic activity, which resulted in reduced proliferation of hPD-1 T cells. In contrast, extending the antibody or introducing the D265A mutation, which reduces FcγR binding[212], increased the numbers of hPD-1 T cells. ADCC, ADCP or CDC are unlikely explanations for these effects as mIgG1 has very low effector functions[204].

1.6 Hypothesis and objectives of this thesis

This thesis aimed to explore new approaches to immune-checkpoint blockade for cancer immunotherapy in two ways.

First, a novel combination approach comprising anti-PD-1 and anti-CD200R antibodies was tested. While PD-1 blockade aims to reactivate T cells, CD200R is an inhibitory receptor mostly found on myeloid cells[144]. Blocking the ligand engagement of CD200R should therefore stimulate myeloid cells. Using mice humanised for PD-1 and CD200R allowed testing of anti-human antibodies and this thesis focused on nivolumab and OX108[297], the respective blocking antibodies for PD-1 and CD200R. Thus, combination of PD-1 and CD200R blockade should stimulate the adaptive and innate immune compartment, respectively. Hypothetically, in addition to activating cytotoxic T cells through nivolumab

treatment, the combination with the anti-CD200R antibody OX108 might increase the co-stimulatory support through activation of myeloid cells. This could be through increased priming of T cells by APCs or a general shift towards a more pro-inflammatory TME, e.g. via the reduction or reprogramming of immunosuppressive myeloid cells.

Second, antibody engineering was used to enhance the efficacy of nivolumab. Increasing the overall dimensions reduced agonistic activity for anti-CD28[296] and anti-PD-1 antibodies[294], but more work is needed to fully understand this effect. Larger and new forms of extended nivolumab were produced with the aim of reducing the inherent agonistic activity, which should correlate with increased *in vivo* anti-tumour efficacy. Based on the KS model for antibody agonism, increasing the size of the receptor/antibody/FcγR complex reduces the chance of triggering the bound receptor. An increase in distance between the antigen-binding domain and the FcγR-binding domain should therefore correlate with a reduced activation of PD-1 and an enhanced T-cell activation. Ultimately, this should also translate in a more effective tumour control *in vivo*. As the flexibility of antibodies could potentially confound the overall size of the complex in the close-contact zone, new hinge-mutants, that should exhibit reduced flexibility, were produced and tested for increased T-cell activation.

All sorts of things can happen when you're open to new ideas and playing around with things.

— Stephanie Kwolek

2 Materials and Methods

Contents

2.1 List of materials 57
2.1.1 List of general and molecular biology reagents 57
2.1.2 List of plasmids 58
2.1.3 List of enzymes 59
2.1.4 List of solutions and buffers 59
2.1.5 List of commercial assays 60
2.1.6 List of cell lines 60
2.1.7 List of cell culture reagents 60
2.1.8 List of primers 61
2.1.9 List of commercial antibodies 62
2.2 Methods 63
2.2.1 Cell culture 63
2.2.2 Molecular cloning 67
2.2.3 Protein purification 70
2.2.4 Flow cytometry 75
2.2.5 RNA sequencing 80
2.2.6 Animal work 81
2.2.7 Statistical analysis 84

2.1 List of materials

2.1.1 List of general and molecular biology reagents

Table 2.1: List of general and molecular biology reagents

Beginning of Table		
Reagent	**Source**	**Catalogue number**
1 kb DNA ladder	Bioline	BIO-33026
2-Mercaptoethanol	Sigma-Aldrich	M3148-25ML
2-Propanol	Sigma-Aldrich	34863-2.5L
Acetic acid glacial	Sigma-Aldrich	A6283-500ML
Agarose	Bioline	BIO-41025
Ampicillin sodium salt	Sigma-Aldrich	A9518-25G
Bovine Serum Albumin	Sigma-Aldrich	A7906-100G
Brilliant Blue G	Sigma-Aldrich	B0770-25G
Centrifugal Filters 10 kDa	Sigma-Aldrich	UFC901024
Chromatography Paper 3MM	VWR	3030-861
CutSmart digestion buffer	New England Biolabs	B7204S
Dimethyl sulfoxide	Thermo Fisher Scientific	BP231-100
ECL Western Blotting Substrate	Thermo Fisher Scientific	32106
Ethanol	VWR	20821.321
Ethidium Bromide	Sigma-Aldrich	E1510-10ML
Ficoll-Paque PREMIUM 1.084	Cytiva	17544602
Gel loading dye	New England Biolabs	B7024A
Glycine	Sigma-Aldrich	G7126-1KG
HBS-EP+ buffer	Cytiva	BR100669
HBS-P+ buffer	Cytiva	BR100671
High-molecular weight marker	Cytiva	17-0445-01
IC Fixation Buffer	Thermo Fisher Scientific	00-8222-49
Imidazole	Sigma-Aldrich	56749-250G
Laemmli Sample Buffer	Bio-Rad	1610737
Low-molecular weight marker	Cytiva	17-0446-01
Lysogeny broth	Sigma-Aldrich	L7275-500TAB
Lysogeny broth with agar	Sigma-Aldrich	L7025-500TAB
Methanol	Thermo Fisher Scientific	M/3950/17
Native Tris-Glycine Sample Buffer	Thermo Fisher Scientific	LC2673
Nickel(II) sulfate	Sigma-Aldrich	N4882-250G
Nitrocellulose blotting membrane 0.45 µm	VWR	10600018
Novex Tris-Glycine Native Running Buffer	Thermo Fisher Scientific	LC2672

Continuation of Table 2.1		
Reagent	**Source**	**Catalogue number**
Novex WedgeWell 8 % Tris-Glycine Gel	Thermo Fisher Scientific	XP00085BOX
NuPAGE 4-12 % Bis-Tris Gel	Thermo Fisher Scientific	NP0323BOX
NuPAGE MES SDS Running Buffer	Thermo Fisher Scientific	NP0002
NuPAGE Transfer Buffer	Thermo Fisher Scientific	NP00061
OneComp eBeads	Thermo Fisher Scientific	01-1111-42
PBS pH 7.4	Thermo Fisher Scientific	10010-015
Phosphate-buffered saline tablets	Thermo Fisher Scientific	BR0014G
Phusion HF buffer	Thermo Fisher Scientific	F-518
Precision Plus Protein All Blue Standards	Bio-Rad	1610373
Rainbow Marker	Sigma-Aldrich	GERPN800E
RBC Lysis Solution	Qiagen	1045695
Sodium Azide	Sigma-Aldrich	71290-100G
Sodium Chloride	Sigma-Aldrich	S9888-1KG
Sodium Hydroxide	Sigma-Aldrich	30620-1KG-M
Sponge Pad for Blotting	Thermo Fisher Scientific	EI9052
Syringe Filter Unit, 0.22 µm, polyethersulfone	Sigma-Aldrich	SLGP033R
T4 DNA Ligase buffer	New England Biolabs	B0202S
TE Buffer	Thermo Fisher Scientific	8019005
Tris base	Sigma-Aldrich	10708976001
Tris-Borate-EDTA buffer	Sigma-Aldrich	T4415-1L
Tris hydrochloride	Sigma-Aldrich	10812846001
TWEEN 20	Sigma-Aldrich	P7949-100ML
Vacuum Filter Bottle System 0.22 µm, PES	Thermo Fisher Scientific	431097
End of Table		

2.1.2 List of plasmids

Table 2.2: List of plasmids

Name	Source	Catalogue number
p8.91	Addgene	187441
pHR	Addgene	187358
pMDG	Addgene	187440

2.1.3 List of enzymes

Table 2.3: List of enzymes

Enzyme	Source	Catalogue number
BamHI-HF	New England Biolabs	R3136L
Collagenase Type D	Sigma-Aldrich	11088866001
Collagenase Type IV	Thermo Fisher Scientific	17104-019
DNase I	Sigma-Aldrich	D5025-150KU
NotI-HF	New England Biolabs	R3189L
Phusion DNA Polymerase	Thermo Fisher Scientific	F-530L
T4 DNA Ligase	New England Biolabs	M0202L
XhoI	New England Biolabs	R0146L

2.1.4 List of solutions and buffers

Table 2.4: List of solutions and buffers

Buffer	Component	Concentration
Binding/Washing buffer pH 9.0	Glycine NaCl Sodium azide	1.5 M 3 M 0.1 % (w/v)
Elution buffer pH 2.5	Glycine Sodium azide	0.2 M 0.1 % (w/v)
FACS buffer	PBS FBS EDTA	1 × 1.0 % (v/v) 0.002 M
HBS azide	HEPES NaCl Sodium azide	0.01 M 0.15 M 0.1 % (w/v)
Lymph node digestion medium	HBSS FBS Collagenase Type D DNase I	1 × 10 % (v/v) 1 mg/mL 0.1 mg/mL
Neutralisation buffer pH 9.0	Tris base/hydrochloride Sodium azide	1 M 0.1 % (w/v)
Tumour digestion medium	HBSS FBS Collagenase Type IV DNase I	1 × 10 % (v/v) 1 mg/mL 0.1 mg/mL

2.1.5 List of commercial assays

Table 2.5: List of commercial assays

Commercial assay	Source	Catalogue number
Alexa Fluor 488 Antibody Labelling Kit	Thermo Fisher Scientific	A20181
HiPure Plasmid Miniprep Kit	Thermo Fisher Scientific	K210003
Pierce Chromogenic Endotoxin Quant Kit	Thermo Fisher Scientific	A39552
Pierce High Capacity Endotoxin Removal	Thermo Fisher Scientific	88276
QIAquick Gel Extraction Kit	Qiagen	28706
QIAshredder	Qiagen	79654
Quantibrite PE Fluorescence Quantitation Kit	BD Biosciences	340495
RNeasy Mini Kit	Qiagen	74104

2.1.6 List of cell lines

Table 2.6: List of cell lines

Cell line	Source	University
BW5147 OKT3-scFv	Peter Steinberger	University of Vienna
CHO-K1	Simon Davis	University of Oxford
HEK293T	Simon Davis	University of Oxford
Jurkat NF-κB-GFP	Peter Steinberger	University of Vienna
LLC1	Vincenzo Cerundolo	University of Oxford
MC38-resistant	Adrian Harris	University of Oxford
MC38-sensitive	Stephen Beers	University of Southampton

2.1.7 List of cell culture reagents

Table 2.7: List of cell culture reagents

Beginning of Table		
Reagent	**Source**	**Catalogue number**
0.5 M EDTA pH 8.0	Thermo Fisher Scientific	15575-038
Cell Stimulation Cocktail	Thermo Fisher Scientific	00-4970-93

Continuation of Table 2.7		
Reagent	**Source**	**Catalogue number**
Cell Strainer 30 µm	Partec	04-004-2326
Cell Strainer 70 µm	Thermo Fisher Scientific	352350
Countess cell counting chamber slides	Thermo Fisher Scientific	C10283
DMEM	Thermo Fisher Scientific	41965-039
Fetal Bovine Serum, heat inactivated	Thermo Fisher Scientific	10500-064
Fetal Bovine Serum, ultra-low IgG	Thermo Fisher Scientific	16250-078
GeneJuice Transfection Reagent	Sigma-Aldrich	70967-1ML
HBSS, calcium, magnesium	Thermo Fisher Scientific	24020-091
HEPES	Thermo Fisher Scientific	15630-056
L-Glutamine solution	Sigma-Aldrich	G7513-100ML
Murine IFN-γ	PeproTech	AF-31-5
Non-essential amino acids	Thermo Fisher Scientific	11140-035
Penicillin-Streptomycin	Sigma-Aldrich	P0781-100ML
RPMI 1640 medium	Thermo Fisher Scientific	21875-034
Sodium pyruvate solution	Sigma-Aldrich	S8636-100ML
Trypsin solution	Sigma-Aldrich	SLCJ1369
End of Table		

2.1.8 List of primers

Table 2.8: List of primers

Name	**Sequence (5'–3')**	**Use**
Oligo FW	TAGTAGGGATCCAAGCTTGCCACC	String cloning
Oligo RV	CTACTATCTAGAGCGGCCGCC	String cloning
Heavy chain FW	CCCAGACCAAGCCTAGAGAG	Sequencing
D265D FW1	TGGTGGTGGACATCTCCAAGG	Mutagenesis
D265D RV1	CCTTGGAGATGTCCACCACCA	Mutagenesis
D265D FW2	GTCGTGGTCGATATCAGCAA	Mutagenesis
D265D RV2	TTGCTGATATCGACCACGAC	Mutagenesis
Truncation mCD32B FW	GGGGGGATCCAAGCTTGCCACCATGGAAAGCAACTG	Truncation
Truncation mCD32B RV	TCTAGAGCGGCCGCTCACAGAGCTGGGACCTGC	Truncation

2.1.9 List of commercial antibodies

All antibodies are anti-mouse, unless otherwise stated.

Table 2.9: List of commercial antibodies

Beginning of Table					
Antigen	**Conjugation**	**Source**	**Catalogue number**	**Clone**	**Dilution**
B220	BV785	BioLegend	103245	RA3-6B2	1:100
CCR7	BUV395	BD Biosciences	740325	4B12	1:100
CD103	PE-Dazzle 594	BioLegend	121429	2E7	1:100
CD11b	BV605	BioLegend	101257	M1/70	1:100
CD11c	PerCP-Cy5.5	BioLegend	117327	N418	1:100
CD16/ CD32 (Fc block)	-	BioLegend	101320	93	1:50
CD16/ CD32 (Fc block)	-	BioLegend	101339	93	100 µg/mL
CD200	APC	BioLegend	123810	OX-90	1:100
CD200	PE	BioLegend	123807	OX-90	1:100
hCD200	APC	BioLegend	329207	OX-104	1:100
hCD200R	PE	Thermo Fisher Scientific	12-9201-42	OX108	1:100
CD206	APC	BioLegend	141708	C068C2	1:100
CD25	BUV395	BD Biosciences	564022	PC61	1:200
CD3	BV650	BioLegend	10229	17A2	1:100
CD32	APC	BioLegend	156405	S17012B	1:100
CD4	PerCP-Cy5.5	BioLegend	116011	RM4-4	1:100
CD44	FITC	BioLegend	103006	IM7	1:200
CD45	PE	BioLegend	147711	13/2.3	1:400
CD45.2	BV510	BioLegend	109838	104	1:100
CD62L	APC	BioLegend	104412	MEL-14	1:200
CD69	PE-Cy7	BioLegend	104512	H1.2F3	1:100
CD8	BV421	BioLegend	100738	53-6.7	1:100
CD8	BV711	BioLegend	100748	53-6.7	1:100
F4/80	eFluor 450	Thermo Fisher Scientific	48-4801-80	BM8	1:200

Continuation of Table 2.9					
Antigen	**Conjugation**	**Source**	**Catalogue number**	**Clone**	**Dilution**
rIgG2a kappa isotype control	PE	BioLegend	400508	RTK2758	1:100
Live/Dead	NIR	BioLegend	77184	-	1:500
Ly-6C	BV785	BioLegend	128041	HK1.4	1:100
Ly-6G	FITC	BioLegend	127605	1A8	1:200
MHC-I (H-2Db)	eFluor 450	BioLegend	48-5999-80	28-14-8	1:100
MHC-II (I-A/I-E)	BV711	BioLegend	107643	M5/ 114.15.2	1:100
Mouse IgG (Fc specific)	HRP	Sigma-Aldrich	A0168	polyclonal	1:2000
NK1.1	APC	BioLegend	108709	PK136	1:100
hPD-1	BUV737	BD Biosciences	612791	EH12.1	1:200
hPD-1	PE	BioLegend	329906	EH12.2H7	1:200
hPD-1	PE-Cy7	BioLegend	329917	EH12.2H7	1:200
PD-L1	PE	Thermo Fisher Scientific	12-5982-81	MIH5	1:100
hPD-L1	-	BioLegend	329745	29E.2A3	100 µg/mL
TCR-β	PE	BioLegend	109207	H57-597	1:200
End of table					

2.2 Methods

2.2.1 Cell culture

2.2.1.1 Maintenance of cell lines

All cell lines were cultured in a humidified incubator at 37 °C and 5 % CO_2 and experiments were conducted in HEPA-filtered cell culture cabinets. Adherent cells were passaged once they reached a confluency of 80-90 %, cells were washed in sterile PBS (supplied by the Human Immunology Unit laboratory management team, University of Oxford) and detached using trypsin, incubated at 37 °C for 2-3 minutes (min). Trypsin was quenched by addition of medium and cells were centrifuged. After centrifugation, the cells were resuspended in medium and

seeded at 10-20 % confluency. For suspension cells, cell density and viability were measured using an automatic cell counter (Countess II, Thermo Fisher Scientific). Cells were diluted 1:1 in 0.4 % trypan blue solution to identify dead cells. Jurkat and BW5147 cells were seeded at a concentration of 2×10^5 and 1×10^5 cells/mL, respectively, and passaged again once they reached a cell density of approximately 1×10^6 cells/mL. Cells (adherent and suspension) were typically passaged every other day. All centrifugation steps were performed at 336 × *g* for 5 min at room temperature (RT). All cells were validated to be negative for mycoplasma (testing performed by Human Immunology Unit laboratory management team, University of Oxford). Furthermore, all cell lines used for *in vivo* work (MC38-sensitive, MC38-resistant, LLC1) were validated through short tandem repeat (STR) profiling (IDEXX BioAnalytics).

All cell lines were cultured with the supplementation of 10 % (v/v) Fetal Bovine Serum (FBS) and 2 mM L-glutamine. HEK293T cells were cultured in DMEM, supplemented with 10 mM HEPES, 100 U/mL penicillin and 100 µg/mL streptomycin. CHO-K1 cells were cultured in DMEM, supplemented with 1 mM sodium pyruvate, 100 U/mL penicillin and 100 µg/mL streptomycin. Jurkat and BW5147 cells were cultured in RPMI 1640 medium, supplemented with 100 U/mL penicillin and 100 µg/mL streptomycin. MC38-sensitive cells were cultured in RPMI 1640 medium, supplemented with 1 mM sodium pyruvate. MC38-resistant cells were cultured in DMEM, supplemented with 1 mM sodium pyruvate. LLC1 cells were cultured in RPMI 1640 medium. Of note, all cell lines used for *in vivo* work were cultured without supplementation of antibiotics.

2.2.1.2 Cryopreservation

Cells were stored in liquid nitrogen tanks for cryopreservation. Adherent cells were detached as described in Section 2.2.1.1. After confirming a viability of $\geq$ 90 %, an appropriate number of cells was pelleted through centrifugation at 336 × *g* for 5 min at 4 °C and resuspended in freezing solution (FBS supplemented with 10 % (v/v) DMSO) at a concentration of 2×10^6 cells/mL. Cells were stored

in 1 mL aliquots (2×10^6 cells) in cryovials and after freezing at -80 °C, they were transferred into a liquid nitrogen tank. For thawing of cells, the cells were incubated at 37 °C until the freezing solution started to thaw. Cells were diluted in their respective medium and pelleted to remove the freezing solution. Cells were resuspended and placed into an appropriate cell culture flask and maintained as described in Section 2.2.1.1.

2.2.1.3 Lentivirus production and transduction

HEK293T cells were used to produce lentivirus. Cells were seeded at 4×10^5 cells/mL in 6-well plates with 2 mL/well. The next day, cells were co-transfected with 1 µg of the corresponding lentiviral plasmid (pHR) and with the lentiviral packaging plasmids p8.91 (0.5 µg) and pMDG (0.25 µg). Addgene catalogue numbers of all original plasmids are provided in Table 2.2. GeneJuice (Sigma-Aldrich) was used for co-transfection. Briefly, 100 µL of serum-free DMEM was mixed with 4.5 µL of GeneJuice and incubated for 5 min at RT. Next, the DNA was added and incubated for another 20 min at RT. Finally, the entire volume was added drop-wise to the cells and the plate was gently rocked for even distribution.

48 to 72 hours after transfection, the supernatant, containing the lentivirus, was collected and passed over a 0.22 µm syringe filter. The supernatant was either used immediately or frozen at -80 °C. For lentiviral transduction, $0.5\text{-}1 \times 10^6$ cells in 1 mL were combined with up to 4 mL of the lentivirus-containing supernatant in a T-25 flask. The following day, the medium was topped up to 10 mL. Three days after the lentiviral transduction, cells were either expanded or passaged as described in Section 2.2.1.1. Upregulated proteins were analysed by flow cytometry (Section 2.2.4.1) and antibody production was validated by performing Western blots of cell-culture supernatants (Section 2.2.3.4). If the upregulation of proteins was not uniform, fluorescence-activated cell sorting was used (Section 2.2.4.5).

2.2.1.4 Protein production

In order to produce proteins, the corresponding lentivirus was produced in HEK293T cells and transduced into CHO-K1 cells (Section 2.2.1.3). For antibody

production, the plasmids encoding the heavy and light chain of the corresponding antibody were transfected separately into HEK293T cells to produce lentiviruses. Following, CHO-K1 cells were transduced with equal volumes of lentiviruses containing the respective heavy and light chain. Typically, 1×10^6 CHO-K1 cells in 1 mL of medium were transduced with 2 mL of virus of each antibody chain. Cells were expanded once they reached confluency, from one T-25 flask to a maximum of 20 T-175 flasks in DMEM, supplemented with 10 % (v/v) FBS, 2 mM L-glutamine, 1 mM sodium pyruvate, 100 U/mL penicillin and 100 µg/mL streptomycin. The expression of the protein was confirmed by Western blot analysis. Once the cells were expanded to the required size and they reached confluency, the medium was switched to DMEM, supplemented with 1 % (v/v) ultra-low IgG FBS, 2 mM L-glutamine, 1 mM sodium pyruvate, 1 × non-essential amino acids (NEAA), 100 U/mL penicillin and 100 µg/mL streptomycin (50 mL/T-175 flask). Of note, for the production of hPD-1-2xHis normal FBS was used instead of the ultra-low IgG FBS. The supernatant was harvested every seven days and this was repeated for a maximum of eight weeks. The supernatant was centrifuged for 10 min at 3739 × g to remove any cells, decanted and supplemented with 0.1 % (w/v) sodium azide and stored at 4 °C until purification (Section 2.2.3.1).

2.2.1.5 *In vitro* IFN-γ stimulation

To analyse the effects of IFN-γ stimulation on different mouse cancer cell lines (MC38-sensitive, MC38-resistant, LLC1), the cells were seeded at 1×10^5 cells/mL in 6-well plates with 2 mL/well. The next day, murine IFN-γ was added at concentrations ranging from 0.01 to 10.00 ng/mL and cells were incubated for 24 hours. Finally, cells were detached using 5 mM EDTA in PBS to prevent the potential digestion of cell surface proteins through trypsin. 2×10^6 cells were used for subsequent flow cytometric analysis of MHC-I, PD-L1 and CD200 expression.

2.2.1.6 *In vitro* T-cell activation assay

For the *in vitro* T-cell activation assay, Jurkat reporter cells expressing GFP under an NF-κB promoter (Jurkat NF-κB-GFP) were co-cultured with BW5147 mouse T cells expressing a membrane-bound anti-CD3 (OKT3) single-chain variable fragment (scFv), referred to as T-cell stimulator (TCS) cells. Both cell lines were kindly provided by Peter Steinberger (University of Vienna) and the assay has been described before[298]. 1.5×10^5 Jurkat T cells were co-cultured with 1.5×10^5 TCS cells in a 96-well U-bottom plate in a total volume of 200 µL at 37 °C and 5 % CO_2. After 16-24 hours, the cells were centrifuged (5 min at 757 × *g*) and analysed as described in Section 2.2.4.4.

Jurkat and TCS cells were lentivirally transduced with the corresponding receptors and ligands to assess the ligand-blocking capacity of the produced antibodies (Section 4.2.1). To assess antibody agonism, mFcγRIIb was transduced into TCS cells (Section 5.2.5). In this assay, commercial blocking antibodies against human PD-L1 and mFcγRIIb expressed by the TCS cells were used at a concentration of 100 µg/mL. Produced antibodies were either titrated (Section 4.2.1) or used at 348.79 nM (Section 5.2.5), which is equivalent to 50 µg/mL of nivolumab mIgG1.

2.2.2 Molecular cloning

2.2.2.1 Overview

All cloning procedures were performed with the lentiviral pHR plasmid (Table 2.2). DNA constructs were ordered as DNA strings from Thermo Fisher Scientific, resuspended in TE buffer and cloned into the pHR vector using restriction enzyme cloning. Protein sequences were retrieved from UniProt (`https://www.uniprot.org`) and constructs were designed *in silico* using SnapGene 4.1.9 (Dotmatics). All protein sequences are provided in the appendix (Section A.1). All DNA sequences were codon optimised using the GeneArt online tool (Thermo Fisher Scientific). Suitable primers for amplification of the DNA strings, sequencing and mutagenesis were designed in SnapGene and ordered from Thermo Fisher Scientific (Table 2.8).

The pHR vector is derived from HIV and produces replication-incompetent lentiviral particles when co-transfected with the packaging plasmids pMDG and p8.91. The protein-encoding genes cloned into pHR are under the SFFV promoter and are flanked by long terminal repeat sequences, which facilitates the integration into the host genome. The plasmid also included GFP under the control of an internal ribosome entry site (IRES), which allowed quick testing of the transduction efficacy. Of note, when pHR was used to upregulated proteins on Jurkat or TCS cells, the IRES-GFP sequence was deleted using restriction enzyme cloning (BamHI + NotI instead of BamHI + XhoI).

2.2.2.2 Polymerase chain reaction

Target DNA ($\sim$ 10 ng) was amplified using polymerase chain reaction (PCR). The final PCR mix included 0.5 U of Phusion DNA polymerase (Thermo Fisher Scientific), 250 nM of the 5' and 3' primer, 250 µM dNTPs, 1 × Phusion HF buffer and Milli-Q water for a 20 µL total volume. Annealing temperatures were determined using the NEB Tm calculator (https://tmcalculator.neb.com). PCR reactions were performed in a Bio-Rad T100 Thermal Cycler. The initial DNA denaturation (3 min at 95 °C) was followed by repeated cycles of denaturation (10 seconds (sec) at 95 °C), annealing (20 sec at variable temperatures) and extension (30 sec/1000 base pairs at 72 °C). After 30 cycles, a final extension step (10 min at 72 °C) was included.

2.2.2.3 Agarose gel electrophoresis

1 % (w/v) agarose was dissolved and heated in 1 × Tris-Borate-EDTA (TBE, Sigma-Aldrich) buffer. While cooling down, 0.5 µg/mL of ethidium bromide (Sigma-Aldrich) was added for DNA visualisation. DNA was diluted 5:1 with gel loading dye (New England Biolabs) and samples were loaded onto the gel, which included a 1 kb DNA ladder (Bioline) to determine DNA product size. Samples were separated by gel electrophoresis in TBE buffer at 100 V for 40 min. Visualisation of DNA bands by UV light allowed the excision from the agarose gel. DNA was isolated using the QIAquick Gel Extraction Kit (Qiagen) according to

the manufacturer's instructions. DNA was eluted in 30 µL elution buffer. DNA concentration and purity was assessed by measuring the absorbance at 260 nm and 280 nm using a spectrophotometer (NanoDrop One^{C}, Thermo Fisher Scientific).

2.2.2.4 Restriction enzyme digest

Gel-purified PCR sequences of the target sequence and plasmid were digested in order to ligate them together. Three different digestion sites within the pHR plasmid were used: (i) BamHI was always used for 5' digestion of the target sequence and vector, (ii) XhoI was used to retain the IRES-GFP sequence within pHR and (iii) NotI was used to remove IRES-GFP during the restriction enzyme digest. All enzymes were purchased from New England Biolabs and used in CutSmart digestion buffer (New England Biolabs). Independently of the final DNA concentration, 25 µL of purified PCR product were digested in a final volume of 50 µL with 800 units/mL of each restriction enzyme. For the vector digest, 4 µg of DNA were digested in 50 µL. DNA was digested for 1 hour at 37 °C. Digested vector DNA was purified as specified in Section 2.2.2.3. Digested PCR products were purified using the QIAquick Gel Extraction Kit (Qiagen) but instead of dissolving the agarose in QG Buffer (Qiagen), the DNA was mixed with 250 µL of a 1:1 mix of QG Buffer and 2-propanol before loading it onto the spin column.

2.2.2.5 Ligation

Purified, digested vector and DNA fragments were ligated using a T4 DNA Ligase (New England Biolabs). 100 ng of digested vector was incubated with varying amounts of digested, purified PCR products (equimolar amounts, three times and five times). Ligation reactions were performed in 20 µL total volume with 20,000 units/mL of T4 DNA Ligase and 1 × T4 DNA Ligase buffer (New England Biolabs). Ligation reactions were incubated overnight at 16 °C.

2.2.2.6 Transformation

For plasmid propagation, vectors were transformed into TOP10 *E. coli* cells (produced in the Davis laboratory, University of Oxford). After thawing cells on

ice, 20 µL of bacteria were mixed with 2 µL of vector DNA and incubated for 30 min on ice. Cells were heat-shocked at 42 °C for 45 sec and incubated on ice for 1 min. 150 µL of lysogeny broth (LB) medium was added and incubated for 1 hour at 37 °C. Bacteria were plated onto LB-agar plates containing 100 µg/mL ampicillin. Plates were incubated at 37 °C for 16 hours.

2.2.2.7 Small-scale preparation of plasmid DNA

Colonies were picked and inoculated in 10 mL of LB medium containing 100 µg/mL ampicillin. Cultures were incubated at 37 °C for 16-18 hours. Bacterial cells were pelleted by centrifugation at 3739 × g for 10 min. DNA was extracted using a HiPure Plasmid Miniprep Kit (Thermo Fisher Scientific) according to the manufacturer's instructions. DNA was eluted in 50 µL TE buffer. DNA concentration and purity was assessed by measuring the absorbance at 260 nm and 280 nm using a spectrophotometer (NanoDrop One^{C}, Thermo Fisher Scientific). All constructs generated were validated by Sanger sequencing (Source Bioscience) and aligned using SnapGene.

2.2.3 Protein purification

2.2.3.1 Protein A purification

Upon harvesting of the supernatant containing the respective antibody (Section 2.2.1.4), the supernatant was diluted with the same volume of Binding and Washing buffer pH 9.0 (Table 2.4) as well as filtered and de-gassed using a vacuum filter system (0.22 µm, PES membrane). Up to two HiTrap MabSelect PrismA protein A columns (Cytiva) were attached in series to an endotoxin-free ÄKTA start chromatography system (Cytiva). To ensure endotoxin-free protein production, before each purification, the system and columns were cleaned with 0.5 M sodium hydroxide for at least three column volumes (CV) with a minimum contact time of 15 min. After equilibration of the column with Binding and Washing buffer pH 9.0, the diluted supernatant was applied using the sample pump. Elution buffer pH 2.5 (Table 2.4) was used to recover the bound antibody

from the column until the absorbance at 280 nm returned to baseline. The collection tubes were pre-filled with an appropriate amount of Neutralisation buffer pH 9.0 (Table 2.4) to achieve a final pH of ∼ 7.0-7.5. The columns were washed with 10 CV Elution buffer pH 2.5, followed by 10 CV Binding and Washing buffer pH 9.0. For storage, the columns were first transferred into Milli-Q water, followed by slow equilibration with 20 % ethanol. Proteins purified using this method were stored at 4 °C for up to seven days. All buffers were filtered and de-gassed using a vacuum filter system (0.22 µm, PES membrane).

2.2.3.2 His purification

His-tagged proteins were purified using Ni-NTA agarose (Qiagen) packed in an Econo-Column (Bio-Rad). The harvested supernatant containing the respective protein (Section 2.2.1.4) was diluted with the same volume of PBS pH 8 as well as filtered and de-gassed using a vacuum filter system (0.22 µm, PES membrane). The column containing the resin was washed with 10 CV Milli-Q water and 10 CV PBS pH 8. The supernatant was applied by gravity flow. The resin was washed with 10 CV of PBS pH 8 0.5 M NaCl, 10 CV of 10 mM imidazole and 15 CV of 20 mM imidazole to disrupt non-specific interactions. His-tagged protein was eluted using 250 mM imidazole. The resin was regenerated by washing with 10 CV Milli-Q water, 5 CV 0.1 M EDTA pH 8, 10 CV Milli-Q water and 3 CV of 100 mM nickel(II) sulfate, which was incubated for 30 min at RT, protected from light. Finally, the resin was washed with 10 CV of Milli-Q water followed by 20 % ethanol for storage. Proteins purified using this method were immediately processed. All buffers were filtered and de-gassed using a vacuum filter system (0.22 µm, PES membrane).

2.2.3.3 Size-exclusion chromatography

To remove aggregated material, affinity-purified proteins were subjected to size-exclusion chromatography (SEC). Fractions containing proteins, as measured by absorbance at 280 nm, were pooled and concentrated using a centrifugal filter with a 10 kDa weight cutoff (Sigma-Aldrich). The final sample was centrifuged at

17,000 × *g* for 10 min at 4 °C. After equilibration, the sample was injected over the column using the sample loop and separated for at least 1.1 CV in the respective buffer. For antibodies, which required endotoxin-free purification, a ProteoSEC 16/60 6-600 HR SEC column (Protein Ark) connected to an endotoxin-free ÄKTA start system (Cytiva) was used with endotoxin-free PBS pH 7.4. For purification of hPD-1-2xHis a Superdex 200 Increase 10/300 GL column (Cytiva) connected to an ÄKTA pure system (Cytiva) was used with HBS azide (Table 2.4). All buffers were filtered and de-gassed using a vacuum filter system (0.22 µm, PES membrane).

For analytical SEC of antibodies, 100 µg of each antibody was injected over a Superdex 200 Increase 10/300 GL column (Cytiva) in PBS pH 7.4. No fractions were collected.

2.2.3.4 Polyacrylamide gel electrophoresis

Polyacrylamide gel electrophoresis (PAGE) was used to further assess the SEC fractions. Most PAGE gels were run as denaturing gels, with sodium dodecyl sulfate (SDS). Only for the analysis of the hinge-deleted antibodies in Section 6.2.4, native PAGE gels were used. Fractions from SEC were diluted 1:1 in Laemmli buffer (non-reducing, denaturing), Laemmli buffer containing 2.5 % (v/v) 2-mercaptoethanol (reducing, denaturing) or Native Tris-Glycine Sample Buffer (non-reducing, non-denaturing). Proteins for SDS-PAGE analysis were incubated for 10 min at 95 °C. Samples were loaded onto NuPAGE 4-12 % Bis-Tris or Novex WedgeWell 8 % Tris-Glycine gels and run at 150 V for 1 hour with NuPAGE MES SDS Running Buffer or Novex Tris-Glycine Native Running Buffer, respectively.

Gels were stained using Coomassie brilliant blue (10 % (v/v) acetic acid, 40 % (v/v) methanol, 1 g/L Brilliant Blue G) for 30 min at RT. After washing gels in distilled water, they were destained using destain solution (10 % (v/v) acetic acid, 12 % (v/v) methanol) overnight. Gels were imaged using a Gel Doc XR+ imaging system (Bio-Rad).

To test for antibody expression after lentiviral transduction (Section 2.2.1.3), protein immunoblotting (Western blotting) was used. After SDS-PAGE, proteins

were transferred onto a nitrocellulose membrane for 60 min at 30 V using the XCell II Blot Module (Thermo Fisher Scientific). Membranes were blocked for 45 min with 3 % (w/v) BSA in PBST (PBS supplemented with 0.1 % (v/v) TWEEN 20). Next, membranes were incubated with an anti-mouse IgG antibody (Fc specific, conjugated to HRP, 1:2000 dilution) for 45 min at RT in 3 % BSA. After washing membranes four times with PBST for 10 min, protein bands were visualised using ECL Western Blotting Substrate (Thermo Fisher Scientific) and detected using an iBright FL1000 imaging system (Thermo Fisher Scientific).

2.2.3.5 Endotoxin testing and removal

Fractions containing monomeric antibodies, as judged by SEC and/or PAGE analysis, were pooled and tested for endotoxin contamination using the Pierce Chromogenic Endotoxin Quant Kit (Thermo Fisher Scientific) according to the manufacturer's instructions. All purified antibodies had no or low ($\leq$ 0.3 Endotoxin Units (EU)/mL) endotoxin contamination, which is in accordance with guidelines for endotoxin limits for preclinical research[299].

AT128, the anti-mFcγRIIb blocking antibody used in Section 5.2.8, was kindly provided by Mark Cragg (University of Southampton). Pierce High Capacity Endotoxin Removal Spin Columns (Thermo Fisher Scientific) were used to remove endotoxin according to the manufacturer's instructions. After two rounds of clean-up, no endotoxin contamination remained.

2.2.3.6 Final sample processing

After confirming that the pooled antibody fractions were endotoxin free, they were filtered using a 0.22 µm syringe filter, adjusted to a final concentration of 13.95 µM, which is equivalent to 2.0 mg/mL of nivolumab mIgG1, using sterile, endotoxin-free PBS pH 7.4 and stored in 1 mL aliquots at -80 °C.

Fractions containing monomeric hPD-1-2xHis, as judged by SEC and PAGE analysis, were pooled and adjusted to a final concentration of 1.0 mg/mL using HBS azide. The protein was aliquoted and frozen at -80 °C.

2.2.3.7 Surface plasmon resonance

Surface plasmon resonance (SPR) was used to validate binding of the produced antibodies to their target antigen as well as to measure their kinetics and affinities. All measurements were performed at 37 °C using a Biacore 8K (Cytiva). The corresponding running buffers, either HBS-P+ or HBS-EP+ (Cytiva), were used to dilute proteins for SPR. All dilution series were 1:3 dilutions. The running buffers were filtered and de-gassed using a vacuum filter system (0.22 µm, PES membrane). Three start-up cycles using the same program as for the analysis cycles were included before every run. MOPC21 was always injected in the reference flow cell (flow cell 1) for reference subtraction. A cycle containing only buffer as an analyte (no protein) was included in every run for blank subtraction. The data were analysed using the Biacore Insight Evaluation Software (Cytiva). All data fits are shown in the appendix (Section A.2).

For multi-cycle analysis of antibodies, a Series S Sensor Chip Protein A (Cytiva) was used. First, MOPC21 (69.76 nM) was injected into the reference flow cell, following by the injection of the corresponding antibody into flow cell 2. Antibodies were captured for 60 sec at a concentration of 69.76 nM. For the analysis of OX108 binding to hCD200R-mFc-His, the remaining Protein A binding sites in both flow cells were blocked through injection of MOPC21 (697.58 nM) for 300 sec. This approach was validated by capture of nivolumab mIgG1 which did not exhibit significant binding upon hCD200R-mFc-His injection (up to 13 RU, Figure A.1 C). The respective analyte protein, hPD-1-2xHis, hCD200R-mFc-His or mFcγRIIb-His, was injected for 60 sec and dissociation was monitored for 360 sec. hPD-1-2xHis was injected with concentrations ranging from 1.27 nM to 308.64 nM, hCD200R-mFc-His with concentrations between 5.48 nM to 1333.33 nM and mFcγRIIb-His with concentrations between 1.029 nM to 250 nM. The Protein A chip was regenerated by injection of Glycine pH 1.5 (Cytiva) for 30 sec. HBS-EP+ was used as running buffer.

A Series S Sensor Chip NTA (Cytiva) was used to assess the bivalent binding properties of nivolumab mIgG1 variants in multi-cycle analysis. Before each run,

the surface of the sensor chip was conditioned by injection of 350 mM EDTA (Cytiva) for 60 sec. The NTA on the sensor chip was saturated by injection of 0.5 mM $NiCl_2$ (Cytiva) before each cycle. hPD-1-2xHis (55.556 nM) was injected for 20 sec into flow cell 2. The antibodies were allowed to associate for 120 sec and dissociation was monitored for 900 sec. The surface was regenerated by injection of 350 mM EDTA for 60 sec. Antibodies were injected with concentrations ranging from 0.032 nM to 69.758 nM. HBS-P+ was used as running buffer.

For single-cycle analysis of nivolumab variants, antibodies (69.76 nM) were captured for 15 sec on a Series S Sensor Chip Protein A. The analyte (hPD-1-2xHis) was injected with increasing concentrations (from 1.7 nM to 2777.78 nM) for 60 sec, following by a short dissociation phase of 60 sec. After the final analyte injection, dissociation was monitored for 180 sec. Glycine pH 1.5 was used to regenerate the chip (30 sec injection). HBS-EP+ was used as running buffer.

2.2.4 Flow cytometry

2.2.4.1 General

All flow cytometry experiments were carried out using a BD LSRFortessa X-20 machine. Whenever possible, 2×10^6 cells were used for each staining. Most stainings were carried out in 96-well U-bottom plates, but for experiments with only few samples 5 mL round-bottom polystyrene tubes were used. All centrifugation steps for 96-well plates were carried out at $757 \times g$ for 2 min. Cells were washed in ice-cold PBS and subsequently stained with Zombie NIR Fixable Viability stain (BioLegend) for 15 min at RT. Whenever necessary, mFcγRs were blocked by incubation with a mouse Fc block (BioLegend) for 10 min on ice. Subsequently, cells were stained in 50 µL of the respective antibody cocktail and incubated for a minimum of 15 min on ice. Cells were washed twice in ice-cold PBS and fixed with IC Fixation Buffer (Thermo Fisher Scientific) for 30 min at RT. After washing the fixed cells twice in PBS, they were resuspended in FACS buffer for subsequent analysis. Fluorescence minus one (FMO) controls and compensation beads were included in every run and

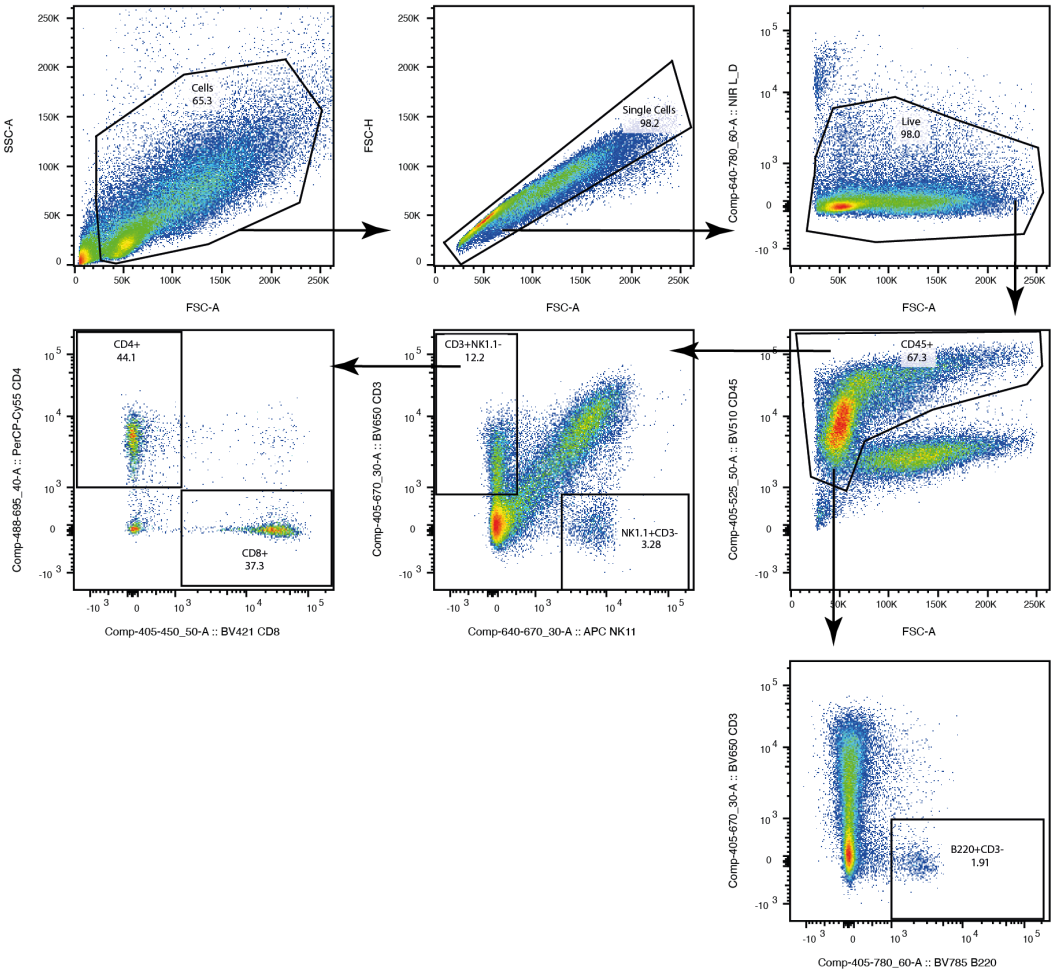


Figure 2.1: Gating strategy for lymphoid immune cells
Representative gating strategy for lymphoid immune cells. Different lymphoid cell subsets were identified using the following markers: Live/Dead, CD45, CD3, NK1.1, B220, CD4 and CD8.
The data shown here were published by Fellermeyer *et al.*[1].

treated identically. All commercial antibodies used are shown in Table 2.9 with the corresponding dilution. Produced antibodies (Section 2.2.3) were conjugated using Alexa Fluor 488 Antibody Labelling Kits (Thermo Fisher Scientific), according to the manufacturer's instructions, and used at a 1:100 dilution. All dilutions were made with PBS. The gating strategies for lymphoid, myeloid and T cells are shown in Figures 2.1, 2.2 and 2.3, respectively. All gating was performed using FlowJo 10.8.1 (BD).

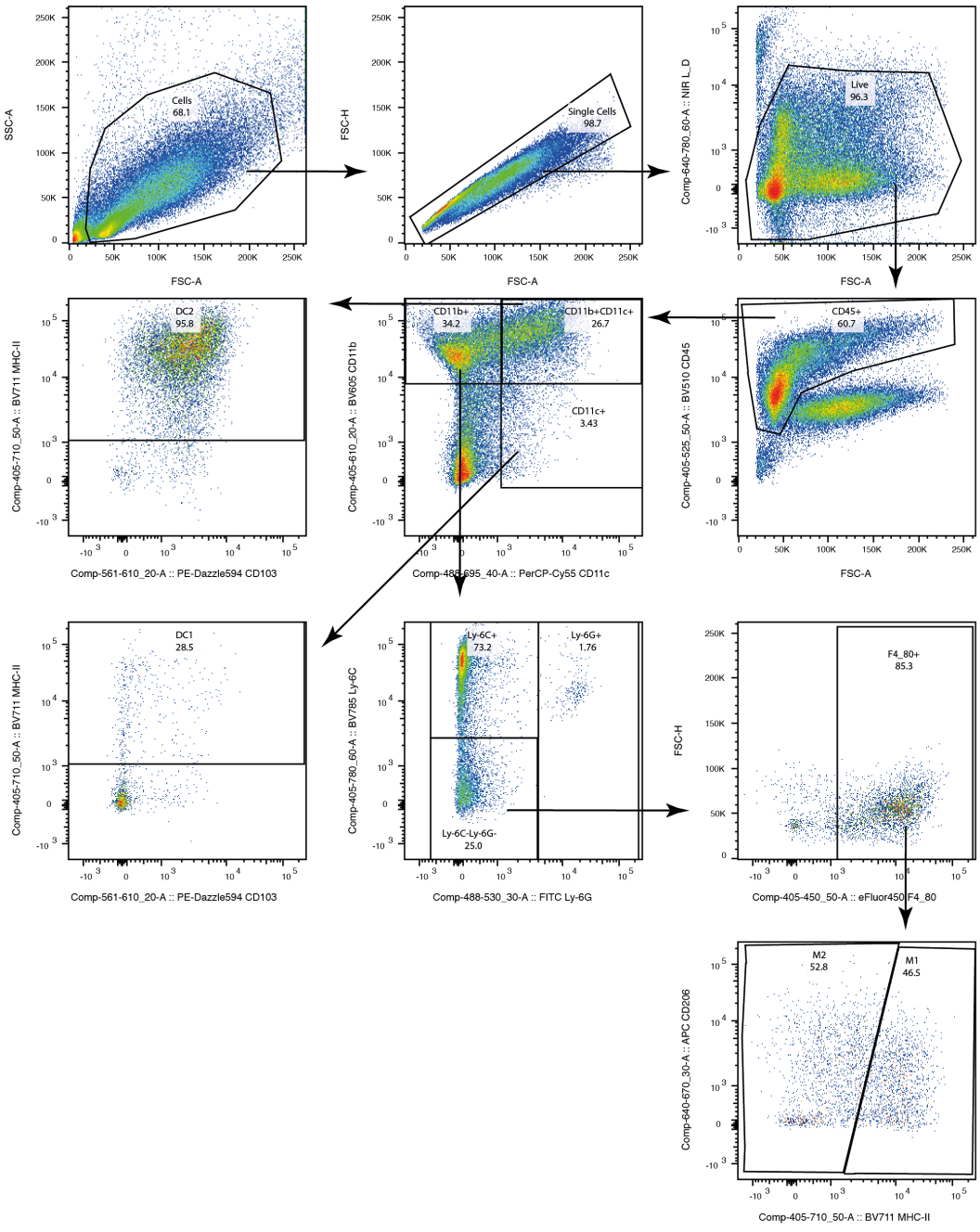


Figure 2.2: Gating strategy for myeloid immune cells
Representative gating strategy for myeloid immune cells. Different myeloid cell subsets were identified using the following markers: Live/Dead, CD45, CD11b, CD11c, Ly-6C, Ly-6G, F4/80, CD206 and MHC-II.
The data shown here were published by Fellermeyer *et al.*[1].

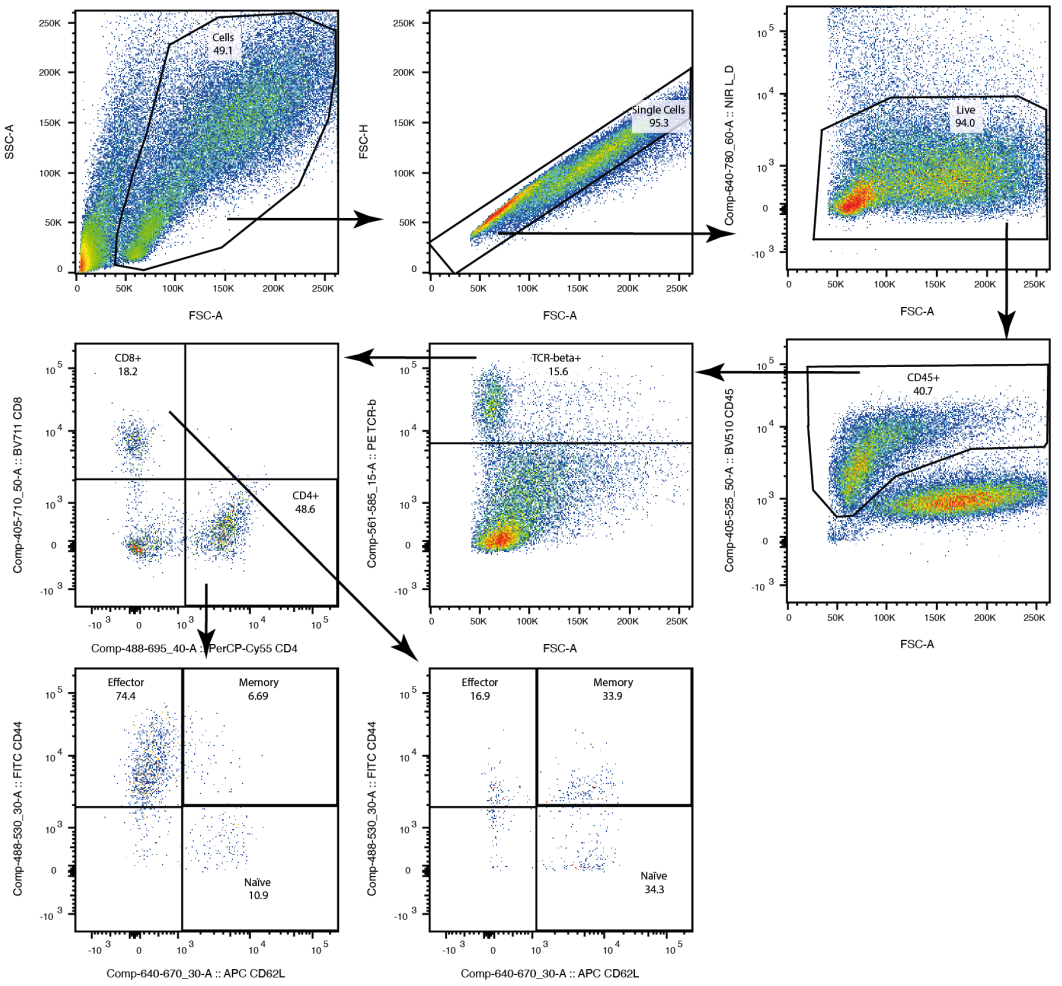


Figure 2.3: Gating strategy for T-cell subsets
Representative gating strategy for T-cell subsets. Different T-cell subsets were identified using the following markers: Live/Dead, CD45, TCR-β, CD4, CD8, CD44 and CD62L. The data shown here were published by Fellermeyer *et al.*[1].

2.2.4.2 Antibody blocking assay

In order to assess whether the produced antibodies (nivolumab mIgG1 and OX108) bind to immune cells from hPD-1/hCD200R mice, splenocytes were isolated (Section 2.2.6.3). 2×10^6 cells were stimulated for 48 hours with control or 81 nM phorbol 12-myristate 13-acetate (PMA) and 1.34 µM ionomycin (Cell Stimulation Cocktail, Thermo Fisher Scientific). Next, MOPC21, nivolumab mIgG1 or OX108 were added to splenocytes at a concentration of 10 µg/mL and were incubated for 20 min on ice. hPD-1 and hCD200R were stained as described in Section 2.2.4.1.

2.2.4.3 Quantibrite

Quantibrite PE beads (BD Biosciences) were used to quantify the levels of CD200 expressed on MC38-sensitive cells and LLC1 cells. Cells were incubated with PE-labelled anti-CD200 or isotype control antibodies for 15 min at RT. Following a wash in PBS, the stained cells were resuspended in FACS buffer and acquired as described in Section 2.2.4.1. The PE beads were resuspended in 0.5 mL PBS. The analysis was performed according to the manufacturer's instructions with a PE:antibody ratio of 1:1.

2.2.4.4 *In vitro* T-cell activation assay

After co-culture of Jurkat and TCS cells (described in Section 2.2.1.6), cells were stained with an anti-mCD45-PE antibody (50 µL/well) for 45 min at RT. Cells were washed once in FACS buffer (250 µL/well). Expression of GFP, indicating T-cell activation, was measured by flow cytometry. TCS wells were excluded by gating on $mCD45^-$ cells. Fold changes of GFP median fluorescence intensity (MFI) values were calculated by dividing all values from co-cultures with the background of the corresponding 'Jurkat only' culture. For pooling of data, all fold changes were normalised against the average of the nivolumab mIgG1 treated cells.

2.2.4.5 Fluorescence-activated cell sorting

To generate cell lines that uniformly express high levels of a target protein, fluorescence-activated cell sorting (FACS) of lentivirally transduced cells (as described in Section 2.2.1.3) was used. Briefly, 1×10^7 cells were stained with an antibody against the protein of interest and incubated for 45 min at RT. After washing in PBS, cells were resuspended in PBS containing 2 % (v/v) FBS and filtered through a 30 µm cell strainer. The WIMM Flow Cytometry Facility performed the cell sorting. After FACS, cells were spun down, resuspended in an appropriate amount of medium and cultured as described in Section 2.2.1.1.

2.2.5 RNA sequencing

2.2.5.1 RNA isolation

RNA for sequencing was isolated from *in vitro* cultured cells. Briefly, after lifting cells using trypsin solution with 0.5 mM EDTA, cells were washed twice in PBS and counted (viability $\geq$ 95 %). 1×10^6 cells were pelleted and resuspended in 350 µL RLT buffer (Qiagen). After mixing, the lysate was transferred to QIAshredder spin columns (Qiagen) and centrifuged for 2 min at 17,000 $\times$ *g*. The solution was transferred into a RNase-free 1.5 mL microcentrifuge tube, snap-frozen in dry ice with isopropanol and stored at -80 °C. The RNA was isolated using the RNeasy Mini kit (Qiagen) according to the manufacturer's instructions. The RNA quality was analysed with the help of Edward Jenkins using an Agilent 4200 TapeSation system according to the manufacturer's instructions. All RNA integrity number equivalent values were above 6.3, indicating intact RNA. RNA sequencing was performed by Novogene. Poly(A) capture was used to enrich messenger RNA (mRNA), which was sequenced using an Illumina platform with a paired-ended 150 base pair sequencing strategy.

2.2.5.2 Data processing and differential gene expression analysis

An in-house script (written by Sumana Sharma) was used for all RNA-seq analysis. RStudio 2022.07.2 with R version 4.2.1 was used. Upon RNA sequencing by Novogene, the raw sequencing reads were mapped against the mouse genome (GRCm38) using the *STAR* package (https://github.com/alexdobin/STAR). Read per gene counts were produced using *featureCounts* from the *Subread* package (https://github.com/ShiLab-Bioinformatics/subread) based on GRCm38 annotation. Genes with less than 2 counts per million (cpm) in only two or less samples were removed using the *cpm* function from the *edgeR* package (https://bioconductor.org/packages/release/bioc/html/edgeR.html). The *voom* function from the *limma* package (https://github.com/cran/limma) was used to normalise read counts and a linear model was applied to the normalised data for identification of differentially expressed genes. Genes with a false discovery

rate (FDR)-corrected p-value < 0.05 and an absolute log-fold change of > 1.5 were considered differentially expressed. The packages *ggplot2* and *ggVennDiagram* (https://github.com/tidyverse/ggplot2 and https://github.com/gaospecial/ggVennDiagram, respectively) were used for data visualisation. Pathway analysis was performed using the *enrichR* package (https://github.com/wjawaid/enrichR) and the KEGG (Kyoto Encyclopedia of Genes and Genomes) database (KEGG_2019_Mouse). Pathways with an adjusted p-value of ≤ 0.1 were considered significantly enriched/depleted.

2.2.5.3 STRING network analysis

Genes from enriched pathways (Section 2.2.5.2) from the Oxford and Sanofi[300] study (Section 3.2.10) were retrieved and used for a STRING network analysis (https://string-db.org). A full STRING network excluding textmining was built with a high confidence threshold for the interaction score (≥ 0.7). The Markov Cluster (MCL) algorithm was used to divide the interactions into different clusters (inflation parameter 1.5) and clusters with more than ten nodes were further investigated.

2.2.6 Animal work

2.2.6.1 General

C57BL/6JOlaHsd mice were humanised for PD-1 and CD200R as described in Section 1.5 and in the DPhil theses of Billur Akkaya[293] and Christopher Paluch[294]. Each strain was designed to express the human extracellular domain as a chimera with the murine transmembrane and cytoplasmic domains. The production was outsourced to InGenious Targeting Laboratory and Taconic Biosciences for the human knock-in CD200R and PD-1 mouse, respectively. hCD200R and hPD-1 mice were crossbred until homozygosity for both transgenes, confirmed through genotyping (carried out by Tanya Cheetham, Cornall laboratory, University of Oxford). Double knock-in humanised CD200R and PD-1 mice were bred and maintained at the Biomedical Services (University of Oxford, establishment

license XEC303F12) in accordance with the Animals (Scientific Procedures) Act 1986. All procedures were approved by local ethics committee and performed under the UK Home Office Project licenses PBA43A2E4 and PP4306634 and the personal licence ID75A4ABD. Depending on the original sex of the cancer cell line, female or male mice between 6-14 weeks of age were used for MC38 and LLC1 tumour models, respectively.

2.2.6.2 Subcutaneous tumour model

For subcutaneous injection, cells were cultured as described in Section 2.2.1.1 with no antibiotics. Cells were washed twice in ice-cold PBS and adjusted to a concentration suitable for injection of 100 µL of cell suspension into mice. Double knock-in hPD-1/hCD200R mice were anaesthetised using isoflurane, the area for injection was shaved and subsequently cleaned using 70 % ethanol. The skin was carefully lifted and cells were injected into the left flank using a 25G needle. 100 µL of ice-cold cell suspension in PBS was injected, containing either 5×10^5 MC38 cells (MC38-sensitive or MC38-resistant) or 1×10^5 LLC1 cells. Upon subcutaneous injection, the ears were punched for identification purposes and the mice were returned to their cage and monitored until they recovered from the anaesthesia. Mice were monitored every other day and caliper measurements were taken as soon as this was sufficiently accurate. Tumours were measured in all three dimensions and tumour volumes were calculated using the following formula: $V = \frac{\pi}{6} \times \text{length} \times \text{width} \times \text{height}$. Treatments were started once the average tumour volume exceeded 40 mm^3 or 20 mm^3 for the MC38 or LLC1 tumour models, respectively. Mice were randomised into groups with a similar average tumour volume using a R code written by Sumana Sharma. All experiments were carried out blinded. Mice were treated four times over the course of two weeks with 1.4 nmol/antibody/treatment, which is equivalent to 200 µg of nivolumab mIgG1. Mice were culled once the tumour volume exceeded 1000 mm^3 or an ulceration persisted over 48 hours. For rechallenge experiments, mice that completely rejected the initial subcutaneous tumour challenge were used. Mice

that have not been used before (naïve mice) were included as control. The same procedure was performed, but this time the cells were injected into the right flank.

2.2.6.3 Spleen isolation

After cervical dislocation, spleens were harvested and transferred into Bijou containers containing 2 mL RPMI, supplemented with 10 % (v/v) FBS. Spleens were mashed through a 70 µm cell strainer using the bottom of a plunger from a 1 mL syringe. Splenocytes were pelleted by centrifugation at 526 × g for 5 min and resuspended in 2 mL RBC Lysis buffer (Qiagen). After incubation for 2 min at RT, 8 mL of medium was added and the cells were pelleted again. Upon resuspension, cells were counted as described in Section 2.2.1.1 and stained (Section 2.2.4.1).

2.2.6.4 Tumour isolation

After cervical dislocation, tumours were harvested and transferred into Bijou containers containing 3 mL tumour digestion medium (Table 2.4). Tumours were cut into small pieces using fine scissors, transferred into 6-well plates and incubated for 45 min at 37 °C. Halfway through the incubation, a 1 mL syringe was used to carefully dissociate the tumour pieces. The digested tumours were mashed through a 70 µm cell strainer using the bottom of a plunger from a 1 mL syringe. The cell suspensions were washed three times using FACS buffer and after the last centrifugation the cells were resuspended in 4 mL FACS buffer. For flow cytometric analysis of tumour cells, cells were counted (Section 2.2.1.1) and stained (Section 2.2.4.1). For analysis of immune cells, Ficoll-Paque density gradient centrifugation was used to enrich for immune cells. 3 mL of Ficoll-Paque were added to a 15 mL conical centrifuge tube. 4 mL of cell suspension were added carefully on top of the Ficoll-Paque. Cells were centrifuged at 400 × g for 40 min, with decreased acceleration (level 3/9) and no brake (level 0/9). Cells in the white opaque ring were carefully collected using a 1 mL pipette. The isolated cells were washed twice with FACS buffer. After the final centrifugation, cells were counted (Section 2.2.1.1) and stained (Section 2.2.4.1).

2.2.6.5 Lymph node isolation

After cervical dislocation, lymph nodes (draining and non-draining) were harvested and transferred into 1.5 mL microcentrifuge tubes containing 0.5 mL lymph node digestion medium (Table 2.4). Lymph nodes were transferred into 24-well plates and pierced and teared using sharp forceps. After a 15 min incubation at 37°C, the cell suspensions were pipetted up and down using a 1 mL pipette and incubated for another 15 min at 37°C. The lymph nodes were mashed through a 70 µm cell strainer using the bottom of a plunger from a 1 mL syringe and washed twice with FACS buffer. After the final centrifugation, cells were counted (Section 2.2.1.1) and stained (Section 2.2.4.1).

2.2.7 Statistical analysis

With exception of the analysis for the RNA-sequencing data (Section 2.2.5), all analyses were performed in Prism 9.5.1 (GraphPad). Immune cell populations were analysed using two-way ANOVA tests with Tukey's multiple comparisons tests. Survival experiments were plotted as Kaplan-Meier curves and analysed by log-rank (Mantel-Cox) tests. Complete responses were analysed by chi-square tests. Individual conditions in the *in vitro* T-cell activation assay (Sections 5.2.5 and 6.2.7) were compared using unpaired t-tests (two-tailed distribution, assuming homoscedasticity). Experiments were only repeated once, unless stated otherwise in the figure legend. Differences were considered statistically significant when $p \leq 0.05$. Unless otherwise stated, significance levels were denoted as follows: p-value $\leq 0.05 = *$, $\leq 0.01 = **$, $\leq 0.001 = ***$, $\leq 0.0001 = ****$

Science, for me, gives a partial explanation for life. In so far as it goes, it is based on fact, experience and experiment.

— Rosalind Franklin

3

Antibody production and cancer models

Contents

3.1 Rationale 85
3.2 Results 86
3.2.1 Design of mIgG1 antibodies 86
3.2.2 Purification of mIgG1 antibodies using Protein A and SEC 87
3.2.3 Endotoxin testing and optimisation 88
3.2.4 SPR validation of antibodies 89
3.2.5 *Ex vivo* validation of antibodies 89
3.2.6 *In vitro* characterisation of MC38 and LLC1 cells . . . 91
3.2.7 *In vivo* profiling of MC38 and LLC1 tumours 93
3.2.8 Response to mNivo monotherapy 95
3.2.9 *In vivo* comparison of different MC38 cell lines 97
3.2.10 Differential gene expression analysis of MC38 cell lines 99
3.2.11 Identification of common pathways in resistant MC38 cells 102
3.3 Discussion 105

3.1 Rationale

THIS thesis aimed to improve on immune-checkpoint therapy by testing new combinations of antibodies as well as through re-engineering of antibodies in order to improve their blocking efficacy. Ultimately, this was tested in tumour

models using mice humanised for the extracellular region of the corresponding receptors. For the *in vivo* work, large amounts of high-quality antibodies were needed. Thus, first, a pipeline to produce recombinant, monomeric, endotoxin-free monoclonal antibodies had to be established.

Cancer models can be divided into 'cold' and 'hot' tumours[301]. This classification describes their responsiveness to immune-checkpoint blockade and is often correlated with the immune cell infiltration before the start of the treatment. 'Cold' tumours demonstrate little proinflammatory immune cell infiltration and cytokine levels, whereas 'hot' tumours exhibit the opposite[301]. It is important to test novel therapeutics in both settings, as the respective requirements for improvement may be very different. Therefore, a PD-1 blockade-sensitive and resistant model were established to test the new antibodies in both scenarios.

3.2 Results

3.2.1 Design of mIgG1 antibodies

Currently, all approved PD-1 blockers are of the human IgG4 isotype, with the aim to reduce antibody effector functions. In order to match this in the murine system, the mouse IgG1 isotype was chosen, as this is also an isotype with low affinity to FcγRs and no capacity to bind complement[204,302]. This 'murinised' form of nivolumab is referred to as mNivo (nivolumab mIgG1). It is important to note that there are key differences between hIgG4 and mIgG1, for example hIgG4 interacts with the high-affinity receptor hFcγRI, whereas mIgG1 only binds to the medium/low-affinity receptors mFcγRIIb and mFcγRIII.

To further reduce FcγR engagement, the D265A mutation[212] was introduced in the mIgG1 backbone to create an Fc-null antibody, with diminished affinity towards FcγRs. Although the D265A mutation abrogates monomeric binding observed via SPR[212], immune complexes of human IgG-D265A antibodies are still capable of binding to FcγRs, though with greatly reduced affinity[213]. Of note, in this chapter as well as in Chapter 4, 'MOPC21', 'OX108' and 'mNivo' refer to the D265A-mutated antibodies. Lastly, mutations (T252M-T254S-M309L)

were introduced that improve binding of mIgG1 to Protein A, to facilitate affinity purification[303]. These mutations replace parts of the Protein A binding site of mIgG1 with the one from hIgG1. Importantly, the binding site of Protein A is different to that from FcγRs, thus not affecting the binding to the latter[200]. Furthermore, binding of the neonatal FcR (FcRn) is also not affected (personal communication from Absolute Antibodies Ltd.). The κ light chain was not modified. All chains were expressed using a hCD33 signal peptide, as recommended by Absolute Antibodies Ltd., and all sequences used are provided in Section A.1.

3.2.2 Purification of mIgG1 antibodies using Protein A and SEC

DNA strings encoding the heavy and light chains of the respective antibodies were cloned into a pHR plasmid. Upon lentivirus production in HEK293T cells, CHO-K1 cells were transduced with the genes encoding the corresponding heavy and light chains. Upon expansion, normal growth medium was replaced by medium containing Ultra Low IgG FBS, which was harvested and replaced every week. The supernatant was purified using Protein A beads, either as resin with gravity-flow columns or via pre-packed columns. Upon elution from the column, fractions containing protein were pooled and concentrated. The concentrated protein was injected over a size-exclusion chromatography (SEC) column to separate monomeric antibody from aggregated material. All antibodies were eluted in PBS pH 7.4. Representative SEC traces for the different antibodies (mNivo, OX108, MOPC21) are shown in Figure 3.1 A. Non-reducing and reducing SDS-PAGE gels (Figures 3.1 B and C) were stained to further evaluate purity. Clear bands indicating the respective chains or full antibodies were observed and only the 'monomeric' fractions were pooled.

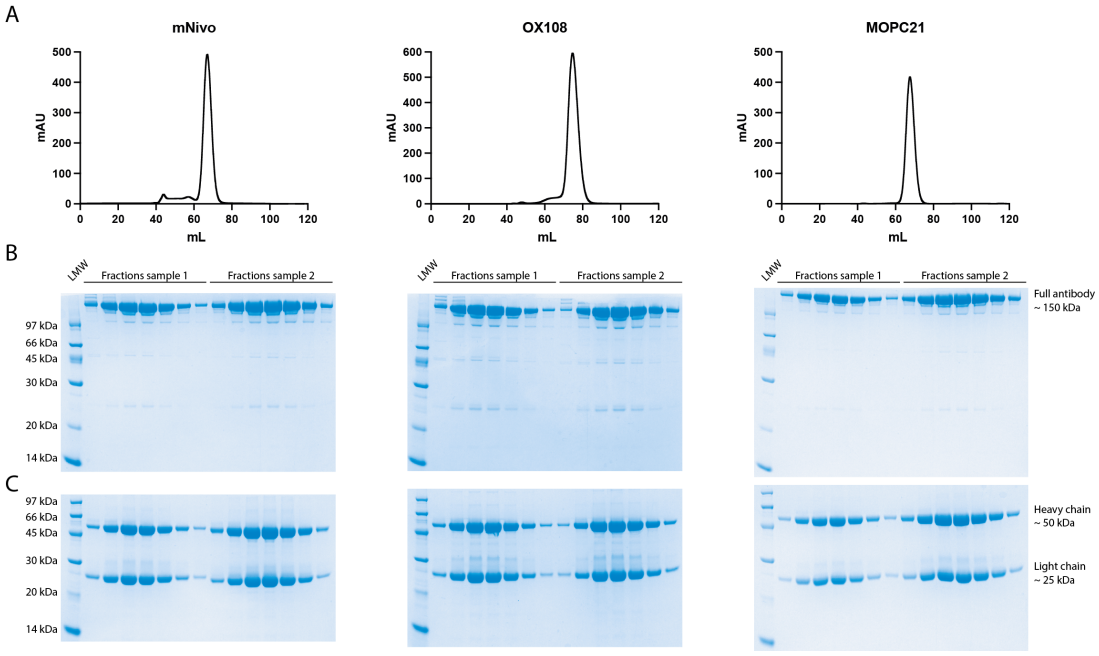


Figure 3.1: Size exclusion of mIgG1 antibodies
(A) SEC traces of mNivo, OX108 and MOPC21 mIgG1. A ProteoSEC 16/60 6-600 column was used.
(B) A non-reducing SDS-PAGE gel was stained with coomassie blue to detect protein bands. Bands corresponding to the size of full antibodies (∼ 150 kDa) were observed. A low-molecular weight (LMW) marker was included.
(B) A reducing SDS-PAGE gel was stained with coomassie blue to detect protein bands. Bands corresponding to the size of heavy chains (∼ 50 kDa) and light chains (∼ 25 kDa) were observed. A low-molecular weight (LMW) marker was included.

3.2.3 Endotoxin testing and optimisation

As the antibodies were ultimately to be used in *in vivo* experiments, zero or low contamination with endotoxin was important[299]. Endotoxin levels were determined using the Limulus Amebocyte Lysate test. The initial plan was to clean up purified antibodies using anion exchange chromatography, however this proved very challenging. The alternative option was to keep all consumables and machines involved in the purification process endotoxin-free. This was achieved by switching to PrismA columns, a mutated form of Protein A that allows for cleaning with up to 1.0 M sodium hydroxide[304]. Through a stringent cleaning protocol and frequent buffer replacement a fully endotoxin-free antibody production pipeline was established and over 1,100 mg of antibodies were produced. All antibodies were eluted in PBS pH 7.4, sterile filtered and frozen at -80 °C until further usage.

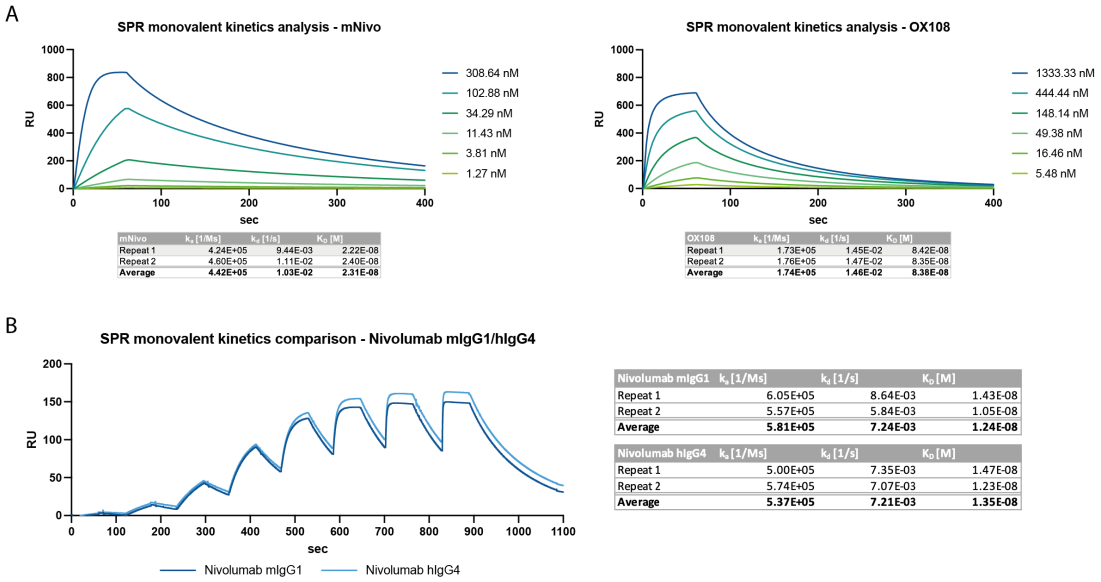
3.2.4 SPR validation of antibodies

To validate the successful production of mNivo (anti-hPD-1), OX108 (anti-hCD200R) and MOPC21 (isotype control), SPR was utilised to test the binding of the antibodies (mNivo and OX108) to their corresponding antigens (PD-1 and CD200R). Human CD200R was available in the Davis laboratory as an Fc-protein with a His-tag (hCD200R-Fc-His, produced by Heather Brouwer), whereas human PD-1 was produced as a double His-tagged protein (hPD-1-2xHis, sequence provided in Section A.1.4). hPD-1-2xHis was purified using Ni-NTA resin and subsequently size-excluded to remove aggregates (data not shown). For SPR, antibodies were immobilised on a Protein A chip, with MOPC21 in the reference channel and mNivo or OX108 in the active channel (60 sec injection at 69.76 nM, equivalent to 0.01 mg/mL). As hCD200R-Fc-His has the potential to bind the Protein A chip, binding sites were blocked through a subsequent injection of MOPC21 at high concentration (300 sec injection at 697.58 nM, equivalent to 0.1 mg/mL). Finally, the corresponding protein was injected, and the observed binding confirmed the specificity of the produced antibodies (Figure 3.2 A).

While the original OX108 clone was already a mIgG1 antibody, nivolumab is used in the clinic as hIgG4 isotype. To validate that isotype switching did not impede the binding capabilities, nivolumab hIgG4 biosimilar and nivolumab mIgG1 (mNivo) were captured on a Protein A chip. As shown in Figure 3.2 B, both antibodies produced near-identical response curves upon hPD-1-2xHis injection and the derived kinetic constants are very similar. Overall, the produced mIgG1 antibodies were confirmed to bind their corresponding proteins and isotype switching of nivolumab was shown to have no impact on its affinity.

3.2.5 *Ex vivo* validation of antibodies

As a final validation, the binding of the antibodies to immune cells from hPD-1/hCD200R mice was tested *ex vivo*. For this, splenocytes from mice were stimulated for 48 hours with PMA/ionomycin and subsequently incubated for 20 minutes with the produced antibodies. Commercial staining antibodies were used to



mNivo	k_a [1/Ms]	k_d [1/s]	K_D [M]
Repeat 1	4.24E+05	9.44E-03	2.22E-08
Repeat 2	4.60E+05	1.11E-02	2.40E-08
Average	**4.42E+05**	**1.03E-02**	**2.31E-08**

OX108	k_a [1/Ms]	k_d [1/s]	K_D [M]
Repeat 1	1.73E+05	1.45E-02	8.42E-08
Repeat 2	1.76E+05	1.47E-02	8.35E-08
Average	**1.74E+05**	**1.46E-02**	**8.38E-08**

Nivolumab mIgG1	k_a [1/Ms]	k_d [1/s]	K_D [M]
Repeat 1	6.05E+05	8.64E-03	1.43E-08
Repeat 2	5.57E+05	5.84E-03	1.05E-08
Average	**5.81E+05**	**7.24E-03**	**1.24E-08**

Nivolumab hIgG4	k_a [1/Ms]	k_d [1/s]	K_D [M]
Repeat 1	5.00E+05	7.35E-03	1.47E-08
Repeat 2	5.74E+05	7.07E-03	1.23E-08
Average	**5.37E+05**	**7.21E-03**	**1.35E-08**

Figure 3.2: Binding validation of mNivo and OX108 through SPR
(A) Multi-cycle analysis of mNivo and OX108. mNivo or OX108 were captured on a Protein A chip and the corresponding protein, hPD-1-2xHis or hCD200R-Fc-His, was injected as analyte with varying concentrations. Sensorgrams were reference- and blank-subtracted. MOPC21 was captured in the reference channel. The Biacore Insight Evaluation Software was used to fit a 1:1 binding model (Figures A.1 A and B) and derived affinity constants (k_a, k_d and K_D) are shown in the tables below.
(B) Single-cycle analysis of nivolumab mIgG1 and hIgG4. Nivolumab mIgG1 (mNivo) or nivolumab hIgG4 were captured on a Protein A chip and hPD-1-2xHis was injected as analyte with varying concentrations ranging from 1.7 nM to 2777.78 nM. Sensorgrams were reference- and blank-subtracted. MOPC21 was captured in the reference channel. The Biacore Insight Evaluation Software was used to fit a 1:1 binding model (Figure A.1 D) and derived affinity constants (k_a, k_d and K_D) are shown in the tables.
The data shown here were published by Fellermeyer *et al.*[1].

detect the corresponding receptor levels, which was analysed by flow cytometry. For CD200R, OX108-PE was commercially available, whereas a different clone (EH12.2H7) was used to measure PD-1 levels. This clone was reported to compete with nivolumab for binding to PD-1[305]. Figure 3.3 demonstrates a clear reduction of PD-1 signal upon pre-incubation with mNivo, whereas no change is observed with OX108 and MOPC21. Similarly, only OX108 blocked binding to CD200R.

Taken together, an endotoxin-free pipeline was established to produce mIgG1 antibodies. The antibodies generated were shown to bind their corresponding protein *in vitro* as well as *ex vivo*.

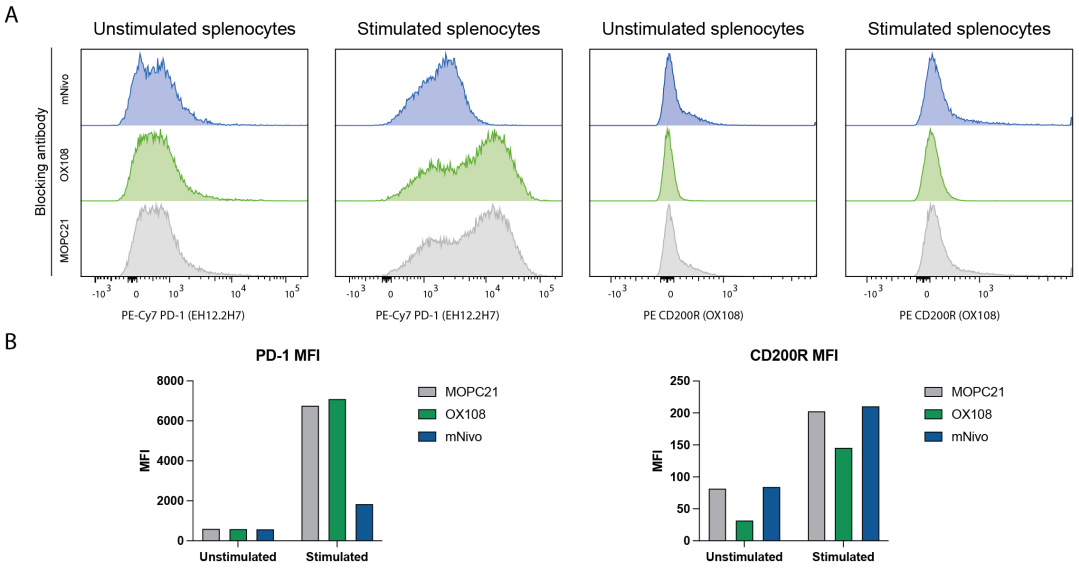


Figure 3.3: *Ex vivo* binding validation to hPD-1/hCD200R splenocytes
(A) Histograms of PD-1 and CD200R receptor levels measured by flow cytometry. Splenocytes were treated with PMA/ionomycin or control for 48 hours and blocked by incubation with produced antibodies. Available receptor epitopes were measured using commercial antibodies that compete with the produced antibodies.
(B) Median Fluorescence Intensity (MFI) was derived and plotted as bar chart to demonstrate the change in binding capacity.
The data shown here were published by Fellermeyer *et al.*[1].

3.2.6 *In vitro* characterisation of MC38 and LLC1 cells

The MC38 colorectal cancer model is often used for testing new immunotherapies as it is very immunogenic and responsive to PD-1 blockade[235,238]. In contrast, the growth of the lung cancer model LLC1 is not inhibited by anti-PD-1 treatment and LLC1 is generally considered to be a 'cold' tumour[306]. Importantly, LLC1 is characterised by a high degree of myeloid cell infiltration[307] as well as accumulation of immature myeloid cells systemically[308]. While the LLC1 cell line was available in the Cerundolo laboratory, MC38 cells were provided by Adrian Harris (University of Oxford, referred to as MC38-Oxford) and Stephen Beers (University of Southampton, named MC38-Southampton). Of note, initially only the MC38-Oxford cell line was available. However, due to initial results that contradicted with the reported responsiveness of MC38 tumours to PD-1 blockade (preliminary data in Figure 1.8, and published studies[235,238]), the Beers laboratory was

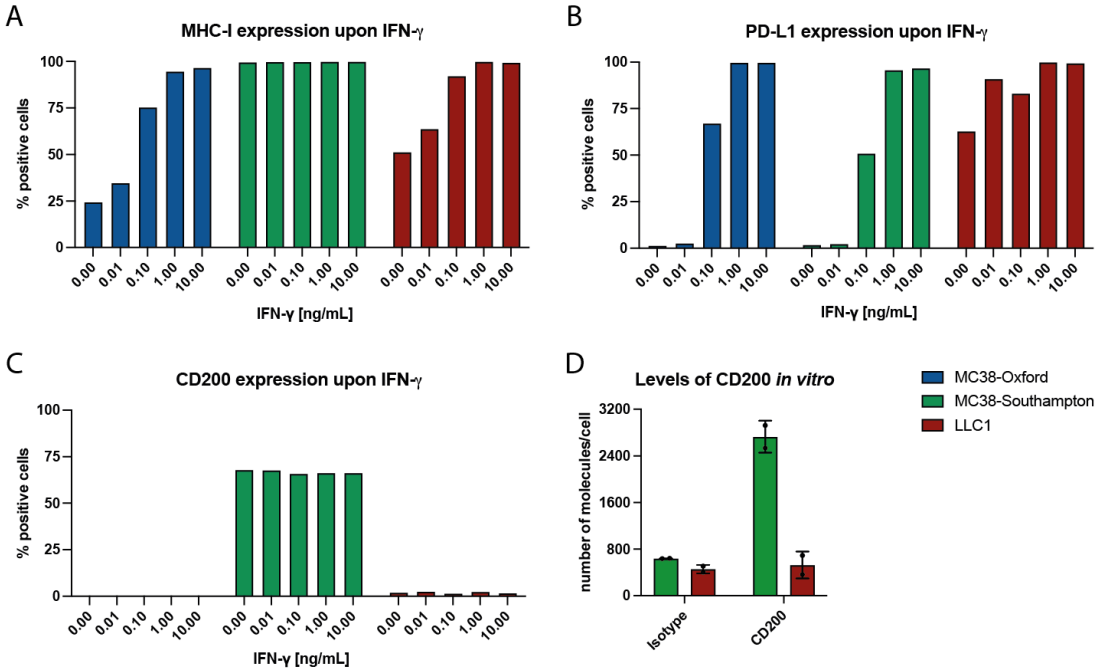


Figure 3.4: *In vitro* analysis of MHC-I, PD-L1 and CD200
(A - C) Different cell lines were treated for 24 hours with varying concentrations of IFN-γ. Subsequently, cells were stained for different surface markers: (A) MHC-I, (B) PD-L1 and (C) CD200. A FMO control was used to determine the negative population. (D) Quantibrite beads were used to measure the levels of CD200 on *in vitro* cultured MC38-Southampton and LLC1 cells.
The data shown here were published by Fellermeyer *et al.*[1].

contacted to obtain their MC38 model[238]. All cell lines were externally validated by short tandem repeat (STR) analysis.

All cell lines were treated with varying concentrations of IFN-γ and the change in expression of MHC-I, PD-L1 and CD200 was investigated. As shown in Figures 3.4 A-C, protein expression levels demonstrated considerable variability. First, while MC38-Oxford and MC38-Southampton cells were both confirmed to have a similar STR profile as the original MC38 cells, they responded differently to IFN-γ treatment. All MC38-Southampton cells constitutively expressed MHC-I, whereas only about 25 % of MC38-Oxford cells did (Figure 3.4 A), but this increased upon IFN-γ exposure. Levels of MHC-I were also upregulated in response to IFN-γ in MC38-Southampton cells as the MFI further increased (data not shown). Similar to MC38-Oxford, LLC1 cells gradually increased MHC-I expression upon treatment. PD-L1 was upregulated in all cell lines upon IFN-γ

exposure, but LLC1 cells expressed this ligand pre-treatment (Figure 3.4 B). As shown in Figure 3.4 C, CD200 expression was not influenced by IFN-γ in the tested cell lines, as levels did not change across the different conditions. Importantly, MC38-Southampton cells displayed a heterogeneous expression of CD200, with around 66 % of all cells being CD200$^+$. Quantibrite beads were used to determine the number of molecules per cell on MC38-Southampton cells. As shown in Figure 3.4 D, approximately 2,700 CD200 molecules were expressed on MC38-Southampton cells, which is comparable to PD-L1 on immature DCs and PD-L2 on mature DCs (5,724 and 5,243 molecules/cell, respectively)[127]. LLC1 cells were included as a negative control, which did not exhibit any increase in protein levels compared to the isotype control.

3.2.7 *In vivo* profiling of MC38 and LLC1 tumours

To investigate the MHC-I, PD-L1 and CD200 levels *in vivo*, all cell lines were subcutaneously injected into hPD-1/hCD200R mice. After 14 days of growth, mice were culled and the tumour excised and digested. Expression of MHC-I, PD-L1 and CD200 was similar to *in vitro* IFN-γ-treated cells (Figure 3.4), as nearly all cells were positive for MHC-I and PD-L1, whereas CD200 was restricted to the MC38-Southampton model (Figure 3.5 A).

Simultaneously, immune cells were enriched by Ficoll-Paque density gradient centrifugation and different populations were identified using a lymphoid and myeloid flow cytometry panel (gating strategies shown in Figures 2.1 and 2.2). In all tested tumours, myeloid cells were the dominating populations, in particular M-MDSCs and macrophages (Figure 3.5 B). In LLC1 tumours, there were fewer macrophages and more G-MDSCs. Few DCs, B cells and T cells were present in the tumours. The percentages of M1/M2 macrophages (Figure 3.5 C) and CD4$^+$/CD8$^+$ T cells (Figure 3.5 D) were similar, but in LLC1 tumours macrophages were skewed towards a M2 phenotype. Lastly, CD200R levels were determined for all immune cells in order to get insights into which cells might be targeted by anti-CD200R treatment (Figure 3.5 E). In accordance with previous

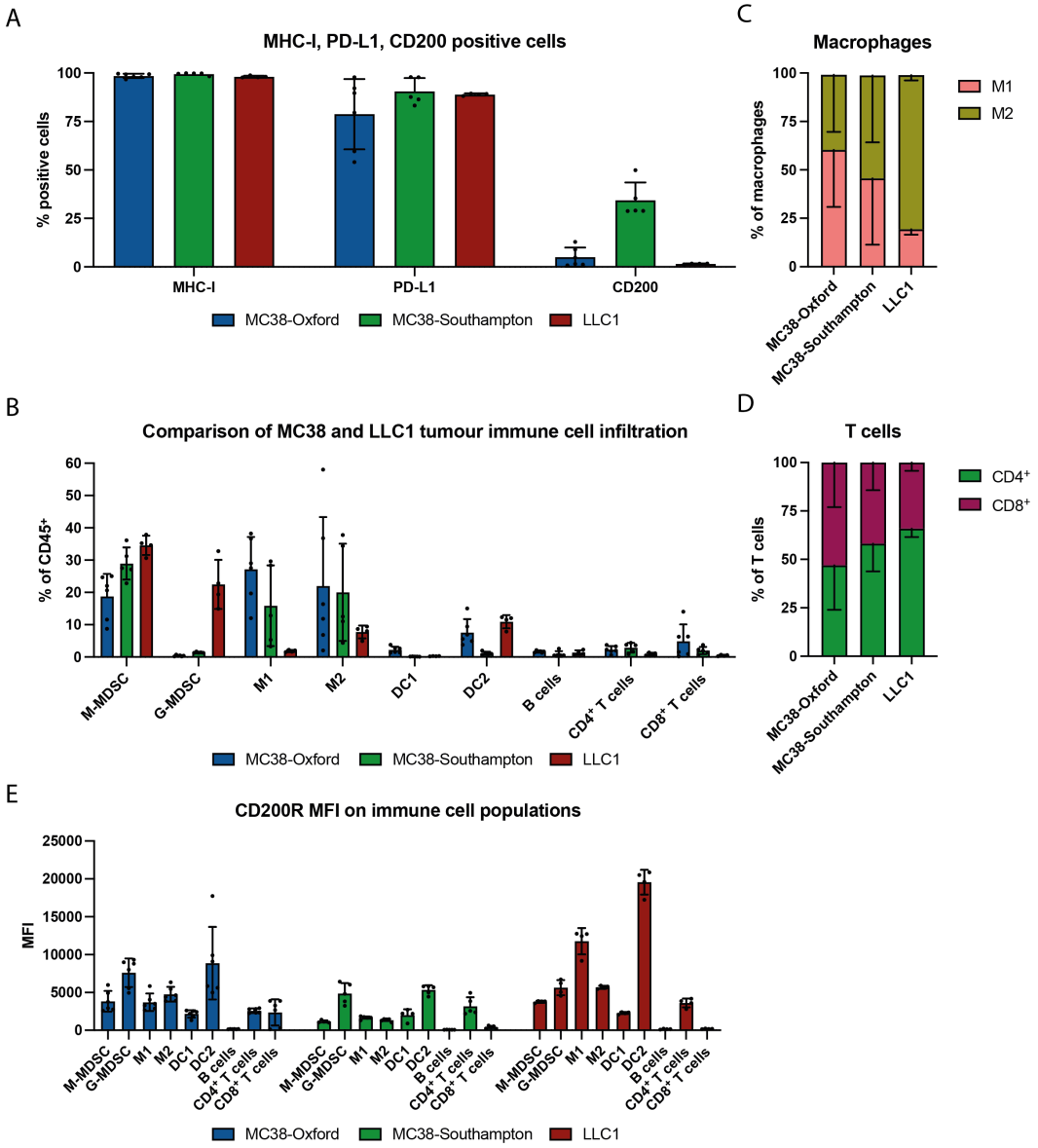


Figure 3.5: *In vivo* tumour and immune cell analysis
After 14 days of *in vivo* growth, tumours were excised and digested. n = 4-6/group
(A) Isolated tumours cells were stained for different surface markers (MHC-I, PD-L1 and CD200) and analysed with flow cytometry.
(B) Immune cells were enriched used Ficoll-Paque density gradient centrifugation. A lymphoid and myeloid flow cytometry panel (gating strategies shown in Figures 2.1 and 2.2) were used to identify different immune cell populations.
(C and D) Percentages of M1/M2 macrophages (C) and $CD4^+$/$CD8^+$ T cells (D) were compared.
(E) MFI of CD200R on identified immune cell populations. Tumours of different cell lines were acquired at different time points, so a direct comparison between the models is not possible.
The data shown here were published by Fellermeyer *et al.*[1].

reports[144], CD200R expression was primarily found on myeloid cells, with all populations expressing CD200R. DC2s were consistently identified as the highest CD200R-expressing immune cells, followed by G-MDSCs and macrophages. In contrast, of the identified lymphoid populations, only $CD4^+$ T cells expressed CD200R, although there were discrepancies between the different tumours.

3.2.8 Response to mNivo monotherapy

Finally, the responsiveness to PD-1 monotherapy was evaluated. The two available MC38 cell lines as well as LLC1 cells were subcutaneously injected into hPD-1/hCD200R mice. Once the tumours reached 40 mm^3 or 20 mm^3 for MC38 and LLC1 models, respectively, mice were randomised and treated with MOPC21 or mNivo. Mice were treated with 200 µg of the respective antibody and treatment was given twice a week for two weeks. All experiments were carried out blinded to reduce bias.

Figure 3.6 shows the individual tumour growth curves as well as survival plots. Surprisingly, there was a striking difference in the responsiveness of the MC38-Oxford and -Southampton model (Figure 3.6 A and B). Most MC38-Southampton tumours completely regressed upon mNivo therapy, leading to a complete response (CR) rate of 70 %. In contrast, the survival of mice bearing MC38-Oxford tumours was only slightly increased and all mice needed to be culled by day 30. Therefore, MC38-Southampton is hereinafter referred to as MC38-sensitive, whereas MC38-Oxford is named MC38-resistant. Finally, in concordance with the literature[306,309], LLC1 tumours did not display any tumour growth inhibition upon treatment with anti-PD-1 antibodies, compared to the isotype control MOPC21 (Figure 3.6 C).

Overall, the LLC1 lung cancer model is indeed a 'cold' tumour, which was resistant to PD-1 blockade. While it did not express CD200 in the tested *in vitro* and *in vivo* conditions, the TME harboured many TAMCs expressing CD200R (Figure 3.5 E), making it a suitable model to test the potential of combined CD200R and PD-1 blockade. Although the two MC38 models exhibited a similar

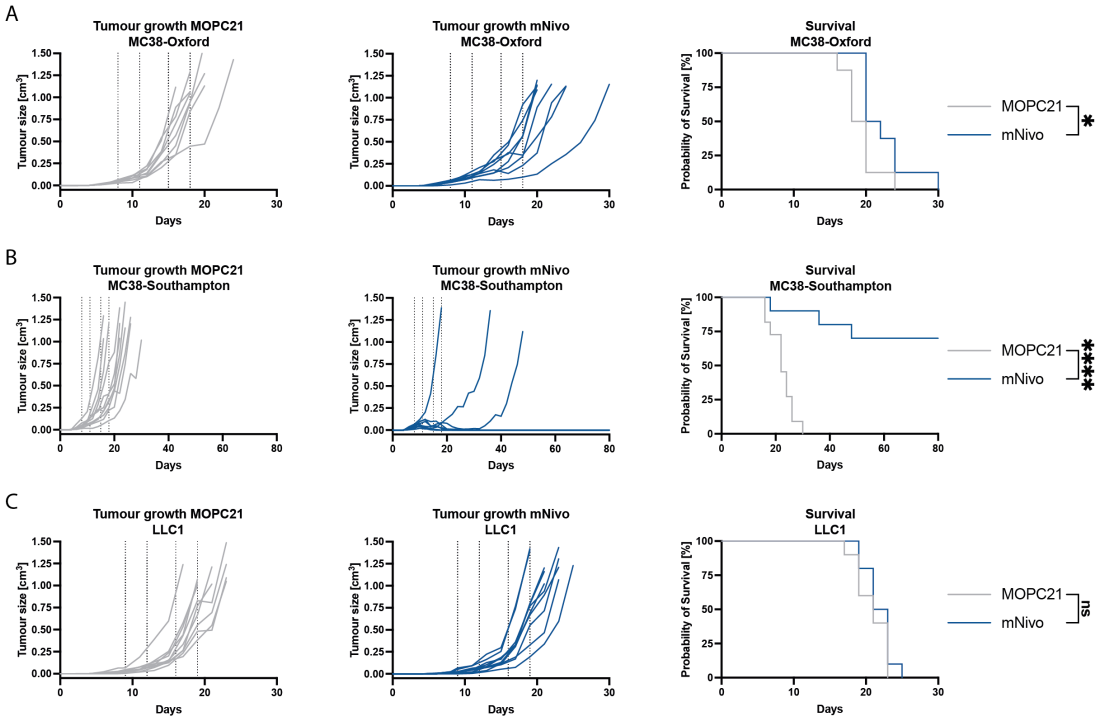


Figure 3.6: *In vivo* response to mNivo in MC38 and LLC1 tumours
Different cell lines were subcutaneously injected into hPD-1/hCD200R mice. Once the average tumour volume had reached a certain threshold, treatment with MOPC21 or mNivo was initiated. Treatment dosage was 200 µg and treatment regimen was twice a week for two weeks, indicated by dashed lines. All experiments were randomised and blinded. n = 10/group
(A) MC38-Oxford cells (5×10^5) were injected subcutaneously. Treatment was started on day 8, once the average tumour volume exceeded 40 mm^3.
(B) MC38-Southampton cells (5×10^5) were injected subcutaneously. Treatment was started on day 8, once the average tumour volume exceeded 40 mm^3.
(C) LLC1 cells (1×10^5) were injected subcutaneously. Treatment was started on day 9, once the average tumour volume exceeded 20 mm^3.
The data shown here were published by Fellermeyer *et al.*[1].

composition of immune cells in the TME (Figure 3.5 B), they differed strikingly in their response to mNivo monotherapy. Interestingly, MC38-Southampton cells expressed CD200, which was absent on all other cell lines tested (Figures 3.4 C and 3.5 A). Expression of the ligand of CD200R might provide an additional route to inhibit infiltrating immune cells.

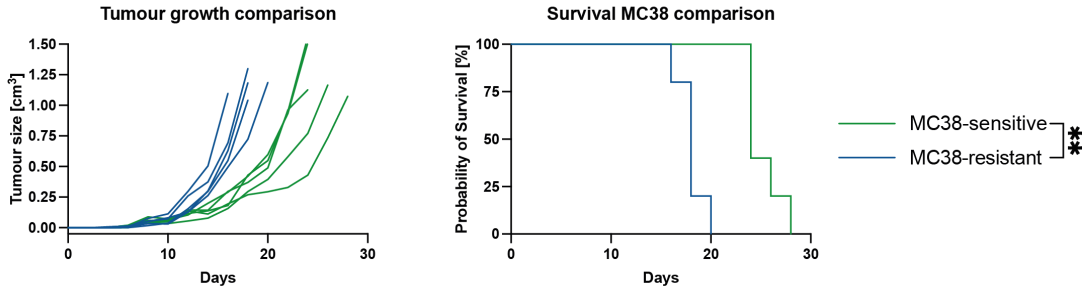


Figure 3.7: *In vivo* growth of MC38-sensitive and -resistant tumours
MC38-sensitive and MC38-resistant cells (5×10^5) were subcutaneously injected into hPD-1/hCD200R mice. Tumour volume was measured every other day using caliper. Tumour growth and survival curves are shown. n = 5/group

3.2.9 *In vivo* comparison of different MC38 cell lines

While both MC38 cell lines were validated through STR profiling, this does not exclude a certain genetic or epigenetic drift over time. Therefore, a direct *in vivo* comparison of the two cell lines was important.

First, MC38-sensitive and MC38-resistant cells were injected into hPD-1/hCD200R mice and the tumour size was measured every other day. While both tumour models demonstrated a rapid growth rate, MC38-resistant tumours grew significantly faster with all mice needed to be culled by day 20, in contrast to day 28 for MC38-sensitive tumours (Figure 3.7).

Second, in order to investigate whether the cell lines expressed similar neoantigens, indicating genetic similarity, rechallenge experiments were conducted. To confirm that there is immunological memory upon complete rejection of MC38-sensitive tumours, mice were first rechallenged with the same cell line. As previously reported[238], mice that exhibited a CR were protected from subsequent challenges with the same cell line (Figure 3.8 A). Importantly, injection of naïve mice at the same time demonstrated normal growth of MC38 tumours. In contrast, no difference between naïve and survivor mice was observed upon subcutaneous injection with LLC1 cells, a cell line that should not share any epitopes with MC38 cells (Figure 3.8 B). Finally, rechallenge with MC38-resistant cells displayed a mixed effect (Figure 3.8 C). When injected with large numbers of MC38-resistant cells (5×10^5), no difference in tumour growth was observed between the two

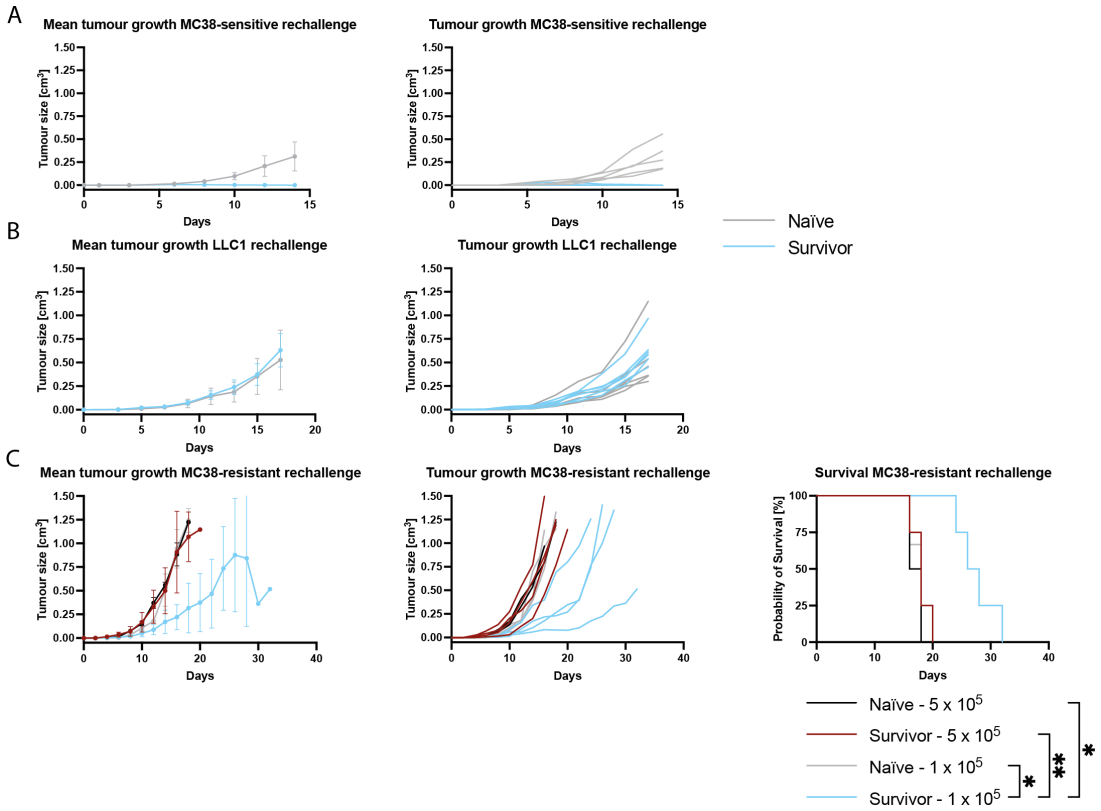


Figure 3.8: Rechallenge of MC38-sensitive survivors with tumour models
MC38-sensitive cells were subcutaneously injected into hPD-1/hCD200R mice. Mice that completely rejected the tumour during their treatment were taken forward for the rechallenge experiment. After a minimum of 65 days post tumour injection, surviving mice as well as naïve control mice were rechallenged on the other flank with different cell lines and tumour growth was monitored. No subsequent treatment was administered.
(A) Mice were rechallenged on day 83 with MC38-sensitive cells (5×10^5). n = 5-7/group
(B) Mice were rechallenged on day 65 with LLC1 cells (1×10^5). n = 6/group
(C) Mice were rechallenged on day 77 with MC38-resistant cells. n = 2-4/group

groups. In contrast, reducing the cell number to 1×10^5 produced a significantly reduced tumour growth in survivor, but not in naïve mice.

Taken together, while mice that rejected an initial challenge with MC38-sensitive cells were protected from a subsequent challenge with the same cell line, this was not observed for the rechallenge with LLC1 and MC38-resistant models. Importantly, rechallenge with a low-dose of MC38-resistant cells led to a significant delay in tumour growth, indicating that there is some immunological memory present that managed to slow down tumour progression. Strikingly, while these two cell lines are indeed genetically similar (as proven by STR profiling

and immunological memory), they differed significantly in their *in vivo* growth (Figure 3.7) and response to anti-PD-1 therapy (Figure 3.6).

3.2.10 Differential gene expression analysis of MC38 cell lines

A PD-1 blockade-resistant MC38 cell line has been described previously by Bernardo *et al.*[300]. In that report, referred to as 'Sanofi study', MC38 cells were injected subcutaneously into C57BL/6J mice and treated with an anti-PD-1 antibody (clone RMP1-14). Treated tumours were excised and passaged *in vitro* for subsequent *in vivo* injection. After three rounds of serial *in vitro* and *in vivo* passaging, the derived cell line was resistant to PD-1 blockade. The authors demonstrated that MHC-I, PD-L1 as well as their responsiveness to IFN-γ treatment was unaffected. Furthermore, they performed bulk RNA sequencing on *in vitro* and *in vivo* grown cells to obtain an unbiased idea of the deregulated pathways in resistant MC38 cells, demonstrating activation of the TGF-β and Notch pathway[300]. Using these insights, the authors designed a novel combination therapy of anti-PD-1, anti-TGF-β antibodies and the Notch1 inhibitor LY3039478, which resulted in significantly improved survival in the PD-1 blockade-resistant model[300].

In order to compare our MC38 models with those from the Sanofi study, the MC38-sensitive and -resistant cells were cultured *in vitro* without any further treatment and RNA was isolated and sent for bulk RNA sequencing. This dataset is referred to as the 'Oxford study'. All RNA-seq analysis described below was performed using an in-house script written by Sumana Sharma. Reanalysis of the Sanofi *in vitro* dataset[300] confirmed the upregulation of the TGF-β pathway in PD-1 blockade-resistant cells (Figure 3.9 B). Furthermore, other immune-related signalling pathways were also found to be enriched, including TNF, NF-κB and NOD-like receptor. In the dataset derived from our models, TNF and NOD-like receptor signalling were also in the ten most enriched pathways in

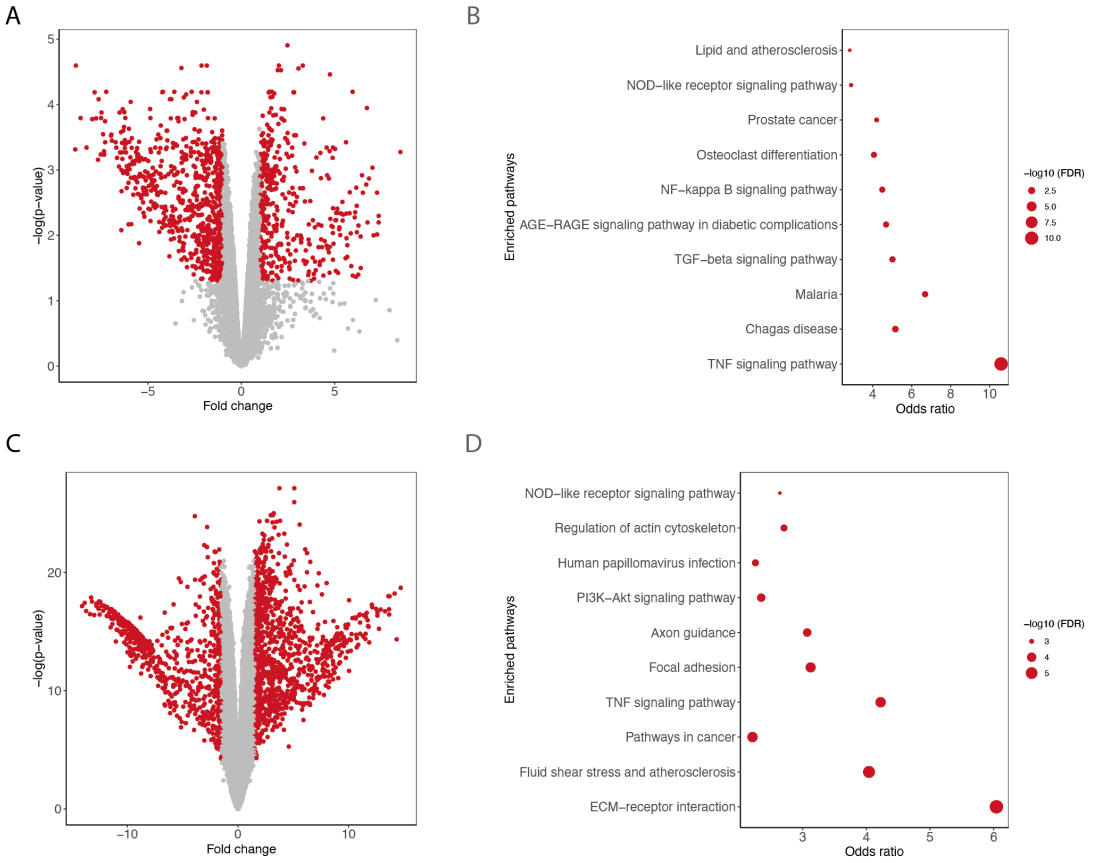


Figure 3.9: *In vitro* RNA sequencing of MC38-sensitive and -resistant cells
Differential gene expression analysis of MC38-sensitive and -resistant cells. RNA sequencing data from the Sanofi study[300] as well as the Oxford study were analysed.
(A and C) Volcano plot of differentially expressed genes in the Sanofi (A) and the Oxford dataset (C). Red dots indicate significant changes.
(B and D) KEGG-pathway analysis of upregulated genes identified in the Sanofi (B) and the Oxford study (D).

resistant MC38 cells (Figure 3.9 D), but apart from this there were no obvious overlaps between the two datasets.

To get an better overview of the differences and similarities between the four cell lines across the two datasets, log-fold changes (LFC) of all genes were compared (Figure 3.10 A). If the same genes were down- or upregulated, they would cluster in the bottom left and top right corner, respectively. However, little clustering was observed, indicating that individual genes are not commonly deregulated. In accordance with this, Venn diagrams comparing significantly up- or downregulated genes (Figure 3.10 B and C) did not demonstrate a large overlap between the two studies (2 % and 1 %, respectively).

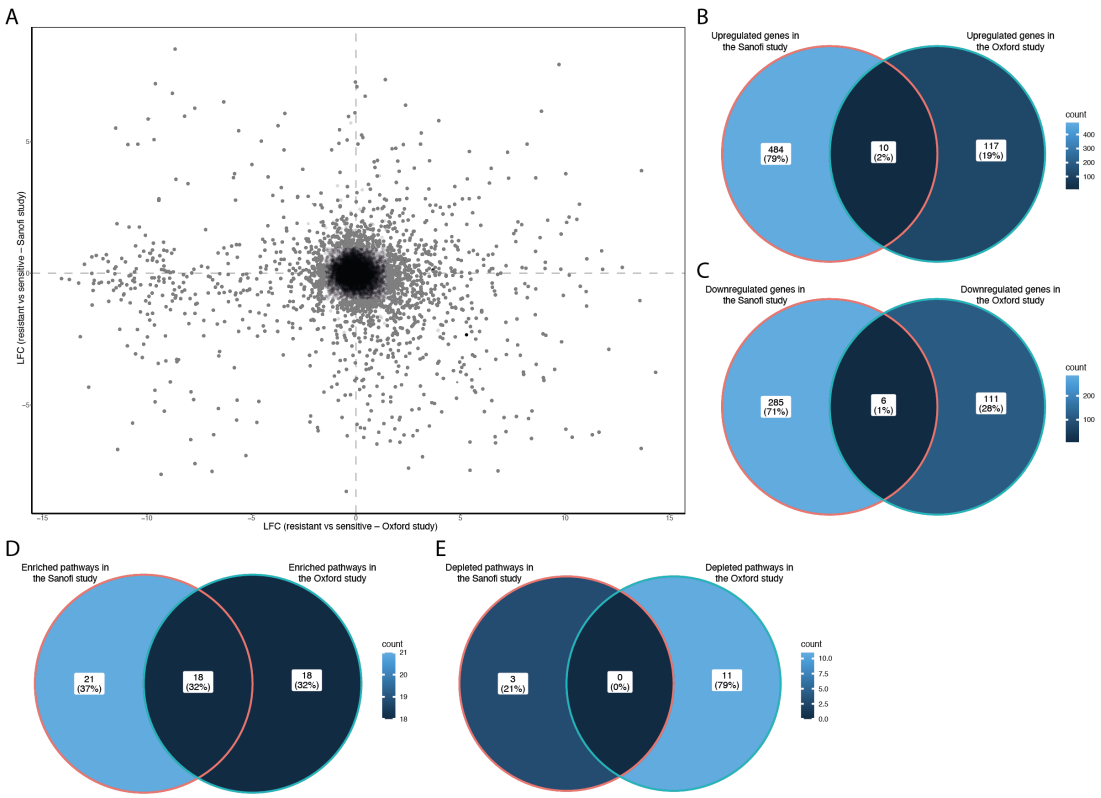


Figure 3.10: Comparison of deregulated genes and pathways in different datasets
Comparison of differentially expressed genes as well as deregulated pathways between two different datasets. Data were taken from the Sanofi study[300] and the Oxford study.
(A) Log-fold changes (LFC) of MC38-sensitive vs. MC38-resistant cells were compared between the two datasets.
(B and C) Venn diagrams comparing the significantly up- (B) or downregulated (C) genes between the two studies.
(D and E) Venn diagrams comparing the significantly enriched (D) or depleted (E) KEGG pathways between the two studies.

In contrast, comparing all significantly deregulated pathways (adjusted p-value ≤ 0.1) revealed a surprising overlap of commonly enriched pathways in PD-1 blockade-resistant MC38 cells (Figure 3.10 D), but not depleted pathways (Figure 3.10 E). Around half of all enriched pathways found in the Oxford study and the Sanofi dataset were shared. This indicates that different PD-1 blockade-resistant MC38 models might use common pathways to achieve resistance, albeit without relying on the same genes.

3.2.11 Identification of common pathways in resistant MC38 cells

The eighteen significantly enriched and overlapping pathways of both datasets are shown in Figure 3.11 A. Of note, the 'Ras signaling pathway' was not significantly enriched in either dataset but was found in the subsequent STRING network analysis discussed below and was included for colour coding. Comparison of the significance of pathway enrichment between the Oxford and Sanofi dataset revealed less significant enrichment in the latter one, with the exception of 'TNF signaling pathway' and 'Malaria'. This also required the use of an increased threshold for the adjusted p-value from 0.05 to 0.1.

In order to find commonly enriched pathways in PD-1 blockade-resistant MC38 cells, the upregulated genes (LFC ≥ 1.5 and adjusted p-value ≤ 0.05) from enriched KEGG pathways were further analysed. Genes from both studies, the Sanofi (80 genes)[300] and Oxford (175 genes) dataset, were retrieved. In line with the previous observation that the two studies shared only a few upregulated genes (Figure 3.10 B), there was little overlap with only 23 genes in common. Protein-protein interactions of the 232 hits were investigated using STRING analysis (`https://string-db.org`)[310]. A full STRING network excluding textmining was built with a high confidence threshold for the interaction score (≥ 0.7). The Markov Cluster (MCL) algorithm was used to divide the interactions into different clusters (inflation parameter 1.5) and clusters with more than ten nodes were further investigated (Figure 3.11 B). From each cluster, the KEGG pathway with the lowest false discovery rate (FDR) was used to colour the respective nodes. Cluster 1 was by far the biggest group comprising 37 genes and was significantly enriched in 'ECM-receptor interactions' (FDR = 1.52×10^{-37}, coloured in red). Clusters 2, 3 and 4 included 15, 14 and 11 genes, respectively. The KEGG terms corresponded to different signalling pathways, i.e. MAPK (FDR = 1.69×10^{-13}, coloured in green), TNF (FDR = 5.98×10^{-18}, coloured in blue) and Ras signalling pathway (FDR = 5.26×10^{-20}, coloured in yellow). As the Ras GTPase is responsible for the activation of the MAP3K Raf, triggering

A

KEGG group	KEGG pathway	Adjusted p-value Oxford	Adjusted p-value Sanofi
Cellular processes	Focal adhesion	**** (5.11E-05)	* (4.34E-02)
Environmental information processing	Cytokine-cytokine receptor interaction	* (6.45E-02)	* (4.34E-02)
Environmental information processing	ECM-receptor interaction	**** (1.08E-06)	* (7.64E-02)
Environmental information processing	MAPK signaling pathway	* (2.88E-02)	* (4.36E-02)
Environmental information processing	PI3K-Akt signaling pathway	*** (2.14E-04)	* (7.64E-02)
Environmental information processing	*Ras signaling pathway*	ns (4.22E-01)	ns (8.11E-01)
Environmental information processing	TNF signaling pathway	**** (3.95E-05)	**** (4.30E-11)
Human diseases	AGE-RAGE signaling pathway in diabetic complications	** (1.13E-03)	* (1.09E-02)
Human diseases	Fluid shear stress and atherosclerosis	**** (7.16E-06)	* (8.22E-02)
Human diseases	Human papillomavirus infection	*** (4.81E-04)	* (7.64E-02)
Human diseases	Malaria	* (8.06E-02)	** (9.46E-03)
Human diseases	Pathways in cancer	**** (3.95E-05)	* (4.31E-02)
Human diseases	Proteoglycans in cancer	** (5.41E-03)	* (7.68E-02)
Human diseases	Rheumatoid arthritis	* (7.70E-02)	* (7.64E-02)
Organismal systems	Axon guidance	*** (2.03E-04)	* (5.35E-02)
Organismal systems	NOD-like receptor signaling pathway	** (1.13E-03)	* (3.93E-02)
Organismal systems	Osteoclast differentiation	* (8.92E-02)	* (1.09E-02)
Organismal systems	Relaxin signaling pathway	* (6.32E-02)	* (5.86E-02)
Organismal systems	Toll-like receptor signaling pathway	* (8.06E-02)	* (5.35E-02)

B

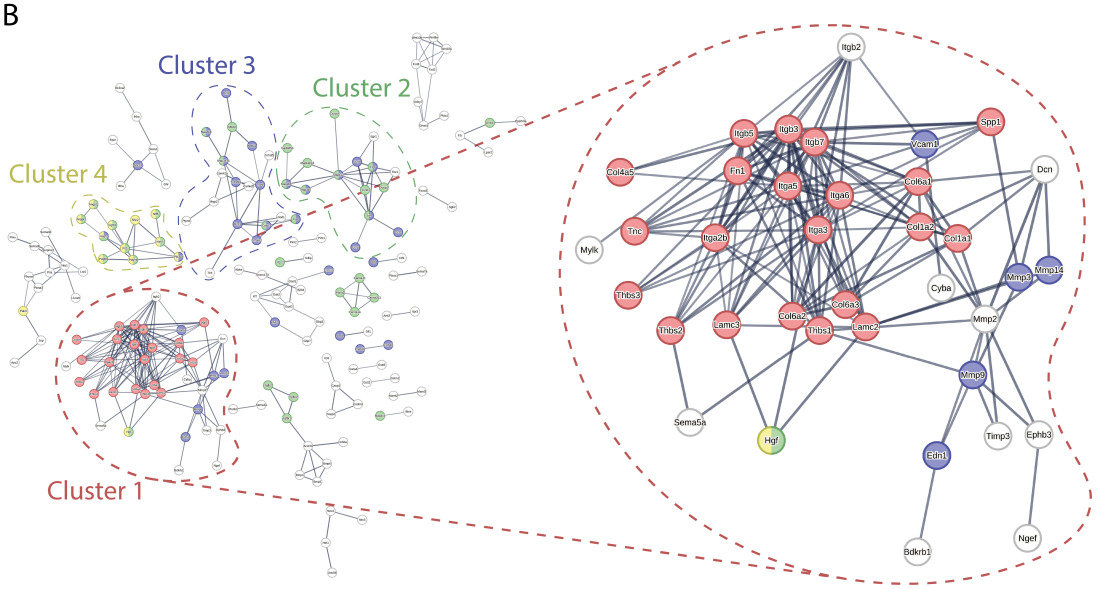


Figure 3.11: Identification of commonly enriched pathways in PD-1 blockade-resistant MC38 cells

(A) Commonly enriched pathways are sorted by alphabetical order of the corresponding KEGG group. Adjusted p-values of the Oxford and Sanofi dataset[300] are shown. Coloured KEGG pathways correspond to the clusters identified in (B). 'Ras signaling pathway' was not commonly enriched, but was included for colour coding purposes. Adjusted p-value $\leq 0.1 = *$, $\leq 0.01 = **$, $\leq 0.001 = ***$, $\leq 0.0001 = ****$

(B) STRING network of all upregulated genes from the enriched pathways of both datasets. MCL clustering was used to separate the different clusters. Clusters with more than ten nodes were highlighted and coloured corresponding to the KEGG pathway with the lowest FDR within this cluster.

the MAPK pathway[311], the overlap of the Ras-MAPK clusters was expected (Figure 3.11 B). Similarly, TNF and MAPK pathways, e.g. p38 MAPKs, are known to interact and stimulate each other[312].

As the Oxford dataset contributed more genes towards this analysis (175 compared to 80), it was important to test whether the identified pathways were disproportionally enriched. Table 3.1 summarises the contribution of the Oxford or Sanofi dataset to each cluster and a comparison of all genes was included as a reference. Only Cluster 4, which was highly enriched for the 'Ras signaling pathway', was disproportionally driven by the Oxford dataset. However, most of the genes within Cluster 4 also mapped to the MAPK pathway (FDR = 7.90×10^{-14} in Cluster 4), potentially suggesting that this is not a novel pathway identified but rather resembles the known overlap of Ras/MAPK signalling[311]. Overall, this analysis demonstrated that the reported pathways might indeed reflect common mechanisms of acquired resistance to PD-1 blockade in MC38 cells. Of note, as there was a small overlap of hits in each cluster, the reported percentages in Table 3.1 do not add up to 100 %.

Table 3.1: Contribution of the Oxford and Sanofi dataset to identified clusters

Group	Oxford dataset	Sanofi dataset	Overlap
All genes	75.43 %	34.48 %	9.91%
Cluster 1	75.68 %	35.14 %	10.82%
Cluster 2	66.67 %	46.67 %	13.34%
Cluster 3	57.14 %	57.14 %	14.28%
Cluster 4	90.91 %	27.27 %	18.18%

The largest cluster was highly enriched in genes of 'ECM-receptor interaction' pathways (FDR = 1.52×10^{-37}), with several collagens, integrins, matrix metalloproteinases and thrombospondins upregulated in PD-1 blockade-resistant cells (Figure 3.11 B). Extracellular matrix (ECM) remodelling as well as the mentioned protein families have been linked to cancer development[313–315], making them an attractive target for therapy[313,315,316]. Importantly, there is an increasing

number of reports associating these ECM components with immune-modulatory properties[314,317,318], providing a potential mode of action for the observed PD-1 blockade resistance.

3.3 Discussion

The work described in this chapter has set the foundation for this thesis to investigate novel improvements of immune-checkpoint inhibitors to treat cancer.

First, an antibody expression pipeline was established that allowed the production of high-quality, endotoxin-free antibodies at great scale. These antibodies were shown to bind to their respective targets as well as to lymphocytes from mice humanised for CD200R and PD-1. While the affinity of nivolumab is reported to be around 3 nM[104,319], the results reported in Section 3.2.4 were lower at around 12-23 nM, depending on whether single- or multi-cycle analysis was used. The discrepancy within this thesis already demonstrates that due to the high sensitivity of SPR small changes can considerably influence the results. Furthermore, the study by Bristol-Myers Squibb used SPR as well as Bio-layer interferometry (BLI), however the BLI measurements were 1000-fold lower at around 3 pM[319]. Thus, comparison of SPR/BLI measurements between different methods, machines or technologies are challenging. More importantly, immobilisation of nivolumab hIgG4 biosimilar resulted in a nearly identical sensorgram compared to the produced nivolumab mIgG1 (Figure 3.2 B), clearly demonstrating that the antibody binding capacity was unchanged for the 'murinised' form of the antibody. For OX108, there is no reported affinity measurement to compare the results with, but a K_D of approximately 84 nM is a rather low-affinity interaction.

Second, baseline characteristics of three different cell lines (MC38-Oxford, MC38-Southampton and LLC1) were investigated with the aim to find a 'hot' and 'cold' tumour model, as outlined in the introduction to this chapter (Section 3.1). As there was already preliminary data available for the colorectal cancer model MC38 (Section 1.5), one of the primary aims was to establish this tumour model.

MC38 cells were provided by two different laboratories, whereas the LLC1 cell line was already available in the Cerundolo group. While there are some discrepancies within the literature regarding responsiveness to PD-1 blockade[309,320], the LLC1 model is generally considered to be a 'cold' tumour model that does not respond to anti-PD-1 therapy, whereas MC38 tumours are very immunogenic. While the LLC1 model was indeed resistant to PD-1 blockade, the two MC38 cell lines differed strikingly in their responsiveness (Section 3.2.8).

Finally, the two MC38 models were compared with *in vivo* tumour challenge and rechallenge experiments (Section 3.2.9) as well as *in vitro* gene expression analysis (Section 3.2.10). Importantly, they still share certain neoepitopes as demonstrated by the reduced tumour growth in mice that were rechallenged with MC38-resistant cells after completely rejecting an initial challenge with MC38-sensitive cells. Furthermore, comparison with another study that induced PD-1 blockade resistance in MC38 cells through serial *in vitro* and *in vivo* passaging revealed an approximately 50 % overlap of enriched KEGG pathways between the two resistant models. In an effort to further investigate the common drivers of resistance, upregulated genes from enriched pathways from both datasets were analysed using a STRING protein-protein network (Section 3.2.11). There were significantly more genes deregulated in the Oxford dataset compared to the Sanofi dataset (Figures 3.9 A and C). This was expected as the two cell lines in our laboratory were provided by different sources, in contrast to the resistant MC38 cell line derived through serial passaging of a sensitive MC38 tumour treated with anti-PD-1 antibodies[300]. The identified clusters of the STRING network analysis highlighted the importance of ECM components and their immune-modulatory effect[314,317,318]. Furthermore, Ras, MAPK and TNF signalling pathways were significantly enriched in the pooled analysis of both datasets and immune-regulatory effects of these were reviewed elsewhere[321,322]. While there is plenty of evidence in the literature implicating the identified pathways with immunoregulatory functions, further investigation and validation is needed. For example, MAPK and Ras signalling might also 'simply' contribute

to anti-PD-1 therapy resistance through increasing cell proliferation[311], without direct immunosuppressive effects on infiltrating immune cells.

What you do makes a difference, and you have to decide what kind of difference you want to make.

— Jane Goodall

4

Combination therapy of nivolumab mIgG1 and OX108

Contents

4.1 Rationale 108
4.2 Results 109
4.2.1 *In vitro* validation of mNivo and OX108 109
4.2.2 Combination therapy in LLC1 tumours 113
4.2.3 Immune cell infiltration in LLC1 upon treatment . . . 115
4.2.4 Combination therapy in PD-1 blockade-sensitive MC38 tumours 115
4.2.5 Immune cell infiltration in MC38-sensitive tumours upon treatment 117
4.3 Discussion 123

4.1 Rationale

THERE is an increasing number of combinations trialled to improve on anti-PD-1 monotherapy[292]. Most immune-checkpoint inhibitors target cytotoxic T cells, which are responsible for tumour killing, in order to reactive them. However, myeloid cells are highly abundant in tumours and can have tumouricidal as well as pro-tumourigenic functions[142]. The cross-talk of myeloid cells, such as DCs, with T cells is crucial in mounting an immune response during

infections, but also tumour development[9]. Thus, targeting myeloid cells can have beneficial effects in several ways. Pro-tumourigenic macrophages can be re-educated towards a more pro-inflammatory phenotype by blocking CXCR2[323] or depleted through treatment with CSF1/CSF1R inhibitors[283]. Alternatively, tumour-cell phagocytosis can be triggered through administration of anti-CD47 antibodies[285] or DCs can be activated by CD40 agonists[278].

CD200R (introduced in Section 1.2.4.3) is an inhibitory immune receptor predominantly found on myeloid cells, therefore providing another potential target that could synergise with PD-1 blockade. While murine studies have yielded conflicting results on whether CD200R is tumouricidal[174,175] or tumour-promoting[170–172], human studies and the development of CD200/CD200R blockers in clinical trials clearly suggest a pro-tumourigenic role of CD200R[186,194]. Thus, the work described in this chapter investigated the potential of combining mNivo (nivolumab mIgG1) with the anti-CD200R blocking antibody OX108. Using mice humanised for PD-1 and CD200R allowed for direct testing of the anti-human antibodies in mouse tumour models.

The PD-1 blockade-sensitive as well as -resistant model MC38 and LLC1 were established in Chapter 3. As discussed in Section 3.2.1, all antibodies were produced as D265A mutants, thereby reducing binding to FcγRs[212]. Thus, this mutation is not further referred to in this chapter.

4.2 Results

4.2.1 *In vitro* validation of mNivo and OX108

First, a T-cell stimulation assay was established to test the blocking and activatory capacity of the produced antibodies *in vitro*. The group of Peter Steinberger (University of Vienna) created a Jurkat-reporter cell line that expresses GFP under an NF-κB promoter[298]. Jurkat T cells are stimulated with T-cell stimulator cells (TCS, BW5147 mouse T cells) which express a membrane-bound anti-CD3-scFv (OKT3). Transduction of Jurkat cells and TCS with different receptor-ligand pairs allows the investigation of antibody-induced changes in activation, measured

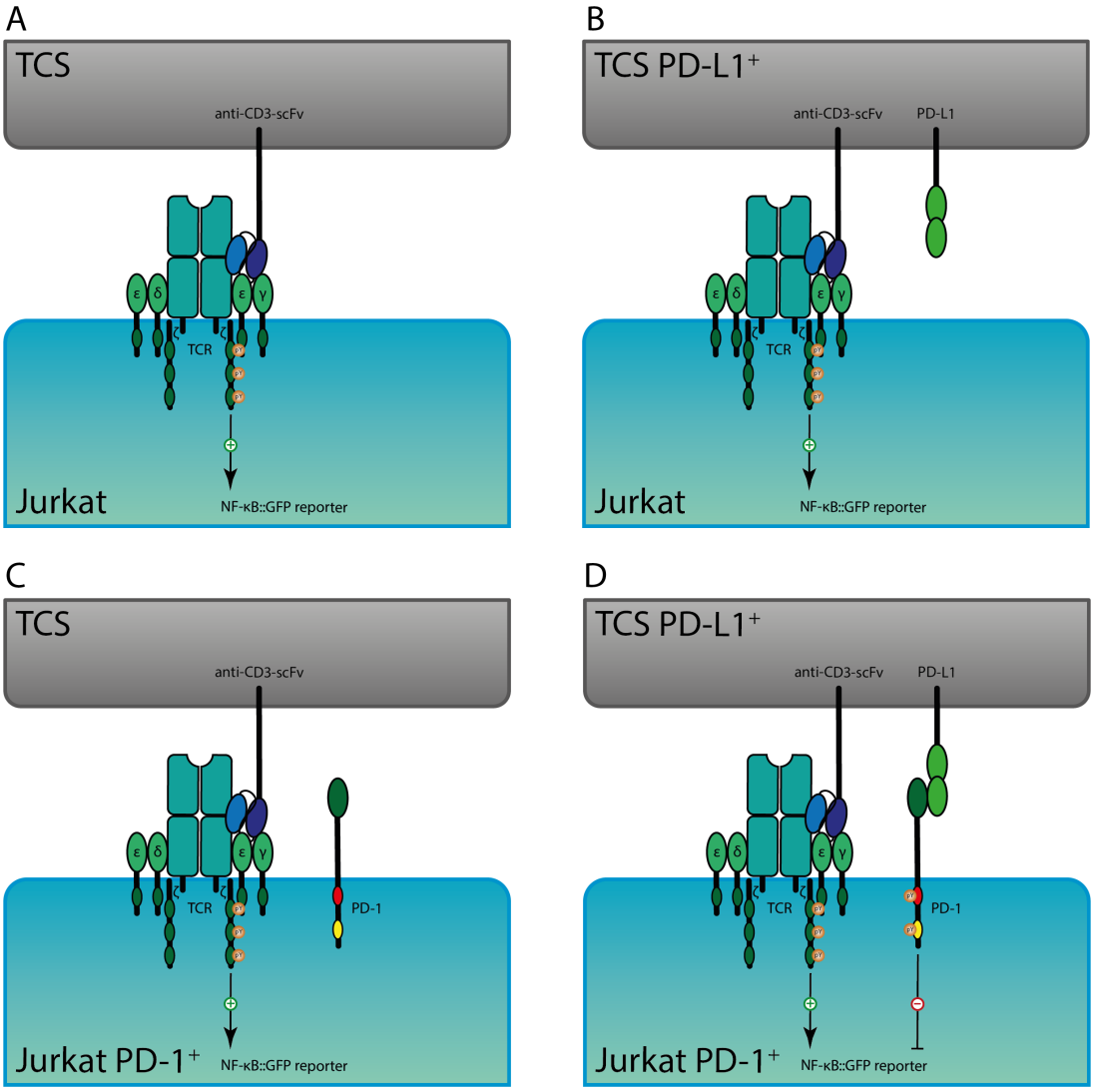


Figure 4.1: *In vitro* T-cell activation assay
Illustration of the setup and different combinations of the two-cell activation assay. Only the combination of Jurkat PD-1$^+$ with TCS PD-L1$^+$ cells (D) results in the downstream activation of PD-1, leading to reduced Jurkat T-cell activation and therefore diminished GFP expression. Figure was adapted from Jutz *et al.*[298].

by GFP, in this simple two-cell system. An illustration depicting the setup of this assay for PD-1/PD-L1 is given in Figure 4.1. Cells are co-incubated for 16-24 hours and TCS cells are excluded by staining with an anti-mCD45 antibody, gating on the negative population (Jurkat cells). Data are analysed by dividing the GFP MFI of the respective condition with the GFP MFI of the corresponding Jurkat cells without TCS cells, giving the fold induction compared to the baseline Jurkat-cell activation level.

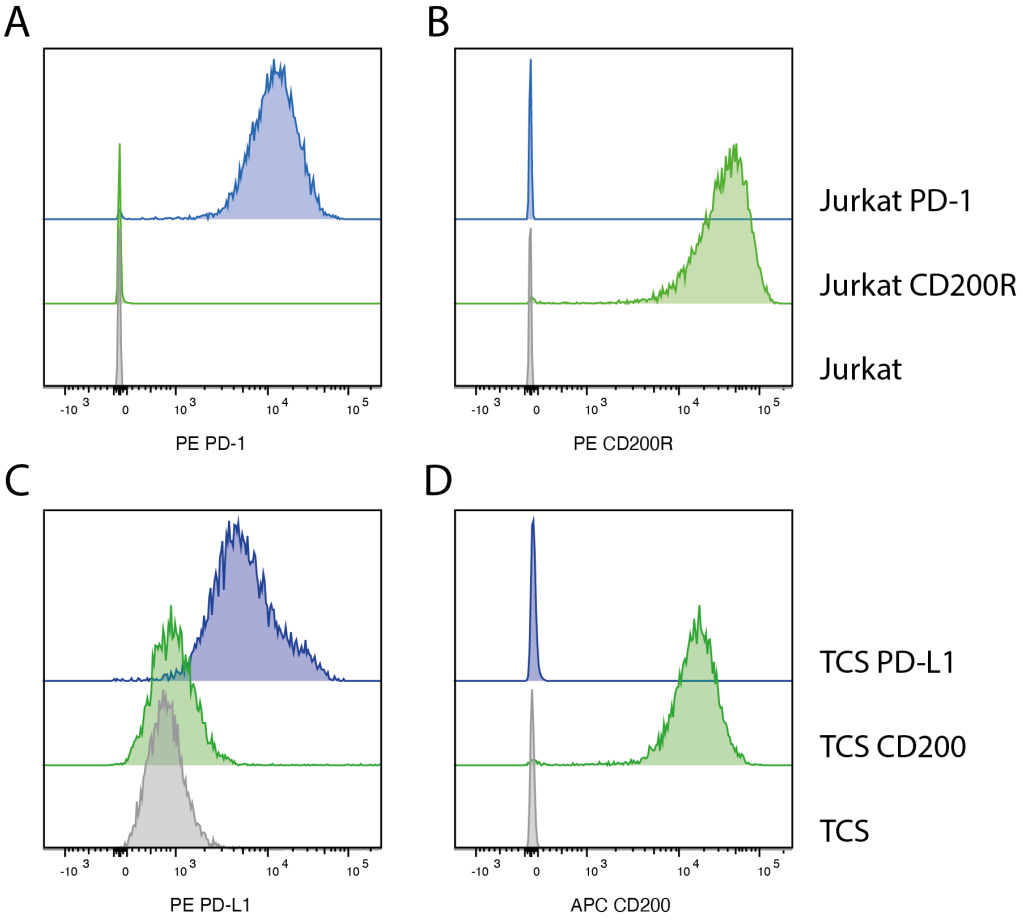


Figure 4.2: Expression levels of respective proteins on Jurkat and TCS cells Expression levels of PD-1 (A), PD-L1 (C), CD200R (B) and CD200 (D) on all used Jurkat and TCS cell lines.

Jurkat, Jurkat PD-1$^+$, TCS as well as TCS PD-L1$^+$ cells were kindly provided by Peter Steinberger. In order to assess the activity of OX108, the CD200R blocking antibody used in this study, a new cell system was created. A chimeric protein comprising the extracellular and transmembrane domains of CD200R and the cytoplasmic domain of PD-1 (sequence provided in Section A.1.1) was transduced into Jurkat cells, while CD200 was upregulated on TCS cells (sequence provided in Section A.1.2). The creation of a chimeric CD200R-PD-1 protein was advised by Christopher Paluch (MiroBio Ltd.) as the CD200R signalling domain only leads to very slight inhibition in Jurkat cells (personal communication). All cell lines were confirmed to express the corresponding protein as demonstrated in Figure 4.2.

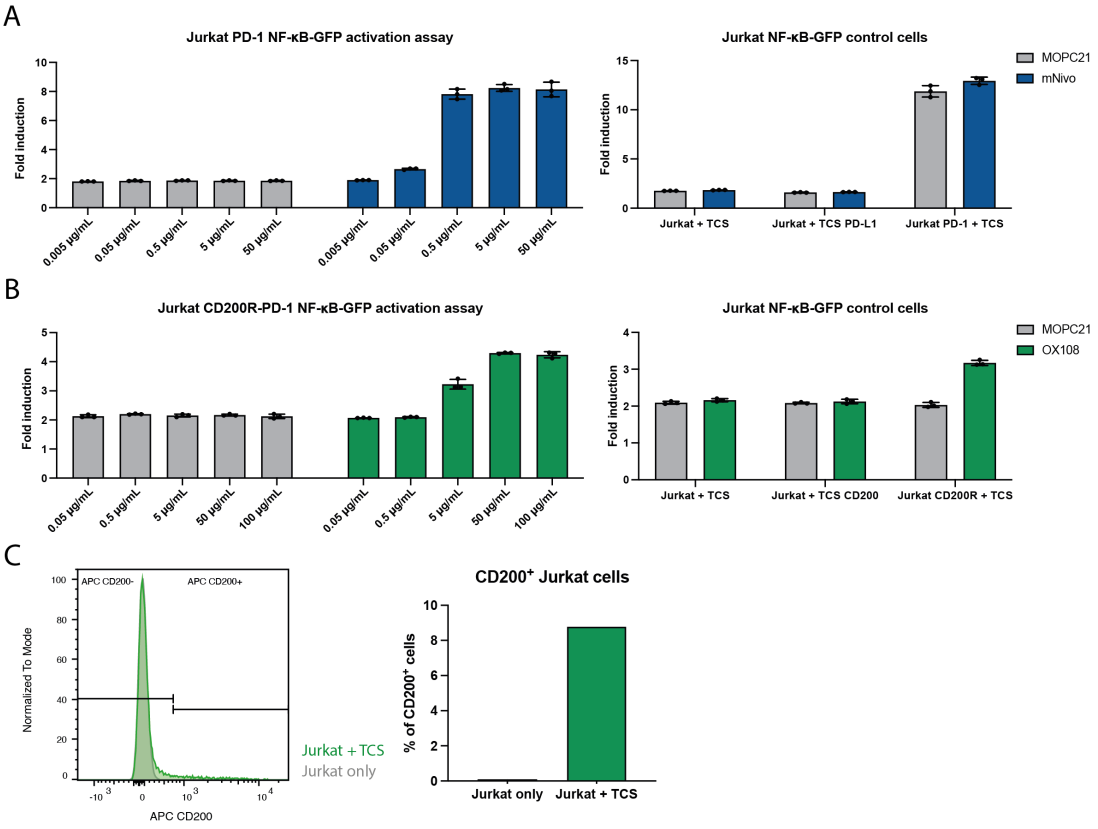


Figure 4.3: *In vitro* blockade validation of mNivo and OX108
(A) Left: Jurkat PD-1$^+$ NF-κB-GFP cells were co-cultured with TCS PD-L1$^+$ and varying concentrations of MOPC21 or mNivo. Right: Control cultures using Jurkat, Jurkat PD-1$^+$, TCS and TCS PD-L1$^+$ cells. Data are representative of three independent repeats.
(B) Left: Jurkat CD200R-PD-1$^+$ NF-κB-GFP cells were co-cultured with TCS CD200$^+$ and varying concentrations of MOPC21 or OX108. Right: Control cultures using Jurkat, Jurkat CD200R$^+$, TCS and TCS CD200$^+$ cells. Data are representative of three independent repeats.
(C) Jurkat cells were co-incubated with or without TCS and CD200 levels were subsequently measured by flow cytometry.
The data shown here were published by Fellermeyer *et al.*[1].

Next, mNivo, OX108 and MOPC21 were titrated into the corresponding Jurkat/TCS co-cultures. When the corresponding receptors and ligands were present on Jurkat and TCS cells, mNivo and OX108 demonstrated a dose-dependent fold induction of GFP, indicating increased T-cell activation (Figures 4.3 A and B, left panels). Thus, mNivo and OX108 can block the inhibitory receptor/ligand interaction between PD-1/PD-L1 and CD200R/CD200, respectively. The right panels of Figures 4.3 A and B show the control co-cultures where either the receptor

or ligand is missing, and therefore no effect of the antibodies was expected. Of note, different Jurkat cell lines can have a different activatory potential upon stimulation, likely due to varying levels of CD3 (personal communication from Sumana Sharma, University of Oxford), leading to a difference in the fold induction observed across cell lines. Similarly, TCS cells have varying capacity to stimulate Jurkat cells, making a comparison between different co-cultures difficult. Importantly, addition of mNivo did not enhance activation in these control setups (Figure 4.3 A, right panel). In contrast, there was an increase in Jurkat CD200R$^+$ cell activation upon treatment with OX108 when stimulated with TCS cells lacking CD200 (Figure 4.3 B, right panel). This might be explained by the reported upregulation of CD200 upon T-cell activation[159]. Indeed, after co-culture of Jurkat cells with TCS cells, the former expressed CD200, possibly leading to an inhibitory effect through CD200R (Figure 4.3 C).

4.2.2 Combination therapy in LLC1 tumours

Upon successful validation of the antibodies *in vitro* as well as establishment of the tumour models (Chapter 3), the combination therapy of mNivo and OX108 was tested in the PD-1 blockade-resistant model LLC1. The experimental outline is shown in Figure 4.4 A.

In accordance with the data from Section 3.2.8, mNivo monotherapy did not lead to a significant change in the tumour growth (Figure 4.4 B). Similarly, OX108 monotherapy as well as the combination of both antibodies had no effect on survival or tumour size, compared to MOPC21 isotype control (Figure 4.4 B). Although most tumours had reached the size threshold by day 23, there were a few individual tumours in all groups except MOPC21 that displayed a small reduction in tumour growth (tumour size at day 23 $\leq$ 0.5 cm^3 $\equiv$ 50 % of size threshold). While this was not a statistically significant effect, it prompted an analysis of the remaining tumours for a potential change in immune cell infiltration.

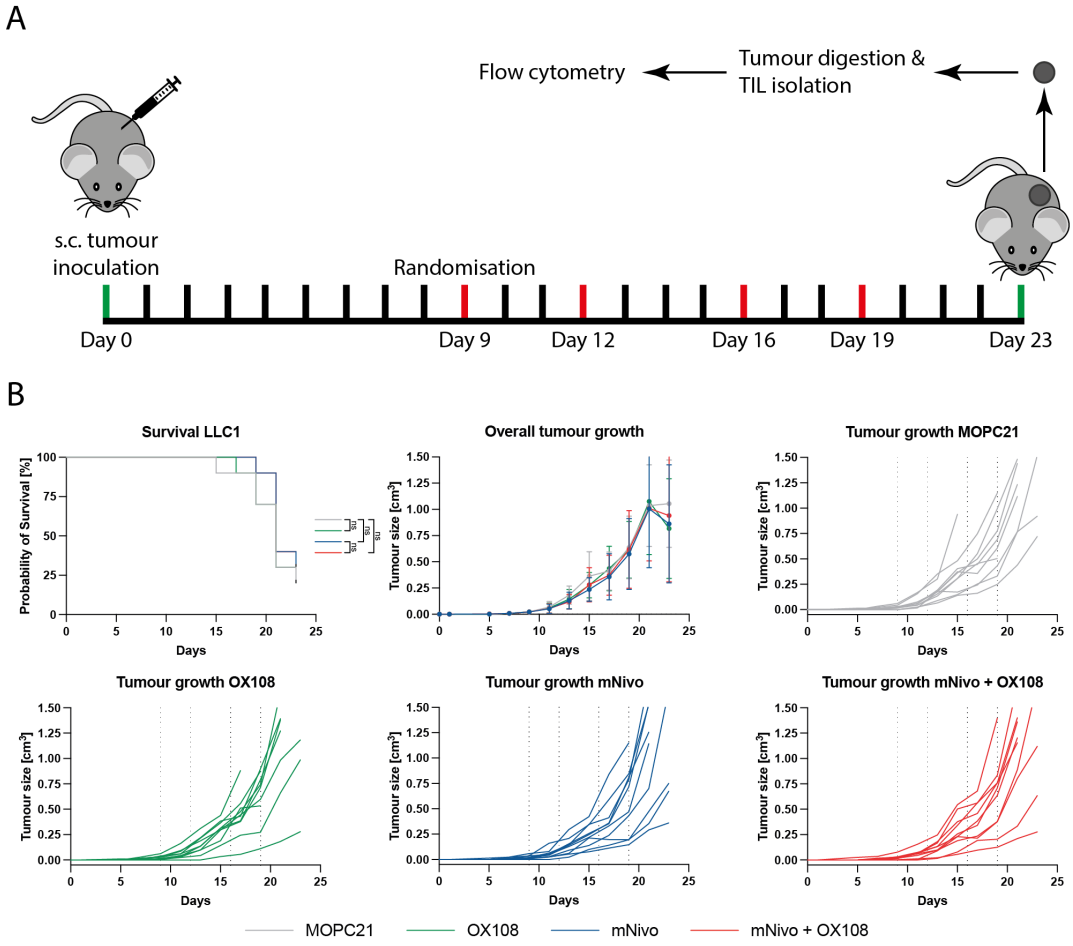


Figure 4.4: Combination therapy of mNivo and OX108 in LLC1 tumours
(A) Illustration depicting the experimental outline for the LLC1 tumour challenge. Mice were randomised once the average tumour volume reached 20 mm^3 (day 9). Mice were treated twice weekly for two weeks with 200 µg/antibody/treatment, indicated by red lines (A) or dashed lines (B). On day 23, all remaining mice were culled, tumours harvested, digested and immune cells isolated for flow cytometric analysis (Figure 4.5). (B) Survival and tumour growth curves of LLC1 tumours treated with MOPC21, OX108, mNivo and mNivo + OX108 are shown.
All experiments were randomised and blinded. n = 10/group
The data shown here were published by Fellermeyer *et al.*[1].

4.2.3 Immune cell infiltration in LLC1 upon treatment

On day 23, the surviving mice were culled and tumours were harvested for subsequent flow cytometric analysis. There were four, three, five and five mice remaining in the groups MOPC21, OX108, mNivo and mNivo + OX018, respectively. Upon harvest, tumours were digested and immune cells enriched by Ficoll-Paque density gradient centrifugation and subsequently stained using a lymphoid and myeloid flow cytometry panel (gating strategies shown in Figures 2.1 and 2.2). Figure 4.5 A shows all identified immune cells across the different treatments arms.

Most of the identified immune cells did not change, with exception of the OX108 treated tumours (Figure 4.5 A). Mice receiving the OX108 monotherapy exhibited a statistically significant reduction of M-MDSCs compared to mNivo and mNivo + OX108 as well as an increase in M2 macrophages compared to mNivo. However, as indicated above, this group only comprised of three animals. As these trends were not seen in the combination therapy, the observed effects might be explained by the low statistical power due to the small sample size. Comparing the respective immune cell abundance with the final tumour volume did not reveal any significant correlations (data not shown). Furthermore, the percentages of M1/M2 macrophages and $CD4^+/CD8^+$ T cells were not influenced by any of the treatments (Figure 4.5 B). Importantly, staining for CD200R using a commercial OX108-PE antibody demonstrated strongly reduced MFIs for all mice receiving OX108, either in monotherapy or in combination with mNivo (Figure 4.5 C). Thus, antibody penetration into the tumour was not an issue.

4.2.4 Combination therapy in PD-1 blockade-sensitive MC38 tumours

CD200R blockade did not enhance efficacy in the PD-1 blockade-resistant lung cancer model LLC1, neither did it lead to a significant reshaping of the immune TME. As mentioned in Section 3.1, it is important to test novel therapies in different models, i.e. ‘cold’ and ‘hot’ tumour models, as the observed effects can

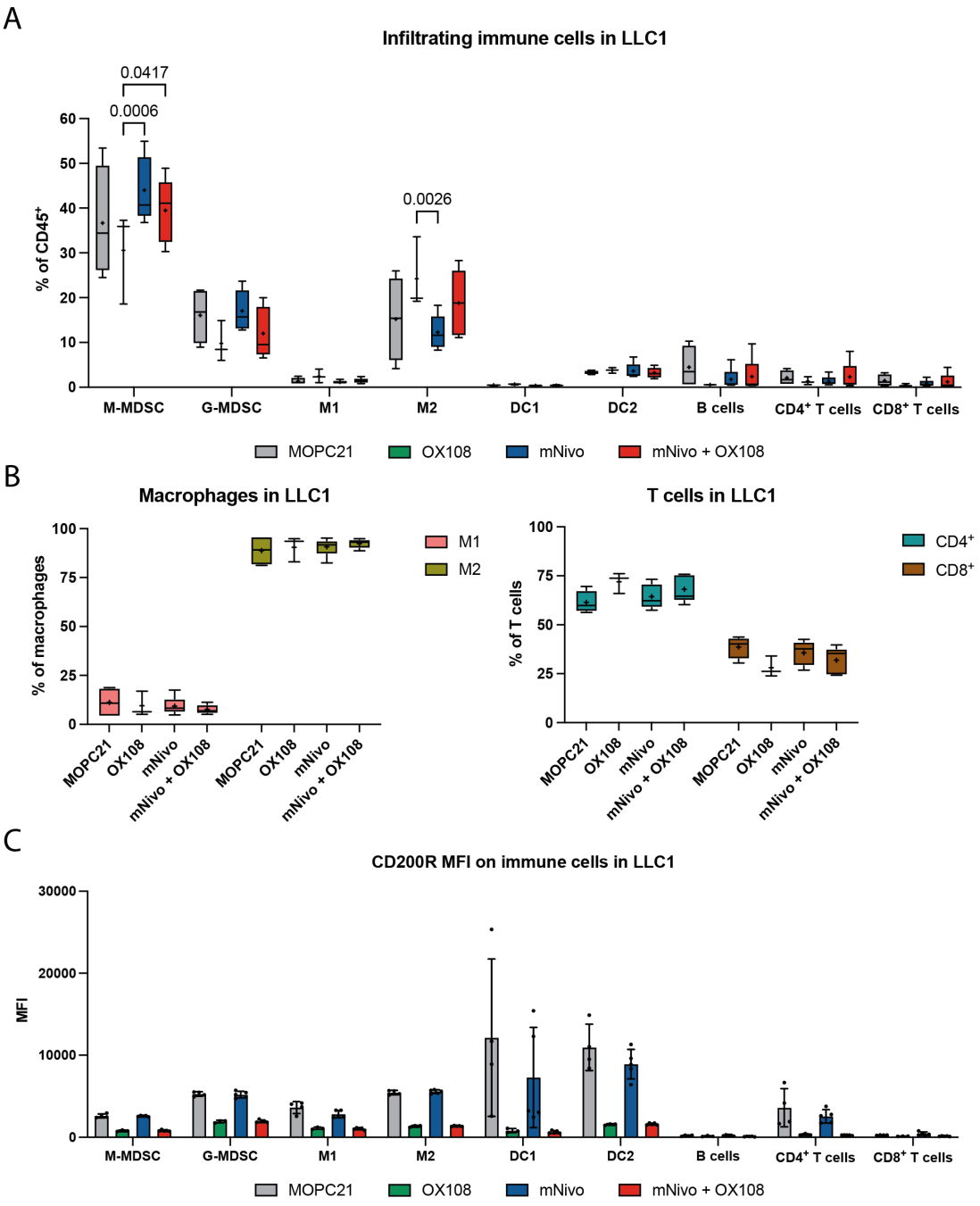


Figure 4.5: Immune cell infiltration in treated LLC1 tumours
Tumours were harvested and immune cells analysed by flow cytometric analysis.
(A) A myeloid and lymphoid flow cytometry panel was used to identify different immune cell subsets.
(B) Percentages of M1/M2 macrophages (left) and $CD4^+/CD8^+$ T cells (right panel).
(C) MFI of CD200R on identified immune cells.
For boxplots, the line shows the median, the '+' shows the mean. Whiskers display the 10-90 percentile. p-values are given for $p \leq 0.05$. For bar graphs, data are shown as mean ± SD.
The data shown here were published by Fellermeyer *et al.*[1].

differ greatly. Therefore, the anti-PD-1 therapy-sensitive colorectal cancer model MC38 was tested next. As some mice injected with MC38-sensitive cells and treated with mNivo will have a complete response (CR), the survival study and the flow cytometric analysis needed to be run separately. The survival study was run twice, whereas the analysis of infiltrating immune cells was repeated three times.

Figure 4.6 A shows the two independent repeats of the survival study separately. Importantly, the two studies were very similar, which allowed the pooling of the datasets, thereby increasing the sample size for statistical analysis (Figure 4.6 B). Thus, the pooled data will be discussed in the following section. As in the case of the LLC1 model, OX108 monotherapy had no effect on tumour growth and survival. In contrast, mNivo monotherapy resulted in a CR in 25 % of all mice. While some tumours completely escaped the therapy, resulting in similar growth compared to the MOPC21 isotype control, there was a subset of tumours that initially regressed, but started relapsing afterwards. Intriguingly, there seemed to be fewer tumours relapsing for the combination treatment, which resulted in a CR rate of 45 %. Although there was a trend for increased CRs in the mNivo + OX108 treated arm, this was not statistically significant ($p = 0.1848$). Importantly, similar results were obtained from the contract research organisation Crown Bioscience (Figure 1.8), indicating that while the potential effect is small, it could be reproduced three separate times in two different environments.

4.2.5 Immune cell infiltration in MC38-sensitive tumours upon treatment

In order to investigate whether CD200R blockade resulted in a change of the immune composition, experiments to compare the infiltrating immune cells upon treatment were undertaken. As some anti-PD-1 treated tumours will ultimately completely regress, mice were only treated twice and one day after the final treatment tumours were harvested and immune cells isolated (Figure 4.7 A). This experiment was repeated three times and the data were pooled.

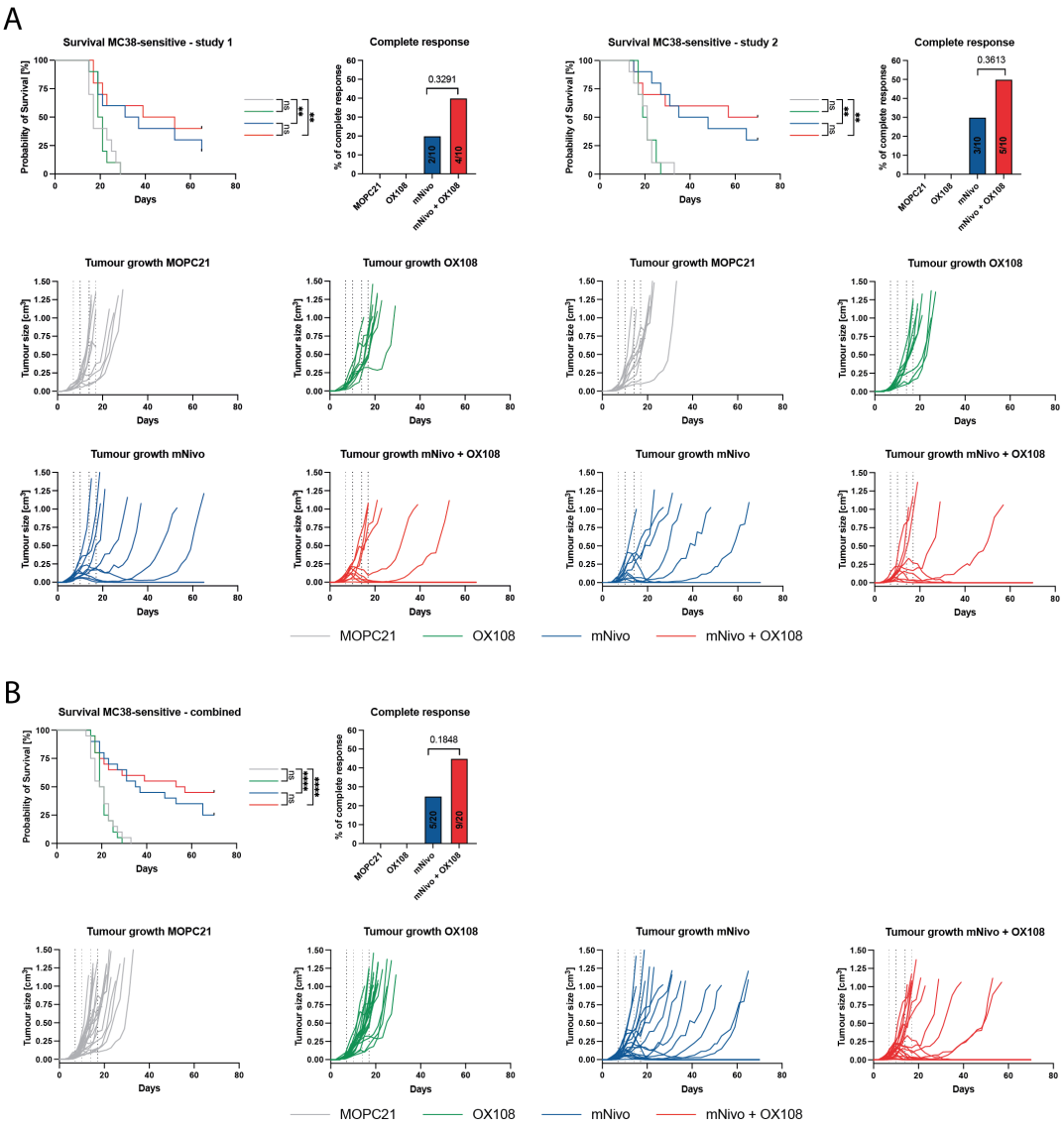


Figure 4.6: Combination therapy of mNivo and OX108 in MC38-sensitive tumours

Mice were randomised once the average tumour volume reached 40 mm^3 (day 7). Mice were treated twice weekly for two weeks with 200 µg/antibody/treatment, indicated by dashed lines. Survival and tumour growth curves of MC38-sensitive tumours treated with MOPC21, OX108, mNivo and mNivo + OX108 are shown. Once all tumours reached the size threshold or completely regressed, complete responses were assessed and compared using chi-square tests.

(A) The two independent repeats are plotted separately (left and right panel).

(B) Data were pooled and plotted together.

All experiments were randomised and blinded. n = 10/group

n = 20/group for pooled data

The data shown here were published by Fellermeyer *et al.*[1].

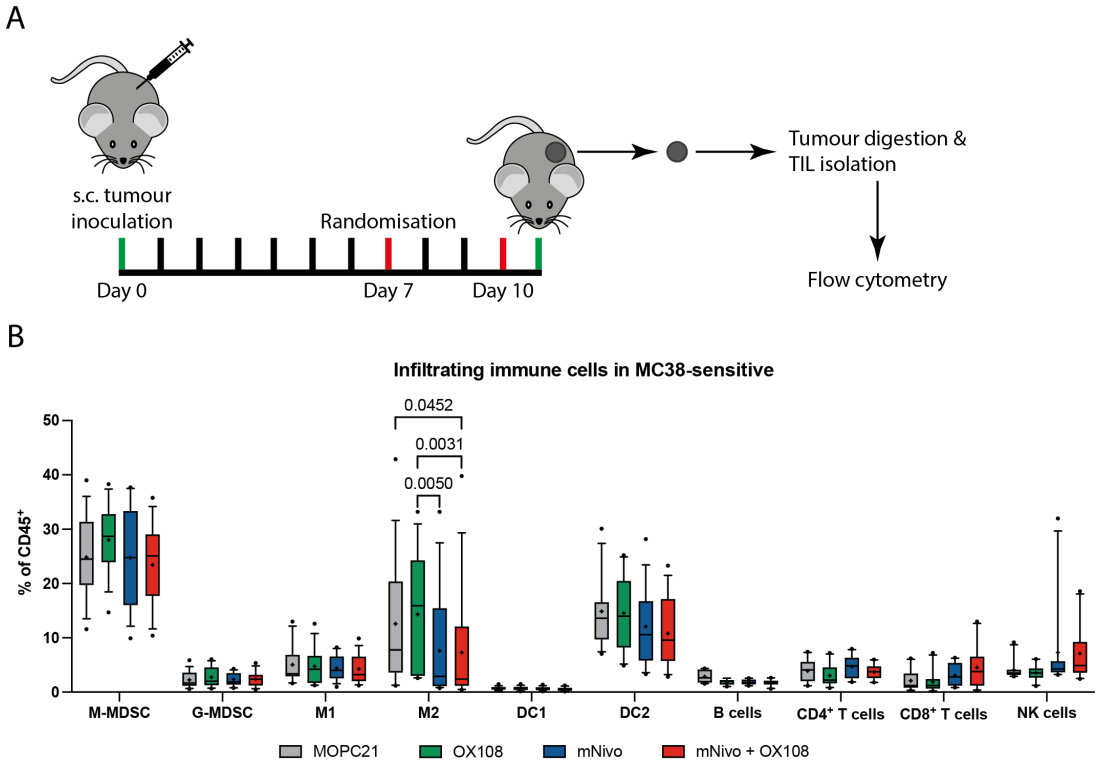


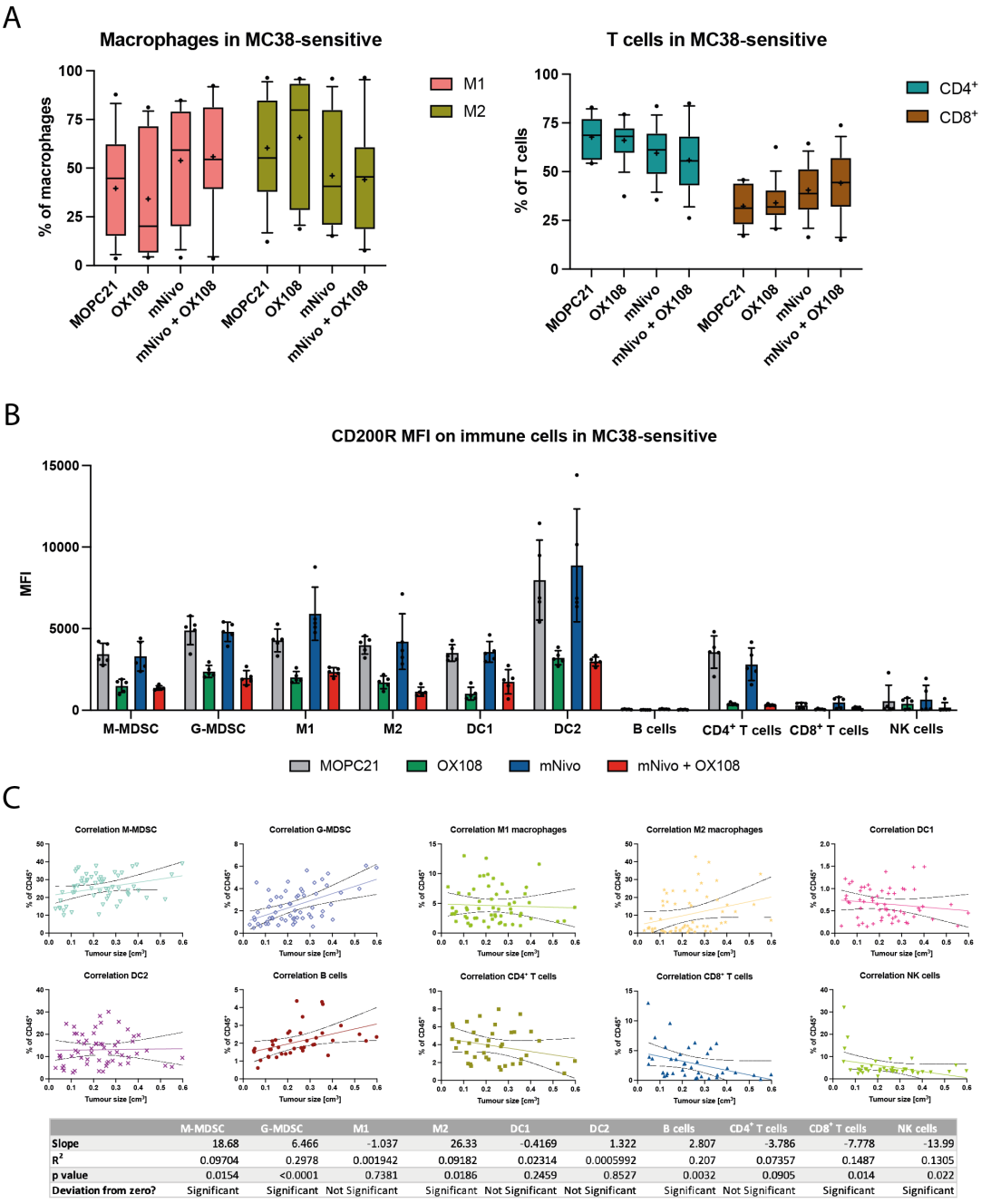
Figure 4.7: Immune cell infiltration in treated MC38-sensitive tumours
Tumours were harvested and immune cells analysed by flow cytometric analysis.
(A) Illustration depicting the experimental outline. Mice were randomised once the average tumour volume reached 40 mm^3 (day 7). Mice were treated twice with 200 µg/antibody/treatment, indicated by red lines. After the final treatment, mice were culled, tumours harvested, digested and immune cells isolated for flow cytometric analysis.
(B) A myeloid and lymphoid flow cytometry panel was used to identify different immune cell subsets. The line shows the median, the '+' shows the mean. Whiskers display the 10-90 percentile. p-values are given for $p \leq 0.05$.
All experiments were randomised and blinded. The experiment was repeated three times and data from all experiments were pooled. Lymphoid cells were only analysed twice. n = 5/group for each experiment
The data shown here were published by Fellermeyer *et al.*[1].

Abundances of all analysed immune cells are plotted in Figure 4.7 B. Considering that some tumours are projected to completely regress (Figure 4.6), the immune cell frequencies changed surprisingly little. There was a significant increase in M2 macrophages in the OX108 treated group, compared to mNivo and mNivo + OX108. In contrast, the combination treatment resulted in a significant decrease of M2 macrophages compared to the MOPC21 isotype control (Figure 4.7 B). Further analysis of the percentages of M1/M2 macrophages and $CD4^+/CD8^+$

T cells did not reveal any significant changes (Figure 4.8 A), however, there was a trend towards more $CD8^+$ T cells in the combination therapy compared to MOPC21 ($p = 0.0665$, in contrast to $p = 0.3077$ for mNivo vs. MOPC21). As in the case of the LLC1 model, antibody penetration into the tumour was validated by staining for CD200R, which exhibited a clear reduction in the OX108 and mNivo + OX108 treatment groups (Figure 4.8 B). Furthermore, comparing immune cell abundances with tumour sizes, irrespective of treatment groups, demonstrated several significant correlations as determined by a simple linear regression model (Figure 4.8 C). While MDSCs, M2 macrophages and B cells were positively correlated with tumour size, $CD8^+$ T cells and NK cells demonstrated a negative association.

As the survival studies (Figure 4.6) suggested that treatment with mNivo + OX108 resulted in more CRs, in one of the the experiments a T-cell flow cytometry panel was used to discriminate between naïve, effector and memory subsets based on CD44 and CD62L expression (Figure 4.9 A, gating strategy shown in Figure 2.3). Although there was a trend towards increased $CD8^+$ T-cell infiltration in mNivo treated groups, primarily comprising $CD8^+$ effector cells, this was not statistically significant ($p = 0.0854$ and 0.2704 for mNivo and mNivo + OX108, respectively).

Finally, in two experiments, draining lymph nodes (dLNs) and non-dLNs were harvested and analysed for myeloid and lymphoid immune-cell subsets (Figure 4.9 B). Myeloid cells remained mostly unchanged, with the exception of DC1s, which were significantly increased in the dLNs of combination regimen-treated animals compared to the isotype control. mNivo monotherapy resulted in a trend towards increased DC1 presence, though this did not reach significance ($p = 0.0796$). Importantly, this was not observed in the non-dLN ($p = 0.9997$ and 0.9961 for mNivo and mNivo + OX108, respectively). While there were changes in the B-cell abundance upon treatment in the dLNs, this was also observed in the non-dLNs. Lastly, there was a significant decrease of $CD4^+$ T cells in the dLNs of mNivo treated mice compared to MOPC21.



	M-MDSC	G-MDSC	M1	M2	DC1	DC2	B cells	CD4⁺ T cells	CD8⁺ T cells	NK cells
Slope	18.68	6.466	-1.037	26.33	-0.4169	1.322	2.807	-3.786	-7.778	-13.99
R^2	0.09704	0.2978	0.001942	0.09182	0.02314	0.0005992	0.207	0.07357	0.1487	0.1305
p value	0.0154	<0.0001	0.7381	0.0186	0.2459	0.8527	0.0032	0.0905	0.014	0.022
Deviation from zero?	Significant	Significant	Not Significant	Significant	Not Significant	Not Significant	Significant	Not Significant	Significant	Significant

Figure 4.8: Immune cell infiltration in treated MC38-sensitive tumours
Tumours were harvested and immune cells analysed by flow cytometric analysis as described in Figure 4.7.
(A) Percentages of M1/M2 macrophages (left) and $CD4^+$/$CD8^+$ T cells (right panel).
(B) MFI of CD200R on identified immune cells.
(C) Correlations of immune cell abundances and tumour volumes. A simple linear regression model was fitted (Prism 9.5.1) and plotted with 95 % confidence intervals.
For boxplots, the line shows the median, the '+' shows the mean. Whiskers display the 10-90 percentile. For bar graphs, data are shown as mean ± SD.
The data shown here were published by Fellermeyer *et al.*[1].

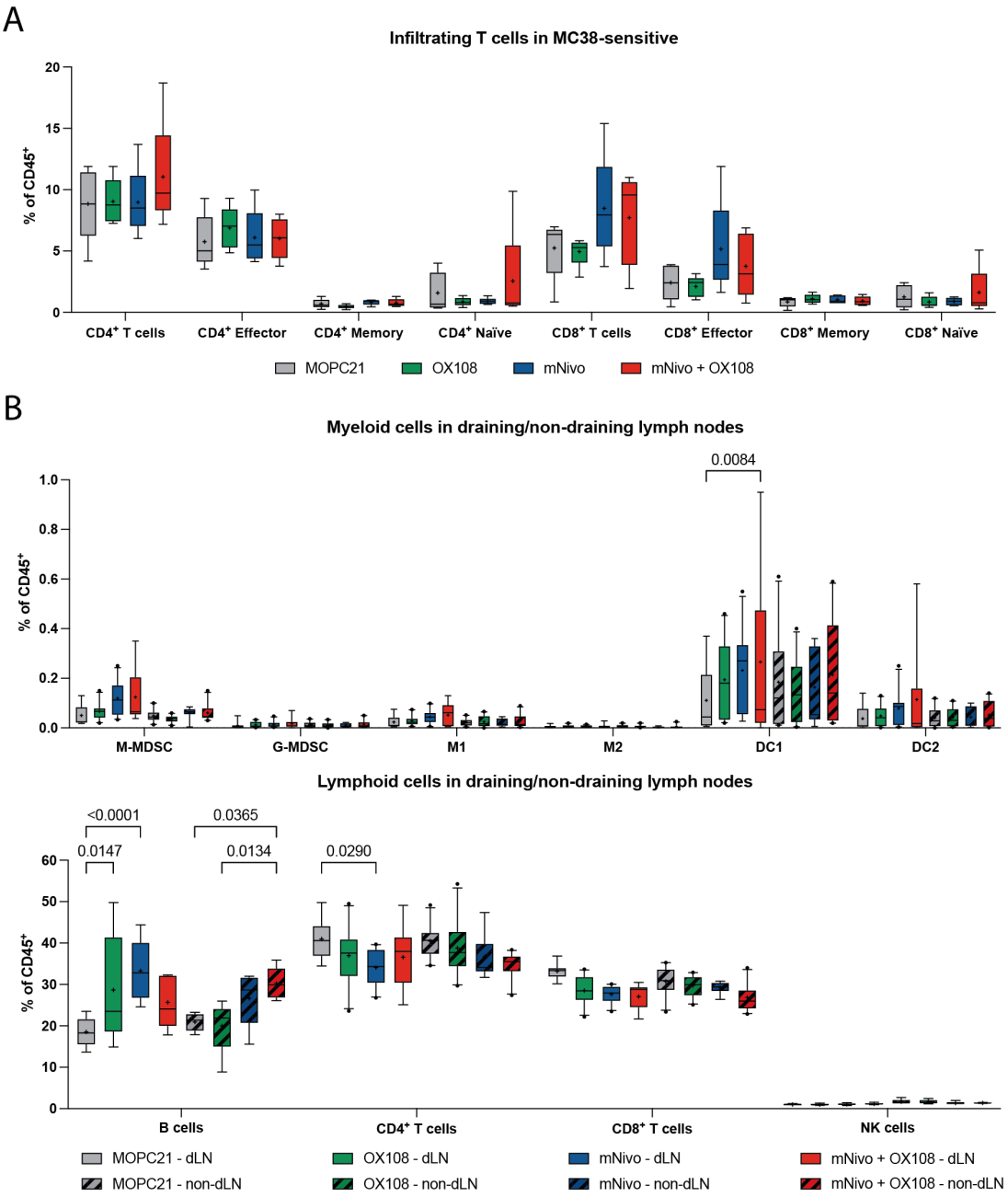


Figure 4.9: T cell and lymph node analysis of the MC38-sensitive tumour model

Tumours and lymph nodes were harvested and immune cells analysed by flow cytometric analysis as described in Figure 4.7.

(A) Different T-cell subsets were identified based on CD44 and CD62L expression.

(B) Harvested draining and non-draining lymph nodes were analysed for myeloid cells (top panel) and lymphoid cells (bottom panel).

The line shows the median, the '+' shows the mean. Whiskers display the 10-90 percentile. p-values are given for $p \leq 0.05$.

Lymph nodes were harvested in two independent experiments. T-cell subsets were analysed once. n = 5/group for each experiment

The data shown here were published by Fellermeyer *et al.*[1].

4.3 Discussion

The work described in this chapter investigated the combination therapy comprising the PD-1 blocker mNivo (nivolumab mIgG1) as well as the CD200R blocker OX108 in two different cancer models. While anti-PD-1 antibodies are thought to mostly act on T cells to induce tumour killing, the inhibitory immune receptor CD200R is predominantly found on myeloid cells[144,145]. Thus, the rationale was to combine the stimulation of T cells through mNivo therapy with a reactivation of myeloid cells through treatment with OX108. There are multiple studies investigating the role of the CD200/CD200R axis in cancer. As discussed in the introduction (Section 1.2.4.3), reports using mouse models revealed contradictory results regarding the ultimate role of CD200R, whether it is pro-tumourigenic[170–172] or tumouricidal[174,175]. In contrast, most human studies support a tumour-promoting role of the CD200/CD200R axis, which ultimately led to the testing of at least two monoclonal blocking antibodies in clinical studies[186,194]. While the clinical study investigating the anti-CD200R blocking antibody 23ME-00610 progressed into a phase II trial due to a good safety profile[194], the phase I clinical trial testing samalizumab (ALXN6000) was terminated by the sponsor due to administrative reasons[186]. Importantly, samalizumab also exhibited a good safety profile and the maximum tolerated dose was not reached[186]. Furthermore, while all participants with multiple myeloma (n = 3) exhibited disease progression, around 60 % of patients with chronic lymphocytic leukemia (14/23) experienced a decreased tumour burden, but only one patient achieved a durable response[186]. Samalizumab will be further investigated as part of the Beat AML phase Ib/II clinical trial[188]. Overall, the combination of CD200R blockade with other immunostimulating treatments, such as mNivo, could be expected to lead to synergistic effects.

First, the blocking activity of mNivo and OX108 was validated *in vitro*. For this, a T-cell activation assay was established to test the efficacy of ligand blockade. The assay is based on a two-cell co-culture, with Jurkat T cells expressing GFP

under an NF-κB promoter as well as TCS cells with a surface-expressed anti-CD3-scFv[298]. Addition of inhibitory ligand and receptors on the TCS and Jurkat cells, respectively, leads to inhibition of the GFP expression. As this is a very simplistic assay it has certain drawbacks. For example, the use of cell lines that constitutively upregulate inhibitory receptors, which are only transiently expressed in primary T cells, does not properly recapitulate the physiological functions of these receptors during T-cell activation. Another issue is the upregulation of certain proteins upon activation, which can result in apparently contradictory results, e.g. an activatory effect of OX108 in a co-culture of Jurkat CD200R$^+$ cells with TCS cells (Figure 4.3 B, right panel). As no ligand is expressed on the stimulating cells, OX108 treatment should not induce GFP expression. However, activated Jurkat T cells upregulate CD200 (Figure 4.3 C), resulting in an engagement of the receptor and thus inhibition. The reason why only a small proportion (8.79 %) of Jurkat cells upregulate CD200 might be related to the varying levels of CD3 present on Jurkat cells, leading to different activatory potentials through anti-CD3-scFv (personal communication from Sumana Sharma, University of Oxford). This might also explain why the degree to which CD200 was upregulated differed greatly (Figure 4.3 C). Importantly, for the aims of this chapter, viz. to establish the blocking efficacy of the produced antibodies, the assay is well-suited despite these disadvantages.

Second, the combination therapy, mNivo + OX108, was tested in the PD-1 blockade-resistant model LLC1 (Section 4.2.2). None of the treatment regimens resulted in a diminished tumour growth or increased survival. Thus, the survival experiment was stopped on day 23 and all remaining tumours were harvested for flow cytometric analysis of infiltrating immune cells. There was a significant decrease of M-MDSCs in the OX108 monotherapy, compared to mNivo and mNivo + OX108, as well as an increase of M2 macrophages compared to anti-PD-1 monotherapy (Figure 4.5 A). A trend towards increased M2 macrophage abundance was also observed in the combination blockade ($p = 0.1091$ for mNivo vs. mNivo + OX108). It is important to note that the OX108 treated group only

comprised three animals, and therefore the statistical power of these comparisons was low. In conclusion, the different antibodies, whether used as monotherapy or combination treatment, had no effect on tumour growth and little effect on infiltrating immune cells, which might be explained by the small group sizes. The treatment start in the LLC1 model was comparatively late at day 9, once the average tumour volume exceeded 20 mm^3. This late time point was chosen as LLC1 cells grew slowly upon injection (Figure 4.4 B). Initiating the treatment earlier could, in principle, result in a reduced tumour growth rate as the immunosuppressive TME might not be fully established. However, while published studies using the LLC1 model started PD-1/PD-L1 blockade earlier (day 3 or day 5[306,309]), there was still no effect on tumour growth in these studies.

Third, as there was promising data (Figure 1.8) demonstrating increased CRs in the PD-1 blockade-sensitive tumours MC38, this model was investigated next. While not statistically significant, pooling of two independent repeats resulted in a trend towards more rejected tumours for the combination treatment ($p = 0.1848$, Figure 4.6 B). More importantly, as this result is in agreement with the study carried out by the contract research organisation Crown Bioscience (Figure 1.8), this may suggest that the small effect is indeed reproducible. This also indicates that the experiments carried out were underpowered. However, assuming that the CR rates remain reproducible, a group size of 44 would have been required, which was technically not feasible in this study.

Similar to the results obtained from the LLC1 model, subsequent analysis of infiltrating immune cells revealed increased M2 macrophages in OX108-treated tumours. As mentioned in Section 1.1.3.1, M2 macrophages are considered to promote tumour growth by creating a more immunosuppressive TME, whereas M1 macrophages are tumouricidal and enhance the anti-tumour immune response[19]. In the MC38-sensitive model, the combination therapy led to a further reduction in M2 macrophages, reaching significance in comparison to the isotype control (Figure 4.7 B), while an opposite trend was observed for the LLC1 model (Figure 4.5 A). The analysis of MC38-sensitive tumours was repeated three

times (n = 5/group for each experiment) and the data were pooled, making them more reliable as the effects were observed consistently. It remains to be determined why the OX108 monotherapy led to an increase of M2 macrophages, whereas OX108 in combination with mNivo reduced them. One possible explanation is that OX108 had no effect on M2 macrophages in the tumour, and the observed differences are caused by mNivo. While not reaching the significance threshold of $p \leq 0.05$, there was a clear trend for M2 macrophage reduction in mNivo treated tumours, compared to MOPC21 ($p = 0.0654$). In contrast, abundances between (i) MOPC21 and OX108 treated groups and (ii) mNivo and mNivo + OX108 groups were very similar ($p = 0.8232$ and $p = 0.9990$, respectively), suggesting that OX108 had no effect. Further studies are needed to fully investigate the observed effects. Published data using the MC38 colorectal model demonstrated increased infiltration of $CD8^+$ T cells into the tumour of anti-PD-1 treated mice[235,238]. However, despite a trend towards more $CD8^+$ T cells as determined by $CD4^+/CD8^+$ T-cell ratio ($p = 0.0665$ for MOPC21 vs. mNivo + OX108, Figure 4.8 A, right panel), there was no overall increase in $CD8^+$ T cell frequencies (Figure 4.7 B). The discrepancies observed between the published studies and this study are likely explained by the different time points chosen for the analysis. The published studies harvested the tumours at a later stage of tumour development (day 15 and day 16[235,238]), compared to this study (day 11). Further analysis of different T-cell subsets (naïve, effector and memory) did not reveal any significant differences in the phenotype of infiltrating T cells (Figure 4.9 A). Interestingly, analysis of immune cells present in dLNs revealed an increase of DC1s in the mNivo + OX108 group compared to MOPC21, which was not observed in the non-dLNs (Figure 4.9 B, upper panel). This is an intriguing finding as DC1s are required for cross-presentation of tumour antigens to $CD8^+$ T cells[24]. However, as these cells were only found at very low frequencies (≤ 1.0 %), follow-up studies are needed to confirm this and clarify the importance of the effect.

As established in the previous chapter (Figures 3.4 C and 3.5 A), the LLC1 tumour was negative for CD200, whereas MC38-sensitive cells expressed the ligand

on approximately 66 % and 34 % of all cells *in vitro* and *in vivo*, respectively. Moreover, quantification of the CD200 levels revealed a similar number of CD200 molecules on MC38-sensitive cells (2,728, Figure 3.4 D) compared to PD-L1 or PD-L2 molecules on immature and mature DCs (5,723 and 5,243, respectively)[127]. While LLC1 tumours did not respond to the different antibodies used in this study, a potential trend towards increased survival was observed for the MC38-sensitive colorectal cancer model comparing mNivo and mNivo + OX108. As tumours that express PD-L1 are more likely to respond to PD-1 blockade[263], this might also apply to the CD200/CD200R axis. However, because (i) the presence of $CD8^+$ or PD-1^+ cells had a more significant association with response compared to PD-$L1^+$ cells[263], (ii) $CD200R^+$ cells were abundant in the TMEs of LLC1 and MC38-sensitive tumours (Figure 3.5 E) and (iii) B-, T-cells and endothelial cells are also known to express CD200[159], the present study did not seek to further manipulate the cancer models. Nevertheless, future work should either focus on cancer models that express higher levels of CD200, or upregulate them artificially. Indeed, CD200 upregulation had already been shown to suppress anti-tumour immune responses, which could be reverted by anti-CD200 treatment[187].

Finally, while this study used antibodies with a D265A mutation to reduce binding to FcγRs[212], another therapeutic approach could be the depletion of $CD200R^+$ cells through an antibody with high effector functions. For this, a mIgG2a isotype is recommended as it has the highest A/I ratio[204]. While a lot of immunosuppressive immune cells, including MDSCs and M2 macrophages, expressed CD200R, the receptor was also present on proinflammatory M1 macrophages as well as DCs, which can act as important APCs (Figure 3.5 E). Thus, a careful analysis of the $CD200R^+$ immune cells in the specific TME would be needed to prevent depletion of tumouricidal immune cells. Furthermore, OX108 is a relatively low-affinity antibody with a K_D of 84 nM. While binding of the antibody in the tumour was validated through the observed reduction of CD200R MFI on infiltrating immune cells (Figures 4.5 C and 4.8 B), CD200R blocking antibodies with a higher affinity

should be tested. An affinity threshold for PD-1 blockers in the MC38 model was reported previously, underpinning the importance of high-affinity antibodies[324].

In conclusion, the combination of anti-CD200R/anti-PD-1 antibodies was tested in two different cancer models, LLC1 and MC38-sensitive. While OX108 monotherapy did not influence tumour growth in both models, the effects observed for the combination with mNivo in the MC38-sensitive model warrants further investigation. Additionally, other models should be screened for the expression of CD200, as this might serve as a prognostic marker for the responsiveness to CD200R blockade.

Unlike teachers or doctors, our efforts improve the lives of people we'll never meet.

— Katie Busch-Sorensen

5

Extending nivolumab mIgG1 to increase efficacy

Contents

5.1 Rationale 129
5.2 Results 131
5.2.1 Design of extended antibodies 131
5.2.2 Purification of extended antibodies using Protein A and SEC 134
5.2.3 Comparison of size using SEC 135
5.2.4 SPR validation of extended antibodies 135
5.2.5 *In vitro* T-cell activation assay 143
5.2.6 *In vivo* tumour challenges with MC38 models 145
5.2.7 *In vivo* challenge with MC38-sensitive mFcγRIIb expressing tumours 149
5.2.8 Combination of PD-1 and mFcγRIIb blockade 152
5.2.9 Comparison of mNivo and mNivo D265A across experiments 152
5.3 Discussion 155

5.1 Rationale

WHILE immune-checkpoint blockade has truly revolutionised cancer treatment, the benefits remain limited to certain tumours and within those subtypes only a fraction of patients respond[230]. The limited response

highlights several areas where further research is needed, including (i) better biomarkers to stratify patient populations, (ii) new combination therapies to expand the pool of responding patients, but also (iii) how to design the optimal immune-checkpoint blocking antibody.

A lot of attention has been paid to developing high-affinity blocking antibodies, and it has been demonstrated that low-affinity blocking antibodies are not as effective as their high-affinity counterparts[324]. However, once all receptor sites were blocked, further increasing the affinity was not beneficial[324]. Epitope position as well as the constant domain of an antibody can be further modified in order to enhance efficacy. There is now a substantial body of evidence demonstrating that PD-1 blocking antibodies which retain their binding capacity to FcγRs have a reduced efficacy compared to Fc-null anti-PD-1 antibodies[235,237–239]. This was discussed in greater detail in Section 1.3.3.3, but it is important to note that the precise mechanism of this is not fully understood. The initial report by Ravetch and colleagues only pointed out a potential involvement of mFcγRIIb, without giving an explanation how[235]. To address this, Arlauckas *et al.* demonstrated through *in vivo* imaging that anti-PD-1 antibodies are quickly captured by TAMs in an FcγR-dependent manner. Furthermore, combination of PD-1 and FcγR blockers increased the efficacy, compared to anti-PD-1 monotherapy[237]. Finally, BeiGene developed a hIgG4 PD-1 blocking antibody with mutations to abrogate FcγR binding (BGB-A317, tislelizumab). While hIgG4 is considered to have low effector functions[214], it was also shown to bind to the high-affinity hFcγRI[202]. The binding of hIgG4 to hFcγRI was responsible for the phagocytosis of $CD8^{+}PD\text{-}1^{+}$ T cells by macrophages *in vitro*[239]. Importantly, in a xenograft model the Fc-engaging antibody demonstrated inferior tumour control compared to the Fc-null antibody. Tislelizumab is currently in phase III clinical trials[240].

Thus, it is now established that FcγR binding is not needed for PD-1 blockers, but rather diminishes their efficacy. Currently, there are different potential mechanisms of actions available to explain these observations. Based on the existing data on the anti-CD28 superagonists as well as the intrinsic agonistic

activity of nivolumab mIgG1 (Section 1.5), another explanation based on antibody-agonism (Figure 1.2) was investigated in this chapter. Most importantly, such an effect should not be limited to PD-1, but can be expanded to all antibodies that bind to small NTRs (defined in Section 1.2).

Based on the KS model (Section 1.2.2 and Figure 1.2), the receptor/antibody/FcγR complex can be held in close contacts depleted from phosphatases, therefore leading to receptor trigger. Extending the receptor or antibody led to a reduced agonistic activity, as shown for the superagonist JJ316 and the receptor CD28[296]. However, while extension of JJ316 through insertion of a heavily glycosylated sequence of mCD43 abrogated the superagonistic activity of JJ316, it was still costimulatory (Figures 1.9 A and B), indicating that some agonistic potential remained. Thus, further extension of the antibody might be necessary to fully abrogate the stimulatory capacity, a possibility that was explored in this chapter using two different approaches for creating larger versions of mNivo (nivolumab mIgG1). Importantly, despite blocking the interaction of PD-1 with its ligands, it was shown that mNivo retains agonistic potential *in vivo* (Figure 1.9 C)[103]. Furthermore, a recent study published by Mark Cragg and colleagues also demonstrated this effect for nivolumab hIgG4, ruling out that this was an artifact of the mIgG1 isotype[103].

5.2 Results

5.2.1 Design of extended antibodies

The first approach for extending antibodies is based on the insertion of a sequence of mCD43 into the hinge region of antibodies, which was described previously for anti-CD28 (JJ316)[296] and anti-PD-1 (nivolumab mIgG1)[294] antibodies. The insertion point of the sequence, connected by a short GS linker, was made immediately downstream of the cysteine that is responsible for HC-LC pairing. The remaining cysteines within the hinge region of mIgG1 form disulfide bonds with the other HC. In order to further extend mNivo (Figure 5.1 A) beyond the previously trialled 50 aa construct (Figure 1.9 C), 100 and 150 aa of mCD43 were

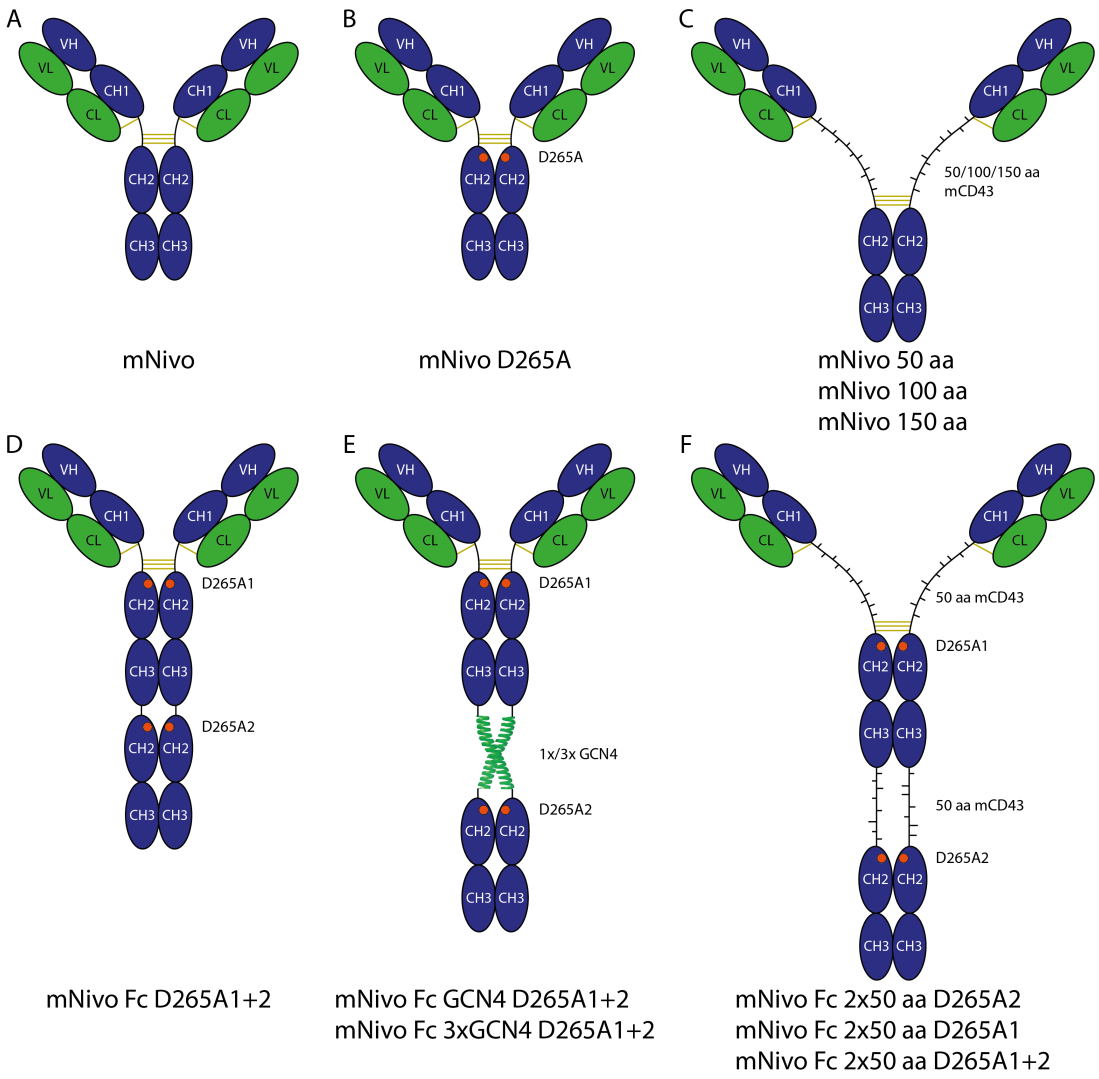


Figure 5.1: Design of extended antibodies
A schematic overview of the different antibody extensions. Heavy chains are coloured in blue, light chains in green. Hinge disulfide bonds are shown in yellow. The D265A mutation is indicated by an orange circle. GCN4 structure Protein Data Bank (PDB) ID: 1IGY[325].

inserted into the hinge region. For a comparative approach, mNivo with a 50 aa extension was also created (Figure 5.1 C). All these hinge-extended antibodies retained binding to FcγRs, as they lacked a D265A mutation.

The second approach is based on Fc multiplexing (Figure 5.1 D), an approach that was devised independently to enhance antibody effector functions[326]. Besides extending the antibody, this approach also allowed the repositioning of FcγR binding, as the D265A mutation[212] can be introduced in either the first, the second or both CH2 domains. In order to facilitate the pairing of all CH2/CH3

domains, a long, flexible linker (GGGGS) was added in between the first CH3 and second CH2 domain. Based on this Fc multiplexing, additional domains were introduced to further elongate the structure. This either consisted of a coiled-coil domain from the yeast protein GCN4 (Figure 5.1 E), or the mCD43 sequence. In the latter case, 50 aa were inserted into the hinge region as well as between the Fc domains (Figure 5.1 F). While all Fc-multiplexed antibodies were designed with two D265A mutations to abrogate binding to FcγRs, two additional variants were created for the last construct, which allowed selective binding of FcγRs to the top (D265A2) or the bottom (D265A1) Fc region (Figure 5.1 F). Non-extended mNivo with and without a D265A mutation were also produced (Figures 5.1 A and B).

CD43 is a heavily glycosylated mucin-like protein on immune cells, with approximately one *O*-linked carbohydrate every three amino acids[327]. This results in a rod-like structure with an extension of approximately 0.2 nm per amino acid[327]. In contrast, an alpha helix elongates by around 0.15 nm per residue. Alpha helices that are coiled together are referred to as coiled coils, which consist of a heptad repeat containing two hydrophobic residues at position one and four. Alterations of these residues allow the creation of dimeric, trimeric and tetrameric conformations[328]. Importantly, coiled-coil proteins have an estimated persistence length of around 150 nm[329] and the coiled-coil dimer ROCK2 was shown to extend over a length of 120 nm[330]. In contrast, the persistence length of mucins is approximately 15 nm[331,332]. Persistence length is a measure to describe the maximum length of a molecule in which it behaves like a rigid rod. Thus, coiled-coil domains offer a robust way to extend a molecule in a linear way. Of note, one coiled-coil domain in this chapter refers to a sequence of four heptad repeats.

In contrast to Chapters 3 and 4, in this chapter all D265A mutations are specifically mentioned, ergo, mNivo refers to the Fc-engaging antibody, without a D265A mutation. Table 5.1 summarises all antibody constructs mentioned in this chapter and gives an overview of the names, modifications and mutations. All sequences are provided in Section A.1.

Table 5.1: Overview of different mNivo antibody constructs

Antibody name	Modification	Mutation
mNivo	No modification	No mutation
mNivo D265A	No modification	D265A
mNivo 50 aa	50 aa mCD43 hinge extension	No mutation
mNivo 100 aa	100 aa mCD43 hinge extension	No mutation
mNivo 150 aa	150 aa mCD43 hinge extension	No mutation
mNivo Fc D265A1+2	Fc multiplexing	D265A1+2
mNivo Fc GCN4 D265A1+2	Fc multiplexing with GCN4 as linker	D265A1+2
mNivo Fc 3xGCN4 D265A1+2	Fc multiplexing with 3xGCN4 as linker	D265A1+2
mNivo Fc 2x50 aa D265A1+2	50 aa mCD43 hinge extension + Fc multiplexing with 50 aa mCD43 as linker	D265A1+2
mNivo Fc 2x50 aa D265A2	50 aa mCD43 hinge extension + Fc multiplexing with 50 aa mCD43 as linker	D265A2 (mutation only in the second Fc)
mNivo Fc 2x50 aa D265A1	50 aa mCD43 hinge extension + Fc multiplexing with 50 aa mCD43 as linker	D265A1 (mutation only in the first Fc)

5.2.2 Purification of extended antibodies using Protein A and SEC

The heavy chain sequences (all mIgG1) were ordered as DNA strings and cloned into a pHR plasmid with the help of Mai Vuong, where necessary. D265A mutations were reverted to the original sequence through PCR mutagenesis. The established antibody purification pipeline (Sections 3.2.2 and 3.2.3) was used for endotoxin-free antibody production. The Fc-multiplexing approach especially resulted in smaller antibody byproducts as shown in representative SEC curves in Figure 5.2. Given the molecular weight of these proteins, as shown through non-reducing SDS-PAGE gels (Figure 5.3), this might be a single HC-LC pair. The estimated molecular weights were calculated using Expasy ProtParam (https://web.expasy.org/protparam/)[333]. Of note, as mCD43 is a heavily glycosylated protein, and glycosylation cannot be accurately predicted by

Expasy ProtParam, the reported molecular weights were usually an underestimate (Figure 5.3). This became especially apparent for mNivo 50 aa, 100 aa and 150 aa.

5.2.3 Comparison of size using SEC

Pooling of the respective monomeric antibody fractions and re-running a small amount of these proteins (100 µg) for analytical SEC analysis revealed a stable monomeric state (Figure 5.4). Importantly, there was a shift towards earlier elution, indicating an increase in the size of the molecule, which was dependent on the degree to which the antibody was extended. While increasing the mCD43 insertion in the hinge region resulted in a significantly earlier elution, addition of three GCN4 coiled-coil domains instead of a single domain made no difference. Furthermore, there was relatively little change of the elution time for the GCN4-containing antibodies in comparison to mNivo Fc D265A1+2, indicating that this insertion might not be as effective at extending antibodies. mNivo with a 50 aa mCD43 insertion into the hinge and between the two Fc regions (mNivo Fc 2x50 aa D265A1+2) eluted between mNivo 50 aa and 100 aa. Of note, re-running of fridge-stored protein after one month resulted in an identical result (data not shown), indicating long-term stability.

5.2.4 SPR validation of extended antibodies

To assess the binding behaviour of the different forms of mNivo, SPR was used to compare the monovalent as well as bivalent binding properties. First, the same approach as used in Section 3.2.4 was employed to compare the monovalent kinetics across the different antibodies. Upon capturing of the antibodies on a Protein A chip, hPD-1-2xHis was injected at increasing concentrations. Extended antibodies did not immobilise as well as the 'parental' mNivo, thus leading to decreased Response Units (RU); a finding that is discussed at the end of this chapter (5.3). However, most importantly, the on-rate (k_a), off-rate (k_d) as well as the dissociation constant (K_D) were highly similar between all tested antibodies.

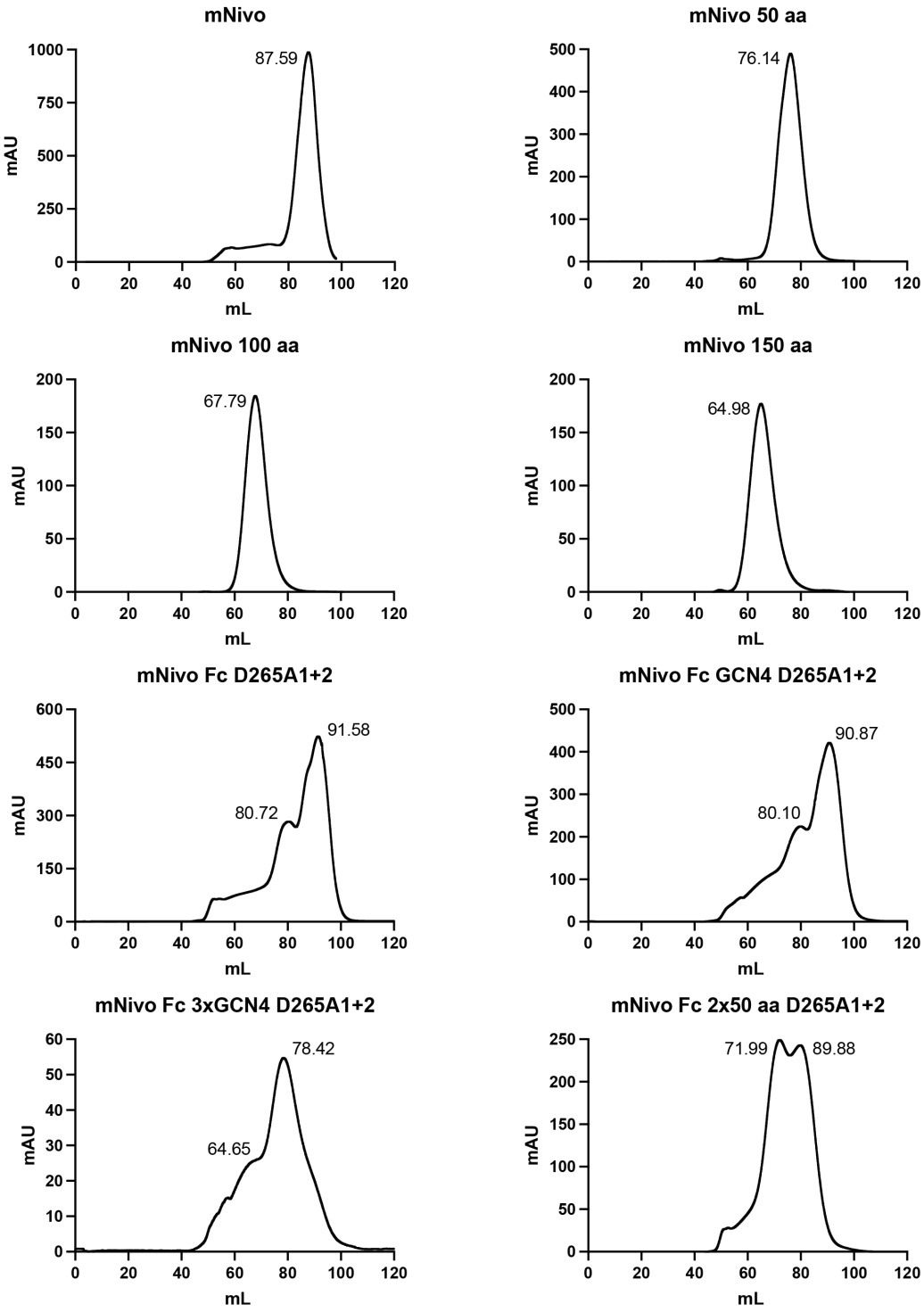


Figure 5.2: SEC curves of extended antibodies
Representative SEC curves of the produced extended antibodies. A ProteoSEC 16/60 6-600 column was used. Elution volumes of major peaks are annotated in each graph.

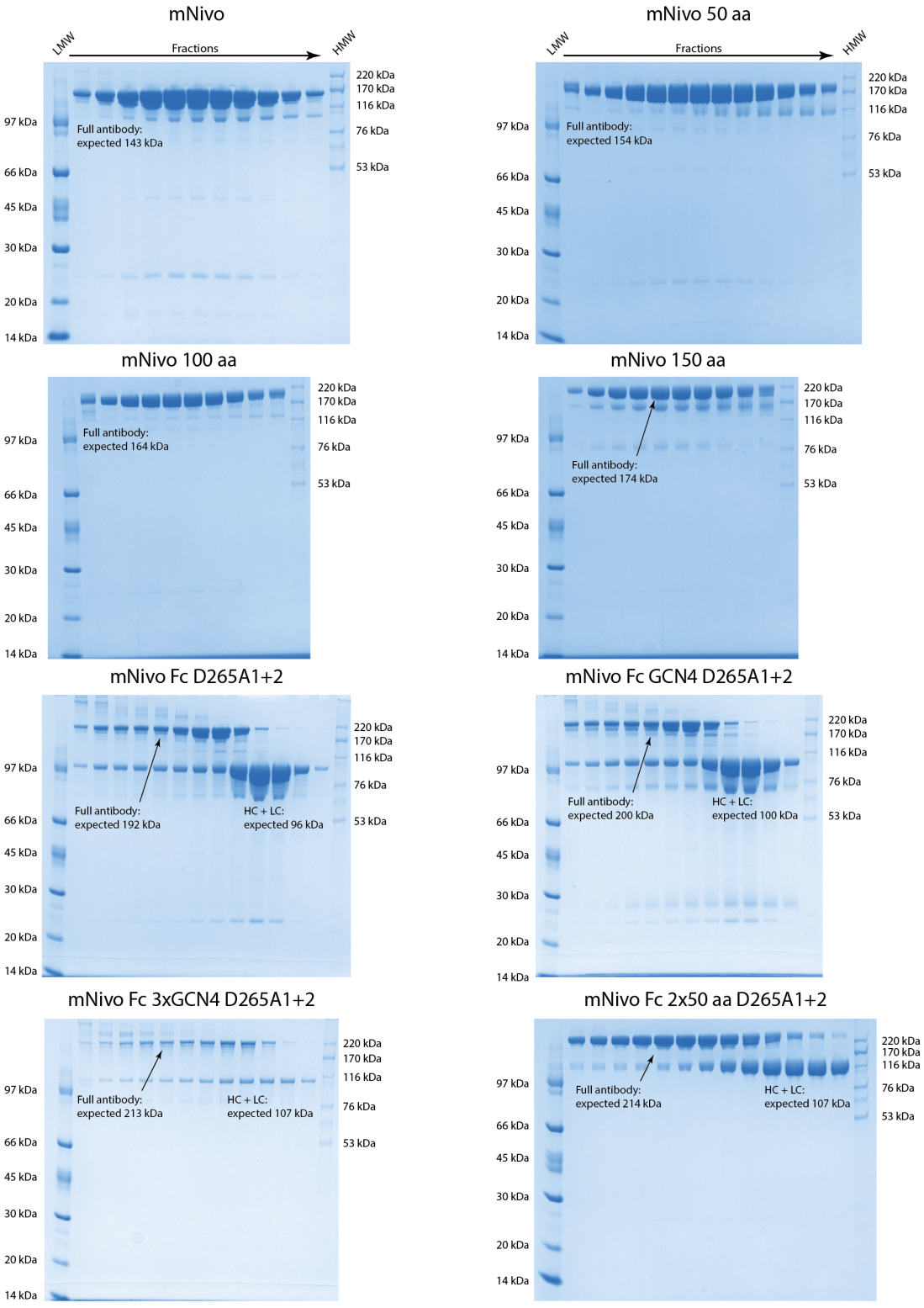


Figure 5.3: Non-reducing SDS-PAGE analysis of extended antibodies
Representative non-reducing SDS-PAGE gels of the produced extended antibodies. A low- and high-molecular weight (LMW and HMW, respectively) ladder were included on each gel. Expected sizes of full antibodies and HC + LC pairs, as calculated by Expasy ProtParam[333], are annotated.

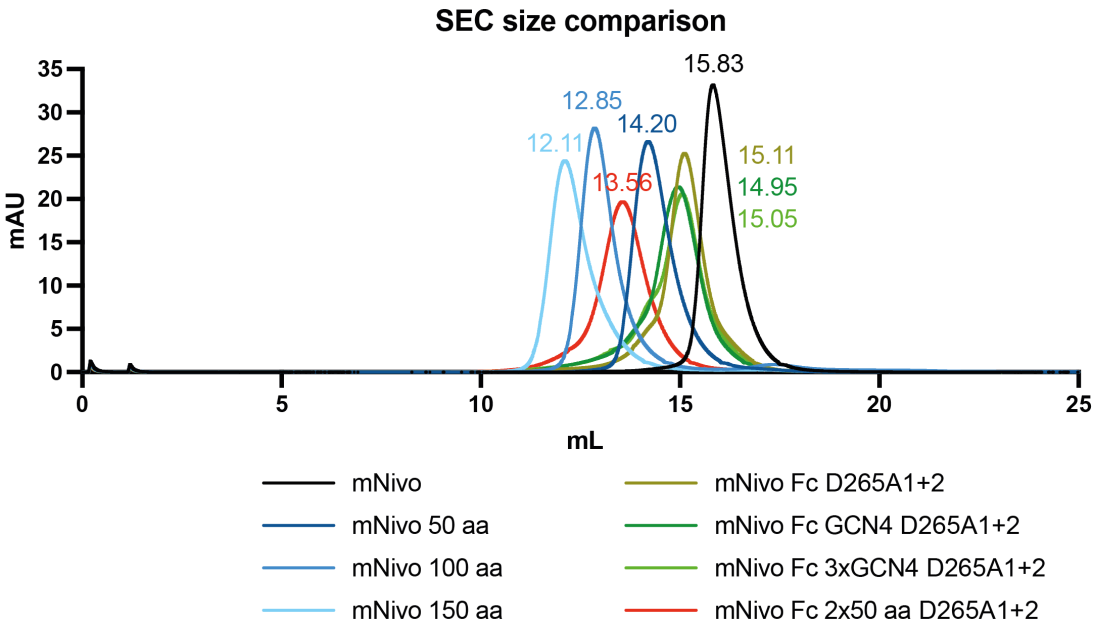
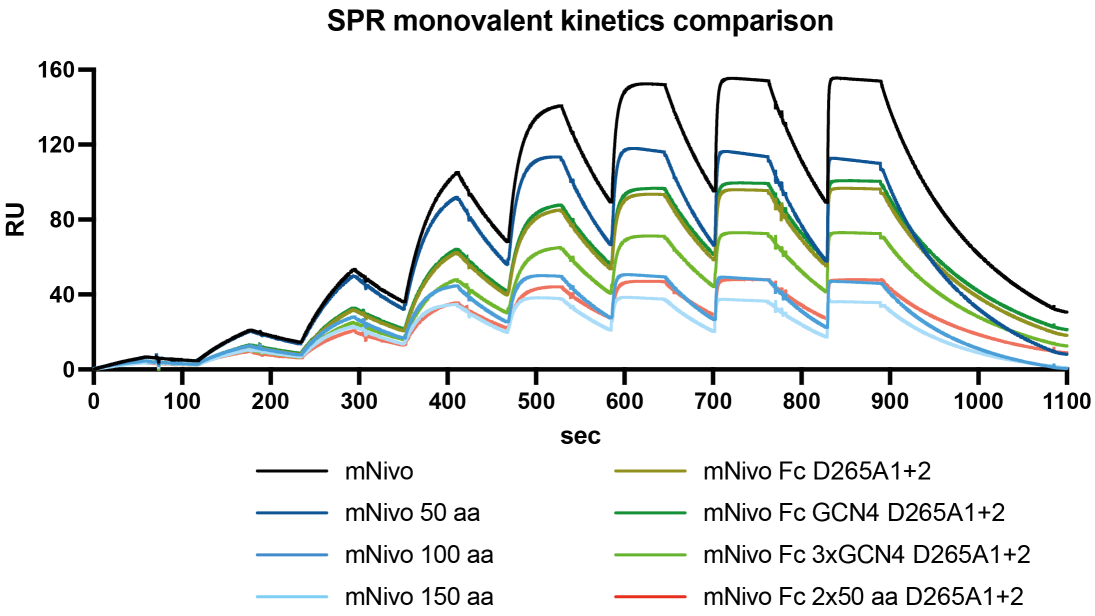


Figure 5.4: Size comparison of extended antibodies using SEC
Analytical SEC analysis of engineered antibodies. A small amount (100 µg) of each antibody was injected over a Superdex 200 Increase 10/300 GL. Elution volumes of major peaks are annotated with the corresponding colour.

This finding demonstrated that the monovalent interactions with the antigen (hPD-1-2xHis) were not impeded by the different modifications. As antibodies have the capacity to bind bivalently, it is also important to assess the avidity/bivalent binding properties. For this, a Sensor Chip NTA was used to capture the histidine-tagged PD-1 protein (hPD-1-2xHis). This sensor chip is conjugated with nitrilotriacetic acid (NTA), which chelates metal ions like nickel (Ni^{2+}), thereby capturing poly-histidine tagged proteins. The chip can be easily regenerated by injection of 350 mM EDTA, which strips the nickel ions and therefore all attached proteins. Due to the slow off-rate, this experiment was performed in a multi-cycle analysis with the analyte (antibody) concentrations varying from 0.032 nM to 68.758 nM (latter is equivalent to 0.01 mg/mL of mNivo). Representative sensorgrams are shown in Figure 5.6.

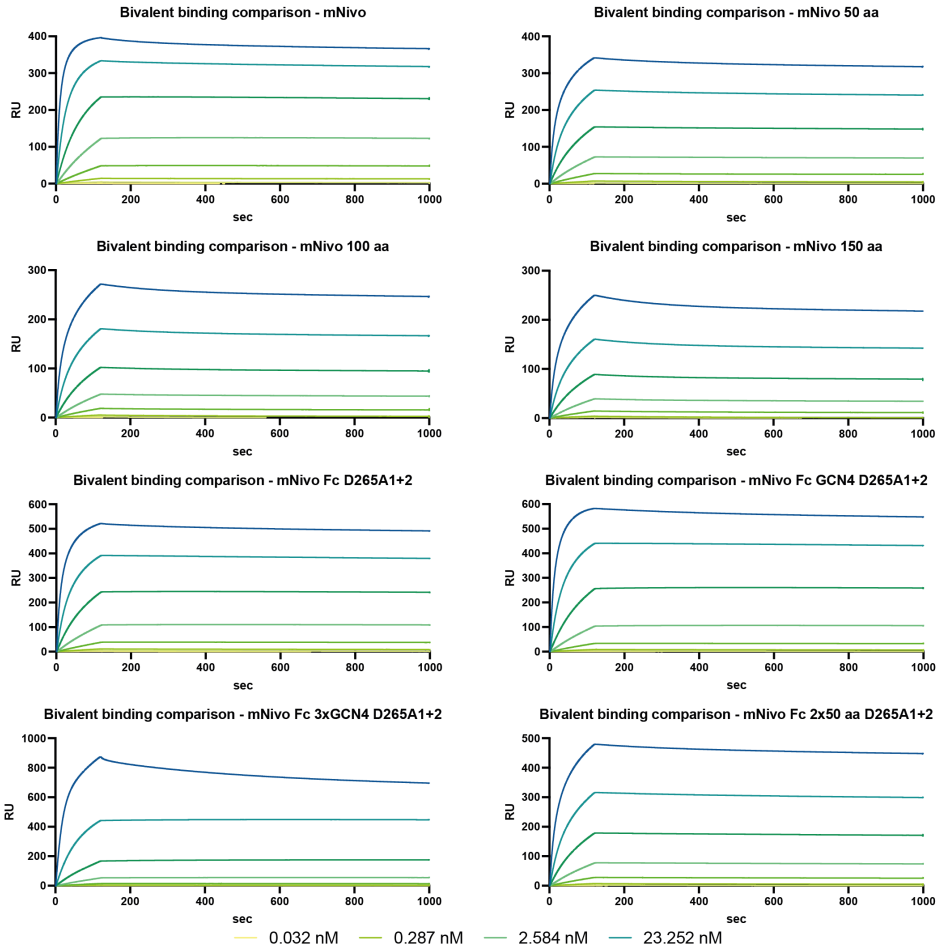
In contrast to the monovalent kinetic analysis, interpretation of this data is more challenging, especially when the dissociation of the analyte protein is low. Using a bivalent analyte model (Figure A.3) revealed a slightly reduced k_{a2} (association rate constant for the second binding event) for the hinge-extended



Antibody	k_a [1/Ms]			k_d [1/s]			K_D [M]		
	Repeat 1	Repeat 2	Average	Repeat 1	Repeat 2	Average	Repeat 1	Repeat 2	Average
mNivo	7.75E+05	8.17E+05	**7.96E+05**	8.68E-03	1.13E-02	**9.98E-03**	1.12E-08	1.38E-08	**1.25E-08**
mNivo 50 aa	1.25E+06	9.31E+05	**1.09E+06**	1.12E-02	1.09E-02	**1.10E-02**	8.90E-09	1.17E-08	**1.03E-08**
mNivo 100 aa	1.95E+06	1.13E+06	**1.54E+06**	1.21E-02	1.02E-02	**1.12E-02**	6.22E-09	9.09E-09	**7.66E-09**
mNivo 150 aa	2.18E+06	1.27E+06	**1.73E+06**	1.19E-02	1.00E-02	**1.09E-02**	5.43E-09	7.87E-09	**6.65E-09**
mNivo Fc D265A1+2	6.65E+05	5.37E+05	**6.01E+05**	8.26E-03	7.35E-03	**7.81E-03**	1.24E-08	1.37E-08	**1.31E-08**
mNivo Fc GCN4 D265A1+2	6.45E+05	5.98E+05	**6.21E+05**	7.89E-03	7.93E-03	**7.91E-03**	1.22E-08	1.33E-08	**1.27E-08**
mNivo Fc 3xGCN4 D265A1+2	7.12E+05	7.58E+05	**7.35E+05**	8.58E-03	9.12E-03	**8.85E-03**	1.21E-08	1.20E-08	**1.20E-08**
mNivo Fc 2x50 aa D265A1+2	9.83E+05	7.70E+05	**8.77E+05**	8.51E-03	9.42E-03	**8.96E-03**	8.65E-09	1.22E-08	**1.04E-08**

Figure 5.5: Comparison of the monovalent kinetics of extended antibodies using SPR
Single-cycle analysis of different forms of mNivo. All variants of mNivo were captured on a Protein A chip and hPD-1-2xHis was injected as analyte with concentrations ranging from 1.7 nM to 2777.78 nM. Sensorgrams were reference- and blank-subtracted. MOPC21 was captured in the reference channel. The Biacore Insight Evaluation Software was used to fit a 1:1 binding model (Figure A.2) and derived affinity constants (k_a, k_d and K_D) are shown in the table below.

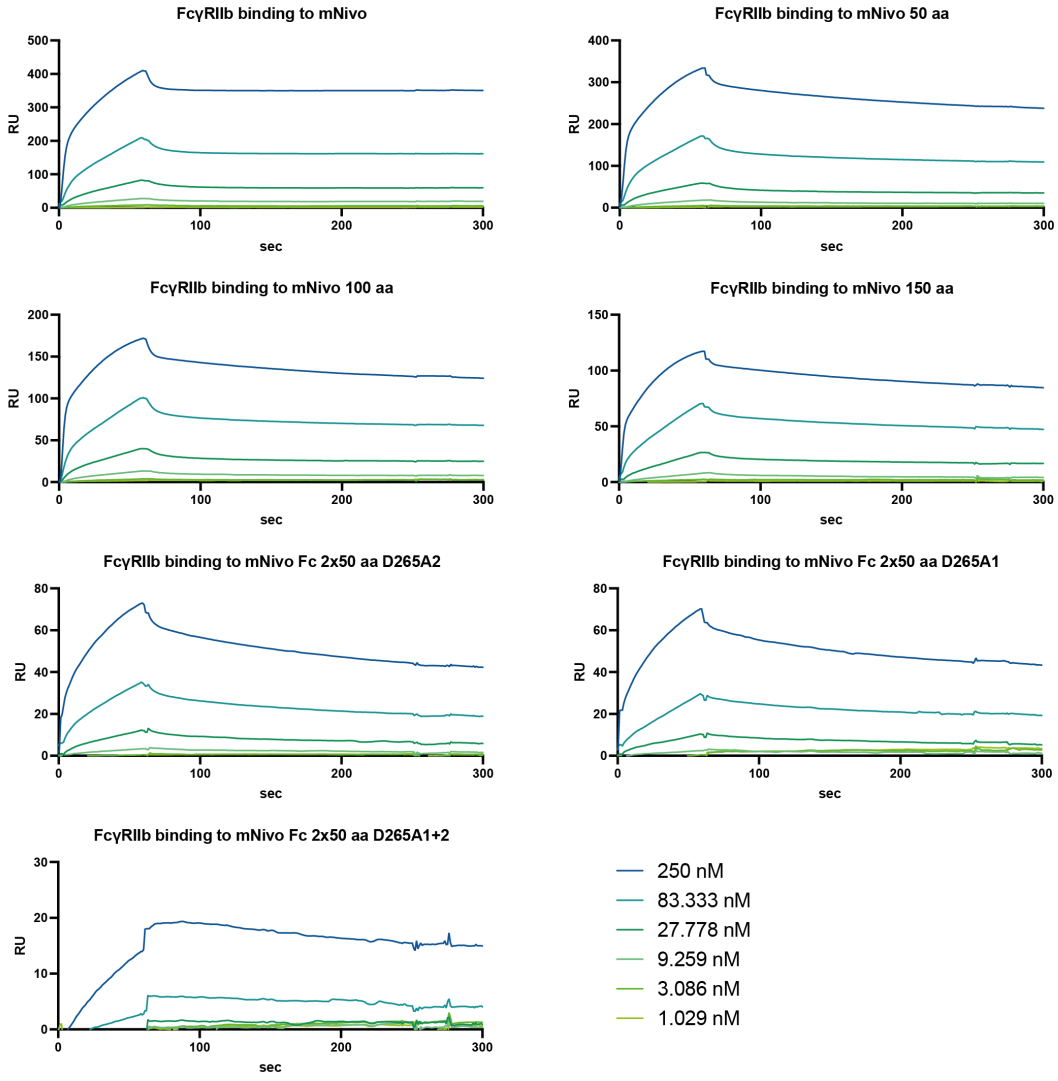
antibodies, indicating that these antibodies required more time to bind with their second 'arm'. In agreement with the previous analysis (Figure 5.5), the k_{a1} was very similar, except for mNivo Fc 3xGCN4 D265A1+2. However, both off-rates (k_{d1} and k_{d2}) were highly different, with k_{d2} values (dissociation rate constant for the second binding event) ranging from 1.77×10^{-1} to 1.32×10^{-6} s^{-1}. This analysis did not fit the data properly, as it was apparent that the off-rates of the antibodies were similar. Thus, a 1:1 dissociation model was fitted to the data to compare the off-rates (Figure A.4). As shown in the right part of the table included in Figure 5.6, the derived k_d rates were very similar, only mNivo 150 aa demonstrated a slightly increased dissociation (2.5-fold higher k_d).



Antibody	Bivalent analyte model - repeat 1						Bivalent analyte model - repeat 2						1:1 dissociation model		
	k_{a1} [1/Ms]	k_{d1} [1/s]	K_{D1} [M]	k_{a2} [1/RUs]	k_{d2} [1/s]	K_{D2} [M]	k_{a1} [1/Ms]	k_{d1} [1/s]	K_{D1} [M]	k_{a2} [1/RUs]	k_{d2} [1/s]	K_{D2} [M]	Repeat 1 [1/s]	Repeat 2 [1/s]	Average [1/s]
mNivo	4.33E+05	1.72E-04	3.97E-10	5.23E-04	3.20E-03	6.11E+00	4.49E+05	2.22E-04	4.96E-10	8.33E-04	2.64E-03	3.17E+00	5.18E-05	3.52E-05	**4.35E-05**
mNivo 50 aa	3.40E+05	9.49E-05	2.79E-10	6.31E-03	2.05E-01	3.26E+01	3.14E+05	9.03E-05	2.88E-10	5.53E-03	1.77E-01	3.20E+01	6.13E-05	4.79E-05	**5.46E-05**
mNivo 100 aa	2.28E+05	1.30E-04	5.68E-10	1.90E-03	7.48E-02	3.94E+01	2.52E+05	1.24E-04	4.92E-10	2.30E-03	6.25E-02	2.72E+01	8.30E-05	6.97E-05	**7.63E-05**
mNivo 150 aa	1.92E+05	2.00E-04	1.04E-09	8.09E-04	3.41E-02	4.22E+01	2.03E+05	1.90E-04	9.35E-10	1.57E-03	7.34E-02	4.69E+01	1.13E-04	1.03E-04	**1.08E-04**
mNivo Fc D265A1+2	4.14E+05	8.95E-06	2.16E-11	1.67E-04	4.22E-03	2.53E+01	4.36E+05	1.14E-04	2.62E-10	6.20E-04	8.40E-03	1.35E+01	4.45E-05	2.57E-05	**3.51E-05**
mNivo Fc GCN4 D265A1+2	3.32E+05	9.12E-05	2.75E-10	1.04E-04	3.16E-03	3.04E+01	5.39E+05	1.57E-02	2.92E-08	5.47E-04	1.32E-06	2.42E-03	4.25E-05	7.00E-06	**2.48E-05**
mNivo Fc 3xGCN4 D265A1+2	2.08E+07	1.30E+01	6.26E-07	3.13E-05	9.78E-05	3.12E+00	1.62E+07	1.15E+01	7.11E-07	2.64E-05	1.03E-04	3.90E+00	1.50E-04	1.06E-08	**7.49E-05**
mNivo Fc 2x50 aa D265A1+2	2.17E+05	9.62E-05	4.44E-10	7.72E-04	5.18E-02	6.71E+01	1.97E+05	9.58E-05	4.87E-10	6.16E-04	4.26E-02	6.92E+01	6.45E-05	5.22E-05	**5.83E-05**

Figure 5.6: Assessment of bivalent binding using SPR
Multi-cycle bivalent binding analysis of different forms of mNivo. hPD-1-2xHis was captured on a NTA chip and antibodies were injected with concentrations ranging from 0.032 nM to 69.758 nM. Sensorgrams were reference- and blank-subtracted. MOPC21 was injected in the reference channel. The Biacore Insight Evaluation Software was used to fit either a bivalent analyte model or a 1:1 dissociation model (Figure A.3 and A.4, respectively) and derived affinity constants (k_{a1}, k_{d1}, K_{D1}, k_{a2}, k_{d2}, K_{D2} and k_d) are shown in the table below.

As the extensions using the coiled-coil protein GCN4 did not result in a significant shift of the elution time in SEC (Figure 5.4), and the antibodies, especially the extension with three GCN4 domains (mNivo Fc 3xGCN4 D26A1+2), were difficult to produce (Figure 5.3), these antibody formats were not further investigated in the subsequent experiments.



Antibody	k_a [1/Ms]	k_d [1/s]	K_D [M]	K_D [M] steady state
mNivo	1.02E+05	1.22E-03	1.20E-08	2.48E-07
mNivo 50 aa	1.01E+05	2.33E-03	2.32E-08	2.53E-07
mNivo 100 aa	1.47E+05	2.11E-03	1.44E-08	1.58E-07
mNivo 150 aa	1.50E+05	1.98E-03	1.32E-08	1.49E-07
mNivo Fc 2x50 aa D265A2	1.02E+05	3.24E-03	3.19E-08	3.07E-07
mNivo Fc 2x50 aa D265A1	8.35E+04	2.81E-03	3.37E-08	6.15E-07
mNivo Fc 2x50 aa D265A1+2	5.22E+03	2.10E-04	4.02E-08	1.60E-03

Figure 5.7: Comparison of binding affinity to mFcγRIIb-His
Multi-cycle binding comparison of mouse FcγRIIb to different forms of mNivo. Antibodies were captured on a Protein A chip and mFcγRIIb-His was injected with varying concentrations ranging from 1.029 nM to 250 nM. Sensorgrams were reference- and blank-subtracted. mNivo D265A was captured in the reference channel. The Biacore Insight Evaluation Software was used to fit a 1:1 binding model (Figure A.5) and a steady-state affinity model and the derived affinity constants (k_a, k_d and K_D) are shown in the table below.

Finally, the binding to a His-tagged mouse FcγRIIb protein (mFcγRIIb-His) was assessed for all hinge-extended antibodies as well as the different D265A-mutated variants of mNivo Fc 2x50 aa (D265A2, D265A1 and D265A1+2, Figure 5.7). This small panel was chosen due to there being limited amounts of mFcγRIIb-His available in our laboratory (produced by Nicole Ashman). Importantly, while it did not comprise all produced antibodies, it included all relevant antibodies, as the remaining ones were all fully mutated to abrogate FcγR binding. mNivo Fc 2x50 aa D265A1+2 was included as a negative control. Likely due to poor protein quality of mFcγRIIb-His, i.e. aggregated material, the sensorgrams did not reflect a typical 1:1 interaction (Figure 5.7). Nevertheless, a 1:1 binding model was used to assess the kinetics and most values were very similar with exception of the mNivo Fc 2x50 aa D265A1/2 constructs, which demonstrated a reduced off-rate. However, the derived affinity constants need to be treated with caution, as the fit of the data was not optimal (Figure A.5) and mNivo Fc 2x50 aa D265A1+2 (negative control) had effectively a very similar K_D, which is in stark contrast to the sensorgram. Importantly, steady-state affinity K_D values were also very similar, with only mNivo Fc 2x50 aa D265A1 demonstrating a slightly reduced affinity ($\sim$ 2.5-fold decrease, Figure 5.7). The derived K_D values from the steady-state analysis are in accordance with published results ranging from 1.5 - 8.3 $\times$ 10^{-7} M[203].

Overall, the SPR analysis demonstrated that the monovalent kinetics remained unchanged. In an effort to investigate the bivalent binding properties of the antibodies, hPD-1-2xHis was captured on a NTA chip. While the dissociation was very similar across all sensorgrams, it was difficult to fit a good model for deriving bivalent kinetic constants. Using a bivalent model to assess the on-rates (k_{a1} and k_{a2}) and a 1:1 dissociation model to compare the off-rates (k_d), only minor differences for the k_{a2} rates of the hinge-extended antibodies were observed. Finally, binding to mFcγRIIb-His was largely comparable across all antibodies tested.

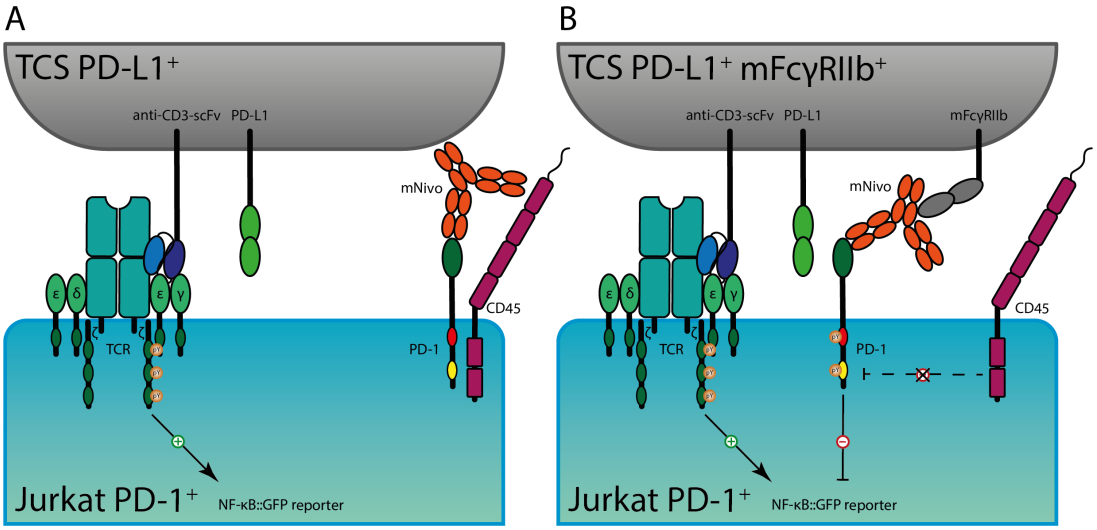


Figure 5.8: *In vitro* T-cell activation assay to assess antibody agonism
Illustration of the adapted two-cell activation assay. The assay depicted in (A) was established in Section 4.2.1 and was modified to express mFcγRIIb as shown in (B).

5.2.5 *In vitro* T-cell activation assay

As the SPR validation demonstrated a broadly similar binding behaviour, the agonistic activity of the antibodies could be tested in an *in vitro* T-cell activation assay. The assay established in Section 4.2.1 was adapted to allow for the investigation of antibody agonism (Figure 5.8). For this, mouse FcγRIIb was lentivirally transduced into TCS cells expressing PD-L1, creating TCS PD-L1$^+$ mFcγRIIb$^+$ cells. Of note, as the inhibitory mFcγRIIb signalling domains might influence the TCS cells, the receptor was truncated to remove all phosphotyrosines (sequence provided in Section A.1.3). According to the KS model for antibody agonism (introduced in Section 1.2.2) and as illustrated in Figure 5.8 A, in the absence of mFcγRIIb, mNivo, bound to PD-1, can exit the close-contact zone and large phosphatases like CD45 can dephosphorylate PD-1. In contrast, when mFcγRIIb binds to mNivo, which in turn binds PD-1, this complex (receptor/antibody/FcγR) should be held in the close contact and, therefore, phosphatases cannot abrogate the activation of PD-1 (Figure 5.8 B). If this model is correct, then Fc-engaging mNivo should act like an agonist when mFcγRIIb is present.

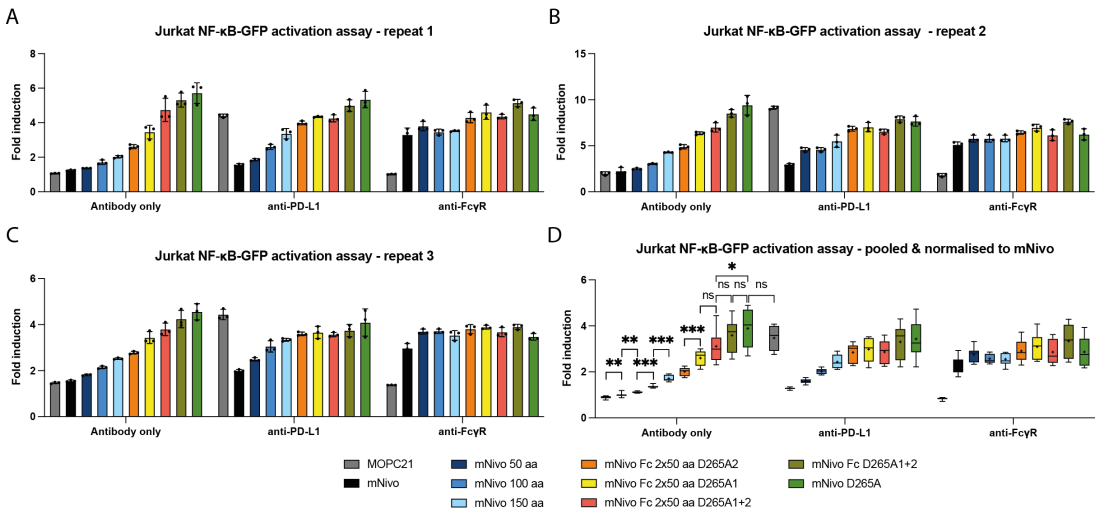


Figure 5.9: *In vitro* T-cell activation assay comparing agonistic activity
Jurkat PD-1$^+$ NF-κB-GFP cells were co-cultured with TCS PD-L1$^+$ mFcγRIIb$^+$ and different antibodies (348.79 nM of each antibody, this is equivalent to 50 µg/mL of mNivo). TCS blocking antibodies (anti-PD-L1 and anti-FcγR) were added at a final concentration of 100 µg/mL.
(A), (B) and (C) depict three independent repeats with three technical replicates each. Normalising the data to mNivo allowed pooling of the data (D).
For bar graphs, data are shown as mean ± SD. For boxplots, the line shows the median, the '+' shows the mean. Whiskers display the 10-90 percentile. Unpaired t-tests were used to compare individual groups.

The T-cell activation assay was further optimised by using commercial blocking antibodies targeted against the human PD-L1 and mFcγRIIb expressed by the TCS cells, instead of co-culturing the Jurkat cells with different TCS cells. This not only allowed for higher throughput, but also enabled the comparison across different groups. This was previously not possible as different Jurkat/TCS cells had varying responding/stimulating capacities, respectively, perhaps due to expression of different TCR levels. Upon optimisation of the blocking conditions (data not shown), the assay was repeated three times.

Figures 5.9 A, B and C show the three independent repeats, whereas for Figure 5.9 D data were normalised against mNivo and pooled. Importantly, upon treatment with an anti-FcγR blocker (clone 93, rIgG2a), all antibodies had a similar capacity to induce GFP expression. However, there were still small differences observed, which can be explained by an incomplete blockade of mFcγRIIb. Treatment with an anti-PD-L1 antibody (clone 29E.2A3, mIgG2b)

served as an additional control to demonstrate that MOPC21 was not suppressing activation, and that the suppressive effects of mNivo were ligand independent. Importantly, blockade with mNivo D265A was not significantly different compared to anti-PD-L1 treatment in the MOPC21 group ($p = 0.217035$). There was a shift towards more activation for all FcγR-engaging mNivo constructs upon treatment with the anti-PD-L1 antibody. This can be readily explained by a competition for mFcγRIIb binding of the anti-PD-1 and anti-PD-L1 antibodies, as the clone used (29E.2A3) is a mIgG2b isotype which exhibits similar affinity to mFcγRIIb as mIgG1[203]. Strikingly, when the co-cultured cells were only treated with mNivo variants or MOPC21, a size-dependent increase in activation was observed (Figure 5.9 D). Comparison of individual groups showed significant differences between the different hinge modifications as well as moving the FcγR binding site from a more hinge-proximal to a hinge-distal site. Although the different antibody constructs greatly improved the *in vitro* T-cell activation compared to mNivo (retaining FcγR binding), there was no improvement over mNivo D265A. While the Fc-multiplexed antibody with no further modification (mNivo Fc D265A1+2) performed as well as mNivo D265A ($p = 0.415282$), there was a small difference between mNivo D265A and mNivo Fc 2x50 aa D265A1+2 ($p = 0.043108$). Furthermore, the best mNivo variant with FcγR binding (mNivo Fc 2x50 aa D265A1) was significantly less potent compared to mNivo D265A ($p = 0.000503$). This indicates that despite the great improvement through extending mNivo, retaining FcγR binding still led to a diminished stimulatory capacity compared to mNivo D265A.

5.2.6 *In vivo* tumour challenges with MC38 models

In order to test whether the effects observed in the *in vitro* T-cell activation model were applicable in an *in vivo* tumour model, the MC38 models were used to compare mNivo, mNivo D265A and two extended variants. In order to account for differences in the molecular weight of each antibody, the treatment regimen

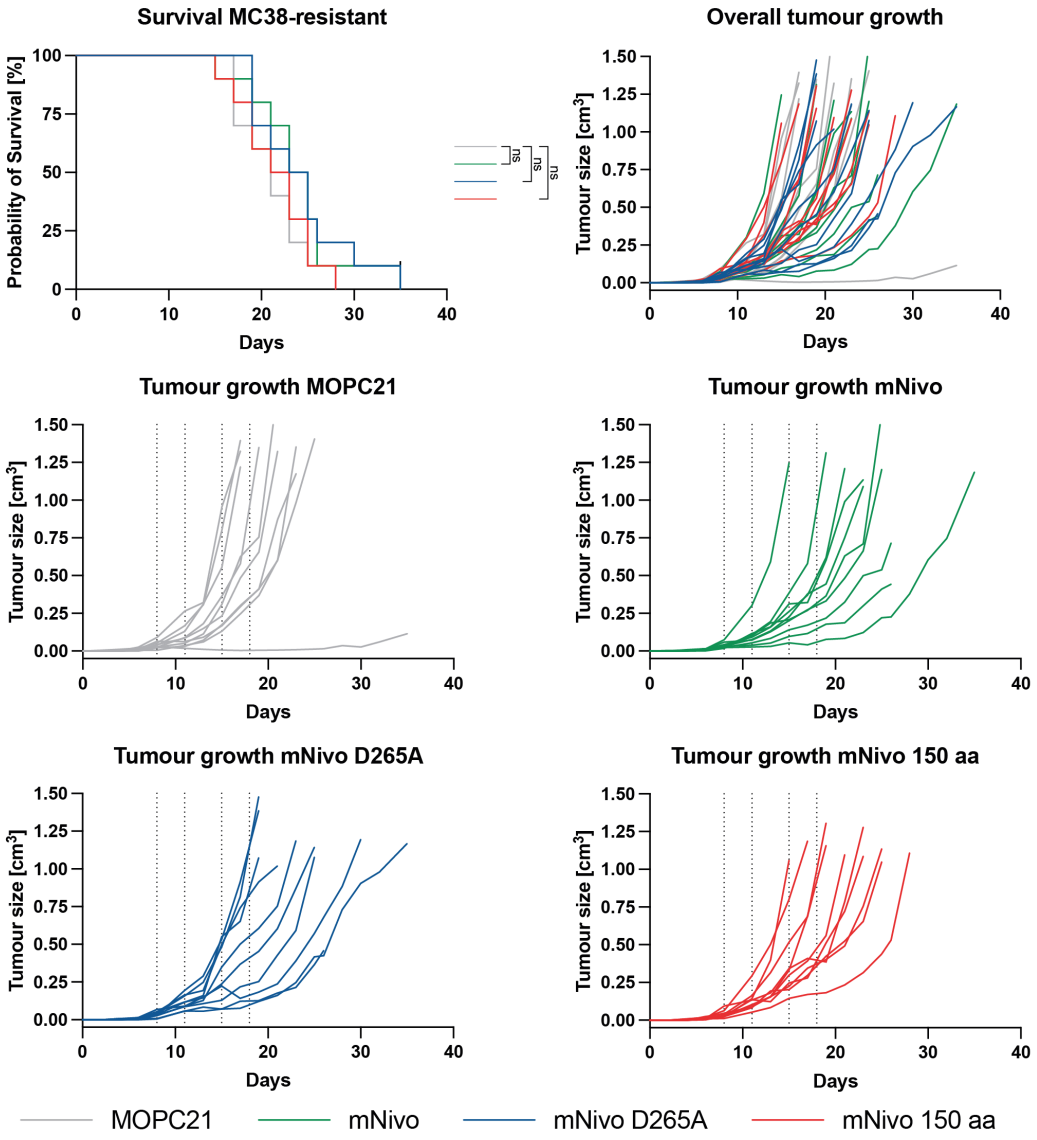


Figure 5.10: Comparison of mNivo variants in the MC38-resistant model Mice were randomised once the average tumour volume reached 40 mm^3 (day 8). Mice were treated twice weekly for two weeks with 1.4 nmol/antibody/treatment, indicated by dashed lines. Survival and tumour growth curves of MC38-resistant tumours treated with MOPC21, mNivo, mNivo D265A and mNivo 150 aa are shown. Mice were culled once the tumour reached the size threshold or an ulceration persisted for over 48 hours. All experiments were randomised and blinded. n = 10/group

was converted to using molar concentrations. All animals were treated with 1.4 nmol/treatment, which is equivalent to 200 µg of mNivo.

First, the largest hinge-extended antibody (mNivo 150 aa), which retained FcγR binding, was tested in the PD-1 blockade-resistant MC38 model (MC38-resistant) in order to investigate whether the modifications could improve efficacy

in a resistant model. As shown in Figure 5.10, no differences were observed for any treatment groups, compared to the MOPC21 isotype control. While there seemed to be individual tumours in the groups treated with mNivo, mNivo D265A and mNivo 150 aa that exhibited a delayed growth (Figure 5.10, top right panel), this was not statistically significant. Furthermore, there was a single mouse in the MOPC21 treated group that had very delayed tumour growth, which only started around day 30.

As no differences were observed between mNivo and mNivo D265A in the MC38-resistant model, the next tumour challenge was carried out using the PD-1 blockade-sensitive MC38 cells (MC38-sensitive). In this experiment, besides MOPC21, mNivo and mNivo D265A, mNivo Fc 2x50 aa D265A1+2 was tested, as this was one of the most potent extended antibodies, as measured by the *in vitro* T-cell activation assay (Figure 5.9 D). Of note, mNivo Fc D265A1+2 and mNivo Fc 2x50 aa D265A1+2 activated Jurkat PD-1$^+$ NF-κB-GFP cells to a similar extent ($p = 0.166386$), however, as the size increase of mNivo Fc D265A1+2 compared to mNivo was relatively small (Figure 5.4), mNivo Fc 2x50 aa D265A1+2 was chosen for further experiments.

As shown in Figure 5.11, while all groups treated with anti-PD-1 antibodies displayed similar numbers of mice with CRs, there was only a significant improvement of survival over the isotype control for mNivo D265A ($p = 0.0026$) and mNivo Fc 2x50 aa D265A1+2 ($p = 0.0145$). Although the final survival outcome was the same between mNivo and the extended variant, as mice treated with mNivo had to be culled earlier, there was no significant difference of the survival curve when compared to the MOPC21-treated group ($p = 0.1766$). Of note, comparing the different mNivo variants with themselves revealed no significant improvements. Thus, while mNivo D265A and mNivo Fc 2x50 aa D265A1+2 performed better than mNivo when compared to the isotype control, this result needs to be treated with caution as the groups did not differ when compared against each other.

Importantly, while long-term stability at 4 °C (Section 5.2.2) as well as short-term stability in cell-culture media at 37 °C (Section 5.2.5) was validated

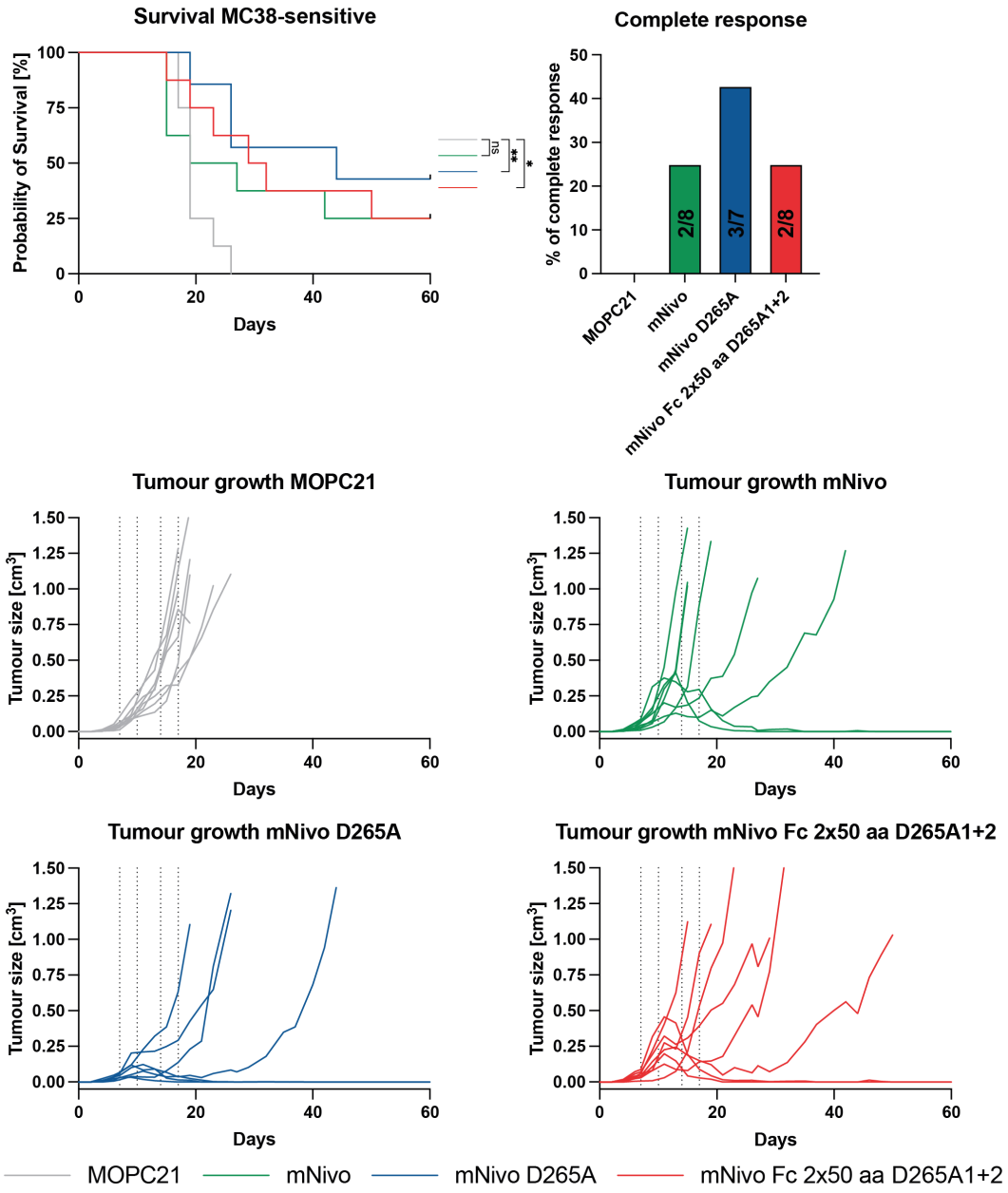


Figure 5.11: Comparison of mNivo variants in the MC38-sensitive model
Mice were randomised once the average tumour volume reached 40 mm^3 (day 7). Mice were treated twice weekly for two weeks with 1.4 nmol/antibody/treatment, indicated by dashed lines. Survival, complete response rate and tumour growth curves of MC38-sensitive tumours treated with MOPC21, mNivo, mNivo D265A and mNivo Fc 2x50 aa D265A1+2 are shown. Mice were culled once the tumour reached the size threshold or an ulceration persisted for over 48 hours.
All experiments were randomised and blinded. n = 8/group
One mouse from the mNivo D265A group needed to be excluded from the study at day 21.

previously, this was the first proof of *in vivo* stability and efficacy of an extended antibody. Considering the significant changes to the overall structure of the antibody, with an approximate 50 % increase in molecular weight, this was an important proof of principle for the overall feasibility of this approach.

5.2.7 *In vivo* challenge with MC38-sensitive mFcγRIIb expressing tumours

The *in vivo* tumour challenge data are in contrast to the strong differences observed between mNivo and mNivo D265A in the *in vitro* T-cell activation assay (Figure 5.9 D) as well as the *in vivo* work by Christopher Paluch, discussed in the introduction, showing a strong improvement upon extension (50 aa of mCD43) or mutation (D265A) of mNivo (Figure 1.9 C). A potential explanation of this phenomenon is the variable availability of FcγR-interactions in the respective models. Thus, in order to test whether increasing FcγR levels within the TME influences the response to mNivo, mFcγRIIb was lentivirally transduced into MC38-sensitive cells. Of note, as the inhibitory mFcγRIIb-signalling domains might influence the tumour cells, the receptor was truncated to remove all phosphotyrosines (sequence provided in Section A.1.3). Thus, the protein should merely bind to antibodies without any signalling effect on the tumour cells.

As shown in Figure 5.12 A, mFcγRIIb was successfully overexpressed on MC38-sensitive cells (referred to as MC38-sensitive-mFcγRIIb). MC38-sensitive-mFcγRIIb cells could bind to mNivo (with FcγR binding capability), but not mNivo D265A or mNivo in combination with an Fc block (anti-FcγR antibodies, Figure 5.12 B). Of note, likely due to an anti-viral response upon lentiviral transduction, MC38-sensitive-mFcγRIIb cells upregulated PD-L1. Over time the expression greatly reduced, however, PD-L1 was still elevated one month after transduction and FACS (Figure 5.12 C). Finally, mFcγRIIb expression was validated *in vivo* by harvesting tumours (MC38-sensitive and MC38-sensitive-mFcγRIIb) after 19 days of growth (Figure 5.12 D).

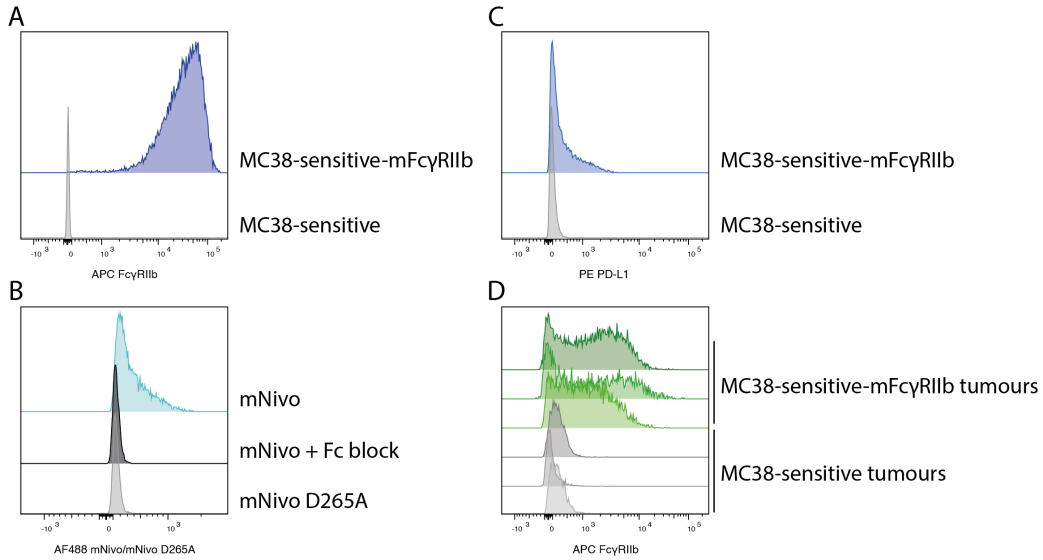


Figure 5.12: Validation of MC38-sensitive cells expressing mFcγRIIb
MC38-sensitive cells were lentivirally transduced with a truncated form of mFcγRIIb.
(A) Comparison of protein levels of mFcγRIIb on parental and transduced MC38-sensitive cells.
(B) mNivo and mNivo D265A were labelled with AF488. Binding to MC38-sensitive cells expressing mFcγRIIb was compared. Cells incubated with an Fc block were used as additional negative control.
(C) Expression level of PD-L1 on parental and transduced MC38-sensitive cells.
(D) After 19 days of *in vivo* growth, MC38-sensitive and MC38-sensitive-mFcγRIIb tumours were harvested. Dead cells and $CD45^+$ cells were excluded by gating. Expression of mFcγRIIb is shown.

Due to the high levels of mFcγRIIb in the TME, mNivo with FcγR binding capability should perform less effectively in MC38-sensitive-mFcγRIIb tumours, compared to the parental tumours. In contrast, mNivo D265A should be unaffected by the presence of mFcγRIIb. Indeed, mNivo D265A performed equally well in the two different MC38 models ($p = 0.3173$), however, the same was also true for mNivo ($p = 0.5336$, Figure 5.13). Furthermore, mNivo D265A led to a significantly increased survival compared to mNivo in the MC38-sensitive-mFcγRIIb model ($p = 0.0494$), but a similar result was also observed in the parental tumours, though not reaching the significance threshold ($p = 0.0554$). Intriguingly, and similar to what was seen in Figure 5.11, when compared against the MOPC21 isotype control treatment, mNivo did not extend the survival significantly ($p = 0.2668$ and 0.4929 for MC38-sensitive and MC38-sensitive-

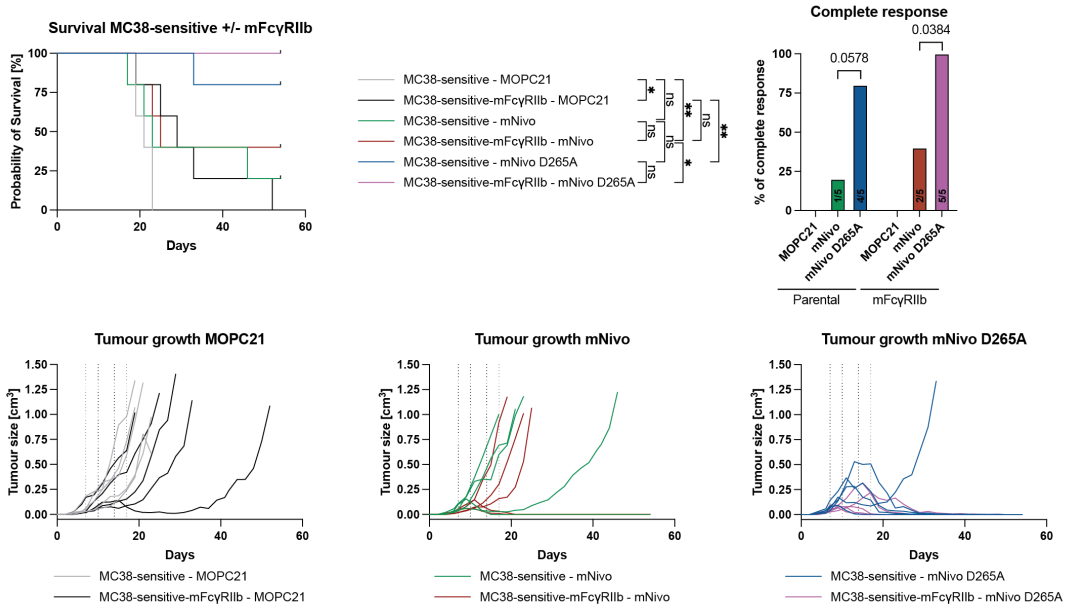


Figure 5.13: Comparison of mNivo and mNivo D265A in MC38-sensitive and MC38-sensitive-mFcγRIIb tumours
Mice were randomised once the average tumour volume across both tumour models reached 40 mm^3 (day 7). MC38-sensitive and MC38-sensitive-mFcγRIIb tumours were randomised independently. Mice were treated twice weekly for two weeks with 200 µg/antibody/treatment, indicated by dashed lines. Survival, complete response rate and tumour growth curves of MC38-sensitive and MC38-sensitive-mFcγRIIb tumours treated with MOPC21, mNivo and mNivo D265A are shown. Mice were culled once the tumour reached the size threshold or an ulceration persisted for over 48 hours. All experiments were randomised and blinded. n = 5/group

mFcγRIIb), whereas this was the case for mNivo D265A (p = 0.0025 and 0.0018 for MC38-sensitive and MC38-sensitive-mFcγRIIb). It is important to note that MC38-sensitive-mFcγRIIb tumours grew more slowly, as evident by the significant differences observed for the MOPC21 isotype control (p = 0.0271). This might be partly explained by a continued antiviral response of the lentivirally transduced cells (MC38-sensitive-mFcγRIIb), indicated by residual baseline PD-L1 levels as shown in Figure 5.12 C.

Overall, this experiment suggests that mNivo D265A is more potent than mNivo in the PD-1 blockade-sensitive MC38 colorectal cancer model, however, upregulation of mFcγRIIb did not influence the efficacy of mNivo. Future experiments will need to establish a better model to further investigate this, as there was a significant difference in the isotype treated animals.

5.2.8 Combination of PD-1 and mFcγRIIb blockade

As explained above, the data in Figure 5.13 indicated that upregulation of mFcγRIIb in the TME did not diminish the potency of mNivo. While the model used requires more optimisation, another possibility for the lack of effect observed might be the location of FcγR expression, as FcγR interactions can also occur in the draining lymph nodes of the tumours. Therefore, to block mFcγRIIb systemically, AT128, an anti-mFcγRIIb blocking antibody[334], was used. The antibody was kindly provided by Mark Cragg (University of Southampton). Due to the limited amounts available, the combination therapy could only be tested for mNivo and mNivo D265A, and not MOPC21. Furthermore, the group sizes had to be limited to 5/group. As shown in Figure 5.14, co-blockade of PD-1 and mFcγRIIb had no effect on the tumour growth and survival, compared to anti-PD-1 monotherapy. Surprisingly, the difference observed between mNivo and mNivo D265A (Figure 5.13) was not reproduced in this experimental cohort.

5.2.9 Comparison of mNivo and mNivo D265A across experiments

As described in Sections 1.3.3.3 and 5.1, there is growing evidence for superior efficacy upon reduction of Fc-engagement of anti-PD-1 antibodies. Using the MC38 colorectal cancer model, Ravetch and colleagues found significantly diminished tumour growth in Fcgr2b$^{-/-}$ mice compared to WT mice[235] and the group of Mikael Pittet demonstrated an augmented response upon combination of PD-1 blockade with Fc blockade (using clone 2.4G2 blocking mFcγRIIb and mFcγRIII)[237]. In contrast, Moreno-Vicente *et al.* found no significant improvement of survival when using a N297A mutated mIgG1 PD-1 antibody (Fc-null), compared to the parental mIgG1 PD-1-blocking antibody in the MC38 tumour model[238]. Although antigen-specific T cells exhibited increased proliferation in a vaccination setting using OVA antigen, the anti-tumour activity was not enhanced. However, they found increased levels of PD-1 on CD8^{+} T cells and more activated myeloid cells, suggesting a stronger activation through the Fc-null anti-PD-1 antibody[238].

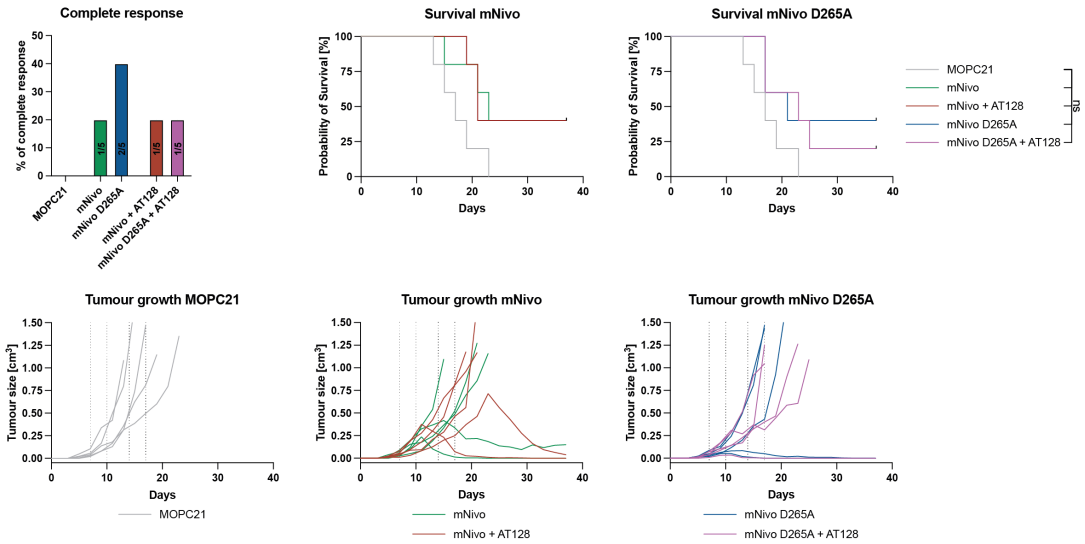


Figure 5.14: Combination of mNivo or mNivo D265A with the anti-mFcγRIIb blocker AT128
Mice were randomised once the average tumour volume reached 40 mm^3 (day 7). Mice were treated twice weekly for two weeks with 200 µg/antibody/treatment, indicated by dashed lines. Survival, complete response rate and tumour growth curves of MC38-sensitive tumours treated with MOPC21, mNivo, mNivo D265A and combinations with AT128 are shown. Mice were culled once the tumour reached the size threshold or an ulceration persisted for over 48 hours.
All experiments were randomised and blinded. n = 5/group

Overall, the effects observed when investigating the Fc-dependency of PD-1 antibodies in MC38 tumours can vary significantly.

In an attempt to create a better model to investigate the confounding effects of FcγR engagement by mNivo, mFcγRIIb was upregulated in the MC38-sensitive model, but no change in mNivo efficacy was observed (Section 5.2.7). Similarly, combination with AT128, an anti-mFcγRIIb blocking antibody, did not enhance potency of mNivo (Section 5.2.8). Finally, extending mNivo (mNivo Fc 2x50 aa D265A1+2) did not result in greater efficacy either (Section 5.2.6). Importantly, while the antibodies tested and models or combinations trialled were distinct in the aforementioned experiments, they all included monotherapy with MOPC21, mNivo and mNivo D265A in the parental MC38-sensitive model. Thus, the data could be pooled to increase the statistical power and investigate an effect across the three datasets.

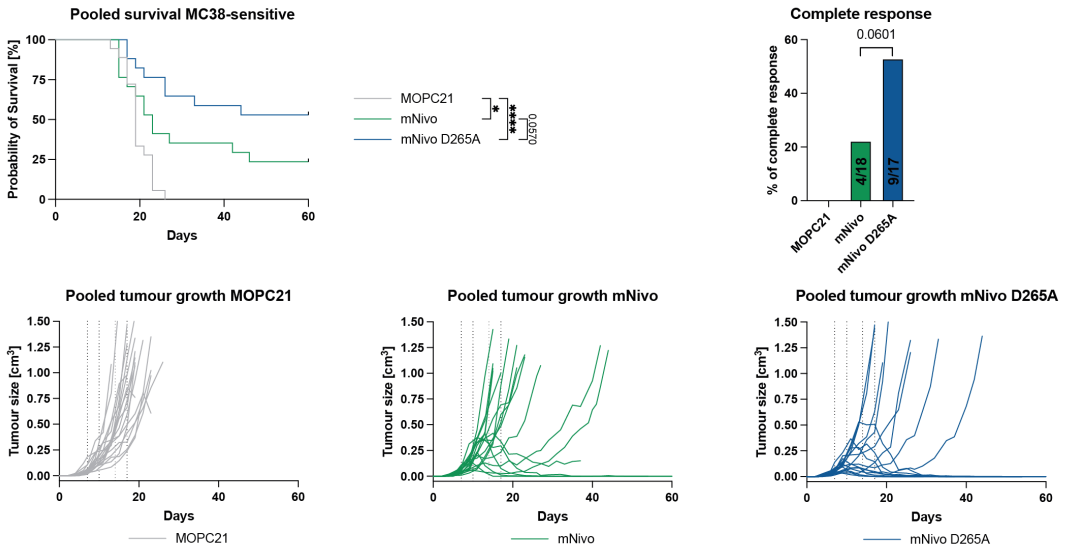


Figure 5.15: Pooled data from experiments comparing MOPC21, mNivo and mNivo D265A
The individual experiments are shown in Figures 5.11, 5.13 and 5.14. Data were pooled of all experiments. As the experiment in Figure 5.14 was stopped at day 37 and there was one mouse with a stable disease, this mouse was excluded from the pooled survival analysis, but it is included in the CR rate and tumour growth curve. Once mice exhibited a CR, they were considered to be long-term survivor, independent of the individual termination of the respective experiment.
In each experiment, mice were randomised once the average tumour volume reached 40 mm^3 (day 7). Mice were treated twice weekly for two weeks with 200 µg/antibody/treatment, indicated by dashed lines. Pooled survival, complete response rate and tumour growth curves of MC38-sensitive tumours treated with MOPC21, mNivo and mNivo D265A are shown. Mice were culled once the tumour reached the size threshold or an ulceration persisted for over 48 hours.
All experiments were randomised and blinded. n = 17-18/group

The pooled data are shown in Figure 5.15. mNivo and mNivo D265A led to a significant extension of survival compared to MOPC21-treated animals ($p = 0.0203$ and < 0.0001, respectively). Most importantly, the survival analysis demonstrated a clear trend towards increased overall survival when comparing mNivo and mNivo D265A ($p = 0.0570$). In fact, using the Gehan-Breslow-Wilcoxon test instead of the Mantel-Cox test to analyse the survival curves resulted in a significant result ($p = 0.0493$). The key difference between those two methods is that the Gehan-Breslow-Wilcoxon test gives more weight to early deaths, whereas the Mantel-Cox test weights all time points equally. Independent of the respective p-values, the trend for improved efficacy is clear when the three

experiments were pooled. This was also supported by the comparison of CR rates using chi-square tests ($p = 0.0601$).

5.3 Discussion

Based on the mounting evidence suggesting an important role of FcγR-binding for immune-checkpoint inhibitor efficacy[209,233,335], the work described in this chapter investigated whether antibody-driven agonism might be one of the confounding properties of Fc-engaging nivolumab. This hypothesis is based on the KS model for receptor triggering (introduced in Sections 1.2.1.3 and 1.2.2), which concludes that the overall size of an NTR, or a complex associated with it, determines its activation. As large phosphatases such as CD45 are sterically excluded from close contacts, proteins that can remain within this zone, due to their small overall size, may get phosphorylated by kinases[55]. Therefore, modulating the distance between the antigen- and FcγR-binding site of the anti-PD-1 antibody nivolumab mIgG1 (mNivo) should influence its triggering ability of PD-1. Using two different approaches for increasing the overall size of the antibody, either by insertion of sections of the highly glycosylated protein mCD43 into the hinge region or by Fc multiplexing, an increase of *in vitro* T-cell activation could be demonstrated (discussed in greater detail in the following paragraph). Importantly, the distance between the antigen- and FcγR-binding site was the determining factor, as shown by the repositioning of the D265A mutation in one of the Fc-multiplexed antibodies. Mutation of the second Fc domain (D265A2), therefore allowing binding in the first, was not as effective at activating T cells compared to the same antibody with a mutation in the first Fc domain (D265A1). However, despite significant improvement over mNivo (Fc-engaging), none of the produced antibodies outperformed mNivo D265A (Fc-null). Finally, likely due to greater variability associated with *in vivo* experiments, this data could not be fully recapitulated in mouse tumour models. An attempt to increase the therapeutic window between mNivo and mNivo D265A by upregulation of a truncated form of mFcγRIIb requires further optimisation. Importantly, mNivo D265A showed

a clear trend for increased anti-tumour activity compared to mNivo. This is in accordance with previous data published for other anti-PD-1 antibodies[235,237,239].

While SEC was used to demonstrate an increase of the antibody size (Figure 5.4), an earlier elution volume did not necessarily correlate with increased T-cell activation *in vitro* (Figure 5.9). Especially the hinge-extended antibodies with 100 and 150 aa extension of mCD43 eluted very early but only showed a modest effect in the *in vitro* assay. It is important to note that an earlier elution in SEC does not necessarily correlate with the actual particle size, but rather with the hydrodynamic radius (Stokes radius)[336], which can be influenced by antibody glycosylation[337]. Thus, due to the insertion of heavily-glycosylated sequences, the two approaches for extending antibodies (hinge-extension and Fc-multiplexing) are difficult to compare with each other in regards to the protein size derived from the SEC analysis. Furthermore, it should be noted that the persistence length of mucins is around 15 nm[331,332]. As mCD43, a mucin-like protein, extends by approximately 0.2 nm per amino acid[327], this would mean that only the first 75 amino acids behave like a rigid rod. Thus, the extension using 100 and 150 aa of mCD43 might not be as effective in increasing the overall size. Furthermore, as the distance between antigen- and FcγR-binding site is the determining factor, the actual size of the antibody might be less meaningful. Importantly, there are novel microscopy-based methods to measure the height of proteins with $\sim$ 1 nm resolution[338], which could be utilised to compare the gap created between the different receptor/antibody/FcγR complexes. An attempt to establish this in our laboratory, in collaboration with João Ferreira Fernandes (Davis group), will require further optimisation.

SPR was used to measure the binding kinetics of the mNivo variants. A reduced capture level of the extended antibodies was observed when immobilising them as ligands on a Protein A chip (Section 5.2.4). It should be noted that both the Protein A as well as the NTA chip are based on the CM5 sensor chip, which has a $\sim$ 100 nm layer of carboxymethylated dextran matrix attached to the gold layer, which is approximately 50 nm thick[339]. The effective penetration depth to detect

changes in the refractive index of the Biacore SPR system is about 150 nm[339]. Thus, molecules need to enter the dextran matrix to get detected, which can prove difficult for large molecules (> 1,000,000 Da)[339]. This should not be the case for our antibodies, though the impact of the glycosylation on this is difficult to predict. Importantly, as no reduced RU were observed when using the antibodies as analytes binding to hPD-1-2xHis captured on a NTA chip, a potential issue with the antibodies being too large to enter the carboxymethylated dextran matrix on the SPR chips can be excluded. Nevertheless, a follow-up experiment could include the use of a CM3 sensor chip, which harbours shorter dextran chains, thereby reducing potential steric effects when injecting large molecules. Furthermore, the impact of the different modifications on the interaction with Protein A is unknown. Theoretically, the Fc-multiplexed variants might bind to two Protein A molecules, therefore reducing the overall availability of Protein A binding sites for each antibody. Importantly, this did not affect the kinetic measurements, thus allowing the comparison of the mNivo variants.

While the monovalent affinities remained unchanged (Figure 5.5), there were subtle differences observed for the on-rates of the second Fab-arm for the hinge-extended antibodies (Figure 5.6). This is not surprising, as the insertion is likely influencing the overall flexibility of the antibodies. While the bivalent analyte model successfully reported on-rates for the first and second binding event, the off-rate analysis proved more difficult. Due to the high monovalent affinity ($K_D = 1.25 \times 10^{-8}$ M, Figure 5.5) of mNivo, there was only little protein dissociating. When bivalently bound to the chip, the antibodies could unbind with one arm and subsequently re-bind, resulting in no change of the sensorgram as only mass changes on the chip can be measured by SPR. Thus, a 1:1 dissociation model was fitted in order to compare the off-rates. Importantly, the off-rates obtained from this analysis did not demonstrate significant changes, except for mNivo 150 aa which had a 2.5-fold higher k_d. In an effort to test whether the reach of the hinge-extended antibodies is increased, very low levels of hPD-1-2xHis were captured on a NTA chip ($\sim$ 10 RU). While a fast dissociation, indicating

increased monovalent binding, was observed for mNivo, this was not the case for the hinge-extended antibodies (data not shown). To address this in more detail, a collaboration with the Dushek laboratory (Sir William Dunn School of Pathology, University of Oxford) was initiated as they have developed a novel algorithm to analyse SPR data, allowing inferences about the reach of an antibody from a bivalent SPR run. This work is still in progress. Finally, mNivo Fc 2x50 aa D265A1 exhibited a slightly reduced affinity for mFcγRIIb (2.5-fold reduction, Figure 5.7). As this antibody harbours a D265A mutation in the first Fc domain, but no mutation in the second Fc domain, this is likely explained by the missing hinge region, which was shown to be important for FcγR binding to hIgG1 and hIgG4[340].

Using an *in vitro* T-cell activation assay, it was shown that nivolumab expressed as mIgG1 (mNivo) harboured strong agonistic activity when co-cultured with stimulating cells expressing mFcγRIIb (Figure 5.9). This itself is a very surprising result, considering that nivolumab hIgG4 is used routinely in the clinic to block PD-1 activation through its ligands. Importantly, this result was confirmed to be true for nivolumab hIgG4 and hFcγRIIb (data not shown) by our collaborator Peter Steinberger (University of Vienna). Furthermore, a recent paper demonstrated inherent agonistic activity of nivolumab hIgG4, which could be increased by reducing its affinity to PD-1[103]. The concept of reduced affinity leading to stronger agonism was discussed in Section 1.2.2.1. Thus, the agonistic activity of mNivo is unlikely to be an artifact of our assay, as it has been observed by other groups. Importantly, the agonism could be reduced in a size-dependent manner as demonstrated by the different amounts of mCD43 inserted into the hinge region (Figure 5.9). Similarly, creating a larger gap between the antigen-binding domain and the FcγR interaction site, without changing the overall size of the antibody, also resulted in reduced PD-1 activation. However, none of the extended antibodies performed better than mNivo D265A, indicating that the removal of the Fc-binding capacity is sufficient to reduce agonism to a minimal level. Furthermore, mNivo Fc 2x50 aa D265A1+2, one of the most potent extended antibody tested (Figure 5.9), was slightly less effective

compared to mNivo D265A. As this antibody harbours D265A mutations in all Fc regions, it should, theoretically, be as effective as mNivo D265A, as the binding characteristics have not changed (Section 5.2.4). The observed differences might have two different explanations. First, while the antibodies were carefully produced and validated, the significant changes made to the overall structure of the antibody might contribute to a less stable molecule, potentially leading to small aggregation over time, which could result in an activation of PD-1. Second, as the antibody comprises two Fc domains, each with a D265A mutation, and the D265A mutation was shown to greatly diminish but not completely abolish FcγR binding[213], this could result in a small increase in affinity towards FcγRs. Indeed, when mNivo Fc 2x50 aa D265A1+2 was used as a negative control in the SPR assay to measure affinity to mFcγRIIb and mNivo D265A was used in the reference channel (Figure 5.7), some binding towards the extended antibody was observed at high concentrations of mFcγRIIb. Importantly, mNivo Fc D265A1+2, which also harbours two Fc domains with two D265A mutations, was as effective as mNivo D265A, making it unlikely that this effect contributed to the reduced efficacy of mNivo Fc 2x50 aa D265A1+2.

The effects observed *in vitro* were not fully recapitulated in the *in vivo* tumour models. As shown in Figures 5.10 and 5.11, there were only small, non-significant trends when comparing mNivo, mNivo D265A and the extended antibodies against each other. This might be explained by the limited FcγR availability within the TME, resulting in little/no agonism. To test this hypothesis, MC38-sensitive cells were engineered to express a truncated form of mFcγRIIb. However, mNivo performed equally well in the MC38-sensitive and MC38-sensitive-mFcγRIIb tumours (Figure 5.13). It is important to note that MC38-sensitive-mFcγRIIb tumours displayed a slower tumour growth, potentially arising from the anti-viral immune response upon lentiviral transduction. Future experiments will focus on optimising this model. Finally, a blocking antibody specific for mFcγRIIb (AT128) was used in combination with mNivo to investigate whether this co-blockade could enhance the efficacy of mNivo. The rationale for testing this

was that mNivo-driven agonism could also take place in tissues outside of the tumour. While no difference was observed upon combining AT128 with mNivo (Figure 5.14), this experiment had two major drawbacks. First, AT128 has a low affinity for mFcγRIIb (K_D = 1.4 × 10^{-7} M[334]), which did not result in a complete blockade of IgG-containing immune complexes[334], as the mIgG1-mFcγRIIb affinity is of similar strength (K_D = 1.5 × 10^{-7} M)[203]. Second, while the work in this chapter solely focused on mFcγRIIb, mIgG1 can also be bound by mFcγRIII with a similar affinity (K_D = 2.3 × 10^{-7} M)[203]. Thus, follow-up experiments should focus on a combination therapy using an antibody blocking both receptors, mFcγRIIb and mFcγRIII, with high affinity. For example, clone 2.4G2 (K_D = 8.7 × 10^{-11} M towards mFcγRIIb[334]) could be used, and it was already demonstrated that combination of 2.4G2 with an anti-PD-1 blocker (clone 29F.1A12, rIgG2a isotype) greatly enhanced efficacy[237]. The rIgG2a isotype has a similar FcγR binding profile compared to mIgG1, as it only binds to mFcγRIIb and mFcγRIII with low affinity[235]. According to the KS model for antibody-agonism (Section 1.2.2), the involved FcγR should not make a difference, as long as the receptor dimensions and affinities are similar. Thus, despite the focus on mFcγRIIb, the observed results should be transferable to other FcγRs. An exception might be the high-affinity receptor FcγRI as it harbours an additional Ig domain, thereby potentially creating larger complexes when bound to an antibody. In accordance with this, reduced agonism when bound to hFcγRI was described for the superagonist TGN1412[85].

Collating of the mouse tumour model data revealed an increased efficacy of mNivo D265A compared to mNivo (Figure 5.15). Although the strength of this effect differed between individual experiments (Figures 5.11, 5.13 and 5.14), it became more obvious upon pooling of all datasets (Figure 5.15). Thus, it is exciting to see the clinical development of tislelizumab (BGB-A317, BeiGene), the first PD-1 blocking antibody with mutations to abrogate FcγR-binding[240]. Of note, BeiGene's rationale for developing an anti-PD-1 antibody with no

Fc engagement was driven by their observation that the WT hIgG4 antibody targeting PD-1 can trigger phagocytosis of PD-1$^+$ T cells *in vitro*[239].

Taken together, the work described in this chapter demonstrated that increasing the size of mNivo (nivolumab mIgG1) greatly reduced FcγR-dependent agonism, with the distance spanning the antigen- and FcγR-binding site being the determining factor. The extended antibodies improved T-cell activation *in vitro* compared to the Fc-engaging mNivo, however, none of the produced variants was more potent than mNivo D265A. Furthermore, while an increased *in vivo* efficacy was observed for mNivo D265A over mNivo, the effects were considerably smaller compared to the *in vitro* data and further work is needed to elucidate this in more detail. Finally, the increase in efficacy *in vivo* can have different contributing factors and follow-up experiments are needed to determine to what extent this is driven by antibody agonism (discussed in more detail in Section 7.1.3).

We especially need imagination in science. It is not all mathematics, nor all logic, but it is somewhat beauty and poetry.

— Maria Mitchell

6

Rigid, extended forms of nivolumab mIgG1 to increase efficacy

Contents

6.1 Rationale 162
6.2 Results 164
6.2.1 Design of hinge-deleted antibodies and Fc-linker optimisation 164
6.2.2 Validation of hinge-deleted antibodies and Fc-linker optimisation 167
6.2.3 Design of rigid, extended antibodies 169
6.2.4 Purification of rigid, extended antibodies using Protein A and SEC 171
6.2.5 Comparison of size using SEC 173
6.2.6 SPR validation of rigid, extended antibodies 173
6.2.7 *In vitro* T-cell activation assay 176
6.2.8 Supported lipid-bilayers for studying nivolumab mIgG1-driven PD-1 contact enrichment 177
6.3 Discussion 181

6.1 Rationale

None of the extended antibodies produced in Chapter 5 performed better compared to mNivo with a D265A mutation. Hypothetically, and based on the KS model for antibody agonism (Section 1.2.2), while mNivo D265A cannot

be held in the close-contact zone through interactions with FcγRs, it can still, in principle, remain in there due to its overall small dimensions, thus potentially resulting in the activation of PD-1. Theoretically, this should also happen independently of ligands or antibodies interacting with the receptor, leading to a constant, subtle signalling of PD-1. The concept of PD-1 tonic signalling was recently investigated by Fernandes *et al.*[341]. First, they demonstrated that knockout of PD-1 in Jurkat T cells led to an increase in T-cell activation upon stimulation with anti-CD3 antibodies[341]. This was independent of PD-1-ligand engagement, as treatment with nivolumab had no effect. Following this, they developed a hetero-bispecific diabody (scFv heterodimer) that binds to PD-1 and the phosphatase CD45 in *cis*, bringing them into close proximity with each other[341]. The PD-1/CD45 diabody, termed receptor inhibition by phosphatase recruitment (RIPR), greatly increased T-cell activation *in vitro* as well as tumour control *in vivo*, compared to traditional anti-PD-1 antibodies. Finally, they extended this concept also to other NTRs (defined in Section 1.2), including CD28, CTLA-4 and SIRPα[341]. Importantly, it was also demonstrated that the binding of molecules that are small enough to remain within close contacts when complexed with the TCR, i.e. a Fab or pMHC, reduced the diffusion of the TCR, therefore prolonging its time within these phosphatase-depleted zones, ultimately resulting in enhanced TCR triggering[70]. This should also hold true for other small NTRs, such as PD-1, when they are bound by an antibody, although an antibody is larger than a Fab or pMHC molecule. Overall, these data suggest the possibility that small complexes formed by PD-1 and antibodies, if they remain in the close contact, might continue to signal even though ligand binding is blocked[70]. Ideally, complete removal of PD-1 from the close contact would be the most effective way to block PD-1 signalling[341].

As the extended forms of mNivo designed in Chapter 5 failed to reduce inhibitory signalling by PD-1 beyond the levels of mNivo D265A, this suggested they did not diminish the potential residual signalling of PD-1 (as described above) and new strategies for engineering nivolumab mIgG1 had to be considered. This

chapter explored the idea that the inherent flexibility of antibodies is the reason for the lack of improvement over mNivo D265A. The hinge region is disordered and very flexible, thereby allowing antibodies to bind epitopes at various distances and arrangements[201]. However, for the extended antibodies in Chapter 5, this could result in an orientation of the antibody that allows the PD-1/antibody complex to remain in the close-contact zone, therefore not reducing tonic PD-1 signalling.

The myeloma proteins Dob and Mcg are hIgG1 antibodies with a deleted hinge region, which resulted in their reduced flexibility and allowed the crystallisation of both molecules[342,343]. Thus, removal of the hinge region should also produce a more rigid form of nivolumab mIgG1. Additionally, the combination of the hinge deletion with Fc multiplexing to extend the overall size of the molecule should result in a rigid, extended antibody, that is sterically excluded from the close contact when bound to PD-1. Ultimately, this might further reduce signalling by PD-1 compared to mNivo D265A, which is small enough to remain within close contacts.

6.2 Results

6.2.1 Design of hinge-deleted antibodies and Fc-linker optimisation

A recent report described the generation of hinge-deleted hIgG1 and hIgG4 antibodies, suggesting that this could indeed be a generalisable approach for creating new forms of monoclonal antibodies[340]. Figure 6.1 A shows the alignment of the heavy chain sequences of mIgG1, hIgG1 and hIgG4, with the respective hinge regions coloured in red. A grey box denotes the deletions observed and created previously for the human isotypes[340,342,343]. As a hinge-deleted mIgG1 has not been reported before, new constructs encoding hinge-deleted forms of mNivo D265A were created by Mai Vuong using chimera PCRs (Figure 6.1 B, grey letters indicate the different deletions for each construct).

As the Fc-multiplexed constructs in Chapter 5 were designed with a long flexible linker (GGGGS) to allow for HC-LC pairing, this introduced additional

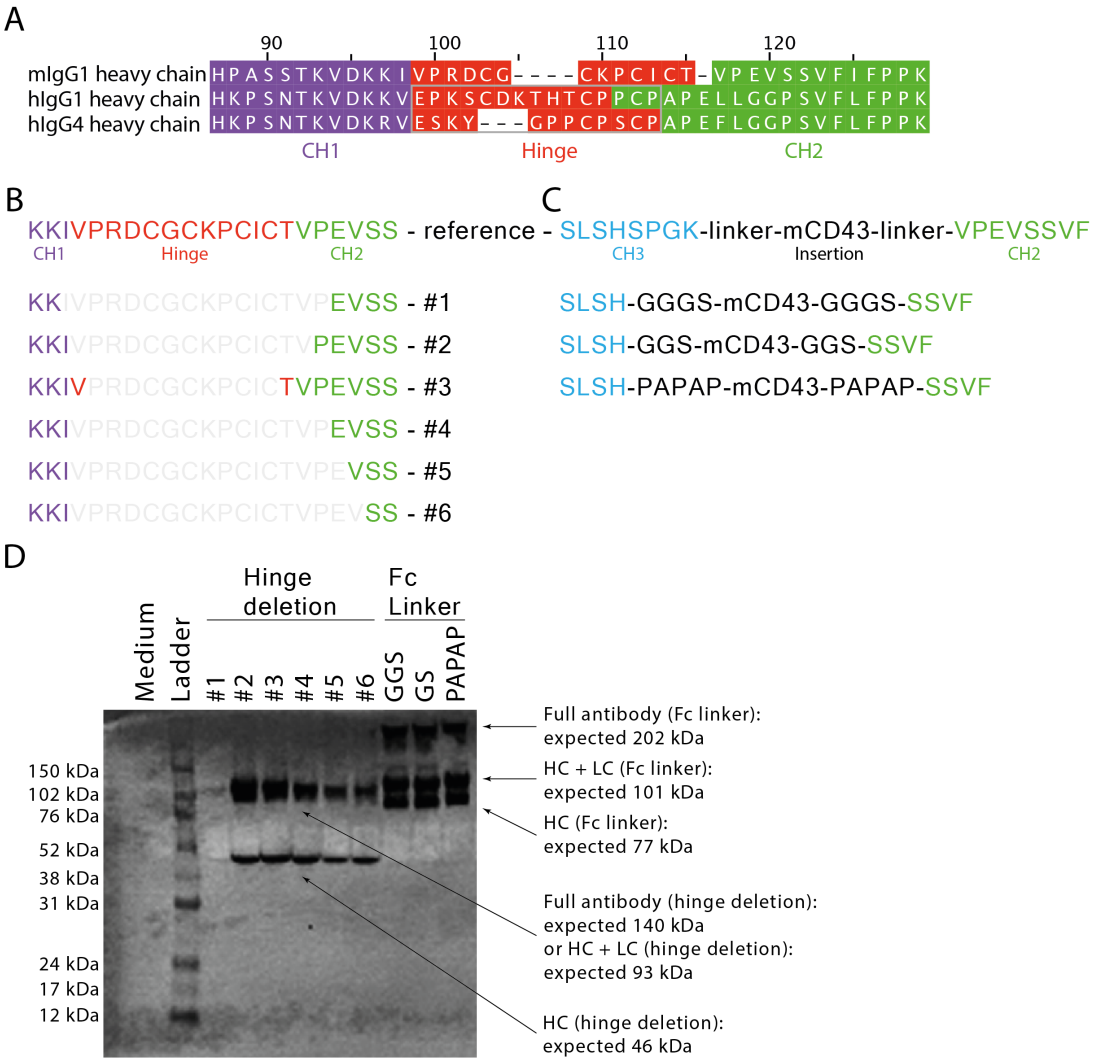


Figure 6.1: Design of hinge-deleted antibodies and Fc-linker optimisation
(A) Alignment of the heavy chains of mIgG1, hIgG1 and hIgG4. Sequences were retrieved from UniProt and aligned using Clustal Omega[344]. CH1 is coloured in purple, the hinge region in red and CH2 in green. A grey box indicates the described deletions in the myeloma proteins Dob[342] and Mcg[343] as well as from a recent report creating hinge-deleted hIgG1 and hIgG4 antibodies[340].
(B) Depiction of the different hinge-deleted mIgG1 constructs designed. Colour scheme as in (A). Grey letters indicate the respective deleted sequence.
(C) Depiction of the different Fc-linker optimisation constructs designed. CH3 of the first Fc is coloured in cyan, CH2 of the second Fc is coloured in green. Structures of mIgG1 CH2 and CH2-CH3 (PDB ID 1CQK[345] and 3HKF[346], respectively) were used to identify potentially flexible amino acids. Different linkers (GGS, GS, PAPAP) were inserted between the constant domains and the 50 aa of mCD43.
(D) Western blot of a non-reducing SDS-PAGE gel using an anti-mouse-Fc-HRP antibody. A rainbow ladder was included for size approximation. Medium served as a negative control. The expected molecular weights were calculated using Expasy ProtParam[333].

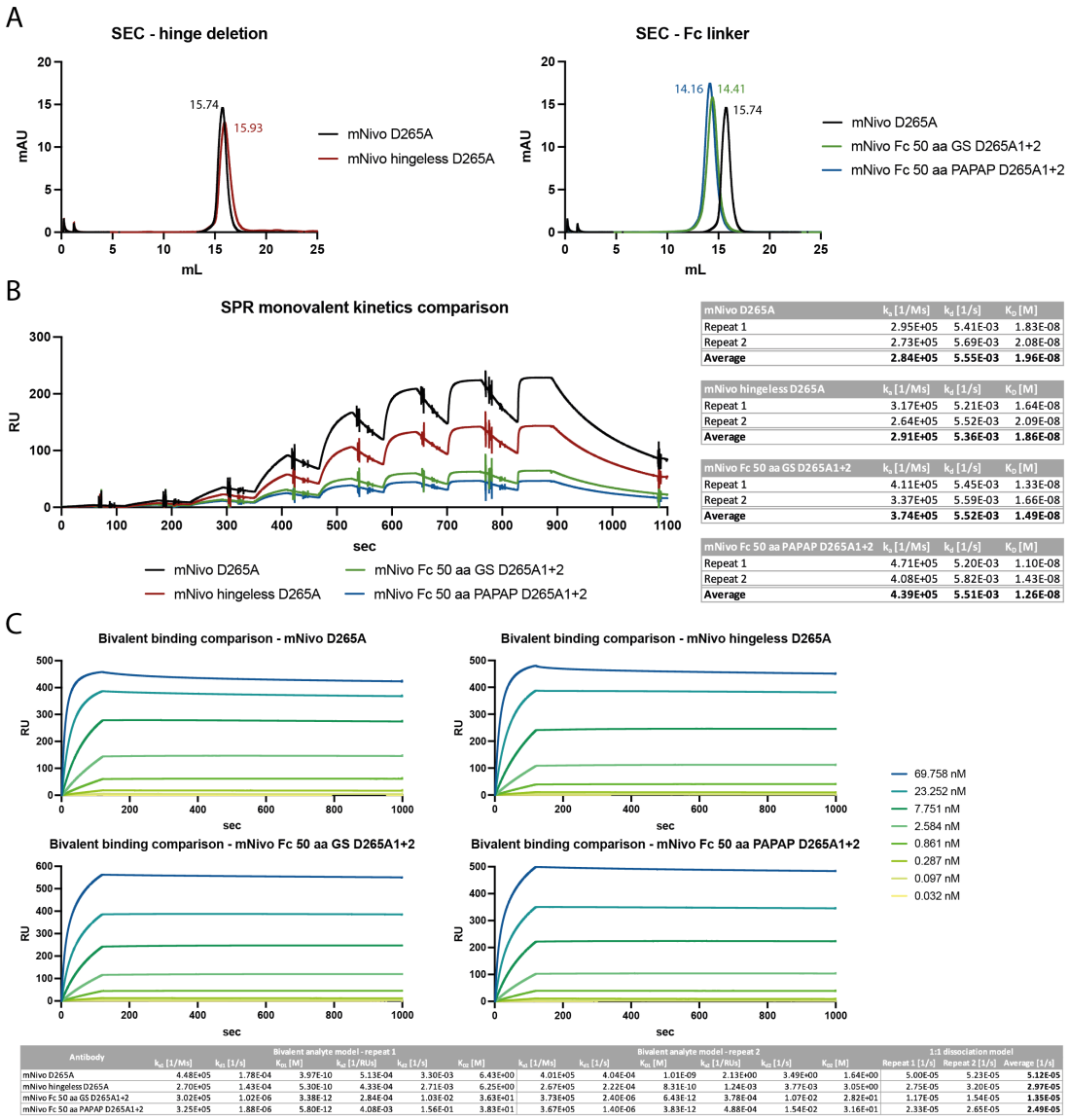
flexibility into the molecule. In an attempt to reduce this, two strategies were employed. First, using published structures of the mIgG1 CH3 (PDB ID 1CQK[345]) and CH2-CH3 (PDB ID 3HKF[346]) domains, amino acids at the base of CH3 as well as the start of CH2 were identified that could not be resolved in the crystal structure, indicating flexibility of these residues. Thus, the last four residues of CH3 and the first four residues of CH2 were removed from the first CH3 and second CH2 of an Fc-multiplexed antibody, respectively. Second, three different linkers were inserted to test whether the GGGGS linker can be shortened (GGS or GS) or replaced by a more rigid linker (PAPAP)[347]. Figure 6.1 C illustrates the different constructs, which were created by chimera PCRs of the mNivo Fc 2x50 aa D265A1+2 construct by Mai Vuong. Of note, as this antibody also harboured a hinge extension, this was replaced by the WT hinge to allow a comparison of the linker variants without an additional modification in the hinge region.

The different heavy chains were cloned into a pHR plasmid and co-transfected with the unmodified nivolumab mouse κ light chain. Four days post lentiviral transduction, a Western blot of the supernatant using an anti-mouse-Fc-HRP detection antibody was run to test for antibody expression. As shown in Figure 6.1 D, the expression levels varied significantly between the different hinge-deleted mNivo antibodies, with construct #1 being not expressed at all. As all four cysteines in the hinge region were deleted, the antibodies were presumably not stable and a singular HC could be detected as well as a potential HC + LC molecule. All Fc-linker constructs were expressed at similar levels. In accordance with what was observed in the previous chapter (Figure 5.3), the Fc-multiplexed antibody folded into two molecules, the full antibody and a single HC + LC protein. A single HC was also identified on the Western blot. The cells expressing the hinge-deleted construct #2 (hereinafter referred to as mNivo hingeless D265A), which demonstrated the highest protein yield, as well as the GS and PAPAP Fc linkers, were taken forward for a more detailed analysis. While the different constructs were designed by the author, all experimental work until the harvest of the supernatant was carried out by Mai Vuong.

6.2.2 Validation of hinge-deleted antibodies and Fc-linker optimisation

The antibodies were produced using the established purification pipeline described in Section 3.2.2. Similar to what was observed in Section 5.2.2, the Fc-multiplexed antibodies displayed non-monomeric byproducts (data not shown). Upon pooling of the fractions containing the monomeric antibody, a small amount (100 µg) of each antibody was analysed using analytical SEC. As shown in Figure 6.2 A, both, mNivo hingeless D265A and the Fc-linker-optimised antibodies, eluted as a single peak, suggesting a stable, monomeric conformation of the proteins. While mNivo hingeless D265A eluted slightly later than mNivo D265A, suggesting that it is more compact, both antibodies harbouring an extra Fc region eluted earlier. Furthermore, the antibody with a rigid linker (PAPAP) had a slightly lower retention volume compared to the antibody harbouring a short linker (GS), suggesting mNivo Fc 50 aa PAPAP D265A1+2 has a larger hydrodynamic radius and size.

SPR was used to compare the monovalent and bivalent binding properties of the new mNivo variants. First, the monovalent kinetics were assessed using single-cycle kinetics, which showed that there was no difference between all antibody formats tested (Figure 6.2 B). The chip that was used (CM5 chip with anti-mouse IgG antibodies immobilised) produced small spikes shortly after the association phase, but this did not influence the fitting of the data (Figure A.6 A). Second, multi-cycle analysis with captured hPD-1-2xHis on a NTA chip was used to compare the bivalent binding (Figure 6.2 C). As discussed in Section 5.2.4, analysis of this data is more challenging, especially as the dissociation of mNivo is very slow. Thus, the bivalent analyte model was fitted to compare the on-rates, whereas a 1:1 dissociation model was used to infer the off-rates. The k_{a1} rates (first association) were very similar and in accordance with the single-cycle analysis. However, the k_{a2} rates (second association) were not consistent between the two runs. Especially, mNivo D265A produced a surprisingly high k_{a2} rate of 2.61 RUs^{-1} in the second repeat, which is in contrast to all values retrieved so far (Figures 5.6



mNivo D265A	k_a [1/Ms]	k_d [1/s]	K_D [M]
Repeat 1	2.95E+05	5.41E-03	1.83E-08
Repeat 2	2.73E+05	5.69E-03	2.08E-08
Average	**2.84E+05**	**5.55E-03**	**1.96E-08**

mNivo hingeless D265A	k_a [1/Ms]	k_d [1/s]	K_D [M]
Repeat 1	3.17E+05	5.21E-03	1.64E-08
Repeat 2	2.64E+05	5.52E-03	2.09E-08
Average	**2.91E+05**	**5.36E-03**	**1.86E-08**

mNivo Fc 50 aa GS D265A1+2	k_a [1/Ms]	k_d [1/s]	K_D [M]
Repeat 1	4.11E+05	5.45E-03	1.33E-08
Repeat 2	3.37E+05	5.59E-03	1.66E-08
Average	**3.74E+05**	**5.52E-03**	**1.49E-08**

mNivo Fc 50 aa PAPAP D265A1+2	k_a [1/Ms]	k_d [1/s]	K_D [M]
Repeat 1	4.71E+05	5.20E-03	1.10E-08
Repeat 2	4.08E+05	5.82E-03	1.43E-08
Average	**4.39E+05**	**5.51E-03**	**1.26E-08**

Antibody	Bivalent analyte model - repeat 1						Bivalent analyte model - repeat 2						1:1 dissociation model		
	k_{a1} [1/Ms]	k_{d1} [1/s]	K_{D1} [M]	k_{a2} [1/RUs]	k_{d2} [1/s]	K_{D2} [M]	k_{a1} [1/Ms]	k_{d1} [1/s]	K_{D1} [M]	k_{a2} [1/RUs]	k_{d2} [1/s]	K_{D2} [M]	Repeat 1 [1/s]	Repeat 2 [1/s]	Average [1/s]
mNivo D265A	4.48E+05	1.78E-04	3.97E-10	5.13E-04	3.30E-03	6.43E+00	4.01E+05	4.04E-04	1.01E-09	2.13E+00	3.49E+00	1.64E+00	5.00E-05	5.23E-05	**5.12E-05**
mNivo hingeless D265A	2.70E+05	1.43E-04	5.30E-10	4.33E-04	2.71E-03	6.25E+00	2.67E+05	2.22E-04	8.31E-10	1.24E-03	3.77E-03	3.05E+00	2.75E-05	3.20E-05	**2.97E-05**
mNivo Fc 50 aa GS D265A1+2	3.02E+05	1.02E-06	3.38E-12	2.84E-04	1.03E-02	3.63E+01	3.73E+05	2.40E-06	6.43E-12	3.78E-04	1.07E-02	2.82E+01	1.17E-05	1.54E-05	**1.35E-05**
mNivo Fc 50 aa PAPAP D265A1+2	3.25E+05	1.88E-06	5.80E-12	4.08E-03	1.56E-01	3.83E+01	3.67E+05	1.40E-06	3.83E-12	4.88E-04	1.54E-02	3.16E+01	2.33E-05	2.65E-05	**2.49E-05**

Figure 6.2: Validation of hinge-deleted antibodies and Fc-linker optimisation
(A) Analytical SEC analysis of mNivo variants. A small amount (100 µg) of each antibody was injected over a Superdex 200 Increase 10/300 GL. Elution volumes of major peaks are annotated with the corresponding colour.
(B) Single-cycle analysis of different mNivo constructs. All variants of mNivo were captured on a CM5 chip with immobilised anti-mouse IgG antibodies and hPD-1-2xHis was injected as analyte with concentrations ranging from 1.7 nM to 2777.78 nM. Sensorgrams were reference- and blank-subtracted. MOPC21 was captured in the reference channel. The Biacore Insight Evaluation Software was used to fit a 1:1 binding model (Figure A.6 A) and derived affinity constants (k_a, k_d and K_D) are shown.
(C) Multi-cycle bivalent binding analysis of different forms of mNivo. hPD-1-2xHis was captured on a NTA chip and antibodies were injected with concentrations ranging from 0.032 nM to 69.758 nM. Sensorgrams were reference- and blank-subtracted. MOPC21 was injected in the reference channel. The Biacore Insight Evaluation Software was used to fit either a bivalent analyte model or a 1:1 dissociation model (Figure A.6 B and C) and derived affinity constants (k_{a1}, k_{d1}, K_{D1}, k_{a2}, k_{d2}, K_{D2} and k_d) are shown.

and 6.2 C). As (i) the sensorgram did not look any different compared to the other runs, (ii) the fit did not reveal abnormalities (Figure A.6 B) and (iii) this value is for reference only, it can be dismissed. Importantly, across the two repeats all forms of mNivo had similar values for the k_{a2} rates. Finally, the k_d rates derived from the 1:1 dissociation models were also similar across all antibodies tested.

Overall, while the different hinge-deleted antibodies were not stable under the non-reducing, denaturing SDS-PAGE conditions (Figure 6.1 D), mNivo hingeless D265A eluted as a single peak when analysed using analytical SEC (Figure 6.2 A, left panel). More importantly, it bound to hPD-1-2xHis and displayed no difference in its monovalent or bivalent binding properties versus mNivo D265A (Figures 6.2, B and C). Finally, as the PAPAP linker between the Fc domains and the 50 aa mCD43 insertion resulted in a lower retention volume (Figure 6.2 A, right panel), this linker was picked for the subsequent design of hinge-deleted, extended antibodies.

6.2.3 Design of rigid, extended antibodies

The combination of the hinge-deletion and the Fc-linker optimisation should result in a more rigid, extended antibody. As the removal of the hinge prevented the hinge-extension used in Chapter 5 (Figure 5.1), the Fc-multiplexing approach was repeated to further increase the overall size of the antibody. The final construct was a hinge-deleted ('hingeless') mNivo with two additional Fc domains added beyond the original CH3. The first and second CH3 domain as well as the second and third CH2 domain were truncated as described in Figure 6.1 C. A rigid PAPAP linker was added between each constant domain and the 50 aa mCD43 linker. This heavy chain sequence was ordered as a DNA string and cloned into a pHR plasmid by Mai Vuong.

As a dissociated HC was observed on the Western blot of the hinge-deleted antibodies (Figure 6.1 D), two additional constructs were created in an attempt to restore the HC-LC disulfide bond. First, a single cysteine was added at the base of CH1, as potentially remaining flexibility might allow this cysteine to link

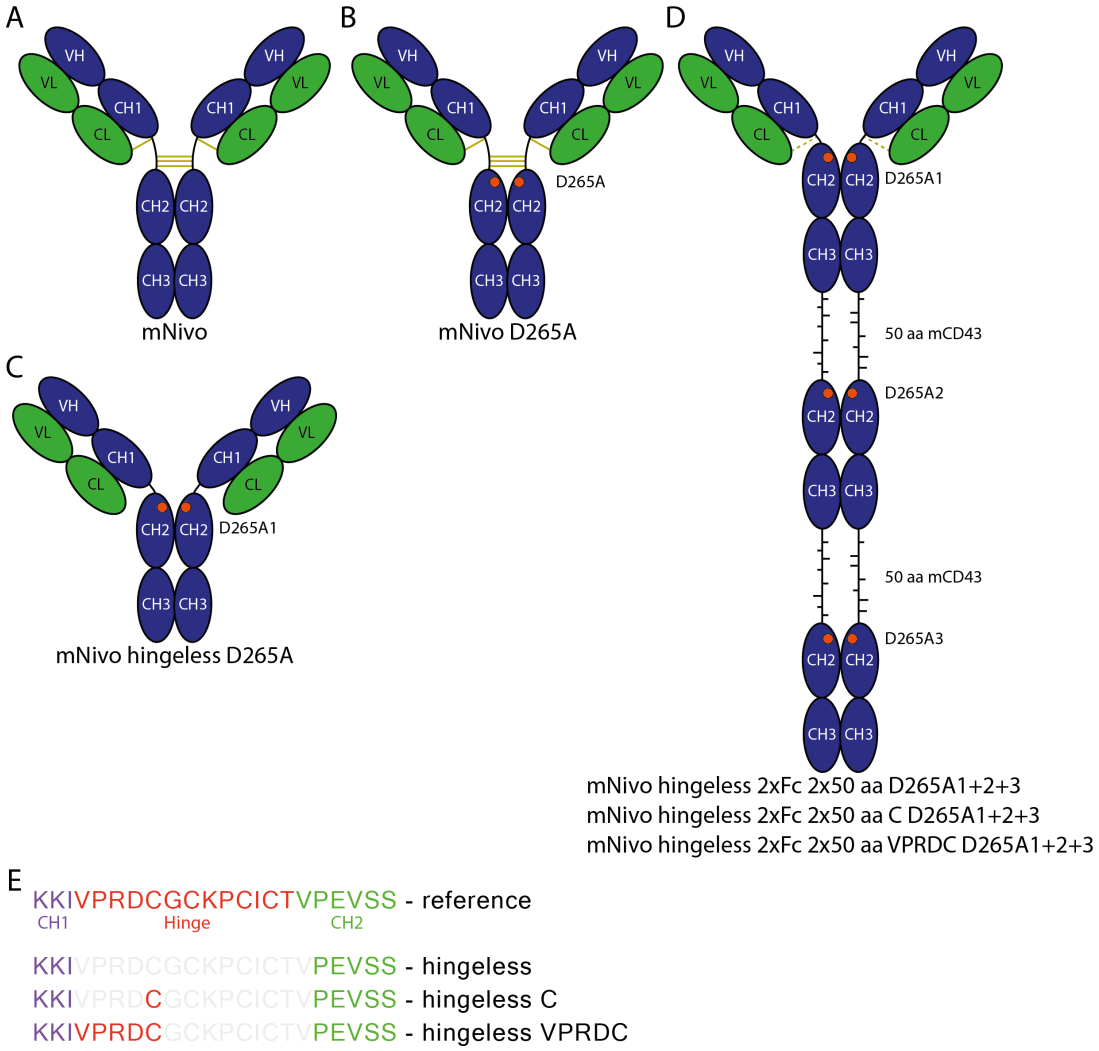


Figure 6.3: Design of hinge-deleted, extended antibodies
(A-D) A schematic overview of the different mNivo variants used in this chapter. Heavy chains are coloured in blue, light chains in green. Hinge disulfide bonds are shown in yellow. The D265A mutation is indicated by an orange circle. As the formation of the hinge HC-LC disulfide bond for some constructs in (D) was not clear, this was illustrated as a dashed line.
(E) Depiction of the different mNivo hingeless 2xFc 2x50 aa constructs designed. Colour scheme as in Figure 6.1 A. Grey letters indicate the respective deleted sequence. Red letters indicate amino acids reintroduced into the hinge region.

with the LC cysteine. Second, the hinge sequence preceding the first cysteine was reintroduced (VPRDC). The cloning of these two constructs was carried out by Mai Vuong. An overview of all mNivo variants tested in this chapter is given in Figure 6.3 and Table 6.1. Of note, all mNivo hingeless 2xFc 2x50 aa constructs harboured a D265A mutation in every Fc region (D265A1+2+3).

Table 6.1: Overview of different mNivo antibody constructs

Antibody name	Modification	Mutation
mNivo	No modification	No mutation
mNivo D265A	No modification	D265A
mNivo hingeless D265A	Hinge deletion	D265A
mNivo hingeless 2xFc 2x50 aa D265A1+2+3	Hinge deletion + 2xFc and 2x50 aa mCD43	D265A1+2+3
mNivo hingeless 2xFc 2x50 aa C D265A1+2+3	Hinge deletion + 2xFc and 2x50 aa mCD43 + C into hinge	D265A1+2+3
mNivo hingeless 2xFc 2x50 aa VPRDC D265A1+2+3	Hinge deletion + 2xFc and 2x50 aa mCD43 + VPRDC into hinge	D265A1+2+3

6.2.4 Purification of rigid, extended antibodies using Protein A and SEC

Of note, the following experiments carried out in Sections 6.2.4 and 6.2.5 were performed by Deborah Greis (University of Tübingen, Germany) under the supervision of the author, as part of a summer internship in the Davis laboratory.

The designed antibodies were expressed and purified using the established pipeline described in Section 3.2.2. As shown in Figure 6.4 A, the SEC curves revealed considerable amounts of aggregated protein. While there seemed to be a difference in the elution volume between the different antibody formats, this is determined with greater accuracy in an analytical SEC upon exclusion of the aggregated material (Section 6.2.5). Due to the high degree of non-monomeric protein, it was crucial to identify the appropriate fractions to pool using protein gels.

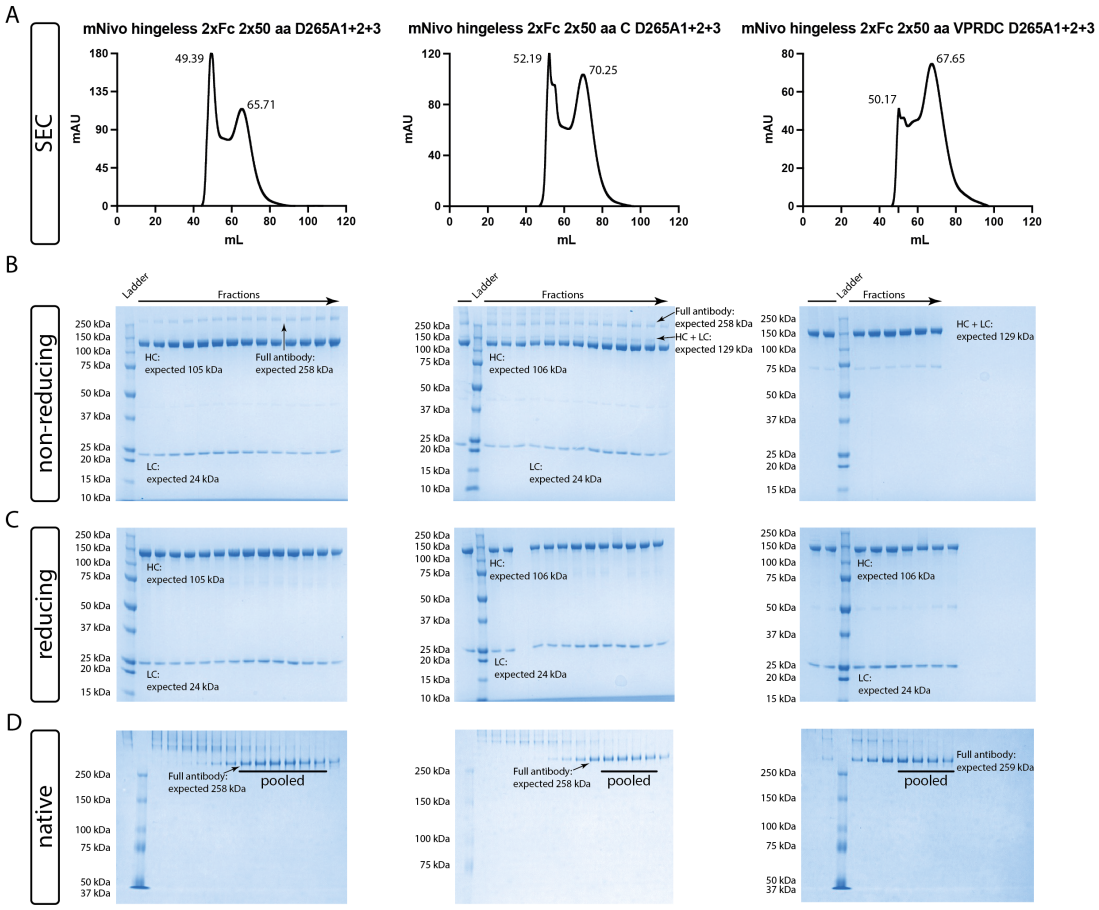


Figure 6.4: Evaluation of purified antibodies using SEC and SDS-PAGE gels

(A) Representative SEC curves of the produced extended antibodies. A ProteoSEC 16/60 6-600 column was used. Elution volumes of major peaks are annotated in each graph.

(B-D) Representative non-reducing (B), reducing (C) and native (D) PAGE gels of the produced antibodies. A protein ladder was included on each gel. Expected sizes of full antibodies, HC + LC pairs, HCs and LCs, as calculated by Expasy ProtParam[333], are annotated.

While the non-reducing, denaturing SDS-PAGE gels of mNivo hingeless 2xFc 2x50 aa D265A1+2+3 and mNivo hingeless 2xFc 2x50 aa C D265A1+2+3 displayed a band likely corresponding to the full antibody, this was very faint and the most intense bands probably represented separated HCs and LCs (Figure 6.4 B). Importantly, while there was no band suggesting the presence of HC + LC pairs in the original hinge-deleted construct (mNivo hingeless 2xFc 2x50 aa D265A1+2+3), this was the case for the antibody with an inserted cysteine into the deleted hinge region. Moreover, upon reintroduction of the hinge sequence

up to the first cysteine (VPRDC), the pairing of HC and LC was fully restored (Figure 6.4 B, right panel). The reducing, denaturing SDS-PAGE gels in Figure 6.4 C confirmed that all proteins comprised heavy and light chains. However, from these SDS-PAGE gels it was difficult to assess the presence of monomeric, full antibodies as the proteins were falling apart under denaturing conditions. Thus, native, non-denaturing, PAGE gels were run to assess the degree of aggregation in each fraction (Figure 6.4 D). While a protein ladder was included on these gels, this needs to be treated with caution as proteins are not only separated by their molecular weight, but also by their charge-to-mass ratio, as no SDS was used. Using these gels, no single heavy or light chains were observed, but only full antibodies as well as aggregated protein, which was in accordance with the SEC curve. Black lines indicate the fractions pooled.

6.2.5 Comparison of size using SEC

To assess the purity of the pooled fractions and compare the sizes of the different antibodies, analytical SEC was used. As shown in Figure 6.5 B-D, while most of the aggregated material was excluded by pooling of the fractions, some remained and a small 'shoulder' was observed for all extended antibodies. Accidentally, most protein of the reference antibody (mNivo D265A) was lost and only little amounts were injected over the column, resulting in low milli absorbance units (mAU) readings (Figure 6.5 A). Importantly, for reference purposes this was sufficient. Only very small changes were observed when comparing the elution volumes of the different extended antibodies (Figure 6.5 E). This was expected as the introduced amino acids should not have a major effect on the overall antibody size.

6.2.6 SPR validation of rigid, extended antibodies

Following this, the monovalent and bivalent binding behaviours of the hinge-deleted, extended antibodies were investigated using SPR. Injection of hPD-1-2xHis over the immobilised antibodies on a Protein A chip revealed no difference in the monovalent binding kinetics for all hinge-deleted antibodies, compared to

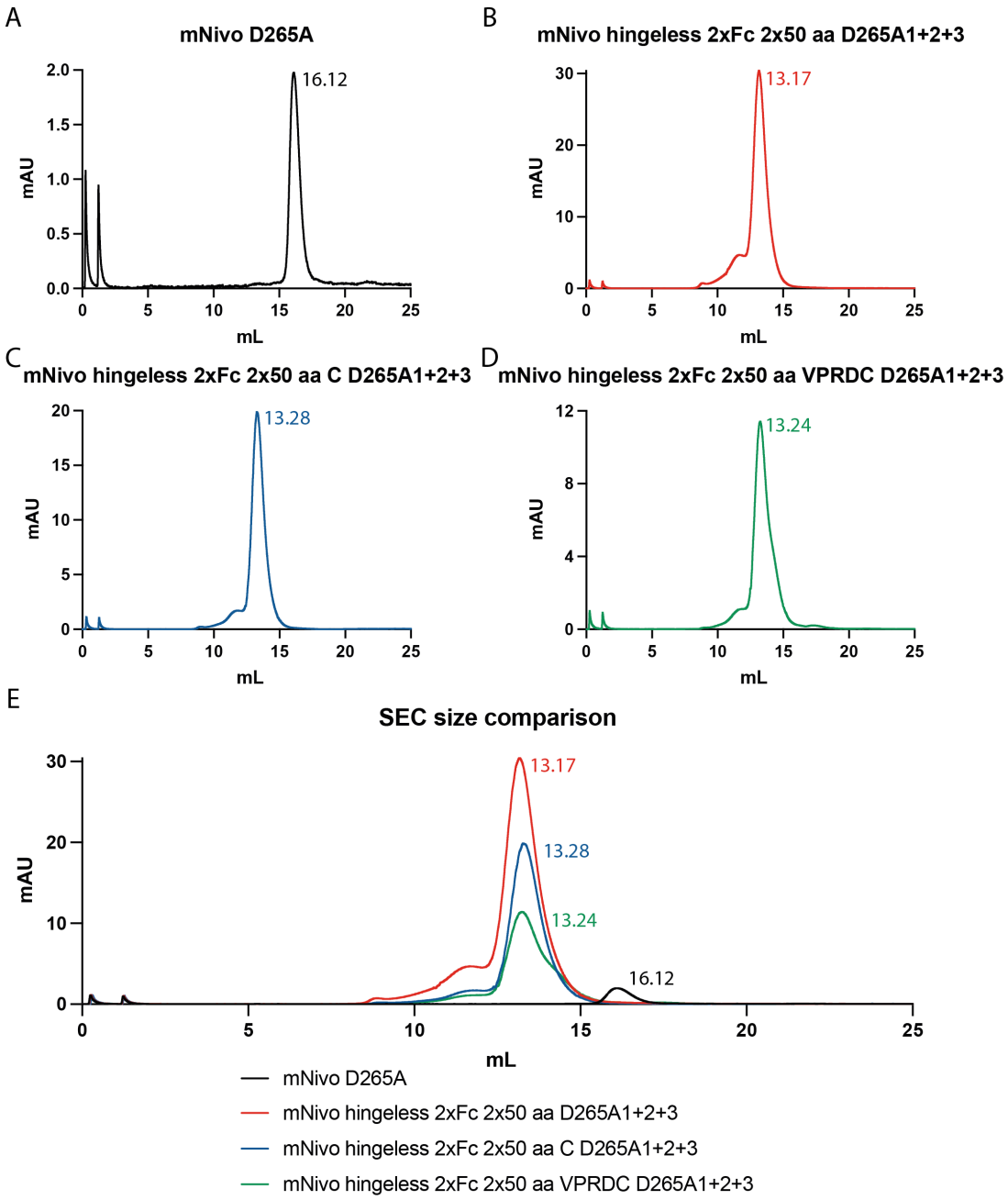
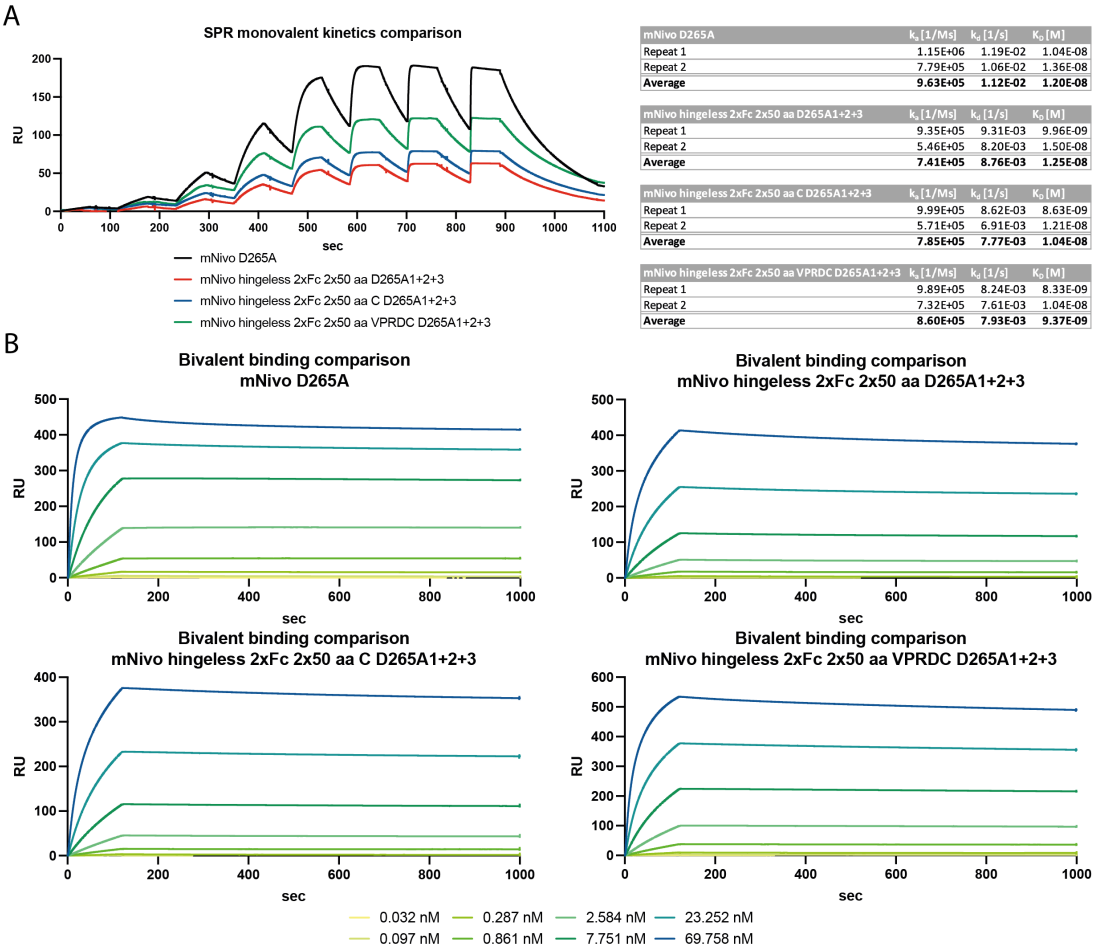


Figure 6.5: Analytical SEC to compare antibody sizes and assess purity
Analytical SEC analysis of engineered antibodies. A small amount (100 µg) of each antibody was injected over a Superdex 200 Increase 10/300 GL. Elution volumes of major peaks are annotated with the corresponding colour.



mNivo D265A	k_a [1/Ms]	k_d [1/s]	K_D [M]
Repeat 1	1.15E+06	1.19E-02	1.04E-08
Repeat 2	7.79E+05	1.06E-02	1.36E-08
Average	**9.63E+05**	**1.12E-02**	**1.20E-08**

mNivo hingeless 2xFc 2x50 aa D265A1+2+3	k_a [1/Ms]	k_d [1/s]	K_D [M]
Repeat 1	9.35E+05	9.31E-03	9.96E-09
Repeat 2	5.46E+05	8.20E-03	1.50E-08
Average	**7.41E+05**	**8.76E-03**	**1.25E-08**

mNivo hingeless 2xFc 2x50 aa C D265A1+2+3	k_a [1/Ms]	k_d [1/s]	K_D [M]
Repeat 1	9.99E+05	8.62E-03	8.63E-09
Repeat 2	5.71E+05	6.91E-03	1.21E-08
Average	**7.85E+05**	**7.77E-03**	**1.04E-08**

mNivo hingeless 2xFc 2x50 aa VPRDC D265A1+2+3	k_a [1/Ms]	k_d [1/s]	K_D [M]
Repeat 1	9.89E+05	8.24E-03	8.33E-09
Repeat 2	7.32E+05	7.61E-03	1.04E-08
Average	**8.60E+05**	**7.93E-03**	**9.37E-09**

Antibody	Bivalent analyte model - repeat 1						Bivalent analyte model - repeat 2						1:1 dissociation model		
	k_{a1} [1/Ms]	k_{d1} [1/s]	K_{D1} [M]	k_{a2} [1/RUs]	k_{d2} [1/s]	K_{D2} [M]	k_{a1} [1/Ms]	k_{d1} [1/s]	K_{D1} [M]	k_{a2} [1/RUs]	k_{d2} [1/s]	K_{D2} [M]	Repeat 1 [1/s]	Repeat 2 [1/s]	Average [1/s]
mNivo D265A	4.87E+05	1.78E-04	3.66E-10	5.22E-04	2.93E-03	5.60E+00	4.03E+05	4.61E-04	1.14E-09	2.61E+00	3.36E+00	1.29E+00	5.10E-05	5.44E-05	**5.27E-05**
mNivo hingeless 2xFc 2x50 aa D265A1+2+3	1.52E+05	1.42E-04	9.34E-10	1.40E-03	1.48E-01	1.05E+02	1.73E+05	1.33E-04	7.69E-10	7.85E-04	7.74E-02	9.86E+01	9.28E-05	9.45E-05	**9.36E-05**
mNivo hingeless 2xFc 2x50 aa C D265A1+2+3	1.50E+05	9.03E-05	6.01E-10	4.94E-04	3.77E-02	7.63E+01	1.57E+05	8.80E-05	5.60E-10	1.06E-03	1.01E-01	9.59E+01	6.14E-05	6.51E-05	**6.32E-05**
mNivo hingeless 2xFc 2x50 aa VPRDC D265A1+2+3	2.91E+05	1.16E-04	3.99E-10	7.58E-04	4.58E-02	6.04E+01	3.01E+05	1.48E-04	4.93E-10	1.59E-03	8.31E-02	5.21E+01	7.74E-05	9.58E-05	**8.66E-05**

Figure 6.6: SPR comparison of rigid, extended antibodies
(A) Single-cycle analysis of different forms of mNivo. All variants of mNivo were captured on a Protein A chip and hPD-1-2xHis was injected as analyte with concentrations ranging from 1.7 nM to 2777.78 nM. Sensorgrams were reference- and blank-subtracted. MOPC21 was captured in the reference channel. The Biacore Insight Evaluation Software was used to fit a 1:1 binding model (Figure A.7 A) and derived affinity constants (k_a, k_d and K_D) are shown in the table.
(B) Multi-cycle bivalent binding analysis of different forms of mNivo. hPD-1-2xHis was captured on a NTA chip and antibodies were injected with concentrations ranging from 0.032 nM to 69.758 nM. Sensorgrams were reference- and blank-subtracted. MOPC21 was injected in the reference channel. The Biacore Insight Evaluation Software was used to fit either a bivalent analyte model or a 1:1 dissociation model (Figure A.7 B and C, respectively) and derived affinity constants (k_{a1}, k_{d1}, K_{D1}, k_{a2}, k_{d2}, K_{D2} and k_d) are shown in the table below.

mNivo D265A (Figure 6.6 A). The bivalent binding analysis revealed a similar problem as observed in Section 6.2.2, wherein the k_{a2} value of mNivo D265A was an outlier. Importantly, the remaining affinity constants were similar, except the k_{a1} rates of mNivo hingeless 2xFc 2x50 aa D265A1+2+3 and mNivo hingeless 2xFc 2x50 aa C D265A1+2+3, which were reduced by up to 3-fold (Figure 6.6 B). The slower association rates were in agreement with the respective sensorgrams, which clearly revealed a diminished on-rate. This may suggest that the extra degrees of freedom given by the WT hinge, and to a lesser extent through reintroduction of VPRDC, is important for association. Overall, while the derived k_a constants were slightly different, the k_d rates from the the 1:1 dissociation model were very similar. Thus, the binding properties of the rigid, extended antibodies demonstrated only small changes compared to mNivo D265A, which should not have a large impact on the overall activity.

6.2.7 *In vitro* T-cell activation assay

To test the *in vitro* activity of the new antibody constructs, the NF-κB-driven activation assay established in Section 5.2.5 was used. This experiment was repeated five times, with all replicates as well as the pooled and normalised data shown in Figure 6.7. Besides the three rigid, extended antibodies, mNivo hingeless D265A as well as the control antibodies MOPC21, mNivo and mNivo D265A were included. Of note, only significant ($p \leq 0.05$) differences between mNivo D265A and all hinge-deleted antibodies in the 'Antibody only' condition are indicated. While there were some significant differences between mNivo D265A and the hingeless antibodies in individual repeats, these results were not reproducibly achieved and the pooled data did not reveal any significant changes ($p = 0.615492$, 0.716073, 0.996507 and 0.977155 for the comparison of mNivo D265A with mNivo hingeless D265A, mNivo hingeless 2xFc 2x50 aa D265A1+2+3, mNivo hingeless 2xFc 2x50 aa C D265A1+2+3 and mNivo hingeless 2xFc 2x50 aa VPRDC D265A1+2+3, respectively). Taken together, despite reducing the flexibility and increasing the overall size, none of the mNivo variants performed

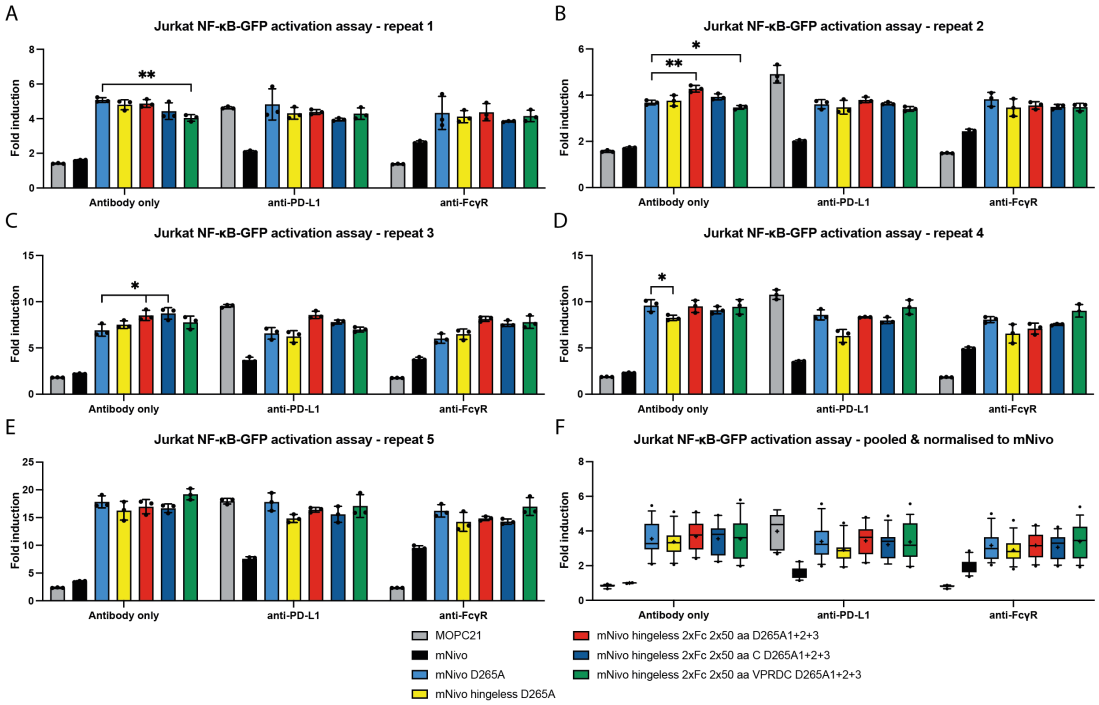


Figure 6.7: *In vitro* T-cell activation assay comparing stimulatory capacity
Jurkat PD-1$^+$ NF-κB-GFP cells were co-cultured with TCS PD-L1$^+$ mFcγRIIb$^+$ and different antibodies (348.79 nM of each antibody, this is equivalent to 50 µg/mL of mNivo). TCS blocking antibodies (anti-PD-L1 and anti-FcγR) were added at a final concentration of 100 µg/mL.
(A-E) depict five independent repeats with three technical replicates each. Normalising the data to mNivo allowed pooling of the data (F).
For bar graphs, data are shown as mean ± SD. For boxplots, the line shows the median, the '+' shows the mean. Whiskers display the 10-90 percentile. Unpaired t-tests were used to compare individual groups.

better than mNivo D265A. Thus, none of these antibody formats were taken forward for *in vivo* tumour challenge experiments.

6.2.8 Supported lipid-bilayers for studying nivolumab mIgG1-driven PD-1 contact enrichment

The work in this section was carried out by Edward Jenkins (Davis group) in collaboration with the group of David Klenerman (University of Cambridge) using the antibodies prepared in this thesis. Supported lipid-bilayers (SLBs) can be used to mimic a cell membrane to study T-cell interactions in a reductionist, tuneable system. Initially, only the extracellular domains of pMHC and the large adhesion molecule ICAM-1 were presented on SLBs[348]. Recently, our laboratory

established a more advanced SLB system referred to as 'second generation' supported lipid-bilayers (SLB2s)[349]. SLB2s simulate the interactions of a T cell with an APC as they present physiological densities of 'null' pMHC, agonist pMHC, ICAM-1, CD58 (a small adhesion molecule) and a model glycocalyx (CD43 and CD45). The added glycoproteins are crucial as T cells normally need to penetrate these types of glycocalyx barriers in order to form small contacts, referred to as 'close contacts', using CD58/CD2 interactions, which in turn promotes ligand recognition of the TCR[349].

SLB2s were adapted to investigate the potential mNivo-driven accumulation of PD-1 via the presentation of mFcγRIIb-His on the SLB2. Using J8 cells ($CD4^{-}CD8^{+}$ 1G4-TCR Jurkat cells) expressing PD-1-HaloTag allowed the tracking of PD-1 in this system. In addition to MOPC21, mNivo and mNivo D265A, mNivo Fc 2x50 aa D265A1+2 (characterised in Chapter 5) and mNivo hingeless 2xFc 2x50 aa D265A1+2+3 were included in order to test for potential differences in PD-1/antibody enrichment/exclusion from close contacts. A bespoke TIRF microscope (Klenerman laboratory, University of Cambridge) was used for imaging. As shown in Figure 6.8, Fc-engaging mNivo was highly enriched in close contacts formed between Jurkat cells and SLB2s. Whenever the glycocalyx of the SLB2 was 'pushed' away by T cells, this created 'black spots' in the bilayer fluorescence, which indicate the formation of a close-contact zone[349]. PD-1 and mNivo (on T cells) were enriched in these areas, resulting in the glycocalyx and PD-1/antibody signals being highly anti-correlated, which is illustrated by the derived line profile. In contrast to this, all other mNivo variants (mNivo D265A, mNivo Fc 2x50 aa D265A1+2 and mNivo hingeless 2xFc 2x50 aa D265A1+2+3) were excluded from the contacts to varying degrees, with the largest effects observable for the extended forms of the antibodies. In order to measure these potential changes with greater accuracy, quantitative image analysis was performed by Daniel Heraghty (Klenerman group, University of Cambridge). Using a code written by Markus Körbel (Klenerman group, University of Cambridge, `https://github.com/mkoerbel/contactanalysis_2D`[349]),

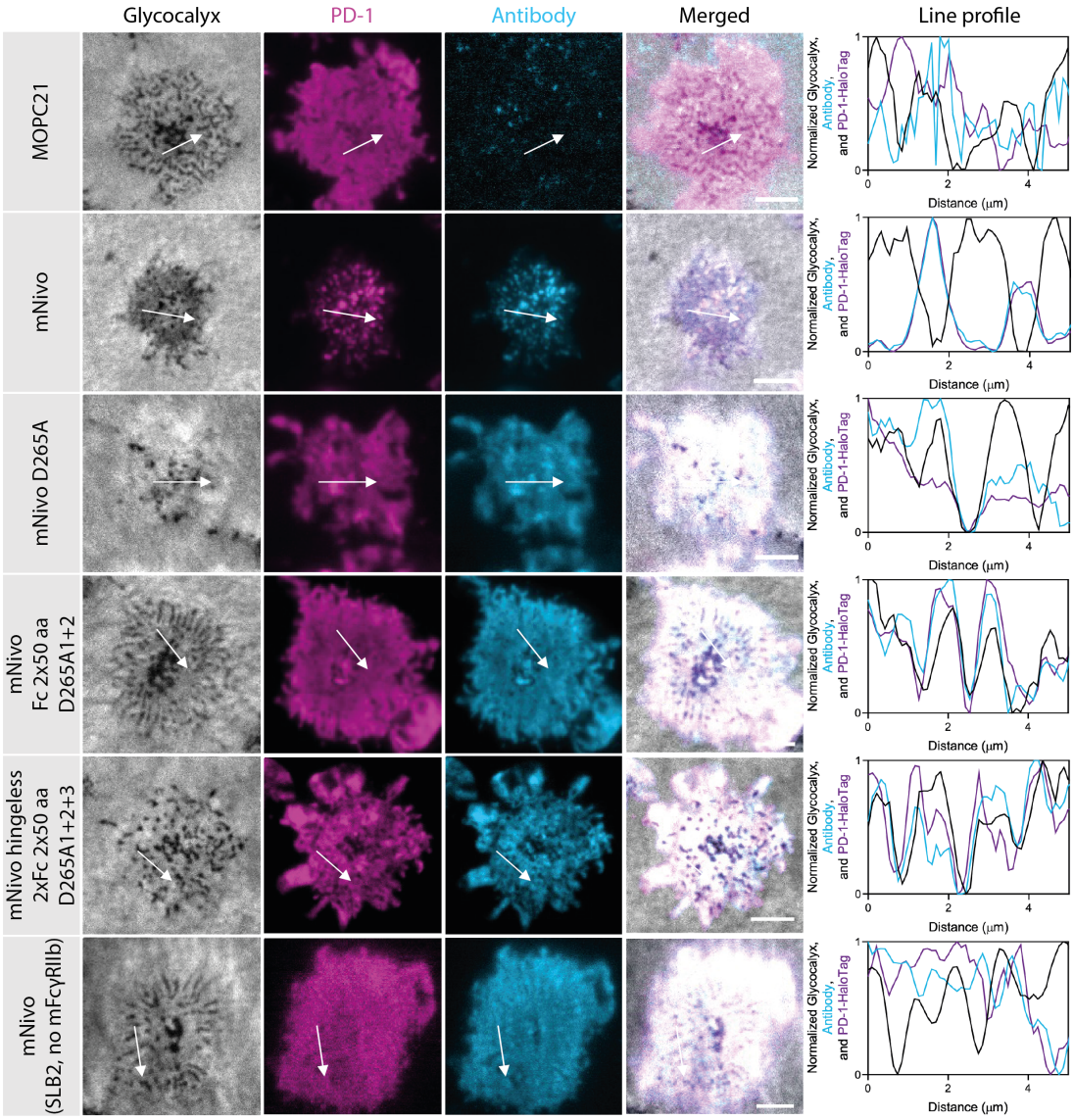


Figure 6.8: SLB2s presenting mFcγRIIb to study antibody-driven PD-1 contact enrichment

J8 cells ($CD4^{-}CD8^{+}$ 1G4-TCR Jurkat cells) expressing PD-1-HaloTag were placed on SLB2s, which also present mFcγRIIb and pMHC9V-lo. Cells were pre-labelled with different antibodies (15 min at 37 °C), washed three times and then placed on the SLB2. Cells were imaged 10 min after being added to the SLB2 using a bespoke three-colour total internal reflection fluorescence (TIRF) microscope. The glycocalyx (CD43 and CD45RABC) was labelled with Alexa Fluor 555 on the SLB2 and shows where cells from close contacts, i.e. areas where CD45 is excluded on the T-cell membrane[349]. The antibodies were labelled with Alexa Fluor 488. HaloTag was labelled with Janelia Fluor 646. The line profiles show the intensity along and in direction of the arrow across the three channels. The scale bar is 5 µm long.

Data were generated and analysed by Edward Jenkins.

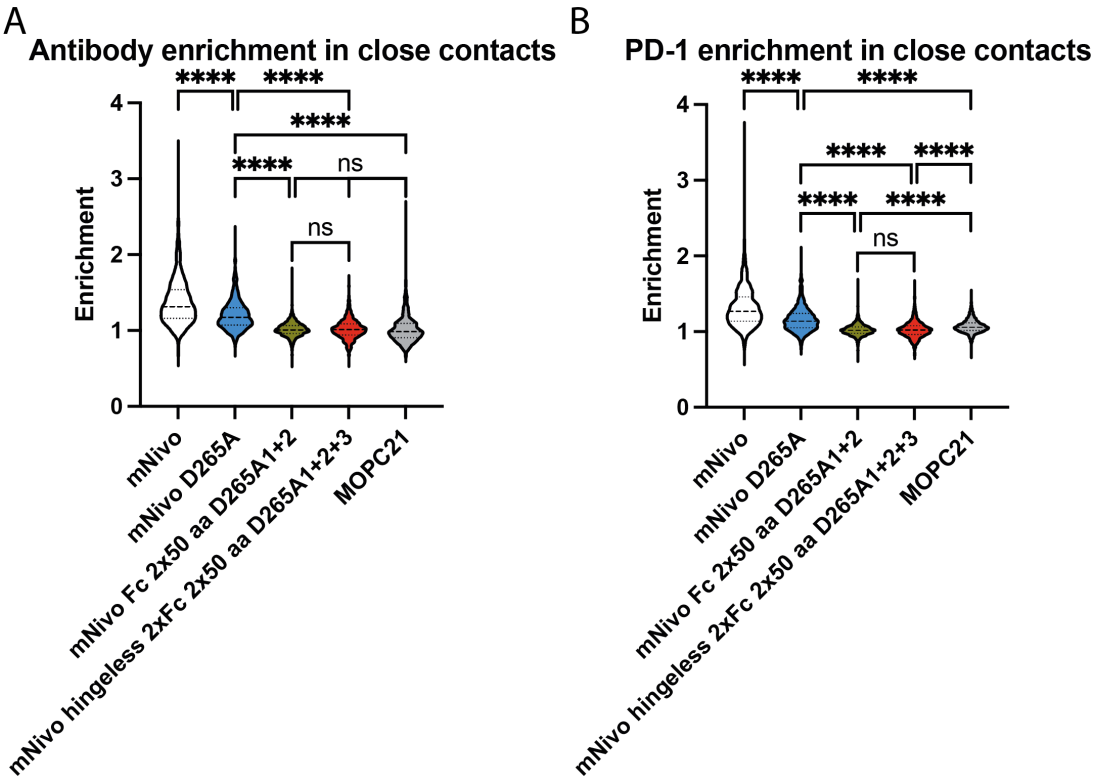


Figure 6.9: Contact-enrichment analysis of SLB2s presenting mFcγRIIb
Images, representative ones are shown in Figure 6.8, were analysed for (A) antibody enrichment and (B) PD-1 enrichment in close contacts. Quantitative image analysis was performed using the contact analysis code written by Markus Körbel (University of Cambridge, `https://github.com/mkoerbel/contactanalysis_2D`[349]). Each data point is a close contact and a minimum of 1,000 data points per antibody were analysed. A minimum of 50 cells were used for each antibody. The dashed line shows the median, the pointed lines show the quartiles. Kruskal-Wallis tests with Dunn's multiple comparisons tests were used to compare the different groups.
Data were analysed by Daniel Heraghty (University of Cambridge).

the enrichment of PD-1 and the antibodies in close contacts was analysed. As shown in Figure 6.9, both extended antibodies were significantly less enriched in close-contact zones compared to mNivo and mNivo D265A, and, importantly, this was also the case for PD-1. While there was no difference between the two extended antibodies, they both exhibited less PD-1 enrichment compared to MOPC21 (Figure 6.9 B), suggesting that they are 'dragging' PD-1 out of the close-contact area. Importantly, Fc-engaging mNivo was not enriched in close contacts when mFcγRIIb was not present in the SLB2, and it instead exhibited a diffuse distribution across the cell surface (Figure 6.8, lower panel). This is an

intriguing finding as it clearly demonstrates that a native antibody, when bound to PD-1, is small enough to remain in close contacts where it could be expected to continue signalling. It should be noted that the central, large close-contact area showed a very slight reduction of mNivo; however, overall, the antibody and PD-1 were very evenly distributed.

6.3 Discussion

Work in this chapter aimed to produce rigid, extended antibodies in an attempt to reduce the signalling by PD-1 when bound by antibodies like nivolumab. The most flexible region within an antibody is the hinge region, which allows the protein to bind to epitopes spanning different distances and arrangements[201]. As there were already reports describing the deletion of the hinge region in myeloma proteins[342,343], which led to a reduced flexibility allowing crystallisation, this approach was also taken to create a more rigid form of mNivo (nivolumab mIgG1). While both myeloma proteins are hIgG1 antibodies[342,343], a recent report separately demonstrated the general feasibility of this approach by creating hIgG1 and hIgG4 hinge-deleted antibodies with the aim to reduce effector functions[340]. For the first time, this concept was applied to mouse antibodies as well as immune-checkpoint blockers. In addition to reducing the core flexibility within the hinge region, the Fc linkers of the Fc-multiplexed antibodies were optimised by removing amino acids that were not resolved in crystal structures of the mIgG1 CH2-CH3 domains[345,346] as well as choosing a rigid linker (PAPAP) instead of a long flexible one (GGGGS) as described in Sections 6.2.1 and 6.2.2.

In order to create a rigid, extended antibody, all approaches were combined and a hingeless mNivo construct with two additional Fc domains, each linked by 50 aa of mCD43, was designed (Figure 6.3 D). Due to the lack of cysteines on the heavy chain, the hinge-deleted antibodies displayed a somewhat unstable nature, resulting in single heavy and light chains under denaturing conditions. To improve on this, constructs with a reintroduction of (i) a single cysteine and (ii) the hinge sequence up to the first cysteine (VPRDC) were created. The

second approach allowed for a complete, stable assembly of HC-LC pairs, however, the HCs still dissociated (Figure 6.4 B, right panel). Importantly, under non-denaturing conditions, all antibodies were stable (Figures 6.4 D and 6.5). All three antibodies were purified and the binding behaviour was assessed using SPR (Section 6.2.6). While the monovalent binding was not changed when the antibodies were captured on a Protein A chip (Figure 6.6 A), surprisingly, there was a slight reduction of the k_{a1} rates when the hingeless, extended antibodies, except for the antibody with a reintroduction of VPRDC, were injected as an analyte over captured hPD-1-2xHis (Figure 6.6 B). This could potentially be explained by the reduced flexibility of the antibodies, as the hinge region is crucial for binding to epitopes at various angles[201]. While this might not influence the epitope recognition as much when the antibodies are pre-bound to the chip, it could slightly reduce the binding radius of an antibody used as an analyte. However, this effect should have also been observed for the mNivo hingeless D265A antibody (Figure 6.2 C), but this was not the case. Thus, the bivalent binding is more likely to be influenced by the Fc multiplexing, which could reduce the rotational freedom of an antibody, thereby reducing the chances to engage with its epitope. Importantly, while these small changes were observed, they are unlikely to have a great impact on the overall efficacy in *in vitro* and *in vivo* assays.

Using the *in vitro* T-cell activation assay described in Section 5.2.5, the different mNivo variants were tested for their immune-activatory capacity in the presence of PD-L1 and mFcγRIIb. As all hinge-deleted antibodies harboured D265A mutations in every Fc domain, they should not be bound by mFcγRIIb. However, in theory, and as outlined in Section 6.1, small proteins, like antibodies, can remain in close contacts, enhancing the probability for the bound receptor to be triggered. This was shown to be the case for TCRs being bound by small molecules, i.e. a Fab or pMHC, which reduced the diffusion speed and resulted in more TCR triggering[70]. Based on these observations, the assay investigated whether rigid, extended antibodies could be sterically excluded from close contacts, leading to less PD-1 signalling and more T-cell activation. However, across five

independent repeats of the T-cell activation assay, no reproducible improvement over mNivo D265A was observed. Thus, none of the rigid, extended antibodies were taken forward for *in vivo* tests.

Importantly, using TIRF microscopy and SLB2s presenting mFcγRIIb, a clear enrichment of Fc-engaging mNivo in close-contact zones was found (Section 6.2.8). This was in stark contrast to mNivo D265A, mNivo Fc 2x50 aa D265A1+2 and mNivo hingeless 2xFc 2x50 aa D265A1+2+3, all of which were not enriched in these areas. Removing the 'anchor' of mNivo on the SLB2 (mFcγRIIb) resulted in a very even distribution of the antibody, clearly demonstrating that nivolumab mIgG1 bound to PD-1 can remain in phosphatase-depleted areas. Hypothetically, this can result in inhibitory signalling by PD-1, irrespective of the receptor being bound (i) directly by its ligand or (ii) indirectly via the interaction of nivolumab with an FcγR. Importantly, the extended antibodies (mNivo Fc 2x50 aa D265A1+2 and mNivo hingeless 2xFc 2x50 aa D265A1+2+3) were significantly less enriched in close-contact zones compared to mNivo D265A as shown by the quantitative image analysis.

There are some technical limitations of the current experimental approach. First, the purified, extended antibodies exhibited some aggregation (Figure 6.5), which can potentially lead to crosslinking of the receptor and triggering of PD-1. Thus, future experiments should focus on pooling only the fractions with absolutely no presence of aggregated protein. Second, and as discussed for the *in vitro* results of Chapter 5, while the D265A mutation greatly reduces the affinity to FcγRs, some binding remains[213]. Therefore, as the novel mNivo variants harboured three Fc domains, the overall avidity towards mFcγRIIb might be slightly increased, which could impede the activity. Third, while the aim of this chapter was to reduce flexibility and increase the overall size of nivolumab mIgG1, these modifications have not been directly validated. As mentioned in Section 5.3, a microscope-based assay to measure the distance between the bound antigen and the FcγR needs further optimisation (in collaboration with João Ferreira Fernandes). Once established, this assay could be used to approximate the size

of the antibody, which should help to validate the approach for extending the antibodies. Furthermore, the novel SPR-based algorithm which infers the reach of antibodies could be used to compare mNivo and mNivo hingeless (in collaboration with Omer Dushek). In addition, biophysical methods such as dynamic light scattering could be utilised to determine the precise hydrodynamic radius, instead of relying on size comparisons using analytical SEC. Finally, while the *in vitro* assay suggested that the new mNivo variants did not improve on T-cell activation, this could also be an artifact of the assay, e.g. the cells cannot get stimulated beyond the levels of mNivo D265A. However, this is rather unlikely as not all cells got fully stimulated upon treatment with mNivo D265A, and there were still significant numbers of Jurkat T cells expressing low or no levels of GFP (data not shown), which indicates NF-κB transcriptional activity. To investigate this, a PD-1-CD45 RIPR molecule[341] (introduced in Section 6.1) was obtained from Ricardo Fernandes to test its stimulatory capacity. Surprisingly, it did not result in any stimulatory effect in the T-cell activation assay (data not shown). This result is still under investigation and novel RIPR formats will be tested.

Overall, while hinge-deleted, extended antibodies were successfully produced, these novel formats failed to improve T-cell activation beyond the levels observed with mNivo D265A. The reasons for this require further investigation.

Life is an experiment you can't repeat.

— Enzo Cerundolo

7 Concluding remarks and future perspectives

Contents

7.1 Summary and general discussion 185
7.1.1 Antibody production and cancer models 186
7.1.2 Combination therapy of mNivo and OX108 191
7.1.3 (Rigid) extended forms of nivolumab mIgG1 to increase efficacy 193
7.2 Concluding remarks 202

7.1 Summary and general discussion

THIS thesis aimed to improve on immune-checkpoint inhibitors to treat cancer with a focus on the PD-1 blocking antibody nivolumab. To achieve this, two major approaches were taken. First, a novel combination therapy with a CD200R blocking antibody was trialled (Chapter 4). As CD200R is an inhibitory immune receptor preferentially expressed on myeloid cells, co-blockade of CD200R and PD-1 might lead to the reactivation of myeloid and lymphoid cells, respectively. Second, based on the hypothesis derived from the KS model for antibody agonism (introduced in Section 1.2.2), antibody engineering

was used to reduce the potential receptor-triggering activity of nivolumab mIgG1 (Chapters 5 and 6). While this agonism should be FcγR-dependent, recent reports also described a constant, tonic signalling activity of PD-1[341]. Thus, besides investigating new antibody formats that reduce agonism (Chapter 5), additional constructs were tested for their capacity to also reduce tonic signalling (Chapter 6). A T-cell activation assay, optimised for antibody agonism, was established to test this *in vitro*. Finally, in order to test anti-human antibodies in mouse tumour models, the previously characterised mice humanised for PD-1[293] and CD200R[294] were used.

7.1.1 Antibody production and cancer models

In order to be able to test the different approaches, an antibody expression pipeline needed to be established. As the produced proteins were ultimately to be used in mice, endotoxin-free, monomeric, sterile antibodies were required. While the results of this were briefly discussed, it should be emphasised that the establishment of this pipeline took over six months and in total more than 1,100 mg of antibodies were produced. The antibodies were validated using SPR and *ex vivo* blocking assays using splenocytes of hPD-1/hCD200R mice.

The fundamental design of the antibodies was discussed in Section 3.2.1. All currently approved PD-1 antibodies in the clinic are of the human IgG4 isotype[121], which exhibits low antibody effector functions[214] and is best matched by the mouse IgG1 isotype, which only binds to the low-affinity receptors mFcγRIIb and mFcγRIII[203]. Thus, in order to study the effects of nivolumab in the murine system, a 'murinised' version of nivolumab (mNivo) was created by linking the respective variable chains with the mIgG1 heavy and the murine κ light chain constant regions. Of note, while mIgG1 is the isotype most similar to hIgG4, there are certain caveats with this approach. First and foremost, hIgG4 was described to interact with the high-affinity receptor hFcγRI[202], which can trigger phagocytosis of PD-1$^+$ T cells *in vitro*[239]. As mIgG1 lacks the capability to engage mFcγRI, this can result in discrepancies when testing the antibodies *in*

vivo. Importantly, the 'default' version of mNivo in Chapters 3 and 4 included a D265A mutation, which heavily reduces binding to FcγRs[212]. This approach was taken as there is growing evidence that Fc-null PD-1 antibodies (no binding to FcγR) are more effective compared to their Fc-engaging counterparts[235,237–239]. Thus, as Chapters 3 and 4 only used Fc-null nivolumab mIgG1 (mNivo D265A), the potential discrepancy introduces by the differential FcγR-binding profiles of hIgG4 and mIgG1 are not applicable in this context. Furthermore, as Chapters 5 and 6 focused on the idea of mNivo-driven agonism, the absence of interaction with mFcγRI by mIgG1, which could trigger phagocytosis, was actually beneficial for the aims of these chapters. Of note, both, mIgG1 and hIgG4, do not activate the complement system as they do not bind to the complement factor C1q[302].

Besides the slight variations in the FcγR-binding profile, there are also differences between mouse and human FcγRs[86]. For example, humans have five activating FcγRs, whereas mice only have three[86]. Importantly, in order to overcome these discrepancies, other groups have mice humanised for FcγRs to investigate human isotypes with greater accuracy in mouse models[215,216]. Overall, while there are some disadvantages with testing anti-human antibodies in the murine IgG/FcγR system, this was the only feasible approach as the hPD-1/hCD200R mice had to be used for the epitope recognition of nivolumab and OX108. Ideally, hPD-1/hCD200R mice could have been crossbred with FcγR-humanised mice, but this was beyond the scope of this thesis. Importantly, as most experiments were carried out with mNivo D265A, the overall impact of the human-mouse discrepancies should be small.

While searching for a 'cold' and 'hot' tumour model, surprising findings were made. While this binary classification is likely an over-simplistic categorisation, it describes the responsiveness of a tumour model to immune-checkpoint blockade, e.g. PD-1-blocking antibodies[301]. A 'hot' tumour generally responds well to immunotherapy and is often characterised by the infiltration of proinflammatory immune cells into the TME, while the opposite is true for a 'cold' tumour model[301]. As it is important to test the potential benefits of novel therapeutics in both

model types, PD-1 blockade-sensitive and -resistant models were sought. The LLC1 model does not respond to PD-1/PD-L1 blockade[306,309] and is characterised by a high degree of myeloid cell infiltration[307] as well as systemic accumulation of immature myeloid cells[308], which makes it an interesting candidate to test the co-blockade of PD-1 and CD200R. In contrast, the MC38 model is commonly used due to its strong therapy response to immune-checkpoint blockade[235,237,238]. While LLC1 cells were available in the Cerundolo laboratory, MC38 cells were initially obtained from Adrian Harris (University of Oxford). However, in contrast to the published data demonstrating reduced tumour growth upon PD-1 blockade[235,237,238], the MC38-Oxford cells did not respond at all. Upon unsuccessful trialling of different treatment regimens (data not shown), another MC38 cell line was obtained from the Beers laboratory (University of Southampton), who have previously used this model for investigating improvements on anti-PD-1 therapy[238]. Indeed, the cells obtained from Stephen Beers differed strikingly in their ability to respond to mNivo therapy. The expression of MHC-I, PD-L1 and CD200 was characterised *in vitro* in response to IFN-γ as well as *in vivo* for all cell lines. Importantly, MC38-Southampton cells were the only cell line expressing CD200, the ligand for CD200R. While only a fraction of the cells expressed CD200, the levels were comparable to PD-L1 on immature DCs and PD-L2 on mature DCs[127]. Finally, the infiltrating immune cells were compared between the different tumour models and the MFI of CD200R was assessed to identify potential target cells for anti-CD200R therapy. In accordance with the literature[144], CD200R was preferentially expressed on myeloid cells, with all identified populations being positive for CD200R, whereas only $CD4^+$ T cells demonstrated consistent expression of CD200R across all tumour models.

The differences between the PD-1 blockade-sensitive MC38 cells, received from Stephen Beers, and the resistant ones, obtained from Adrian Harris, were further investigated. While both cell lines were validated through STR profiling externally, they showed a slight discrepancy in the analysed loci (data not shown). However, there are two different STR profiles available, one from the provider of

the cell line (James Hodge, NCI/NIH) and one from the distributor (Kerafast). Furthermore, the company validating the cells highlighted that they observe a lot more variability in MC38 cells compared to other cell lines (personal communication from IDEXX BioAnalytics), which suggests a high mutagenesis rate of MC38 cells. Thus, while there are differences between the two MC38 models used, this seemed to be a general problem with this particular cell line. In addition to the contrasting response towards mNivo treatment, the resistant model also exhibited a significantly faster *in vivo* growth. Importantly, mice that previously completely rejected a PD-1 blockade-sensitive MC38 tumour demonstrated a significantly reduced tumour growth when injected with the resistant MC38 cells, suggesting that the two cell lines are indeed genetically similar, as there was immunological memory present. To investigate these differences on a global transcriptomic level, bulk RNA sequencing was performed of *in vitro* cultured cells. In addition to comparing the differentially expressed genes between the two MC38 cell lines available in our laboratory (Oxford study), another RNA-seq dataset of PD-1 blockade-sensitive and -resistant MC38 cells from a previously published study were included (Sanofi study)[300]. Of note, while the described upregulation of TGF-β was confirmed, Bernardo *et al.* also reported an increased activation of the Notch pathway[300], something that was not observed upon reanalysis of their dataset. This might be explained by the different pathway analysis tools utilised, as the authors used the QIAGEN Ingenuity Pathway Analysis, a tool that is not publicly accessible. Intriguingly, there was a large overlap of commonly enriched KEGG pathways between the Oxford and Sanofi study in PD-1 blockade-resistant MC38 cells.

To investigate this in more detail, a STRING network analysis was used. Analysis of all genes from significantly enriched pathways from both datasets revealed that the KEGG pathway 'ECM-receptor interaction' is a major driver of resistance to anti-PD-1 therapy in MC38 cells. Specifically, there were several collagens, integrins, thrombospondins and matrix-metalloproteinases upregulated. The immunomodulatory effects of these protein families, which can contribute to

resistance, are versatile and some of them will be highlighted below. For example, collagen-rich matrices exhibited an increased stiffness, and this was shown to correlate with a reduced ability of $CD8^+$ T cells to proliferate[317]. Additionally, T cells cultured in a 3D-high-density matrix exhibited a shift towards a regulatory T-cell phenotype[317]. Furthermore, collagen can also have a direct effect on T-cell signalling via LAIR1, an inhibitory immunoreceptor binding collagen, which was shown to directly promote resistance to anti-PD-1 therapy through induction of $CD8^+$ T-cell exhaustion[350]. Finally, an increased collagen density was also linked to a more immunosuppressive macrophage phenotype, which inhibited T-cell proliferation[351]. A summary of the different immune-modulatory properties of collagen was recently reviewed elsewhere[314]. Thrombospondin-1 (encoded by the *Thbs1* gene) was found to be upregulated in the PD-1 blockade-resistant MC38 cells and is a potent endogenous inhibitor of angiogenesis[352]. While induction of angiogenesis is a hallmark of cancer[3], it can also result in increased immune-cell infiltration[352]. A knockdown of THBS1 was shown to facilitate tumour vascularisation, resulting in increased T-cell infiltration and reduced TGF-β levels. Most importantly, the reduction of THBS1 also increased the responsiveness of the 4T1 mouse breast cancer model to anti-PD-1 therapy[352]. Similarly, integrins, in particular $\alpha_V\beta$ integrins, were shown to convert the latent form of TGF-β (LAP-TGF-β) into its active form[353]. Importantly, knockout of integrin α_V (encoded by *Itgav*) decreased levels of active TGF-β and sensitised B16-F10 cells to anti-PD-1 treatment[353]. Finally, matrix-metalloproteinases can facilitate tumour progression through a variety of mechanisms, including the modulation of cytokines and chemokines (reviewed by Gialeli *et al.*[313]). Taken together, there is a substantial body of evidence offering potential explanations for the PD-1 blockade resistance of MC38 cells. However, a more in-depth characterisation of the two MC38 cell lines available in our laboratory was beyond the scope of this study. Future work could focus on a transcriptional comparison of *in vivo* MC38 tumours, PD-1 blockade-sensitive and -resistant, treated with MOPC21 or mNivo, at different time points using bulk RNA sequencing. This should also

help to identify at which stage the sensitive model is forced into remission by infiltrating immune cells. Finally, single-cell RNA sequencing could be used to decipher how the different immune cell subsets work together to eradicate the tumour in the sensitive model, but fail to do so in the resistant tumour.

Overall, the work presented in Chapter 3 successfully established the antibody production pipeline as well as the tumour models. Future work will characterise the two MC38 cell lines in more detail and will aim to validate some of the findings, e.g. through testing combination therapies that might reverse the resistance to PD-1 blockade.

7.1.2 Combination therapy of mNivo and OX108

Upon successful validation of the *in vitro* blocking efficacy of mNivo and OX108, the combination immunotherapy of both antibodies was trialled in the PD-1 blockade-resistant model LLC1 and the sensitive model MC38. While the co-blockade of PD-1 and CD200R did not improve the survival of mice bearing LLC1 tumours, there was a trend towards more complete responses in the MC38 model, though not reaching statistical significance. In addition, tumour-infiltrating myeloid and lymphoid cells were compared between the different treatment groups. Infiltrating immune cells in LLC1 tumours did not change convincingly, and observed differences are likely explained by the small group size of the OX108 treatment arm (n = 3). In contrast, there was a reduction of M2 macrophages observed for mNivo and mNivo + OX108 treated animals across three independent repeats. Interestingly, treatment with mNivo and OX108 also led to a statistically significant increase in DC1s in the dLN of mice bearing MC38 tumours. While these cells are only present at very low frequencies in the lymph node ($\leq$ 1.0 %), they are important for mounting an anti-tumour response. As discussed in Section 1.4.3, DC1s are responsible for the cross-presentation of tumour antigens to $CD8^+$ T cells[24]. However, DC1s are extremely sparse in the TME[23], and it was demonstrated that increasing the numbers of DC1s synergised with PD-1/PD-L1 blockade[25,278,279]. As shown in Section 3.2.7, DC1s in the

TME express CD200R, albeit at a lower level compared to DC2s or G-MDSCs. While it is important to note that the measurement of the reported CD200R MFI is based on DC1s within the tumour, the same trend was observed for immune cells in the LNs (data not shown). Overall, despite not being the highest CD200R-expressing immune cell population, the significant increase of DC1s in the dLN upon co-blockade of PD-1 and CD200R is an intriguing result that might be linked with the trend towards more complete responses. Follow-up studies are required to investigate this in greater detail.

The trend for a survival benefit in the MC38-sensitive model coupled with the observation that these cells expressed CD200 is interesting, as it suggests that the CD200/CD200R axis might be an additional route for suppression of infiltrating immune cells in these tumours. However, while MC38-sensitive cells expressed CD200 levels similar to PD-L1 and PD-L2 on immature and mature DCs[127], it should be noted that DCs also increase their levels of PD-L1 by more than 10-fold upon maturation (from 5,724 to 80,372 molecules[127]). Therefore, the subtle effects observed upon combining PD-1 with CD200R blockade might be explained by the low receptor engagement in the MC38-sensitive TME. Thus, follow-up studies should preferentially investigate CD200R blockade in models with high levels of CD200, either by screening for high CD200 baseline levels across several cell lines or through forced upregulation, e.g. using a lentiviral transduction approach.

Furthermore, a recent paper described an affinity threshold for murine anti-PD-1 antibodies[324]. As OX108, the antibody used for blocking CD200R in this study, has a relatively low affinity of 83.8 nM, this might contribute to the small effects observed upon treatment. Previous work by Christopher Paluch identified a high-affinity blocking antibody against CD200R[294]. Therefore, this antibody, referred to as mAb26, was produced and validated to have a 10-fold lower K_D of 8.10 nM (data not shown). Future experiments could compare the co-blockade of mNivo with OX108 or mAb26.

A limitation of this study is the utilised tumour models. The MC38 and LLC1 models were chosen due to their contrasting responsiveness to anti-PD-1

monotherapy, however, both cell lines were subcutaneously injected, which may not recapitulate the site of origin[354]. Furthermore, both models are very fast growing tumours, which does not adequately mimic the typical slow tumour development[354]. Thus, future studies should focus on more advanced tumour models, such as orthotopic tumours or patient-derived xenografts.

Taken together, the fact that a minimum of two anti-CD200(R) antibodies are currently in clinical trials[188,194] underpins the therapeutic importance of this immune axis in cancer. However, the present study did not demonstrate a significant improvement over nivolumab mIgG1 monotherapy when combined with OX108. This might be explained by (i) the weak affinity of the CD200R blocking antibody used, (ii) the low ligand engagement within the two tumour models tested or (iii) a small contribution of this pathway to immune suppression. Future studies should investigate these caveats by using high-affinity antibodies in tumour models with a high expression of CD200.

7.1.3 (Rigid) extended forms of nivolumab mIgG1 to increase efficacy

In order to test whether the decreased efficacy observed for Fc-engaging PD-1 blockers[235,237–239] might be due to an agonistic activity of these antibodies, mNivo without a D265A mutation was produced. According to the KS model, antibody agonism is dependent on the distance between the antigen- and the FcγR-binding domains of the antibody (explained in Section 1.2.2). Thus, two different strategies for increasing this distance were trialled in order to reduce potential agonism of nivolumab mIgG1. First, the previously tested[294,296] extension of the hinge region through insertion of 50 aa of mCD43 was used, this time doubling and tripling the number of amino acids inserted. Second, an Fc-multiplexing approach, which has been described to increase antibody effector functions[326], was used to increase the size of the 'base' of the antibody. Importantly, as D265A mutations were introduced in all Fc regions, there should be no increase in antibody effector functions. Finally, for one antibody construct, both modifications were

combined, creating a hinge-extended Fc-multiplexed mNivo. Using this antibody, different FcγR-binding variants were designed through repositioning of the D265A mutation, thereby modifying the distance between antigen- and FcγR-binding domain, without changing the overall size of the antibody.

Upon purification and validation of the mNivo variants, an *in vitro* T-cell activation assay was modified to allow the assessment of antibody agonism via upregulation of mFcγRIIb. Strikingly, Fc-engaging mNivo indeed harboured strong agonistic activity in this assay, which is in line with previous *in vivo* observations from Christopher Paluch for nivolumab mIgG1 (Figure 1.9 C)[294]. Furthermore, there is *in vitro* data for nivolumab hIgG4 from our collaborator Peter Steinberger (Lippert *et al.*, manuscript submitted) as well as Mark Cragg and colleagues demonstrating agonistic activity[103]. Thus, this rules out that the observed effect is an artifact of (i) choosing the mIgG1 isotype instead of hIgG4 or (ii) the *in vitro* T-cell activation assay used in this study.

However, no clear differences could be observed when comparing the different mNivo antibodies against each other in mouse tumour models. As the agonism of mNivo was dependent on the presence of mFcγRIIb in the *in vitro* assay, the potential lack of FcγR binding in the TME might explain the contrasting results. Thus, a truncated form of mFcγRIIb was overexpressed on PD-1 blockade-sensitive MC38 cells in an attempt to make them more resistant to treatment with Fc-engaging mNivo. While mNivo D265A was more effective compared to mNivo, the efficacy of mNivo was not influenced by the levels of mFcγRIIb. However, this approach needs further optimisation in order to draw final conclusions, as the two tumour models (with/without mFcγRIIb) exhibited a significantly different growth rate for the isotype-treated arm. A combination therapy using mNivo or mNivo D265A and AT128, a blocking antibody specific for mFcγRIIb, also did not result in any differences between the treatment groups. However, the low affinity of AT128 as well as the presence of other FcγRs might be the reason for the lack of increased efficacy observed. Finally, while the effects observed when comparing mNivo and mNivo D265A differed between experiments, pooling

of all datasets increased the statistical power enough to uncover a significantly improved survival for treatment with mNivo D265A.

As discussed in Section 6.1, the flexibility of antibodies might allow them to remain in close contacts despite their large size, which would lead to inhibitory signalling by PD-1 according to the KS model. As there was data suggesting that there is tonic signalling of PD-1[341] and, surprisingly, none of the extended antibodies from Chapter 5 improved over mNivo D265A, a novel way of engineering mNivo was considered. First, the feasibility of different approaches was trialled in an attempt to reduce this flexibility, namely deletion of the hinge region and optimisation of the Fc linkage through (i) removal of potentially flexible amino acids of CH2 and CH3 and (ii) replacement of the flexible linker (GGGGS) with a rigid one (PAPAP). Following this, rigid, extended forms of mNivo were designed. Of note, due to the HC-LC dissociation observed for hinge-deleted nivolumab mIgG1 antibodies, different constructs were designed with the aim of restoring the HC-LC disulfide bond. Upon purification and SPR validation, the rigid, extended antibodies were tested in the *in vitro* T-cell activation assay, however, none of them improved over mNivo D265A. Of note, while mNivo hingeless 2xFc 2x50 aa VPRDC D265A1+2+3 successfully restored the HC-LC disulfide bond, demonstrated by an increased stability under denaturing conditions, this did not have an impact on the *in vitro* blocking efficiency.

In collaboration with Edward Jenkins and the group of David Klenerman (University of Cambridge), TIRF microscopy on SLB2s presenting mFcγRIIb was used to test for a potential mNivo-driven enrichment of PD-1 in close contacts. Indeed, Fc-engaging mNivo was highly enriched in phosphatase-depleted areas supporting the agonistic principle, but this was not the case for the other mNivo variants tested (mNivo D265A, mNivo Fc 2x50 aa D265A1+2 and mNivo hingeless 2xFc 2x50 aa D265A1+2+3). Importantly, when mFcγRIIb was removed from the SLB2, mNivo and PD-1 were distributed evenly across the cell membrane, which demonstrates that PD-1, bound by an antibody, is small enough to remain in close contacts. Quantitative image analysis revealed that both extended antibodies

tested were significantly less enriched in close-contact zones compared to mNivo D265A. Furthermore, PD-1 was more excluded when compared to the MOPC21 isotype control, suggesting that due to the large size of the antibodies PD-1 was 'pushed out'. The microscopy analysis raises two issues that need to be investigated in greater detail. First, what makes mNivo D265A (on SLB2s with mFcγRIIb) appear to be more excluded from close contacts compared to mNivo on SLB2s without mFcγRIIb? More experiments are needed to exclude the possibility that this observation is an artifact of having imaged different stages of close-contact formation. As T cells land on the SLB2, they interact with the surface, scanning for pMHC. While the experiments followed a stringent protocol, it may be possible that the time required for the cells to establish close contacts differed, which could have an effect on the extent of antibody exclusion. Second, despite the significantly reduced enrichment of the extended antibodies compared to mNivo D265A in close-contact zones, none of the former increased the *in vitro* T-cell activation over mNivo D265A. While the differences in enrichment were significant, the overall effect of this on PD-1 signalling needs to be tested. To address this, Edward Jenkins created J8 cells expressing SHP-2-HaloTag to investigate whether the recruitment of SHP-2, the first protein that binds to phosphorylated PD-1, is impacted by the different mNivo antibodies. This should help decipher whether not only PD-1 enrichment is influenced by the bound antibody, but also SHP-2 recruitment, which is a surrogate for signalling. This is currently work in progress.

A general drawback of this study was the lack of validation for the different antibody modifications. While the extensions were carefully chosen and designed (explained in Sections 5.2.1, 6.2.1 and 6.2.3), a direct validation of an overall increased size or a reduced flexibility has not been demonstrated. Thus, the biophysical characterisation of the antibodies needs further attention and different techniques should be utilised to address this, which was discussed in Sections 5.3 and 6.3.

Importantly, while the extended antibodies were very useful for a proof of concept of antibody agonism driven by the KS model, the translational potential of

this approach needs to be further tested. Although the antibodies were validated to retain their *in vitro* stability and binding behaviour, as well as efficacy *in vitro* and *in vivo*, more validation, especially *in vivo*, is necessary. For example, the pharmacokinetics (effect of the body on the drug) and pharmacodynamics (effect of the drug on the body) of the extended antibodies need to be investigated in greater detail. Due to the modifications and increase in overall size of the antibody, a potential reduction of the half-life could be expected. While there was an overall increased binding of FcRn to Fc-multiplexed antibodies, the pharmacokinetic analysis displayed a faster clearance *in vivo*[326]. Interestingly, this effect was dependent on FcγR binding, as mutation of the FcγR-binding sites reversed this[326]. Overall, the existing data on Fc-multiplexed antibodies clearly demonstrates that the interaction with the body might be influenced by the introduced modifications[326]. Finally, the changes made to the antibody structure might also result in increased immunogenicity, which would need careful consideration if this approach was to be taken forward for clinical development.

In contrast to the uncertain translational potential of extended antibodies, Fc-null PD-1 and PD-L1 blocking antibodies (atezolizumab, durvalumab and tislelizumab) are already used in the clinic[121,240], demonstrating the feasibility of abrogating FcγR binding of antibodies. As none of the extended antibodies improved over mNivo D265A, and Fc-silencing requires only little modifications, mNivo D265A might be the best candidate for subsequent clinical development. However, while the D265A mutation heavily reduces FcγR binding[212], it does not completely abolish the antibody-FcγR interaction[213]. Importantly, there are more and more novel Fc-null variants designed, all aiming to fully abrogate FcγR interactions[209]. Recently, a new company, mAbsolve, was formed solely focusing on developing mutations that completely abolish Fc effector functions of monoclonal antibodies[210]. Thus, future work should introduce novel mutations, which are more effective in reducing antibody-FcγR interactions, into mNivo, in order to test whether this increases the efficacy over that of mNivo D265A.

The potential for clinical development is especially exciting considering the general applicability of this approach to NTRs (defined in Section 1.2). There are currently several monoclonal antibodies targeting small receptors under clinical development[355]. The concept of antibody-driven agonism, which should be reduced by creating Fc-null antibodies, is, theoretically, applicable to all of these antibodies. Similarly, while using a different approach, Fernandes *et al.* demonstrated that the recruitment of the phosphatase CD45 could inhibit the activation of different receptors, including PD-1, CD28, CTLA-4 and SIRPα[341]. In addition, other targets could include NTRs like TIM-3, LAG-3, TIGIT, BTLA, CD200R and many more.

As discussed in Sections 1.3.3.3 and 5.1, multiple reports have described the detrimental effects of FcγR-engagement for PD-1 blocking antibodies and demonstrated an increased efficacy of Fc-null PD-1 blockers compared to their Fc-engaging counterpart[235,237–239]. Ravetch and colleagues were the first to show an increased anti-tumour activity of anti-PD-1 antibodies harbouring a D265A mutation. Importantly, while not describing a precise mechanism of action, they found a delay in proliferation of $CD8^+$ T cells when treating WT animals with a rIgG2a anti-PD-1 antibody (similar effector functions as mIgG1), compared to $Fcgr2b^{-/-}$ mice[235]. Following up on this, Pittet and colleagues used an *in vivo* imaging approach to decipher a potential mode of action. While the intravenously administered rIgG2a anti-PD-1 antibody initially bound to $PD\text{-}1^+$ T cells, it was quickly taken up by FcγR-expressing macrophages ($PD\text{-}1^-$)[237]. Therefore, the authors argued, FcγR-antibody interactions limit the therapy response due to insufficient blockade. Similar to the results from Christopher Paluch (Figure 1.9 C), the Beers laboratory found that in a vaccination setting using OVA antigen, a mIgG1-N297A (Fc-null) PD-1 blocking antibody led to an increased proliferation of antigen-specific T cells compared to mIgG1[238]. Importantly, they demonstrated the same effect in FcγR-humanised mice using hIgG4 and hIgG4-FALA (Fc-null) PD-1 blocking antibodies. While they did not find a significant improvement of survival for Fc-null PD-1 blockers using two different tumour

models, they showed increased levels of PD-1 on $CD8^+$ T cells as well as more activated myeloid cells, underlining a greater activation potential[238]. Of note, introducing mutations to abrogate FcγR binding (D265A or N297A) did not influence the antibody half-life[235,238]. This is expected as FcRn has a separate binding epitope compared to FcγRs. In contrast to the currently FDA-approved anti-PD-1 antibodies, which are all hinge-stabilised hIgG4 antibodies with no mutations to reduce FcγR binding[121], BeiGene have developed an Fc-null hIgG4 anti-PD-1 antibody (tislelizumab, BGB-A317). They demonstrated superior efficacy of the Fc-null antibody in a tumour xenograft model compared to the Fc-engaging antibody[239]. Furthermore, they showed that hIgG4 has a high affinity to hFcγRI, which can lead to phagocytosis of PD-1^+ T cells *in vitro*[239]. Tislelizumab is currently in phase III clinical trials[240]. Taken together, it is now established that FcγR binding is not needed for PD-1 blocking antibodies, and, in contrast, it rather diminishes their efficacy. As outlined above, there are different potential mechanisms of actions available to explain these observations. Here, another explanation based on antibody agonism was presented.

However, a thorough *in vivo* analysis of this is needed. Although the *in vitro* T-cell activation assay convincingly demonstrated antibody-driven agonism, the mechanisms driving the increased efficacy of mNivo D265A compared to mNivo in mouse tumor models are more complex. As mentioned above, other reports studying the effects of FcγR engagement on anti-PD-1 antibodies have focused on different explanations[235,237–239]. However, the observed *in vitro* phagocytosis, driven by hFcγRI, of PD-1^+ T cells upon treatment with Fc-engaging tislelizumab[239] is very unlikely in our model, as mIgG1 does not bind to mFcγRI[203]. In contrast, the other findings could indeed contribute to the increased efficacy observed for mNivo D265A compared to mNivo. Importantly, (i) the observed delay in proliferation of $CD8^+$ T cells when treating WT animals with an anti-PD-1 blocking antibody compared to Fcgr2b$^{-/-}$ mice[235] as well as (ii) the increased upregulation of PD-1 on $CD8^+$ T cells upon treatment with an Fc-null blocker compared to the Fc-engaging counterpart[238] could, theoretically,

be explained by a reduced agonistic activity of the anti-PD-1 antibodies in the respective condition. To investigate the *in vivo* results in more detail, follow-up studies will, among other things, focus on the optimisation of the MC38-sensitive-mFcγRIIb tumour model. There was a significant difference in growth between MC38-sensitive and MC38-sensitive-mFcγRIIb tumours upon treatment with the isotype control MOPC21. Thus, no conclusion can be drawn for the comparison of mNivo between these models, which was the main aim of this experiment. Instead of using the parental cell line (MC38-sensitive), an 'empty' lentivirus was cloned, which does not upregulate any protein and only mimics the lentiviral transduction (data not shown). Future experiments will compare the growth rates of these two cell lines (MC38-sensitive-mock and MC38-sensitive-mFcγRIIb). As mFcγRIIb is truncated, i.e. with no signalling capacity into tumour cells, this should be a good model to test the effects of antibody agonism. Furthermore, *ex vivo* proliferation assays are planned with OVA-specific T cells to test the effects of FcγR engagement under more physiological conditions. Finally, a single-cell RNA sequencing experiment might reveal differentially activated PD-1$^+$ immune cells within the TME or dLN of mice treated with mNivo or mNivo D265A.

The work described in this thesis might also provide important insights into the characteristics needed for agonistic antibodies. Specifically, while this study aimed to reduce agonistic activity through extending antibodies or reducing FcγR engagement, the reverse approach could be used to increase agonism. This is also of great clinical relevance, e.g. for stimulation of inhibitory immune receptors for the treatment of autoimmune diseases or triggering of activatory receptors for cancer immunotherapy. Potential approaches for this could include:

1. Finding antibodies that bind to membrane-proximal epitopes, thereby reducing the gap created between the antigen- and FcγR-binding domain. This has been shown for anti-CD28 agonists[80,81], where membrane-proximal binding antibodies resulted in a $\sim$ 10 nm more-compact gap[55]. Importantly, this concept was recently validated for anti-PD-1 antibodies by Suzuki *et*

al.[87]. The identified PD-1 agonist was used to treat body weight loss in a colitis mouse model, demonstrating the clinical relevance[87].

2. Increasing the affinity for FcγRs should enhance the agonistic activity of antibodies, as hFcγRIIb upregulation was shown to be crucial for the superagonistic activity of the anti-CD28 antibody TGN1412[84]. Similarly, mFcγRIIb was also important for the agonism of anti-CD40 antibodies[356] and increasing the affinity to hFcγRIIb through a S267E mutation[357] enhanced the agonistic activity[358]. Importantly, while the agonism according the KS model should not be dependent on the specific FcγR that binds the antibody, as long as the dimensions are the same, increasing the affinity towards activating FcγRs can result in unwanted ADCC or ADCP. Thus, strategies to increase FcγRIIb binding should be favoured.

3. Hypothetically, the agonism should not be dependent on FcγRs per se, but rather on the antibody interacting with a protein on an opposed (cell) surface. For example, BiTEs aim to redirect T cells towards cancer cells by binding simultaneously to a tumour antigen and the TCR (usually via anti-CD3), resulting in T-cell activation and subsequent killing of the cancer cell. Other bispecific molecules target two cell-surface receptors, such as the DuoBody-CD40x4-1BB (GEN1042/BNT312). This protein was found to trigger both receptors, CD40 and 4-1BB, but this was conditional on the presence of both targets[359], demonstrating that agonism does not require FcγR binding. Interestingly, increasing the distance between the two target epitopes of a BiTE resulted in a diminished cytotoxicity[72], as would be explained by the KS model[55].

Overall, based on the results generated in our laboratory on how antibody can induce signalling, a spinout company, MiroBio, was founded in 2019. The insights led to the development of MiroBio's discovery platform I-ReSToRE (REceptor Selection and Targeting to Reinstate immune Equilibrium), which facilitated the development of anti-PD-1 and anti-BTLA agonists, with the

latter already being trialled in phase I clinical trials[360]. In 2022, MiroBio was acquired by Gilead Sciences[360].

7.2 Concluding remarks

The work described in this thesis aimed to improve on immune-checkpoint blockade using two different approaches. First, a novel combination therapy comprising nivolumab mIgG1 and OX108, a CD200R blocking antibody, was trialled to reactivate the lymphoid and myeloid immune cell populations, respectively. As most current immunotherapies focus on the reactivation of T cells, this is a concept worth exploring in more detail, despite only modest changes observed in this study. Second, changing the dimensions of antibodies that bind to NTRs can change their signalling outcome. It was shown that increasing the size of nivolumab mIgG1 increased T-cell activation, suggesting a KS-based mechanism of receptor triggering. However, further investigation is needed to uncover the mechanism behind the increased efficacy of Fc-null anti-PD-1 antibodies observed *in vivo*. Finally, the data presented here also suggest that while extended antibodies had a greater capability to 'move' PD-1 out of close contacts, this did not lead to a reduction of PD-1 signalling compared to antibodies less capable of removing PD-1 from the contacts (nivolumab mIgG1 D265A). Clearly, there is still more to be learned about the behaviour of antibodies at cell contacts and how this influences signalling.

References

1. Fellermeyer, M. *et al.* Combination CD200R/PD-1 blockade in a humanised mouse model. *Immunotherapy Advances* **3,** ltad006 (2023).
2. Sung, H. *et al.* Global Cancer Statistics 2020: GLOBOCAN Estimates of Incidence and Mortality Worldwide for 36 Cancers in 185 Countries. *CA: A Cancer Journal for Clinicians* **71,** 209–249 (2021).
3. Hanahan, D. & Weinberg, R. A. The Hallmarks of Cancer. *Cell* **100,** 57–70 (2000).
4. Burnet, F. M. Cancer—A Biological Approach. *British Medical Journal* **1,** 779–786 (1957).
5. Thomas, L. On immunosurveillance in human cancer. *The Yale Journal of Biology and Medicine* **55,** 329–33 (1982).
6. Burnet, F. M. The Concept of Immunological Surveillance. *Progress in Tumor Research* **13,** 1–27 (1970).
7. Hanahan, D. & Weinberg, R. A. Hallmarks of Cancer: The Next Generation. *Cell* **144,** 646–674 (2011).
8. Hanahan, D. Hallmarks of Cancer: New Dimensions. *Cancer Discovery* **12,** 31–46 (2022).
9. Chen, D. S. & Mellman, I. Oncology Meets Immunology: The Cancer-Immunity Cycle. *Immunity* **39,** 1–10 (2013).
10. Dunn, G. P., Bruce, A. T., Ikeda, H., Old, L. J. & Schreiber, R. D. Cancer immunoediting: from immunosurveillance to tumor escape. *Nature Immunology* **3,** 991–998 (2002).
11. Cornel, A. M., Mimpen, I. L. & Nierkens, S. MHC Class I Downregulation in Cancer: Underlying Mechanisms and Potential Targets for Cancer Immunotherapy. *Cancers* **12,** 1760 (2020).
12. Labani-Motlagh, A., Ashja-Mahdavi, M. & Loskog, A. The Tumor Microenvironment: A Milieu Hindering and Obstructing Antitumor Immune Responses. *Frontiers in Immunology* **11,** 940 (2020).
13. Qian, B.-Z. & Pollard, J. W. Macrophage diversity enhances tumor progression and metastasis. *Cell* **141,** 39–51 (2010).
14. Franklin, R. A. *et al.* The cellular and molecular origin of tumor-associated macrophages. *Science* **344,** 921–925 (2014).
15. Arwert, E. N. *et al.* A Unidirectional Transition from Migratory to Perivascular Macrophage Is Required for Tumor Cell Intravasation. *Cell Reports* **23,** 1239–1248 (2018).

16. Zhu, Y. *et al.* Tissue-Resident Macrophages in Pancreatic Ductal Adenocarcinoma Originate from Embryonic Hematopoiesis and Promote Tumor Progression. *Immunity* **47,** 323–338.e6 (2017).

17. Hourani, T. *et al.* Tumor Associated Macrophages: Origin, Recruitment, Phenotypic Diversity, and Targeting. *Frontiers in Oncology* **11,** 788365 (2021).

18. Qian, B.-Z. *et al.* CCL2 recruits inflammatory monocytes to facilitate breast-tumour metastasis. *Nature* **475,** 222–225 (2011).

19. Quatromoni, J. G. & Eruslanov, E. Tumor-associated macrophages: function, phenotype, and link to prognosis in human lung cancer. *American Journal of Translational Research* **4,** 376–89 (2012).

20. Curiel, T. J. *et al.* Specific recruitment of regulatory T cells in ovarian carcinoma fosters immune privilege and predicts reduced survival. *Nature Medicine* **10,** 942–949 (2004).

21. Cassetta, L. *et al.* Human Tumor-Associated Macrophage and Monocyte Transcriptional Landscapes Reveal Cancer-Specific Reprogramming, Biomarkers, and Therapeutic Targets. *Cancer Cell* **35,** 588–602.e10 (2019).

22. Cassetta, L. & Pollard, J. W. Targeting macrophages: therapeutic approaches in cancer. *Nature Reviews Drug Discovery* **17,** 887–904 (2018).

23. Broz, M. L. *et al.* Dissecting the Tumor Myeloid Compartment Reveals Rare Activating Antigen-Presenting Cells Critical for T Cell Immunity. *Cancer Cell* **26,** 638–652 (2014).

24. Roberts, E. W. *et al.* Critical Role for CD103+/CD141+ Dendritic Cells Bearing CCR7 for Tumor Antigen Trafficking and Priming of T Cell Immunity in Melanoma. *Cancer Cell* **30,** 324–336 (2016).

25. Salmon, H. *et al.* Expansion and Activation of CD103+ Dendritic Cell Progenitors at the Tumor Site Enhances Tumor Responses to Therapeutic PD-L1 and BRAF Inhibition. *Immunity* **44,** 924–938 (2016).

26. Böttcher, J. P. & Sousa, C. R. E. The Role of Type 1 Conventional Dendritic Cells in Cancer Immunity. *Trends in Cancer* **4,** 784–792 (2018).

27. Gabrilovich, D. I. & Nagaraj, S. Myeloid-derived suppressor cells as regulators of the immune system. *Nature Reviews Immunology* **9,** 162–174 (2009).

28. Movahedi, K. *et al.* Identification of discrete tumor-induced myeloid-derived suppressor cell subpopulations with distinct T cell–suppressive activity. *Blood* **111,** 4233–4244 (2008).

29. Youn, J.-I., Nagaraj, S., Collazo, M. & Gabrilovich, D. I. Subsets of myeloid-derived suppressor cells in tumor-bearing mice. *The Journal of Immunology* **181,** 5791–5802 (2008).

30. Waldman, A. D., Fritz, J. M. & Lenardo, M. J. A guide to cancer immunotherapy: from T cell basic science to clinical practice. *Nature Reviews Immunology* **20,** 651–668 (2020).

31. Gooden, M. J. M., Bock, G. H. d., Leffers, N., Daemen, T. & Nijman, H. W. The prognostic influence of tumour-infiltrating lymphocytes in cancer: a systematic review with meta-analysis. *British Journal of Cancer* **105,** 93–103 (2011).

32. Vignali, D. A. A., Collison, L. W. & Workman, C. J. How regulatory T cells work. *Nature Reviews Immunology* **8,** 523–532 (2008).

33. Godfrey, D. I., Nours, J. L., Andrews, D. M., Uldrich, A. P. & Rossjohn, J. Unconventional T Cell Targets for Cancer Immunotherapy. *Immunity* **48,** 453–473 (2018).

34. Vito, C. D. *et al.* NK cells to cure cancer. *Seminars in Immunology* **41,** 101272 (2019).

35. Imai, K., Matsuyama, S., Miyake, S., Suga, K. & Nakachi, K. Natural cytotoxic activity of peripheral-blood lymphocytes and cancer incidence: an 11-year follow-up study of a general population. *The Lancet* **356,** 1795–1799 (2000).

36. Rocca, Y. S. *et al.* Altered phenotype in peripheral blood and tumor-associated NK cells from colorectal cancer patients. *Innate Immunity* **19,** 76–85 (2012).

37. Laumont, C. M., Banville, A. C., Gilardi, M., Hollern, D. P. & Nelson, B. H. Tumour-infiltrating B cells: immunological mechanisms, clinical impact and therapeutic opportunities. *Nature Reviews Cancer* **22,** 414–430 (2022).

38. Sautès-Fridman, C., Petitprez, F., Calderaro, J. & Fridman, W. H. Tertiary lymphoid structures in the era of cancer immunotherapy. *Nature Reviews Cancer* **19,** 307–325 (2019).

39. Hua, Z. & Hou, B. The role of B cell antigen presentation in the initiation of CD4+ T cell response. *Immunological Reviews* **296,** 24–35 (2020).

40. Cui, C. *et al.* Neoantigen-driven B cell and CD4 T follicular helper cell collaboration promotes anti-tumor CD8 T cell responses. *Cell* **184,** 6101–6118.e13 (2021).

41. Biswas, S. *et al.* IgA transcytosis and antigen recognition govern ovarian cancer immunity. *Nature* **591,** 464–470 (2021).

42. Ng, K. W. *et al.* Antibodies against endogenous retroviruses promote lung cancer immunotherapy. *Nature* **616,** 563–573 (2023).

43. Ishikawa, T. *et al.* Tumor-specific immunological recognition of frameshift-mutated peptides in colon cancer with microsatellite instability. *Cancer Research* **63,** 5564–72 (2003).

44. Reuschenbach, M., Doeberitz, M. v. K. & Wentzensen, N. A systematic review of humoral immune responses against tumor antigens. *Cancer Immunology, Immunotherapy* **58,** 1535 (2009).

45. Soussi, T. p53 Antibodies in the sera of patients with various types of cancer: a review. *Cancer Research* **60,** 1777–88 (2000).

46. Nielsen, J. S. *et al.* CD20+ Tumor-Infiltrating Lymphocytes Have an Atypical CD27- Memory Phenotype and Together with CD8+ T Cells Promote Favorable Prognosis in Ovarian Cancer. *Clinical Cancer Research* **18,** 3281–3292 (2012).

47. Garaud, S. *et al.* Antigen Specificity and Clinical Significance of IgG and IgA Autoantibodies Produced in situ by Tumor-Infiltrating B Cells in Breast Cancer. *Frontiers in Immunology* **9,** 2660 (2018).

48. Michaud, D., Steward, C. R., Mirlekar, B. & Pylayeva-Gupta, Y. Regulatory B cells in cancer. *Immunological Reviews* **299,** 74–92 (2021).

49. Ouyang, F.-Z. *et al.* Dendritic cell-elicited B-cell activation fosters immune privilege via IL-10 signals in hepatocellular carcinoma. *Nature Communications* **7,** 13453 (2016).

50. Dushek, O., Goyette, J. & Merwe, P. A. Non-catalytic tyrosine-phosphorylated receptors. *Immunological Reviews* **250,** 258–276 (2012).

51. Isakov, N. Immunoreceptor tyrosine-based activation motif (ITAM), a unique module linking antigen and Fc receptors to their signaling cascades. *Journal of Leukocyte Biology* **61,** 6–16 (1997).

52. Daëron, M., Jaeger, S., Pasquier, L. D. & Vivier, E. Immunoreceptor tyrosine-based inhibition motifs: a quest in the past and future. *Immunological Reviews* **224,** 11–43 (2008).

53. Le Borgne, M. & Shaw, A. S. SAP Signaling: A Dual Mechanism of Action. *Immunity* **36,** 899–901 (2012).

54. Secrist, J., Burns, L., Karnitz, L., Koretzky, G. & Abraham, R. Stimulatory effects of the protein tyrosine phosphatase inhibitor, pervanadate, on T-cell activation events. *Journal of Biological Chemistry* **268,** 5886–5893 (1993).

55. Davis, S. J. & Merwe, P. A. v. d. The kinetic-segregation model: TCR triggering and beyond. *Nature Immunology* **7,** 803–809 (2006).

56. Lemmon, M. A. & Schlessinger, J. Cell Signaling by Receptor Tyrosine Kinases. *Cell* **141,** 1117–1134 (2010).

57. Cooper, J. A. & Qian, H. A Mechanism for Src Kinase-Dependent Signaling by Noncatalytic Receptors. *Biochemistry* **47,** 5681–5688 (2008).

58. Tolar, P. & Pierce, S. K. in *Immunological Synapse* (ed T. Saito, F. B.) 155–169 (Springer, Berlin, Heidelberg, 2009).

59. Xu, C. *et al.* Regulation of T Cell Receptor Activation by Dynamic Membrane Binding of the CD3epsilon Cytoplasmic Tyrosine-Based Motif. *Cell* **135,** 702–713 (2008).

60. Li, Y.-C. *et al.* Cutting Edge: Mechanical Forces Acting on T Cells Immobilized via the TCR Complex Can Trigger TCR Signaling. *The Journal of Immunology* **184,** 5959–5963 (2010).

61. Ma, Z., Discher, D. E. & Finkel, T. H. Mechanical Force in T Cell Receptor Signal Initiation. *Frontiers in Immunology* **3,** 217 (2012).

62. Chang, V. T. *et al.* Initiation of T cell signaling by CD45 segregation at 'close contacts'. *Nature Immunology* **17,** 574–582 (2016).

63. Kjer-Nielsen, L. *et al.* A Structural Basis for the Selection of Dominant ab T Cell Receptors in Antiviral Immunity. *Immunity* **18,** 53–64 (2003).

64. Rudolph, M. G., Stanfield, R. L. & Wilson, I. A. How TCRs Bind MDCs, Peptides, and Coreceptors. *Annual Review of Immunology* **24,** 419–466 (2006).

65. Sušac, L. *et al.* Structure of a fully assembled tumor-specific T cell receptor ligated by pMHC. *Cell* **185,** 3201–3213.e19 (2022).

66. He, H.-T., Lellouch, A. & Marguet, D. Lipid rafts and the initiation of T cell receptor signaling. *Seminars in Immunology* **17,** 23–33 (2005).

67. Hashimoto-Tane, A. *et al.* T-Cell Receptor Microclusters Critical for T-Cell Activation Are Formed Independently of Lipid Raft Clustering. *Molecular and Cellular Biology* **30,** 3421–3429 (2010).

68. Su, X. *et al.* Phase separation of signaling molecules promotes T cell receptor signal transduction. *Science* **352,** 595–599 (2016).

69. Burroughs, N. J., Lazic, Z. & Merwe, P. A. v. d. Ligand Detection and Discrimination by Spatial Relocalization: A Kinase-Phosphatase Segregation Model of TCR Activation. *Biophysical Journal* **91,** 1619–1629 (2006).

70. Chen, K. Y. *et al.* Trapping or slowing the diffusion of T cell receptors at close contacts initiates T cell signaling. *Proceedings of the National Academy of Sciences* **118,** e2024250118 (2021).

71. Hudecek, M. *et al.* The Nonsignaling Extracellular Spacer Domain of Chimeric Antigen Receptors Is Decisive for In Vivo Antitumor Activity. *Cancer Immunology Research* **3,** 125–135 (2015).

72. Bluemel, C. *et al.* Epitope distance to the target cell membrane and antigen size determine the potency of T cell-mediated lysis by BiTE antibodies specific for a large melanoma surface antigen. *Cancer Immunology, Immunotherapy* **59,** 1197–1209 (2010).

73. Yokosuka, T. *et al.* Spatiotemporal Regulation of T Cell Costimulation by TCR-CD28 Microclusters and Protein Kinase C theta Translocation. *Immunity* **29,** 589–601 (2008).

74. Yokosuka, T. *et al.* Spatiotemporal Basis of CTLA-4 Costimulatory Molecule-Mediated Negative Regulation of T Cell Activation. *Immunity* **33,** 326–339 (2010).

75. Yokosuka, T. *et al.* Programmed cell death 1 forms negative costimulatory microclusters that directly inhibit T cell receptor signaling by recruiting phosphatase SHP2. *Journal of Experimental Medicine* **209,** 1201–1217 (2012).

76. Köhler, K. *et al.* Matched Sizes of Activating and Inhibitory Receptor/Ligand Pairs Are Required for Optimal Signal Integration by Human Natural Killer Cells. *PLoS ONE* **5,** e15374 (2010).

77. Goodridge, H. S. *et al.* Activation of the innate immune receptor Dectin-1 upon formation of a 'phagocytic synapse'. *Nature* **472,** 471–475 (2011).

78. Bakalar, M. H. *et al.* Size-Dependent Segregation Controls Macrophage Phagocytosis of Antibody-Opsonized Targets. *Cell* **174,** 131–142.e13 (2018).

79. Tacke, M., Hanke, G., Hanke, T. & Hünig, T. CD28-mediated induction of proliferation in resting T cells in vitro and in vivo without engagement of the T cell receptor: Evidence for functionally distinct forms of CD28. *European Journal of Immunology* **27,** 239–247 (1997).

80. Lühder, F. *et al.* Topological Requirements and Signaling Properties of T Cell–activating, Anti-CD28 Antibody Superagonists. *Journal of Experimental Medicine* **197,** 955–966 (2003).

81. Evans, E. J. *et al.* Crystal structure of a soluble CD28-Fab complex. *Nature Immunology* **6,** 271–279 (2005).

82. Ganesh, S. *et al.* Cytokine Storm in a Phase 1 Trial of the Anti-CD28 Monoclonal Antibody TGN1412. *The New England Journal of Medicine* **355,** 1018–1028 (2006).

83. Römer, P. S. *et al.* Preculture of PBMCs at high cell density increases sensitivity of T-cell responses, revealing cytokine release by CD28 superagonist TGN1412. *Blood* **118,** 6772–6782 (2011).

84. Hussain, K. *et al.* Upregulation of FcgammaRIIb on monocytes is necessary to promote the superagonist activity of TGN1412. *Blood* **125,** 102–110 (2015).

85. Dudek, S. *et al.* Human Fcgamma receptors compete for TGN1412 binding that determines the antibody's effector function. *European Journal of Immunology* **49,** 1117–1126 (2019).

86. Bruhns, P. & Jönsson, F. Mouse and human FcR effector functions. *Immunological Reviews* **268,** 25–51 (2015).

87. Suzuki, K. *et al.* Anti–PD-1 antibodies recognizing the membrane-proximal region are PD-1 agonists that can down-regulate inflammatory diseases. *Science Immunology* **8,** eadd4947 (2023).

88. Paluch, C., Santos, A. M., Anzilotti, C., Cornall, R. J. & Davis, S. J. Immune Checkpoints as Therapeutic Targets in Autoimmunity. *Frontiers in Immunology* **9,** 2306–11 (2018).

89. Wang, L. *et al.* The Fas–FADD death domain complex structure reveals the basis of DISC assembly and disease mutations. *Nature Structural & Molecular Biology* **17,** 1324–1329 (2010).

90. Lin, S.-C., Lo, Y.-C. & Wu, H. Helical assembly in the MyD88–IRAK4–IRAK2 complex in TLR/IL-1R signalling. *Nature* **465,** 885–890 (2010).

91. Zhang, P. *et al.* Ligand-Blocking and Membrane-Proximal Domain Targeting Anti-OX40 Antibodies Mediate Potent T Cell-Stimulatory and Anti-Tumor Activity. *Cell Reports* **27,** 3117–3123.e5 (2019).

92. Yu, X. *et al.* Complex Interplay between Epitope Specificity and Isotype Dictates the Biological Activity of Anti-human CD40 Antibodies. *Cancer Cell* **33,** 664–675.e4 (2018).

93. Chin, S. M. *et al.* Structure of the 4-1BB/4-1BBL complex and distinct binding and functional properties of utomilumab and urelumab. *Nature Communications* **9,** 4679 (2018).

94. White, A. L. *et al.* Fcgamma Receptor Dependency of Agonistic CD40 Antibody in Lymphoma Therapy Can Be Overcome through Antibody Multimerization. *The Journal of Immunology* **193,** 1828–1835 (2014).

95. Zhang, D. *et al.* Functional optimization of agonistic antibodies to OX40 receptor with novel Fc mutations to promote antibody multimerization. *mAbs* **9,** 1129–1142 (2017).

96. White, A. L. *et al.* Conformation of the Human Immunoglobulin G2 Hinge Imparts Superagonistic Properties to Immunostimulatory Anticancer Antibodies. *Cancer Cell* **27,** 138–148 (2015).

97. Orr, C. M. *et al.* Hinge disulfides in human IgG2 CD40 antibodies modulate receptor signaling by regulation of conformation and flexibility. *Science Immunology* **7,** eabm3723 (2022).

98. Yu, X. *et al.* TNF receptor agonists induce distinct receptor clusters to mediate differential agonistic activity. *Communications Biology* **4,** 772 (2021).

99. Mayes, P. A., Hance, K. W. & Hoos, A. The promise and challenges of immune agonist antibody development in cancer. *Nature Reviews Drug Discovery* **17,** 509–527 (2018).

100. Liu, H. *et al.* Optimal target saturation of ligand-blocking anti-GITR antibody IBI37G5 dictates FcgammaR-independent GITR agonism and antitumor activity. *Cell Reports Medicine* **3,** 100660 (2022).

101. Stebbings, R. *et al.* "Cytokine Storm" in the Phase I Trial of Monoclonal Antibody TGN1412: Better Understanding the Causes to Improve PreClinical Testing of Immunotherapeutics. *The Journal of Immunology* **179,** 3325–3331 (2007).

102. Chodorge, M. *et al.* A series of Fas receptor agonist antibodies that demonstrate an inverse correlation between affinity and potency. *Cell Death & Differentiation* **19,** 1187–1195 (2012).

103. Yu, X. *et al.* Reducing affinity as a strategy to boost immunomodulatory antibody agonism. *Nature* **614,** 539–547 (2023).

104. European Medicines Agency. *OPDIVO* Assessment report EMA/CHMP/76688/2015 (European Medicines Agency, 2015).

105. Romagnani, S. Immunological tolerance and autoimmunity. *Internal and Emergency Medicine* **1,** 187–196 (2006).

106. Xing, Y. & Hogquist, K. A. T-Cell Tolerance: Central and Peripheral. *Cold Spring Harbor Perspectives in Biology* **4,** a006957 (2012).

107. Tivol, E. A. *et al.* Loss of CTLA-4 leads to massive lymphoproliferation and fatal multiorgan tissue destruction, revealing a critical negative regulatory role of CTLA-4. *Immunity* **3,** 541–547 (1995).

108. Waterhouse, P. *et al.* Lymphoproliferative disorders with early lethality in mice deficient in Ctla-4. *Science* **270,** 985–988 (1995).

109. Nishimura, H., Minato, N., Nakano, T. & Honjo, T. Immunological studies on PD-1 deficient mice: implication of PD-1 as a negative regulator for B cell responses. *International Immunology* **10,** 1563–1572 (1998).

110. Nishimura, H., Nose, M., Hiai, H., Minato, N. & Honjo, T. Development of Lupus-like Autoimmune Diseases by Disruption of the PD-1 Gene Encoding an ITIM Motif-Carrying Immunoreceptor. *Immunity* **11,** 141–151 (1999).

111. Leach, D. R., Krummel, M. F. & Allison, J. P. Enhancement of antitumor immunity by CTLA-4 blockade. *Science* **271,** 1734–1736 (1996).

112. Iwai, Y., Terawaki, S. & Honjo, T. PD-1 blockade inhibits hematogenous spread of poorly immunogenic tumor cells by enhanced recruitment of effector T cells. *International Immunology* **17,** 133–144 (2005).

113. Rudd, C. E., Taylor, A. & Schneider, H. CD28 and CTLA-4 coreceptor expression and signal transduction. *Immunological Reviews* **229,** 12–26 (2009).

114. Collins, A. V. *et al.* The Interaction Properties of Costimulatory Molecules Revisited. *Immunity* **17,** 201–210 (2002).

115. Qureshi, O. S. *et al.* Trans-Endocytosis of CD80 and CD86: A Molecular Basis for the Cell-Extrinsic Function of CTLA-4. *Science* **332,** 600–603 (2011).

116. Kennedy, A. *et al.* Differences in CD80 and CD86 transendocytosis reveal CD86 as a key target for CTLA-4 immune regulation. *Nature Immunology* **23,** 1365–1378 (2022).

117. Wing, K. *et al.* CTLA-4 Control over Foxp3+ Regulatory T Cell Function. *Science* **322,** 271–275 (2008).

118. Peggs, K. S., Quezada, S. A., Chambers, C. A., Korman, A. J. & Allison, J. P. Blockade of CTLA-4 on both effector and regulatory T cell compartments contributes to the antitumor activity of anti–CTLA-4 antibodies. *Journal of Experimental Medicine* **206,** 1717–1725 (2009).

119. Simpson, T. R. *et al.* Fc-dependent depletion of tumor-infiltrating regulatory T cells co-defines the efficacy of anti–CTLA-4 therapy against melanoma. *Journal of Experimental Medicine* **210,** 1695–1710 (2013).

120. Vargas, F. A. *et al.* Fc Effector Function Contributes to the Activity of Human Anti-CTLA-4 Antibodies. *Cancer Cell* **33,** 649–663.e4 (2018).

121. Zahavi, D. & Weiner, L. Monoclonal Antibodies in Cancer Therapy. *Antibodies* **9,** 34 (2020).

122. Boutros, C. *et al.* Safety profiles of anti-CTLA-4 and anti-PD-1 antibodies alone and in combination. *Nature Reviews Clinical Oncology* **13,** 473–486 (2016).

123. Rowshanravan, B., Halliday, N. & Sansom, D. M. CTLA-4: a moving target in immunotherapy. *Blood* **131,** 58–67 (2018).

124. Chemnitz, J. M., Parry, R. V., Nichols, K. E., June, C. H. & Riley, J. L. SHP-1 and SHP-2 Associate with Immunoreceptor Tyrosine-Based Switch Motif of Programmed Death 1 upon Primary Human T Cell Stimulation, but Only Receptor Ligation Prevents T Cell Activation. *The Journal of Immunology* **173,** 945–954 (2004).

125. Agata, Y. *et al.* Expression of the PD-1 antigen on the surface of stimulated mouse T and B lymphocytes. *International Immunology* **8,** 765–772 (1996).

126. Patsoukis, N., Wang, Q., Strauss, L. & Boussiotis, V. A. Revisiting the PD-1 pathway. *Science Advances* **6,** eabd2712 (2020).

127. Cheng, X. *et al.* Structure and Interactions of the Human Programmed Cell Death 1 Receptor. *Journal of Biological Chemistry* **288,** 11771–11785 (2013).

128. Youngnak, P. *et al.* Differential binding properties of B7-H1 and B7-DC to programmed death-1. *Biochemical and Biophysical Research Communications* **307,** 672–677 (2003).

129. Dong, H. *et al.* Tumor-associated B7-H1 promotes T-cell apoptosis: A potential mechanism of immune evasion. *Nature Medicine* **8,** 793–800 (2002).

130. Abiko, K. *et al.* IFN-gamma from lymphocytes induces PD-L1 expression and promotes progression of ovarian cancer. *British Journal of Cancer* **112,** 1501–1509 (2015).

131. Celis-Gutierrez, J. *et al.* Quantitative Interactomics in Primary T Cells Provides a Rationale for Concomitant PD-1 and BTLA Coinhibitor Blockade in Cancer Immunotherapy. *Cell Reports* **27,** 3315–3330.e7 (2019).

132. Xu, X., Masubuchi, T., Cai, Q., Zhao, Y. & Hui, E. Molecular features underlying differential SHP1/SHP2 binding of immune checkpoint receptors. *eLife* **10,** e74276 (2021).

133. Rota, G. *et al.* Shp-2 Is Dispensable for Establishing T Cell Exhaustion and for PD-1 Signaling In Vivo. *Cell Reports* **23,** 39–49 (2018).

134. Xu, X. *et al.* PD-1 and BTLA regulate T cell signaling differentially and only partially through SHP1 and SHP2. *Journal of Cell Biology* **219,** e201905085 (2020).

135. Hui, E. *et al.* T cell costimulatory receptor CD28 is a primary target for PD-1–mediated inhibition. *Science* **355,** 1428–1433 (2017).

136. Sheppard, K.-A. *et al.* PD-1 inhibits T-cell receptor induced phosphorylation of the ZAP70/CD3zeta signalosome and downstream signaling to PKCtheta. *FEBS Letters* **574,** 37–41 (2004).

137. Wherry, E. J. *et al.* Molecular Signature of CD8+ T Cell Exhaustion during Chronic Viral Infection. *Immunity* **27,** 670–684 (2007).

138. Sugiura, D. *et al.* Restriction of PD-1 function by cis-PD-L1/CD80 interactions is required for optimal T cell responses. *Science* **364,** 558–566 (2019).

139. Zhao, Y. *et al.* PD-L1:CD80 Cis-Heterodimer Triggers the Co-stimulatory Receptor CD28 While Repressing the Inhibitory PD-1 and CTLA-4 Pathways. *Immunity* **51,** 1059–1073.e9 (2019).

140. Mayoux, M. *et al.* Dendritic cells dictate responses to PD-L1 blockade cancer immunotherapy. *Science Translational Medicine* **12,** eaav7431 (2020).

141. Zhao, Y. *et al.* Antigen-Presenting Cell-Intrinsic PD-1 Neutralizes PD-L1 in cis to Attenuate PD-1 Signaling in T Cells. *Cell Reports* **24,** 379–390.e6 (2018).

142. Haas, L. & Obenauf, A. C. Allies or Enemies—The Multifaceted Role of Myeloid Cells in the Tumor Microenvironment. *Frontiers in Immunology* **10,** 2746 (2019).

143. Hoek, R. M. *et al.* Down-regulation of the macrophage lineage through interaction with OX2 (CD200). *Science* **290,** 1768–1771 (2000).

144. Wright, G. J. *et al.* Characterization of the CD200 receptor family in mice and humans and their interactions with CD200. *The Journal of Immunology* **171,** 3034–3046 (2003).

145. Rijkers, E. S. K. *et al.* The inhibitory CD200R is differentially expressed on human and mouse T and B lymphocytes. *Molecular Immunology* **45,** 1126–1135 (2008).

146. Wright, G. J. *et al.* Lymphoid/neuronal cell surface OX2 glycoprotein recognizes a novel receptor on macrophages implicated in the control of their function. *Immunity* **13,** 233–242 (2000).

147. Hatherley, D., Lea, S. M., Johnson, S. & Barclay, A. N. Structures of CD200/CD200 receptor family and implications for topology, regulation, and evolution. *Structure* **21,** 820–832 (2013).

148. Zhang, S., Cherwinski, H., Sedgwick, J. D. & Phillips, J. H. Molecular mechanisms of CD200 inhibition of mast cell activation. *The Journal of Immunology* **173,** 6786–6793 (2004).

149. Mihrshahi, R., Barclay, A. N. & Brown, M. H. Essential roles for Dok2 and RasGAP in CD200 receptor-mediated regulation of human myeloid cells. *The Journal of Immunology* **183,** 4879–4886 (2009).

150. Mihrshahi, R. & Brown, M. H. Downstream of tyrosine kinase 1 and 2 play opposing roles in CD200 receptor signaling. *The Journal of Immunology* **185,** 7216–7222 (2010).

151. Vlist, M. v. d. *et al.* Signaling by the inhibitory receptor CD200R is rewired by type I interferon. *Science Signaling* **14,** eabb4324 (2021).

152. Broderick, C. *et al.* Constitutive retinal CD200 expression regulates resident microglia and activation state of inflammatory cells during experimental autoimmune uveoretinitis. *The American Journal of Pathology* **161,** 1669–1677 (2002).

153. Gorczynski, R. M. Transplant tolerance modifying antibody to CD200 receptor, but not CD200, alters cytokine production profile from stimulated macrophages. *European Journal of Immunology* **31,** 2331–2337 (2001).

154. Barclay, A. N. Different reticular elements in rat lymphoid tissue identified by localization of Ia, Thy-1 and MRC OX 2 antigens. *Immunology* **44,** 727–736 (1981).

155. Webb, M. & Barclay, A. N. Localisation of the MRC OX-2 glycoprotein on the surfaces of neurones. *Journal of Neurochemistry* **43,** 1061–1067 (1984).

156. Kretz-Rommel, A. *et al.* Blockade of CD200 in the presence or absence of antibody effector function: implications for anti-CD200 therapy. *The Journal of Immunology* **180,** 699–705 (2008).

157. Rosenblum, M. D. *et al.* CD200 is a novel p53-target gene involved in apoptosis-associated immune tolerance. *Blood* **103,** 2691–2698 (2004).

158. Chen, Z., Marsden, P. A. & Gorczynski, R. M. Cloning and characterization of the human CD200 promoter region. *Molecular Immunology* **43,** 579–587 (2006).

159. Wright, G. J., Jones, M., Puklavec, M. J., Brown, M. H. & Barclay, A. N. The unusual distribution of the neuronal/lymphoid cell surface CD200 (OX2) glycoprotein is conserved in humans. *Immunology* **102,** 173–179 (2001).

160. Minas, K. & Liversidge, J. Is the CD200/CD200 receptor interaction more than just a myeloid cell inhibitory signal? *Critical Reviews in Immunology* **26,** 213–230 (2006).

161. Akkaya, M. & Barclay, A. N. Heterogeneity in the CD200R paired receptor family. *Immunogenetics* **62,** 15–22 (2010).

162. Hatherley, D., Cherwinski, H. M., Moshref, M. & Barclay, A. N. Recombinant CD200 protein does not bind activating proteins closely related to CD200 receptor. *The Journal of Immunology* **175,** 2469–2474 (2005).

163. Barclay, A. N. & Hatherley, D. The counterbalance theory for evolution and function of paired receptors. *Immunity* **29,** 675–678 (2008).

164. Foster-Cuevas, M., Wright, G. J., Puklavec, M. J., Brown, M. H. & Barclay, A. N. Human herpesvirus 8 K14 protein mimics CD200 in down-regulating macrophage activation through CD200 receptor. *Journal of Virology* **78,** 7667–7676 (2004).

165. Cameron, C. M., Barrett, J. W., Liu, L., Lucas, A. R. & McFadden, G. Myxoma Virus M141R Expresses a Viral CD200 (vOX-2) That Is Responsible for Down-Regulation of Macrophage and T-Cell Activation In Vivo. *Journal of Virology* **79,** 6052–6067 (2005).

166. Shiratori, I. *et al.* Down-regulation of basophil function by human CD200 and human herpesvirus-8 CD200. *The Journal of Immunology* **175,** 4441–4449 (2005).

167. Kwong, L. S., Akkaya, M., Barclay, A. N. & Hatherley, D. Herpesvirus orthologues of CD200 bind host CD200R but not related activating receptors. *Journal of General Virology* **97,** 179–84 (2015).

168. Ramos, M. I. P. *et al.* CD200R1L is a functional evolutionary conserved activating receptor in human neutrophils. *Journal of Leukocyte Biology* **11,** 367–377 (2022).

169. Choe, D. & Choi, D. Cancel cancer: The immunotherapeutic potential of CD200/CD200R blockade. *Frontiers in Oncology* **13,** 1088038 (2023).

170. Gorczynski, R. M. *et al.* Breast cancer cell CD200 expression regulates immune response to EMT6 tumor cells in mice. *Breast Cancer Research and Treatment* **123,** 405–415 (2010).

171. Gorczynski, R. M., Chen, Z., Khatri, I., Podnos, A. & Yu, K. Cure of metastatic growth of EMT6 tumor cells in mice following manipulation of CD200:CD200R signaling. *Breast Cancer Research and Treatment* **142,** 271–282 (2013).

172. Moertel, C. L. *et al.* CD200 in CNS tumor-induced immunosuppression: the role for CD200 pathway blockade in targeted immunotherapy. *Journal for ImmunoTherapy of Cancer* **2,** 46–10 (2014).

173. Wang, L. *et al.* Tumor expression of CD200 inhibits IL-10 production by tumor-associated myeloid cells and prevents tumor immune evasion of CTL therapy. *European Journal of Immunology* **40,** 2569–2579 (2010).

174. Talebian, F. *et al.* Melanoma cell expression of CD200 inhibits tumor formation and lung metastasis via inhibition of myeloid cell functions. *PLoS ONE* **7,** e31442–10 (2012).

175. Erin, N. *et al.* Bidirectional effect of CD200 on breast cancer development and metastasis, with ultimate outcome determined by tumor aggressiveness and a cancer-induced inflammatory response. *Oncogene* **34,** 3860–3870 (2015).

176. Liu, J.-Q. *et al.* A Critical Role for CD200R Signaling in Limiting the Growth and Metastasis of CD200+ Melanoma. *The Journal of Immunology* **197,** 1489–1497 (2016).

177. Erin, N. *et al.* CD200fc enhances anti-tumoral immune response and inhibits visceral metastasis of breast carcinoma. *Oncotarget* **9,** 19147–19158 (2018).

178. Pilch, Z. *et al.* The pro-tumor effect of CD200 expression is not mimicked by agonistic CD200R antibodies. *PLoS ONE* **14,** e0210796 (2019).

179. Moreaux, J. *et al.* CD200 is a new prognostic factor in multiple myeloma. *Blood* **108,** 4194–4197 (2006).

180. Tonks, A. *et al.* CD200 as a prognostic factor in acute myeloid leukaemia. *Leukemia* **21,** 566–568 (2007).

181. Wong, K. K., Brenneman, F., Chesney, A., Spaner, D. E. & Gorczynski, R. M. Soluble CD200 is critical to engraft chronic lymphocytic leukemia cells in immunocompromised mice. *Cancer Research* **72,** 4931–4943 (2012).

182. Moreaux, J., Veyrune, J. L., Reme, T., Vos, J. D. & Klein, B. CD200: a putative therapeutic target in cancer. *Biochemical and Biophysical Research Communications* **366,** 117–122 (2008).

183. Bisgin, A., Meng, W.-J., Adell, G. & Sun, X.-F. Interaction of CD200 Overexpression on Tumor Cells with CD200R1 Overexpression on Stromal Cells: An Escape from the Host Immune Response in Rectal Cancer Patients. *Journal of Oncology* **2019,** 5689464 (2019).

184. Zhang, Y., He, W. & Zhang, S. Seeking for Correlative Genes and Signaling Pathways With Bone Metastasis From Breast Cancer by Integrated Analysis. *Frontiers in Oncology* **9,** 138 (2019).

185. Coles, S. J. *et al.* The immunosuppressive ligands PD-L1 and CD200 are linked in AML T-cell immunosuppression: identification of a new immunotherapeutic synapse. *Leukemia* **29,** 1952–1954 (2015).

186. Mahadevan, D. *et al.* Phase I study of samalizumab in chronic lymphocytic leukemia and multiple myeloma: blockade of the immune checkpoint CD200. *Journal for ImmunoTherapy of Cancer* **7,** 227 (2019).

187. Kretz-Rommel, A. *et al.* CD200 expression on tumor cells suppresses antitumor immunity: new approaches to cancer immunotherapy. *The Journal of Immunology* **178,** 5595–5605 (2007).

188. Kovacsovics, T. & Raetz, E. Personalizing Therapy: The Beat AML Trial. *The Hematologist* **14,** 7134 (2017).

189. Rastogi, N. *et al.* Use of an anti-CD200-blocking antibody improves immune responses to AML in vitro and in vivo. *British Journal of Haematology* **193,** 155–159 (2020).

190. Pfizer. *Pfizer Completes Acquisition of Trillium Therapeutics* Press release (2021).

191. Fang, X. *et al. Abstract 603: Discovery of CD200R1 as a novel immuno-oncology target using pleiotropic signals from 23andMe's genetic and health survey database* in *Cancer Research* **82** (American Association For Cancer Research Annual Meeting, 2022), 603.

192. Fenaux, J. *et al. Abstract 602: 23ME-00610 is a first-in-class monoclonal antibody that targets the CD200R1 immune checkpoint to enhance T cell-mediated antitumor activity* in *Cancer Research* **82** (American Association For Cancer Research Annual Meeting, 2022), 602.

193. Rasco, D. *et al.* 758 A phase 1 dose escalation and expansion study of the anti-CD200R1 antibody 23ME-00610 in patients with advanced solid malignancies. *Journal for ImmunoTherapy of Cancer,* A789 (2022).

194. Kummar, S. *et al. Abstract CT174: First-in-class anti-CD200R1 antibody 23ME-00610 in patients with advanced solid malignancies: Phase 1 results* in *Cancer Research* **83** (American Association For Cancer Research Annual Meeting, 2023), CT174.

195. Lu, R.-M. *et al.* Development of therapeutic antibodies for the treatment of diseases. *Journal of Biomedical Science* **27,** 1 (2020).

196. Harris, L. J., Skaletsky, E. & McPherson, A. Crystallographic structure of an intact IgG1 monoclonal antibody. *Journal of Molecular Biology* **275,** 861–872 (1998).

197. Vidarsson, G., Dekkers, G. & Rispens, T. IgG subclasses and allotypes: from structure to effector functions. *Frontiers in Immunology* **5,** 520 (2014).

198. Krapp, S., Mimura, Y., Jefferis, R., Huber, R. & Sondermann, P. Structural Analysis of Human IgG-Fc Glycoforms Reveals a Correlation Between Glycosylation and Structural Integrity. *Journal of Molecular Biology* **325,** 979–989 (2003).

199. Tao, M. H. & Morrison, S. L. Studies of aglycosylated chimeric mouse-human IgG. Role of carbohydrate in the structure and effector functions mediated by the human IgG constant region. *The Journal of Immunology* **143,** 2595–2601 (1989).

200. Chiu, M. L., Goulet, D. R., Teplyakov, A. & Gilliland, G. L. Antibody Structure and Function: The Basis for Engineering Therapeutics. *Antibodies* **8,** 55 (2019).

201. Sandin, S., Öfverstedt, L.-G., Wikström, A.-C., Wrange, Ö. & Skoglund, U. Structure and Flexibility of Individual Immunoglobulin G Molecules in Solution. *Structure* **12,** 409–415 (2004).

202. Bruhns, P. *et al.* Specificity and affinity of human Fcgamma receptors and their polymorphic variants for human IgG subclasses. *Blood* **113,** 3716–3725 (2009).

203. Dekkers, G. *et al.* Affinity of human IgG subclasses to mouse Fc gamma receptors. *mAbs* **9,** 767–773 (2017).

204. Nimmerjahn, F. & Ravetch, J. V. Divergent Immunoglobulin G Subclass Activity Through Selective Fc Receptor Binding. *Science* **310,** 1510–1512 (2005).

205. Nimmerjahn, F., Bruhns, P., Horiuchi, K. & Ravetch, J. V. FcgammaRIV: A Novel FcR with Distinct IgG Subclass Specificity. *Immunity* **23,** 41–51 (2005).

206. Clynes, R. & Ravetch, J. V. Cytotoxic antibodies trigger inflammation through Fc receptors. *Immunity* **3,** 21–26 (1995).

207. Gaetano, N. D. *et al.* Complement Activation Determines the Therapeutic Activity of Rituximab In Vivo. *The Journal of Immunology* **171,** 1581–1587 (2003).

208. Silveira, S. A. d. *et al.* Complement Activation Selectively Potentiates the Pathogenicity of the IgG2b and IgG3 Isotypes of a High Affinity Anti-Erythrocyte Autoantibody. *Journal of Experimental Medicine* **195,** 665–672 (2002).

209. Liu, R., Oldham, R. J., Teal, E., Beers, S. A. & Cragg, M. S. Fc-Engineering for Modulated Effector Functions—Improving Antibodies for Cancer Treatment. *Antibodies* **9,** 64 (2020).

210. Wilkinson, I. *et al.* Fc-engineered antibodies with immune effector functions completely abolished. *PLoS ONE* **16,** e0260954 (2021).

211. Shields, R. L. *et al.* High Resolution Mapping of the Binding Site on Human IgG1 for FcgammaRI, FcgammaRII, FcgammaRIII, and FcRn and Design of IgG1 Variants with Improved Binding to the FcgammaR. *Journal of Biological Chemistry* **276,** 6591–6604 (2001).

212. Baudino, L. *et al.* Crucial Role of Aspartic Acid at Position 265 in the CH2 Domain for Murine IgG2a and IgG2b Fc-Associated Effector Functions. *The Journal of Immunology* **181,** 6664–6669 (2008).

213. Lux, A., Yu, X., Scanlan, C. N. & Nimmerjahn, F. Impact of Immune Complex Size and Glycosylation on IgG Binding to Human FcgammaRs. *The Journal of Immunology* **190,** 4315–4323 (2013).

214. Tao, M. H., Smith, R. I. & Morrison, S. L. Structural features of human immunoglobulin G that determine isotype-specific differences in complement activation. *Journal of Experimental Medicine* **178,** 661–667 (1993).

215. Smith, P., DiLillo, D. J., Bournazos, S., Li, F. & Ravetch, J. V. Mouse model recapitulating human Fcgamma receptor structural and functional diversity. *Proceedings of the National Academy of Sciences* **109,** 6181–6186 (2012).

216. Casey, E. *et al.* A new mouse expressing human Fcgamma receptors to better predict therapeutic efficacy of human anti-cancer antibodies. *Leukemia* **32,** 547–549 (2018).

217. Pavlasova, G. & Mraz, M. The regulation and function of CD20: an "enigma" of B-cell biology and targeted therapy. *Haematologica* **105,** 1494–1506 (2020).

218. Maloney, D. G. *et al.* IDEC-C2B8 (Rituximab) Anti-CD20 Monoclonal Antibody Therapy in Patients With Relapsed Low-Grade Non-Hodgkin's Lymphoma. *Blood* **90,** 2188–2195 (1997).

219. Lazar, G. A. *et al.* Engineered antibody Fc variants with enhanced effector function. *Proceedings of the National Academy of Sciences* **103,** 4005–4010 (2006).

220. Abès, R., Gélizé, E., Fridman, W. H. & Teillaud, J.-L. Long-lasting antitumor protection by anti-CD20 antibody through cellular immune response. *Blood* **116,** 926–934 (2010).

221. DiLillo, D. J. & Ravetch, J. V. Differential Fc-Receptor Engagement Drives an Anti-tumor Vaccinal Effect. *Cell* **161,** 1035–1045 (2015).

222. Monteverde, M. *et al.* The relevance of ADCC for EGFR targeting: A review of the literature and a clinically-applicable method of assessment in patients. *Critical Reviews in Oncology/Hematology* **95,** 179–190 (2015).

223. Nami, B., Maadi, H. & Wang, Z. Mechanisms Underlying the Action and Synergism of Trastuzumab and Pertuzumab in Targeting HER2-Positive Breast Cancer. *Cancers* **10,** 342 (2018).

224. Amatore, F., Gorvel, L. & Olive, D. Inducible Co-Stimulator (ICOS) as a potential therapeutic target for anti-cancer therapy. *Expert Opinion on Therapeutic Targets* **22,** 343–351 (2018).

225. Melero, I., Hirschhorn-Cymerman, D., Morales-Kastresana, A., Sanmamed, M. F. & Wolchok, J. D. Agonist Antibodies to TNFR Molecules That Costimulate T and NK Cells. *Clinical Cancer Research* **19,** 1044–1053 (2013).

226. Dahan, R. *et al.* Therapeutic Activity of Agonistic, Human Anti-CD40 Monoclonal Antibodies Requires Selective FcgammaR Engagement. *Cancer Cell* **29,** 820–831 (2016).

227. Oaknin, A. *et al.* Safety and antitumor activity of dostarlimab in patients with advanced or recurrent DNA mismatch repair deficient/microsatellite instability-high (dMMR/MSI-H) or proficient/stable (MMRp/MSS) endometrial cancer: interim results from GARNET—a phase I, single-arm study. *Journal for ImmunoTherapy of Cancer* **10,** e003777 (2022).

228. Tawbi, H. A. *et al.* Relatlimab and Nivolumab versus Nivolumab in Untreated Advanced Melanoma. *New England Journal of Medicine* **386,** 24–34 (2022).

229. Bhatia, S., Tykodi, S. S. & Thompson, J. A. Treatment of metastatic melanoma: an overview. *Oncology (Williston Park, N.Y.)* **23,** 488–96 (2009).

230. Wolchok, J. D. *et al.* Overall Survival with Combined Nivolumab and Ipilimumab in Advanced Melanoma. *The New England Journal of Medicine* **377,** 1345–1356 (2017).

231. Bagchi, S., Yuan, R. & Engleman, E. G. Immune Checkpoint Inhibitors for the Treatment of Cancer: Clinical Impact and Mechanisms of Response and Resistance. *Annual Review of Pathology: Mechanisms of Disease* **16,** 1–27 (2020).

232. Stewart, R., Hammond, S. A., Oberst, M. & Wilkinson, R. W. The role of Fc gamma receptors in the activity of immunomodulatory antibodies for cancer. *Journal for ImmunoTherapy of Cancer* **2,** 29 (2014).

233. Chen, X., Song, X., Li, K. & Zhang, T. FcgammaR-Binding Is an Important Functional Attribute for Immune Checkpoint Antibodies in Cancer Immunotherapy. *Frontiers in Immunology* **10,** 292 (2019).

234. Sharma, A. *et al.* Anti-CTLA-4 Immunotherapy Does Not Deplete FOXP3+ Regulatory T Cells (Tregs) in Human Cancers. *Clinical Cancer Research* **25,** 1233–1238 (2019).

235. Dahan, R. *et al.* FcgammaRs Modulate the Anti-tumor Activity of Antibodies Targeting the PD-1/PD-L1 Axis. *Cancer Cell* **28,** 285–295 (2015).

236. Saban, N. C. *et al.* Fc glycoengineering of a PD-L1 antibody harnesses Fcgamma receptors for increased antitumor efficacy. *Science Immunology* **8,** eadd8005 (2023).

237. Arlauckas, S. P. *et al.* In vivo imaging reveals a tumor-associated macrophage–mediated resistance pathway in anti–PD-1 therapy. *Science Translational Medicine* **9,** eaal3604 (2017).

238. Moreno-Vicente, J. *et al.* Fc-null anti-PD-1 monoclonal antibodies deliver optimal checkpoint blockade in diverse immune environments. *Journal for ImmunoTherapy of Cancer* **10,** e003735 (2022).

239. Zhang, T. *et al.* The binding of an anti-PD-1 antibody to FcgammaRI has a profound impact on its biological functions. *Cancer Immunology, Immunotherapy* **67,** 1079–1090 (2018).

240. Shen, L. *et al.* Tislelizumab Versus Chemotherapy as Second-Line Treatment for Advanced or Metastatic Esophageal Squamous Cell Carcinoma (RATIONALE-302): A Randomized Phase III Study. *Journal of Clinical Oncology* **40,** 3065–3076 (2022).

241. Silva, J.-P., Vetterlein, O., Jose, J., Peters, S. & Kirby, H. The S228P Mutation Prevents in Vivo and in Vitro IgG4 Fab-arm Exchange as Demonstrated using a Combination of Novel Quantitative Immunoassays and Physiological Matrix Preparation. *Journal of Biological Chemistry* **290,** 5462–5469 (2015).

242. Youngblood, B. *et al.* Chronic Virus Infection Enforces Demethylation of the Locus that Encodes PD-1 in Antigen-Specific CD8+ T Cells. *Immunity* **35,** 400–412 (2011).

243. Wherry, E. J. & Kurachi, M. Molecular and cellular insights into T cell exhaustion. *Nature Reviews Immunology* **15,** 486–499 (2015).

244. Cornberg, M. *et al.* Clonal Exhaustion as a Mechanism to Protect Against Severe Immunopathology and Death from an Overwhelming CD8 T Cell Response. *Frontiers in Immunology* **4,** 475 (2013).

245. Blank, C. U. *et al.* Defining 'T cell exhaustion'. *Nature Reviews Immunology* **19,** 665–674 (2019).

246. Blackburn, S. D., Shin, H., Freeman, G. J. & Wherry, E. J. Selective expansion of a subset of exhausted CD8 T cells by anti-PD-L1 blockade. *Proceedings of the National Academy of Sciences* **105,** 15016–15021 (2008).

247. McLane, L. M., Abdel-Hakeem, M. S. & Wherry, E. J. CD8 T Cell Exhaustion During Chronic Viral Infection and Cancer. *Annual Review of Immunology* **37,** 1–39 (2015).

248. Im, S. J. *et al.* Defining CD8+ T cells that provide the proliferative burst after PD-1 therapy. *Nature* **537,** 417–421 (2016).

249. Zajac, A. J. *et al.* Viral Immune Evasion Due to Persistence of Activated T Cells Without Effector Function. *Journal of Experimental Medicine* **188,** 2205–2213 (1998).

250. Siddiqui, I. *et al.* Intratumoral Tcf1+PD-1+CD8+ T Cells with Stem-like Properties Promote Tumor Control in Response to Vaccination and Checkpoint Blockade Immunotherapy. *Immunity* **50,** 195–211.e10 (2019).

251. Miller, B. C. *et al.* Subsets of exhausted CD8+ T cells differentially mediate tumor control and respond to checkpoint blockade. *Nature Immunology* **20,** 326–336 (2019).

252. Mandala, S. *et al.* Alteration of Lymphocyte Trafficking by Sphingosine-1-Phosphate Receptor Agonists. *Science* **296,** 346–349 (2002).

253. Wu, T. D. *et al.* Peripheral T cell expansion predicts tumour infiltration and clinical response. *Nature* **579,** 274–278 (2020).

254. Leun, A. M. v. d., Thommen, D. S. & Schumacher, T. N. CD8+ T cell states in human cancer: insights from single-cell analysis. *Nature Reviews Cancer* **20,** 218–232 (2020).

255. Zuazo, M. *et al.* Functional systemic CD4 immunity is required for clinical responses to PD-L1/PD-1 blockade therapy. *EMBO Molecular Medicine* **11,** e10293 (2019).

256. Kamada, T. *et al.* PD-1+ regulatory T cells amplified by PD-1 blockade promote hyperprogression of cancer. *Proceedings of the National Academy of Sciences* **116,** 9999–10008 (2019).

257. Kumagai, S. *et al.* The PD-1 expression balance between effector and regulatory T cells predicts the clinical efficacy of PD-1 blockade therapies. *Nature Immunology* **21,** 1346–1358 (2020).

258. Russo, G. L. *et al.* Antibody-Fc/FcR Interaction on Macrophages as a Mechanism for Hyperprogressive Disease in Non-Small Cell Lung Cancer Subsequent to PD-1/PD-L1 Blockade. *Clinical Cancer Research* **25,** 989–999 (2018).

259. Garcia-Diaz, A. *et al.* Interferon Receptor Signaling Pathways Regulating PD-L1 and PD-L2 Expression. *Cell Reports* **19,** 1189–1201 (2017).

260. Herbst, R. S. *et al.* Predictive correlates of response to the anti-PD-L1 antibody MPDL3280A in cancer patients. *Nature* **515,** 563–567 (2014).

261. Powles, T. *et al.* MPDL3280A (anti-PD-L1) treatment leads to clinical activity in metastatic bladder cancer. *Nature* **515,** 558–562 (2014).

262. Reck, M. *et al.* Pembrolizumab versus Chemotherapy for PD-L1–Positive Non–Small-Cell Lung Cancer. *The New England Journal of Medicine* **375,** 1823–1833 (2016).

263. Tumeh, P. C. *et al.* PD-1 blockade induces responses by inhibiting adaptive immune resistance. *Nature* **515,** 568–571 (2014).

264. Snyder, A. *et al.* Genetic Basis for Clinical Response to CTLA-4 Blockade in Melanoma. *The New England Journal of Medicine* **371,** 2189–2199 (2014).

265. Allen, E. M. V. *et al.* Genomic correlates of response to CTLA-4 blockade in metastatic melanoma. *Science* **350,** 207–211 (2015).

266. Rizvi, N. A. *et al.* Mutational landscape determines sensitivity to PD-1 blockade in non-small cell lung cancer. *Science* **348,** 124–128 (2015).

267. Yarchoan, M., Alexander, H. & Jaffee, E. M. Tumor Mutational Burden and Response Rate to PD-1 Inhibition. *New England Journal of Medicine* **377,** 2500–2501 (2017).

268. Le, D. T. *et al.* PD-1 Blockade in Tumors with Mismatch-Repair Deficiency. *New England Journal of Medicine* **372,** 2509–2520 (2015).

269. Le, D. T. *et al.* Mismatch repair deficiency predicts response of solid tumors to PD-1 blockade. *Science* **357,** 409–413 (2017).

270. Marcus, L., Lemery, S. J., Keegan, P. & Pazdur, R. FDA Approval Summary: Pembrolizumab for the Treatment of Microsatellite Instability-High Solid Tumors. *Clinical Cancer Research* **25,** 3753–3758 (2019).

271. Routy, B. *et al.* Gut microbiome influences efficacy of PD-1–based immunotherapy against epithelial tumors. *Science* **359,** 91–97 (2018).

272. Matson, V. *et al.* The commensal microbiome is associated with anti–PD-1 efficacy in metastatic melanoma patients. *Science* **359,** 104–108 (2018).

273. Chowell, D. *et al.* Patient HLA class I genotype influences cancer response to checkpoint blockade immunotherapy. *Science* **359,** 582–587 (2018).

274. Li, H., Merwe, P. A. v. d. & Sivakumar, S. Biomarkers of response to PD-1 pathway blockade. *British Journal of Cancer* **126,** 1663–1675 (2022).

275. Kusmartsev, S., Nagaraj, S. & Gabrilovich, D. I. Tumor-Associated CD8+ T Cell Tolerance Induced by Bone Marrow-Derived Immature Myeloid Cells. *The Journal of Immunology* **175,** 4583–4592 (2005).

276. Engelhardt, J. J. *et al.* Marginating Dendritic Cells of the Tumor Microenvironment Cross-Present Tumor Antigens and Stably Engage Tumor-Specific T Cells. *Cancer Cell* **21,** 402–417 (2012).

277. Alloatti, A. *et al.* Critical role for Sec22b-dependent antigen cross-presentation in antitumor immunity. *Journal of Experimental Medicine* **214,** 2231–2241 (2017).

278. Garris, C. S. *et al.* Successful Anti-PD-1 Cancer Immunotherapy Requires T Cell-Dendritic Cell Crosstalk Involving the Cytokines IFN-g and IL-12. *Immunity* **49,** 1148–1161.e7 (2018).

279. Chow, M. T. *et al.* Intratumoral Activity of the CXCR3 Chemokine System Is Required for the Efficacy of Anti-PD-1 Therapy. *Immunity* **50,** 1498–1512.e5 (2019).

280. Kumar, V., Patel, S., Tcyganov, E. & Gabrilovich, D. I. The Nature of Myeloid-Derived Suppressor Cells in the Tumor Microenvironment. *Trends in Immunology* **37,** 208–220 (2016).

281. Zhang, Q.-w. *et al.* Prognostic Significance of Tumor-Associated Macrophages in Solid Tumor: A Meta-Analysis of the Literature. *PLoS ONE* **7,** e50946 (2012).

282. Sanchez, L. R. *et al.* The emerging roles of macrophages in cancer metastasis and response to chemotherapy. *Journal of Leukocyte Biology* **106,** 259–274 (2019).

283. Zhu, Y. *et al.* CSF1/CSF1R blockade reprograms tumor-infiltrating macrophages and improves response to T-cell checkpoint immunotherapy in pancreatic cancer models. *Cancer Research* **74,** 5057–5069 (2014).

284. Jensen, J. L. *et al.* Tumoricidal Effects of Macrophage-Activating Immunotherapy in a Murine Model of Relapsed/Refractory Multiple Myeloma. *Cancer Immunology* **3,** 881–890 (2015).

285. Tseng, D. *et al.* Anti-CD47 antibody-mediated phagocytosis of cancer by macrophages primes an effective antitumor T-cell response. *Proceedings of the National Academy of Sciences* **110,** 11103–11108 (2013).

286. Beatty, G. L. *et al.* CD40 Agonists Alter Tumor Stroma and Show Efficacy Against Pancreatic Carcinoma in Mice and Humans. *Science* **331,** 1612–1616 (2011).

287. Hoves, S. *et al.* Rapid activation of tumor-associated macrophages boosts preexisting tumor immunity. *Journal of Experimental Medicine* **215,** 859–876 (2018).

288. Chen, S.-H. *et al.* Dual checkpoint blockade of CD47 and PD-L1 using an affinity-tuned bispecific antibody maximizes antitumor immunity. *Journal for ImmunoTherapy of Cancer* **9,** e003464 (2021).

289. Ma, H. S. *et al.* A CD40 agonist and PD-1 antagonist antibody reprogram the microenvironment of non-immunogenic tumors to allow T cell-mediated anticancer activity. *Cancer Immunology Research* **7,** 428–442 (2019).

290. Koning, N. *et al.* Expression of the inhibitory CD200 receptor is associated with alternative macrophage activation. *Journal of Innate Immunity* **2,** 195–200 (2010).

291. Pilch, Z. *et al.* Antitumor Activity of TLR7 Is Potentiated by CD200R Antibody Leading to Changes in the Tumor Microenvironment. *Cancer Immunology Research* **6,** 930–940 (2018).

292. Yi, M. *et al.* Combination strategies with PD-1/PD-L1 blockade: current advances and future directions. *Molecular Cancer* **21,** 28 (2022).

293. Akkaya, B. *Modulation of the PD-1 pathway by inhibitory antibody superagonists* DPhil thesis (University of Oxford, 2012).

294. Paluch, C. *Manipulating immune checkpoint signalling pathways with antibodies* DPhil thesis (University of Oxford, 2019).

295. Magiera-Mularz, K. *et al.* Human and mouse PD-L1: similar molecular structure, but different druggability profiles. *iScience* **24,** 101960 (2021).

296. Aßmann, M. C. *Imaging-based analysis of antibody superagonism* DPhil thesis (University of Oxford, 2016).

297. Hatherley, D. & Barclay, A. N. The CD200 and CD200 receptor cell surface proteins interact through their N-terminal immunoglobulin-like domains. *European Journal of Immunology* **34,** 1688–1694 (2004).

298. Jutz, S. *et al.* A cellular platform for the evaluation of immune checkpoint molecules. *Oncotarget* **8,** 64892–64906 (2017).

299. Malyala, P. & Singh, M. Endotoxin limits in formulations for preclinical research. *Journal of Pharmaceutical Sciences* **97,** 2041–2044 (2008).

300. Bernardo, M. *et al.* An experimental model of anti-PD-1 resistance exhibits activation of TGFbeta and Notch pathways and is sensitive to local mRNA immunotherapy. *OncoImmunology* **10,** 1881268 (2021).

301. Duan, Q., Zhang, H., Zheng, J. & Zhang, L. Turning Cold into Hot: Firing up the Tumor Microenvironment. *Trends in Cancer* **6,** 605–618 (2020).

302. Lilienthal, G.-M. *et al.* Potential of Murine IgG1 and Human IgG4 to Inhibit the Classical Complement and Fcgamma Receptor Activation Pathways. *Frontiers in Immunology* **9,** 958 (2018).

303. Nagaoka, M. & Akaike, T. Single amino acid substitution in the mouse IgG1 Fc region induces drastic enhancement of the affinity to protein A. *Protein Engineering, Design and Selection* **16,** 243–245 (2003).

304. Wetterhall, M. *et al.* Investigation of alkaline effects on Protein A affinity ligands and resins using high resolution mass spectrometry. *Journal of Chromatography B* **1162,** 122473 (2021).

305. Yanagihara, T., Tanaka, K. & Matsumoto, K. A measuring method for occupancy of immune checkpoint inhibitors in the cell surface. *Biochemical and Biophysical Research Communications* **527,** 213–217 (2020).

306. Sun, C. *et al.* Neoantigen Dendritic Cell Vaccination Combined with Anti-CD38 and CpG Elicits Anti-Tumor Immunity against the Immune Checkpoint Therapy-Resistant Murine Lung Cancer Cell Line LLC1. *Cancers* **13,** 5508 (2021).

307. Xu, B.-L. *et al.* In vivo growth of subclones derived from Lewis lung carcinoma is determined by the tumor microenvironment. *American Journal of Cancer Research* **12,** 5255–5270 (2022).

308. Shin-Ya, M. *et al.* Interleukin-2 Abolishes Myeloid Cell Accumulation Induced by Lewis Lung Carcinoma. *Journal of Interferon & Cytokine Research* **23,** 631–638 (2003).

309. Mosely, S. I. *et al.* Rational Selection of Syngeneic Preclinical Tumor Models for Immunotherapeutic Drug Discovery. *Cancer Immunology Research* **5,** 29–41 (2017).

310. Szklarczyk, D. *et al.* The STRING database in 2023: protein–protein association networks and functional enrichment analyses for any sequenced genome of interest. *Nucleic Acids Research* **51,** D638–D646 (2022).

311. Zhang, W. & Liu, H. T. MAPK signal pathways in the regulation of cell proliferation in mammalian cells. *Cell Research* **12,** 9–18 (2002).

312. Zarubin, T. & Han, J. Activation and signaling of the p38 MAP kinase pathway. *Cell Research* **15,** 11–18 (2005).

313. Gialeli, C., Theocharis, A. D. & Karamanos, N. K. Roles of matrix metalloproteinases in cancer progression and their pharmacological targeting. *The FEBS Journal* **278,** 16–27 (2011).

314. Rømer, A. M. A., Thorseth, M.-L. & Madsen, D. H. Immune Modulatory Properties of Collagen in Cancer. *Frontiers in Immunology* **12,** 791453 (2021).

315. Bergonzini, C., Kroese, K., Zweemer, A. J. M. & Danen, E. H. J. Targeting Integrins for Cancer Therapy - Disappointments and Opportunities. *Frontiers in Cell and Developmental Biology* **10,** 863850 (2022).

316. Xu, S. *et al.* The role of collagen in cancer: from bench to bedside. *Journal of Translational Medicine* **17,** 309 (2019).

317. Kuczek, D. E. *et al.* Collagen density regulates the activity of tumor-infiltrating T cells. *Journal for ImmunoTherapy of Cancer* **7,** 68 (2019).

318. Deligne, C. *et al.* Matrix-Targeting Immunotherapy Controls Tumor Growth and Spread by Switching Macrophage Phenotype. *Cancer Immunology Research* **8,** 368–382 (2020).

319. Wang, C. *et al.* In Vitro Characterization of the Anti-PD-1 Antibody Nivolumab, BMS-936558, and In Vivo Toxicology in Non-Human Primates. *Cancer Immunology Research* **2,** 846–856 (2014).

320. Fu, L. *et al.* DGKA Mediates Resistance to PD-1 Blockade. *Cancer Immunology Research* **9,** 371–385 (2021).

321. Bedognetti, D., Roelands, J., Decock, J., Wang, E. & Hendrickx, W. The MAPK hypothesis: immune-regulatory effects of MAPK-pathway genetic dysregulations and implications for breast cancer immunotherapy. *Emerging Topics in Life Sciences* **1,** 429–445 (2017).

322. Montfort, A. *et al.* The TNF Paradox in Cancer Progression and Immunotherapy. *Frontiers in Immunology* **10,** 1818 (2019).

323. Mitri, D. D. *et al.* Re-education of Tumor-Associated Macrophages by CXCR2 Blockade Drives Senescence and Tumor Inhibition in Advanced Prostate Cancer. *Cell Reports* **28,** 2156–2168.e5 (2019).

324. Cowles, S. C. *et al.* An affinity threshold for maximum efficacy in anti-PD-1 immunotherapy. *mAbs* **14,** 2088454 (2022).

325. Gonzalez, L., Woolfson, D. N. & Alber, T. Buried polar residues and structural specificity in the GCN4 leucine zipper. *Nature Structural Biology* **3,** 1011–1018 (1996).

326. Wang, Q. *et al.* Enhancement of antibody functions through Fc multiplications. *mAbs* **9,** 393–403 (2017).

327. Cyster, J. G., Shotton, D. M. & Williams, A. F. The dimensions of the T lymphocyte glycoprotein leukosialin and identification of linear protein epitopes that can be modified by glycosylation. *The EMBO Journal* **10,** 893–902 (1991).

328. Harbury, P. B., Zhang, T., Kim, P. S. & Alber, T. A switch between two-, three-, and four-stranded coiled coils in GCN4 leucine zipper mutants. *Science* **262,** 1401–1407 (1993).

329. Wolgemuth, C. W. & Sun, S. X. Elasticity of alpha-helical coiled coils. *Physical Review Letters* **97,** 248101 (2006).

330. Truebestein, L., Elsner, D. J., Fuchs, E. & Leonard, T. A. A molecular ruler regulates cytoskeletal remodelling by the Rho kinases. *Nature Communications* **6,** 10029 (2015).

331. Stokke, B. T., Elgsaeter, A., Skjrak-Brjek, G. & Smidsrød, O. The molecular size and shape of xanthan, xylinan, bronchial mucin, alginate, and amylose as revealed by electron microscopy. *Carbohydrate Research* **160,** 13–28 (1987).

332. Shogren, R., Gerken, T. A. & Jentoft, N. Role of glycosylation on the conformation and chain dimensions of O-linked glycoproteins: light-scattering studies of ovine submaxillary mucin. *Biochemistry* **28,** 5525–5536 (1989).

333. Duvaud, S. *et al.* Expasy, the Swiss Bioinformatics Resource Portal, as designed by its users. *Nucleic Acids Research* **49,** W216–W227 (2021).

334. Williams, E. L. *et al.* Development and characterisation of monoclonal antibodies specific for the murine inhibitory FcgammaRIIB (CD32B). *European Journal of Immunology* **42,** 2109–2120 (2012).

335. Teige, I., Mårtensson, L. & Frendéus, B. L. Targeting the Antibody Checkpoints to Enhance Cancer Immunotherapy–Focus on FcgammaRIIB. *Frontiers in Immunology* **10,** 481 (2019).

336. Grubisic, Z., Rempp, P. & Benoit, H. A universal calibration for gel permeation chromatography. *Journal of Polymer Science Part B: Polymer Letters* **5,** 753–759 (1967).

337. Zheng, K., Bantog, C. & Bayer, R. The impact of glycosylation on monoclonal antibody conformation and stability. *mAbs* **3,** 568–576 (2011).

338. Son, S. *et al.* Molecular height measurement by cell surface optical profilometry (CSOP). *Proceedings of the National Academy of Sciences* **117,** 14209–14219 (2020).

339. GE Healthcare. *Biacore Sensor Surface Handbook* BR-1005-71 Edition AB (1998).

340. Valeich, J. *et al.* Taking the Hinge off: An Approach to Effector-Less Monoclonal Antibodies. *Antibodies* **9,** 50 (2020).

341. Fernandes, R. A. *et al.* Immune receptor inhibition through enforced phosphatase recruitment. *Nature* **586,** 779–784 (2020).

342. Steiner, L. A. & Lopes, A. D. Crystallizable human myeloma protein Dob has a hinge-region deletion. *Biochemistry* **18,** 4054–4067 (1979).

343. Guddat, L. W., Herron, J. N. & Edmundson, A. B. Three-dimensional structure of a human immunoglobulin with a hinge deletion. *Proceedings of the National Academy of Sciences* **90,** 4271–4275 (1993).

344. Madeira, F. *et al.* Search and sequence analysis tools services from EMBL-EBI in 2022. *Nucleic Acids Research* **50,** W276–W279 (2022).

345. Thies, M. J. *et al.* Folding and association of the antibody domain CH3: prolyl isomerization preceeds dimerization. *Journal of Molecular Biology* **293,** 67–79 (1999).

346. Feige, M. J. *et al.* Structure of the Murine Unglycosylated IgG1 Fc Fragment. *Journal of Molecular Biology* **391,** 599–608 (2009).

347. Chen, X., Zaro, J. L. & Shen, W.-C. Fusion protein linkers: Property, design and functionality. *Advanced Drug Delivery Reviews* **65,** 1357–1369 (2013).

348. Grakoui, A. *et al.* The Immunological Synapse: A Molecular Machine Controlling T Cell Activation. *Science* **285,** 221–227 (1999).

349. Jenkins, E. *et al.* Antigen discrimination by T cells relies on size-constrained microvillar contact. *Nature Communications* **14,** 1611 (2023).

350. Peng, D. H. *et al.* Collagen promotes anti-PD-1/PD-L1 resistance in cancer through LAIR1-dependent CD8+ T cell exhaustion. *Nature Communications* **11,** 4520 (2020).

351. Larsen, A. M. H. *et al.* Collagen Density Modulates the Immunosuppressive Functions of Macrophages. *The Journal of Immunology* **205,** 1461–1472 (2020).

352. Marcheteau, E. *et al.* Thrombospondin-1 Silencing Improves Lymphocyte Infiltration in Tumors and Response to Anti-PD-1 in Triple-Negative Breast Cancer. *Cancers* **13,** 4059 (2021).

353. Malenica, I. *et al.* Integrin-alphaV-mediated activation of TGF-beta regulates anti-tumour CD8 T cell immunity and response to PD-1 blockade. *Nature Communications* **12,** 5209 (2021).

354. Guerin, M. V., Finisguerra, V., Eynde, B. J. V. d., Bercovici, N. & Trautmann, A. Preclinical murine tumor models: A structural and functional perspective. *eLife* **9,** e50740 (2020).

355. Kaplon, H., Crescioli, S., Chenoweth, A., Visweswaraiah, J. & Reichert, J. M. Antibodies to watch in 2023. *mAbs* **15,** 2153410 (2023).

356. White, A. L. *et al.* Interaction with FcgammaRIIB Is Critical for the Agonistic Activity of Anti-CD40 Monoclonal Antibody. *The Journal of Immunology* **187,** 1754–1763 (2011).

357. Chu, S. Y. *et al.* Inhibition of B cell receptor-mediated activation of primary human B cells by coengagement of CD19 and FcgammaRIIb with Fc-engineered antibodies. *Molecular Immunology* **45,** 3926–3933 (2008).

358. Li, F. & Ravetch, J. V. Inhibitory Fcgamma Receptor Engagement Drives Adjuvant and Anti-Tumor Activities of Agonistic CD40 Antibodies. *Science* **333,** 1030–1034 (2011).

359. Muik, A. *et al.* DuoBody-CD40x4-1BB induces dendritic-cell maturation and enhances T-cell activation through conditional CD40 and 4-1BB agonist activity. *Journal for ImmunoTherapy of Cancer* **10,** e004322 (2022).

360. Business Wire. *Gilead Sciences to Acquire MiroBio* Press release (2022).

Appendices

A Appendix

A.1 Protein sequences

Below are the protein sequences that make up all proteins produced or over-expressed in this thesis. A short annotation of the sequence is provided by colouring of the text, where appropriate. All heavy/light chains were designed with an N-terminal hCD33 signal peptide (MPLLLLLPLLWAGALA). $*$ indicates a stop codon.

A.1.1 hCD200R-hPD-1

hCD200R signal peptide domain-hCD200R extracellular domain-hCD200R transmembrane domain-hPD-1 cytoplasmic domain

MLCPWRTANLGLLLILTIFLVAASSSLCMDEKQITQNYSKVLAEVNTSWPV
KMATNAVLCCPPIALRNLIIITWEIILRGQPSCTKAYKKETNETKETNCTDE
RITWVSRPDQNSDLQIRTVAITHDGYYRCIMVTPDGNFHRGYHLQVLVTP
EVTLFQNRNRTAVCKAVAGKPAAHISWIPEGDCATKQEYWSNGTVTVKS
TCHWEVHNVSTVTCHVSHLTGNKSLYIELLPVPGAKKSAKLYIPYIILTIIIL
TIVGFIWLLCSRAARGTIGARRTGQPLKEDPSAVPVFSVDYGELDFQWREK
TPEPPVPCVPEQTEYATIVFPSGMGTSSPARRGSADGPRSAQPLRPEDGHC
SWPL$*$

A.1.2 hCD200

hCD200 signal peptide domain-hCD200 extracellular domain-hCD200 transmembrane domain-hCD200 cytoplasmic domain

MERLVIRMPFSHLSTYSLVWVMAAVVLCTAQVQVVTQDEREQLYTPASLK
CSLQNAQEALIVTWQKKKAVSPENMVTFSENHGVVIQPAYKDKINITQLGL
QNSTITFWNITLEDEGCYMCLFNTFGFGKISGTACLTVYVQPIVSLHYKFS
EDHLNITCSATARPAPMVFWKVPRSGIENSTVTLSHPNGTTSVTSILHIKD
PKNQVGKEVICQVLHLGTVTDFKQTVNKGYWFSVPLLLSIVSLVILLVLISIL
LYWKRHRNQDRGELSQGVQKMT*

A.1.3 Truncated mFcγRIIb

The truncation site was picked shortly after a sequence of positively charged amino acids (KKK) to facilitate membrane-anchoring. Importantly, this truncation removes all phosphotyrosines.

mFcγRIIb signal peptide domain-mFcγRIIb extracellular domain-mFcγRIIb transmembrane domain-mFcγRIIb truncated cytoplasmic domain

MESNWTVHVFSRTLCHMLLWTAVLNLAAGTHDLPKAVVKLEPPWIQVLK
EDTVTLTCEGTHNPGNSSTQWFHNGRSIRSQVQASYTFKATVNDSGEYRC
QMEQTRLSDPVDLGVISDWLLLQTPQLVFLEGETITLRCHSWRNKLLNRIS
FFHNEKSVRYHHYSSNFSIPKANHSHSGDYYCKGSLGRTLHQSKPVTITVQ
GPKSSRSLPVLTIVAAVTGIAVAAIVIILVSLVYLKKKQVPAL*

A.1.4 hPD-1-2xHis

hPD-1 signal peptide-hPD-1 extracellular domain-double His-tag

MQIPQAPWPVVWAVLQLGWRPGWFLDSPDRPWNPPTFSPALLVVTEG
DNATFTCSFSNTSESFVLNWYRMSPSNQTDKLAAFPEDRSQPGQDCRFR
VTQLPNGRDFHMSVVRARRNDSGTYLCGAISLAPKAQIKESLRAELRVT
ERRAEVPTAHPSPSPRPAGQFQHHHHHHSRAWRHPQFGGHHHHHH*

A.1.5 Mouse κ light chain

Mouse κ constant light chain

RADAAPTVSIFPPSSEQLTSGGASVVCFLNNFYPKDINVKWKIDGSERQNG
VLNSWTDQDSKDSTYSMSSTLTLTKDEYERHNSYTCEATHKTSTSPIVKSF
NRNEC*

A.1.6 Nivolumab light chain

Nivolumab variable light chain. This sequence was combined with the mouse κ constant light chain sequence (Sequence A.1.5) on the C-terminus.

EIVLTQSPATLSLSPGERATLSCRASQSVSSYLAWYQQKPGQAPRLLIYDA
SNRATGIPARFSGSGSGTDFTLTISSLEPEDFAVYYCQQSSNWPRTFGQGT
KVEIK

A.1.7 OX108 light chain

OX108 variable light chain. This sequence was combined with the mouse κ constant light chain sequence (Sequence A.1.5) on the C-terminus.

DIVLTQSPASLAVSLGQRATISCRASKSVSTSGYSYMHWYQQKPGQPPKLLI
YLASNLESGVPARFSGSGSGTDFTLNIHPVEEEDAATYYCQHSRELLTFGA
GTKLELK

A.1.8 MOPC21 light chain

MOPC21 variable light chain. This sequence was combined with the mouse κ constant light chain sequence (Sequence A.1.5) on the C-terminus.

NIVMTQSPKSMSMSVGERVTLTCKASENVVTYVSWYQQKPEQSPKLLIYG
ASNRYTGVPDRFTGSGSATDFTLTISSVQAEDLADYHCGQGYSYPYTFGG
GTKLEIK

A.1.9 Mouse IgG1 heavy chain

The D265A mutation in the CH2 domain is underlined. This mutation was reversed for some antibodies in Chapter 5.

CH1-Hinge-CH2-CH3

AKTTPPSVYPLAPGSAAQTNSMVTLGCLVKGYFPEPVTVTWNSGSLSSGV
HTFPAVLQSDLYTLSSSVTVPSSTWPSQTVTCNVAHPASSTKVDKKIVPRD
CGCKPCICTVPEVSSVFIFPPKPKDVLMISLTPKVTCVVVAISKDDPEVQFS
WFVDDVEVHTAQTKPREEQINSTFRSVSELPILHQDWLNGKEFKCRVNSA
AFPAPIEKTISKTKGRPKAPQVYTIPPPKEQMAKDKVSLTCMITNFFPED
ITVEWQWNGQPAENYKNTQPIMDTDGSYFVYSKLNVQKSNWEAGNTFT
CSVLHEGLHNHHTEKSLSHSPGK*

A.1.10 Nivolumab heavy chain

Nivolumab variable heavy chain. This sequence was combined with the mouse IgG1 heavy chain sequence (Sequence A.1.9) on the C-terminus.

QVQLVESGGGVVQPGRSLRLDCKASGITFSNSGMHWVRQAPGKGLEWVA
VIWYDGSKRYYADSVKGRFTISRDNSKNTLFLQMNSLRAEDTAVYYCATN
DDYWGQGTLVTVSS

A.1.11 OX108 heavy chain

OX108 variable light chain. This sequence was combined with the mouse IgG1 heavy chain sequence (Sequence A.1.9) on the C-terminus.

EFQLQQSGPELVKPGASVKMSCKASGYTFTSYVMHWVKQKPGQGLEWIG
YINPYNDDTNYNEKFKGKATLTSDKSSSTAYMELSSLTSEDSAVYYCARED
YYGSRWGYWGQGTTLTVSS

A.1.12 MOPC21 heavy chain

MOPC21 variable heavy chain. This sequence was combined with the mouse IgG1 heavy chain sequence (Sequence A.1.9) on the C-terminus.

DVQLVESGGGLVQPGGSRKLSCAASGFTFSSFGMHWVRQAPEKGLEWVA
YISSGSSTLHYADTVKGRFTISRDNPKNTLFLQMTSLRSEDTAMYYCARW
GNYPYYAMDYWGQGTSVTVSS

A.1.13 Mouse CD43 sequences

For the hinge extension, the following sequences were inserted, flanked by a short GS linker on both termini, into the hinge region at the position indicated by an arrow: VPRDC↓GCKPCICT
To extend between Fc-multiplexed antibodies, the 50 aa mCD43 extension was inserted using a flexible linker (GGGGS, Chapter 5) or a rigid linker (PAPAP, Chapter 6) on both termini.

50 aa mCD43 extension
RTTMLPSTPHITAPSTSEAQNASPSVSVGSGTVDSKETISPWGQTTIPVS

100 aa mCD43 extension
RTTMLPSTPHITAPSTSEAQNASPSVSVGSGTVDSKETISPWGQTTIPVSL
TPLETTELSSLETSAGASMSTPVPEPTASQEVSSKTSALLPEPSNVASD

150 aa mCD43 extension
RTTMLPSTPHITAPSTSEAQNASPSVSVGSGTVDSKETISPWGQTTIPVSL
TPLETTELSSLETSAGASMSTPVPEPTASQEVSSKTSALLPEPSNVASDPPV
TAANPVTDGPAANPVTDGTAASTSISKGTSAPPTTVTTSSNETSGPS

A.1.14 GCN4 sequences

To extend between Fc-multiplexed antibodies, a single or tripled coiled-coil domain from GCN4 was inserted using a flexible linker (GGGGS, Chapter 5).
Single GCN4 extension
MKQLEDKVEELLSKKYHLENEVARLKKL

Tripled GCN4 extension
MKQLEDKVEELLSKKYHLENEVARLKKLMKQLEDKVEELLSKKYHLEN
EVARLKKLMKQLEDKVEELLSKKYHLENEVARLKKL

A.2 Fitting of SPR data

Fits generated by the Biacore Insight Evaluation Software (Cytiva) for all presented SPR experiments described in this thesis are shown below. The black lines are the fit, the coloured lines refer to the original sensorgrams.

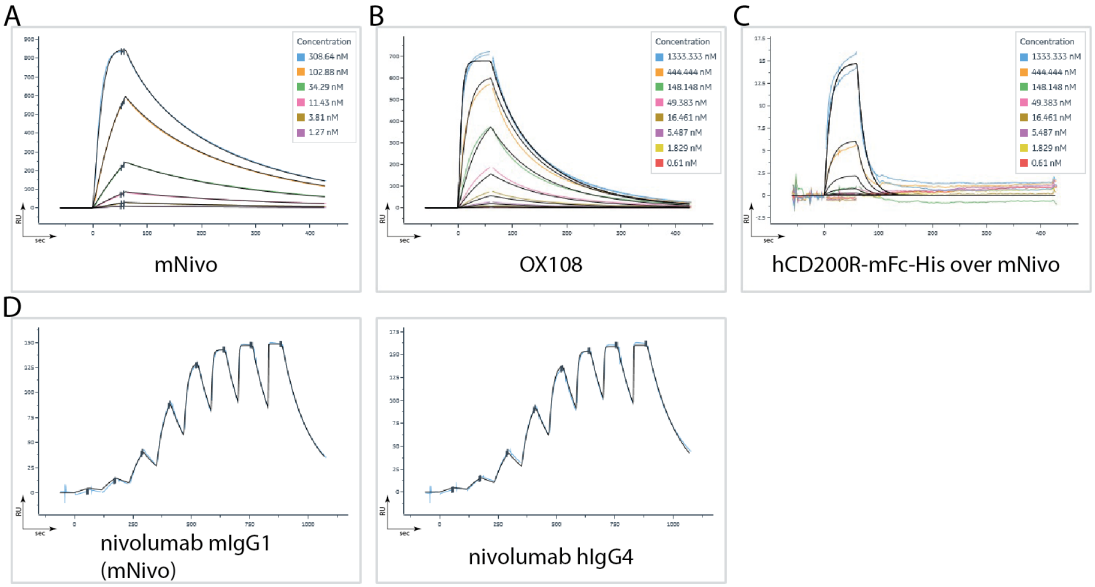


Figure A.1: SPR fitting for Figure 3.2
1:1 binding fits generated by the Biacore Insight Evaluation Software are shown for SPR experiments from Figure 3.2. Experiment was conducted as explained in the main figure.

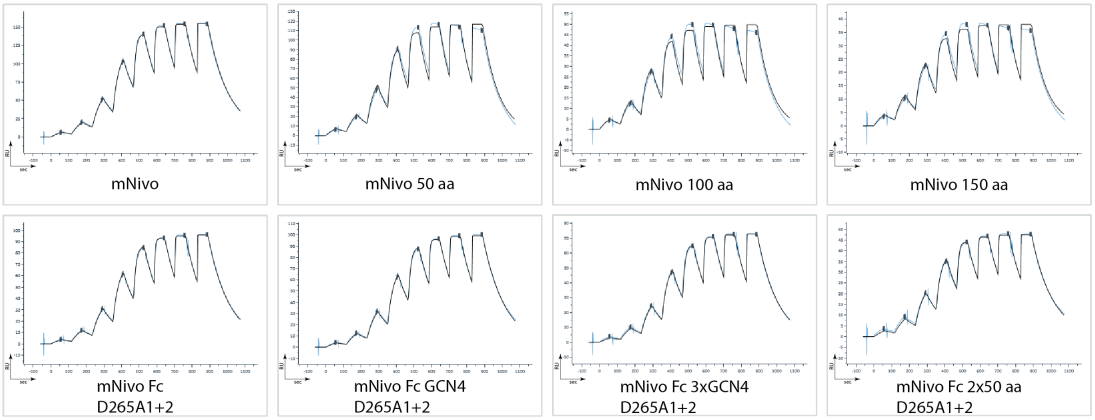


Figure A.2: SPR fitting for Figure 5.5
1:1 binding fits generated by the Biacore Insight Evaluation Software are shown for SPR experiments from Figure 5.5. Experiment was conducted as explained in the main figure.

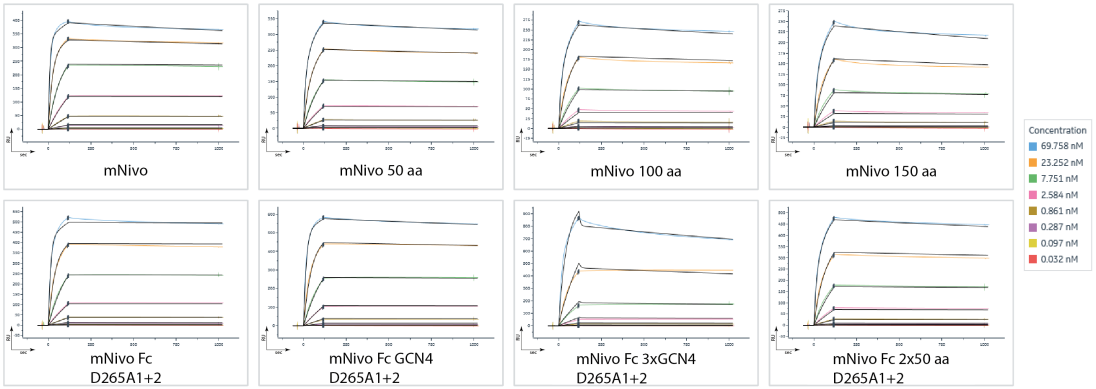


Figure A.3: SPR fitting for Figure 5.6
Bivalent binding fits generated by the Biacore Insight Evaluation Software are shown for SPR experiments from Figure 5.6. Experiment was conducted as explained in the main figure.

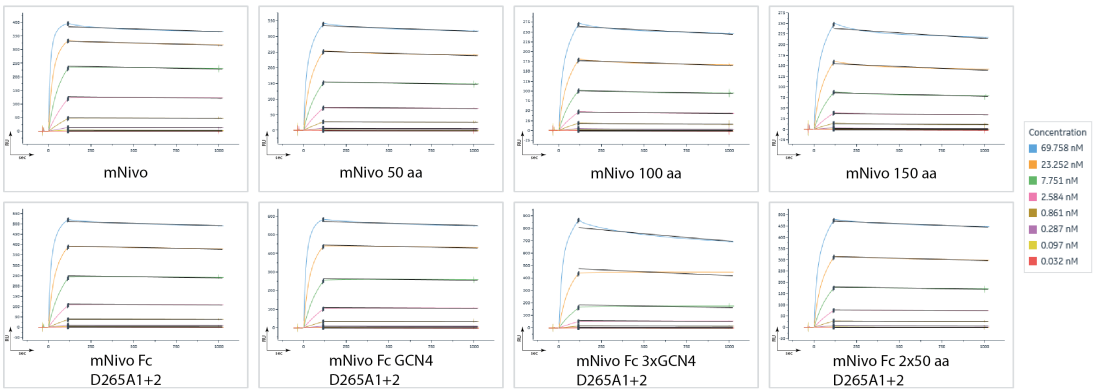


Figure A.4: SPR fitting for Figure 5.6
1:1 dissociation fits generated by the Biacore Insight Evaluation Software are shown for SPR experiments from Figure 5.6. Experiment was conducted as explained in the main figure.

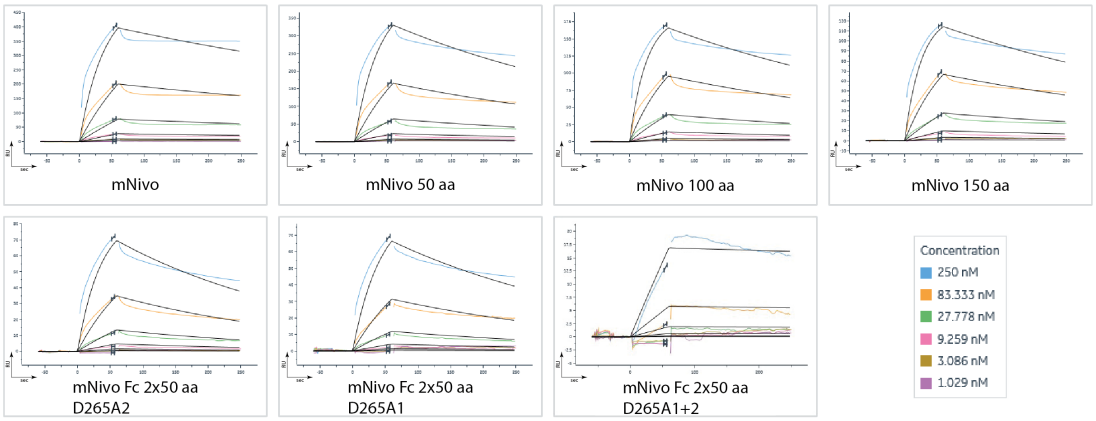


Figure A.5: SPR fitting for Figure 5.7
1:1 binding fits generated by the Biacore Insight Evaluation Software are shown for SPR experiments from Figure 5.7. Experiment was conducted as explained in the main figure.

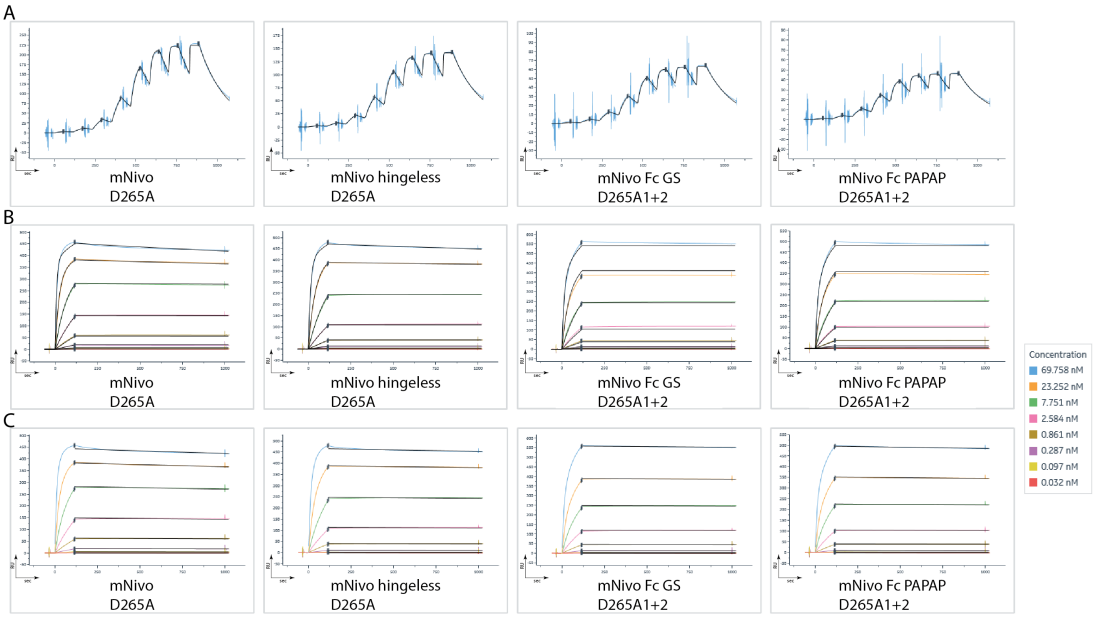


Figure A.6: SPR fitting for Figure 6.2
1:1 binding (A), bivalent binding (B) and 1:1 dissociation (C) fits generated by the Biacore Insight Evaluation Software are shown for SPR experiments from Figure 6.2. Experiment was conducted as explained in the main figure.

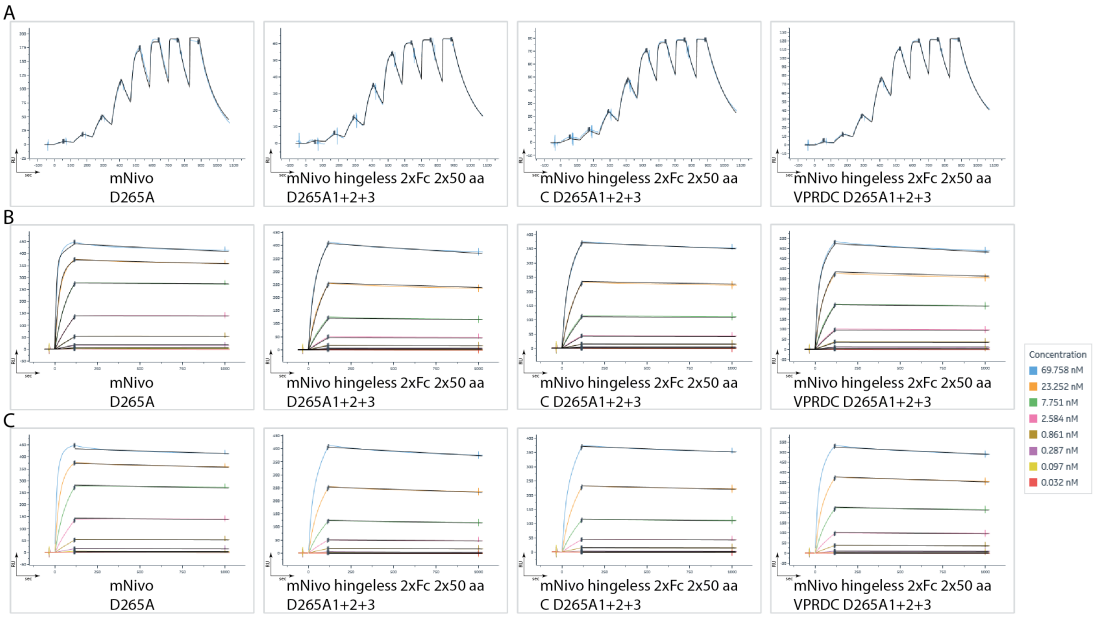


Figure A.7: SPR fitting for Figure 6.6
1:1 binding (A), bivalent binding (B) and 1:1 dissociation (C) fits generated by the Biacore Insight Evaluation Software are shown for SPR experiments from Figure 6.6. Experiment was conducted as explained in the main figure.